INVESTIGATING THE ROLES OF VACUOLES IN IRON TRAFFICKING IN *SACCHAROMYCES CEREVISIAE*

A Dissertation

by

ALLISON LEIGH COCKRELL

Submitted to the Office of Graduate and Professional Studies of
Texas A&M University
in partial fulfillment of the requirements for the degree of

DOCTOR OF PHILOSOPHY

Approved by:

Chair of Committee,	Paul A. Lindahl
Committee Members,	Frank Raushel
	Tatyana Igumenova
	Craig Kaplan
Head of Department,	Gregory Reinhart

December 2013

Major Subject: Biochemistry

ABSTRACT

Transition metals play essential roles in biological systems, but Fe can also be toxic to cells. In order to maintain this balance between necessity and toxicity mechanisms are employed for regulating and storing intracellular Fe. In *Saccharomyces cerevisiae,* vacuoles are responsible for sequestering, storing, and supplying Fe to the cytosol. Many of the proteins and regulatory pathways involved in Fe trafficking and storage in *S. cerevisiae* have been identified, but the forms of Fe which are involved in these processes have not been fully characterized.

In these studies, biophysical and bioanalytical techniques were used to study intracellular Fe distributions in *S. cerevisiae* cells and organelles. Ultimately, Fe-containing species were biophysically characterized and absolute Fe concentrations in cells and organelles were quantified. The motivation for these studies stemmed from previous studies which revealed that the majority of the whole-cell Fe is a non-heme, high-spin (NHHS) form of Fe^{3+}. This Fe is not localized to the mitochondria. The purpose of these studies was to determine if the vacuoles contained this NHHS Fe^{3+}.

A large-scale isolation procedure was developed to obtain purified vacuoles from *S. cerevisiae* and to investigate the Fe in these organelles. Mössbauer and EPR analysis revealed that the primary form of Fe in vacuoles is a mononuclear, NHHS Fe^{3+} species. A second form of Fe was also observed as superparamagnetic ferric phosphate nanoparticles (NP). By investigating model compounds of Fe and polyphosphate we determined that a shift in vacuolar pH induces the conversion between NHHS Fe^{3+} and

NP. These results showed that there are at least two forms of Fe in vacuoles, and that the ratio of these two forms is dependent upon the pH of these organelles.

Biophysical analyses of whole cells also revealed the presence of low concentrations of a non-heme, high-spin Fe^{2+} species. The goal of these next projects was to determine if this NHHS Fe^{2+} species was localized to the cytosol. Genetic strains lacking or over-expressing the vacuolar Fe import protein Ccc1p were studied by Mössbauer spectroscopy (Δ*CCC1* and *CCC1-up*, respectively). Δ*CCC1* cells showed low vacuolar Fe (NHHS Fe^{3+} and NP), and increased NHHS Fe^{2+}. We hypothesize that this NHHS Fe^{2+} is cytosolic Fe. We also propose that this NHHS Fe^{2+} is involved in the regulating intracellular Fe levels.

CCC1-up cells accumulated more Fe than wild-type (WT) cells, and showed elevated levels of vacuolar Fe (NHHS Fe^{3+} and NP). These cells also accumulated high levels of NHHS Fe^{2+}. The *CCC1-up* cells exhibited an adenine deficient phenotype, where the cells developed a red color during growth. With excess adenine the levels of NHHS Fe^{2+} declined, which indicated that this Fe accumulation was related to adenine deficiency. We conclude that adenine deficiency leads to the accumulation of a sequestered (possibly vacuolar) form of NHHS Fe^{2+}. Overall, we have identified two separate pools of NHHS Fe^{2+} in Δ*CCC1* and *CCC1-up* cells. In Δ*CCC1* cells the NHHS Fe^{2+} pool is localized to the cytosol and is sensed by the cell. In *CCC1-up* cells the NHHS Fe^{2+} is sequestered from the Fe regulatory mechanism- possibly in the vacuoles. These data have helped us better understand the roles of vacuoles in Fe trafficking and the dynamics of vacuolar Fe trafficking.

DEDICATION

For my grandparents, Anthony and Elaine Moreau, and Emmit “Slim” Cockrell and Esther Cockrell, who knew the value of education but did not have the opportunities to pursue their own.

ACKNOWLEDGEMENTS

I would like to thank my advisor, Dr. Paul A. Lindahl, for giving me the opportunity to study in his laboratory. Thank you for your encouragement, your advice, and your patience over these years. I appreciate your attention to detail, dedication to answering complex scientific questions, and ability to constantly think about the future directions of your research group. Thank you for doing anything and everything for your students and for being available to us at any time.

I would also like to thank my committee members, Dr. Frank Raushel, Dr. Tatyana Igumenova, and Dr. Craig Kaplan, for their constructive criticism, comments and suggestions throughout the course of this research. Thank you to Dr. Brad Pierce (University of Texas Arlington), for allowing us to collect EPR in his lab. Thank you to Dr. Jerry Kaplan (University of Utah) for generously providing us with the Δ*CCC1* and *CCC1-up* strains and the Ccc1p antibody used in this dissertation, and for his insightful and encouraging comments during his visits to Texas A&M University. Special thanks to Ms. Ann Ellis for her instruction and guidance for the TEM experiments. Also thanks to Dr. Kevin Burgess for providing Compound 5. Thanks to the National Institutes of Health and the Robert A. Welch Foundation for providing the funds required to perform this research. Thanks also to Texas A&M University, the Department of Biochemistry and Biophysics and Department of Chemistry for allowing me to perform this research and giving me the opportunity to pursue this degree.

Thank you to former members of the Lindahl group, Dr. Jessica Garber-Morales, Dr. Ren Miao, Dr. Gregory Holmes-Hampton, and Dr. Nema Jhurry, for performing the

initial experiments which led to the development of this project. Thank you to the current Lindahl group members for their helpful comments and questions during group meetings and discussions. Thanks to Dr. Mrinmoy Chakrabrti for sharing his extensive knowledge about spectroscopy and bioinorganic chemistry, and for answering my questions about EPR and Mössbauer. Thanks to Mr. Sean McCormick for performing the ICP-MS experiments and LC-ICP-MS experiments presented in these studies, and for sharing conversations and coffee breaks with me during our time as lab- and office-mates. Thanks to Mr. Michael Moore for being the always-smiling "Hines Ward" of the lab, and for listening patiently as I worked through ideas. Thank you to Mr. Jinkyu Park for his insightful comments and suggestions during meetings and discussions. Special thanks to Dr. Lora Lindahl, who willingly shared her knowledge of anatomy and physiology and patiently taught us how to perform animal-related experiments. Thank you, Lora and Paul, for opening your home to the group to host lab get-togethers.

Thanks to the Department of Biochemistry and Biophysics and Department of Chemistry staff for their assistance during this time. Special thanks to Mr. Will Seward, for his willingness to teach the graduate student machining workshop, and for being constantly available to help with our projects. Thank you to my close friends and colleagues at Texas A&M University (Dr. Katherine Leehy, Mrs. Brittany Duncan, Mrs. Amy Whitaker, Dr. Alissa Goble, Ms. Zuzanna Barnova, and Mrs. Michal Holland) for their friendship, support, and discussions.

Thank you to my wonderful parents, Mr. Ervin and Mrs. Denise Cockrell, for their constant support and encouragement during this time, and for teaching me that

persistence is an important part of achieving my goals. Thank you to my sisters, Ashlyn, Alayne, Alyssa, and Amanda Cockrell, for always knowing what to say and for listening to me talk about my research. Finally, thank you to Dr. David Zugell, II for his love and support over these years. Thank you for listening to me repeat ideas about iron trafficking (and had nothing to do with polymer chemistry), for always having a positive attitude, and for being the voice of reason in my life.

NOMENCLATURE

BPS	Bathophenanthrolinesulfonate
CCC1	Gene encoding Ccc1p
Ccc1p	Fe importer protein on the vacuolar membrane
CCC1-up	Yeast strain with Ccc1p over-expressed
Compound 5	Fluroescent compound described in (Burgess)
CPY	Carboxypeptidase Y
D1	Δ*CCC1* cells grown with 1 μM FC
D10	Δ*CCC1* cells grown with 10 μM FC
D20	Δ*CCC1* cells grown with 20 μM FC
D40	Δ*CCC1* cells grown with 40 μM FC
DDDI	Double-distilled and deionized
DDSA	Dodecenyl succinic anhydride
DEAE	Diethylaminoethyl
DTT	dithiothreitol
EPR	Electron paramagnetic resonance
Fe	Iron
FC	Ferric citrate
Fe_4S_4	4 Iron – 4 Sulfur cluster
Fe_2S_2	2 Iron – 2 Sulfur cluster
HS	High-Spin
ICP-MS	Inuductively coupled plasma mass spectrometry

ISC	Iron sulfur cluster
LC	Liquid chromatography
LS	Low-Spin
MB	Mössbauer
NH	Non-Heme
NP	Ferric phosphate nanoparticles
PGK	Phosphoglycerate kinase
PIPES	Piperazine-N,N'-bis(2-ethanesulfonic acid)
PS buffer	Buffer containing 20 mM PIPES and 0.2 M Sorbitol, pH 6.8
ROS	Reactive oxygen species
SEC	Size exclusion chromatography
TCEP	Tris(2-carboxyethyl) phosphine
TEM	Transmission electron microscopy
TMG	Trace metal grade
UV-vis	UV-Visible spectroscopy
UP1	Cells over-expressing *CCC1*, grown with 1 μM FC
UP0	Cells over-expressing *CCC1*, grown with 10 μM FC
UP20	Cells over-expressing *CCC1*, grown with 20 μM FC
UP40	Cells over-expressing *CCC1*, grown with 40 μM FC
UP2x1	Cells over-expressing *CCC1*, grown with 1 μM ferric citrate and 100 mg/L adenine

UP2x40	Cells over-expressing *CCC1*, grown with 40 μM ferric citrate and 100 mg/L adenine
WT	Wild Type
YPAD	Standard rich medium containing glucose and adenine
δ	Isomer shift
Δ*CCC1*	Yeast strain with *CCC1* deleted
ΔE_Q	Quadrupole splitting

TABLE OF CONTENTS

Page

LIST OF FIGURES

Page

LIST OF TABLES

Page

LIST OF SCHEMES

Page

CHAPTER I

INTRODUCTION AND LITERATURE REVIEW

Transition metals are essential components in every biological system, from plants to humans *(1)*. These metals are extremely useful for cells because they are stable in multiple redox states, which allow enzymes to efficiently catalyze reactions such as those involving electron transfer *(2-4)*, respiration *(5-7)*, and DNA replication and repair *(8-11)*.

One of the most widely-used transition metals in biology is iron (Fe) *(12)*. Iron can exist in many oxidation states, with the two most common being ferrous (Fe^{2+}) and ferric (Fe^{3+}). In cellular systems, iron is utilized as heme centers, in iron-sulfur (Fe/S) clusters, and others *(12)*. Iron can also be detrimental to cells due to its ability to do Fenton chemistry [$Fe^{2+} + H_2O_2 \rightarrow Fe^{3+} + {}^{-}OH + {}^{\bullet}OH$], which leads to the formation of reactive oxygen species (ROS) *(13)*. ROS can damage lipids *(14)*, proteins *(15)*, and DNA *(16)* which can eventually lead to cell death *(17, 18)*. The need for iron in cells is well established, but the route for iron incorporation into different centers and proteins is poorly understood. The objective of the studies presented in this dissertation was to investigate the ways Fe distributions change under various conditions. The conclusions shown have provided insight for Fe regulation and trafficking within cells.

Iron Uptake in Yeast Cells

Iron trafficking- the way iron moves within cells- has been studied extensively for decades, and while many pathways have been identified, others remain elusive.

Many studies have been conducted in higher organisms (*i.e.*, mammals), but much of iron trafficking knowledge has been ascertained by studying single-celled eukaryotic organisms like *Saccharomyces cerevisiae*. This organism is a good model system for iron trafficking because many of the proteins in yeast are homologous to those in humans. Yeast is also easy to grow in large cultures, and doing so is cost effective.

Iron is brought into the yeast cell through two primary pathways *(19-21)*. The first pathway utilizes siderophores, or small molecules which chelate metals *(21)*. While *Saccharomyces cerevisiae* does not produce its own siderophores, yeast are able to import Fe^{3+}- binding siderophores through Arn and Sit proteins on the plasma membrane *(21, 22)*. In the absence of siderophore-bound iron these proteins are localized to intracellular vesicles *(22)*. When siderophores are present or extracellular iron concentrations are low, these proteins are trafficked to the plasma membrane *(22)*. This complex is endocytosed upon the iron-containing substrate binding to its receptor *(22)*. Once the siderophore-binding proteins are endocytosed, the endocytotic vesicle is acidified and the iron-bound siderophore is released into the cytosol *(22)*. The siderophore can accumulate in intracellular vesicles or be degraded *(23)*. In the cytosol, iron is chelated by an unknown trafficking compound. The cytosolic iron pool is hypothesized to exist as Fe^{2+}, rather than Fe^{3+}, which would imply that some reducing agent is involved in the metal ion transfer process *(24)*.

The second pathway of iron import to the yeast cell is a reductive uptake mechanism. Fre1p and Fre2p are ferric reductase proteins on the plasma membrane which are responsible for reducing Fe^{3+} to Fe^{2+}. These reductases contain binding sites

for NADH, FAD, and hemes, which accommodate electron transfer from NADH to Fe^{3+} *(25, 26)*. The reductive-uptake mechanism is active when iron is available as ferric citrate and ferric chelates *(27)*. Without Fre1p, iron will not be transported through the reductive uptake system, as Fre1p is responsible for >90% of iron reduction on the plasma membrane *(26, 28)*. The ferrous iron resulting from this step can then be transported to a high-affinity or low-affinity transport system *(26)*.

The high-affinity uptake system is composed of Fet3p and Ftr1p and has a high binding affinity for Fe^{2+} (K_m = 0.2μM) *(29)*. When ferric iron is available in the extracellular environment it is necessary for Fet3p/Ftr1p to acquire ferrous iron from Fre1p; however, when ferrous iron is available to cells it can be transported through Fet3p/Ftr1p without Fre1p *(30)*. This high affinity system is active under low iron concentrations (*i.e.,* <1uM) *(31)* while high iron conditions lead to degradation of the complex *(32)*. The first step of high-affinity iron transport involves the oxidation of Fe^{2+} to Fe^{3+} by Fet3p, a multi-copper oxidase *(26, 28, 33)*. Ftr1 is a ferric permease *(33, 34)*. The Fet3/Ftr1 complex forms in the Golgi before the proteins are trafficked to the plama membrane *(20, 28, 34)*. If one of these proteins is deleted the other will be degraded in the vacuoles *(35)*, and if this complex is not formed copper will not be inserted into Fet3p *(20, 28, 34, 35)*. The mechanism of iron transfer between these proteins remains to be elucidated.

The low-affinity pathway (Smf1p, Smf2p, and Fet4p) directly transports Fe^{2+} from Fre1p into the cytosol *(36-38)*. *Saccharomyces cerevisiae* expresses three Smf proteins- Smf1p, Smf2p, and Smf3p *(38-40)*. Smf1p and Smf2p increase cellular iron

levels when they are over-expressed, but Smf3p does not *(39)*. Smf1p and Smf2p are located on the plasma membrane, and they also transport the divalent metals including Mn^{2+}, Zn^{2+}, Co^{2+} and Cu^{2+} *(38, 39)*. Smf3p is localized to the vacuoles and will be discussed later in this chapter. While Smf1p and Smf2p increase intracellular iron levels, they are regulated on a protein level by Mn^{2+} *(41-43)*. Under high Mn^{2+} conditions Smf1p and Smf2p are degraded in the vacuoles, and when Mn^{2+} levels are low these proteins localize to the plasma membrane *(43)*. It is unclear how Mn^{2+} levels control this protein localization *(43)*.

Fet4p is also part of the low-affinity Fe^{2+} transport system and it can also transport other metals including Zn^{2+}, Cu^{2+}, Mn^{2+}, and Cd^{2+} *(36)*. This protein is regulated by Rox1p and Aft1p, although the two regulatory mechanisms are independent of one another *(37)*. Rox1p is an oxygen-sensitive transcription factor *(44)*. In aerobic conditions, Rox1p binds to the promoter region of *FET4* and represses gene expression *(37)*. This oxygen-responsive regulation mechanism allows cells to acquire Fe under anaerobic growth conditions *(45)*. This is advantageous to the cell because the Fet3p/Ftr1p pathway requires oxygen for activity (Fet3p is a multi-copper oxidase) *(20)*.

The second regulatory system for Fet4 expression involves Aft1p. Aft1p is a low-iron sensing transcription factor which induces the expression of a number of genes related to iron import and trafficking *(46)*. More details of this regulatory system are discussed later in this chapter. An additional, poorly characterized iron regulation system is also responsible for controlling Fet4p expression, in that the expression of this protein is lower than WT levels in iron-replete conditions in Δ*aft1*Δ*aft2* cells *(44)*. There

are many other iron-related proteins whose iron regulating mechanisms are not fully understood, so it is possible that another pathway is responsible for regulating an iron-induced response.

Intracellular Iron Trafficking

Once iron has been transported into the cell, it will accumulate in a "labile iron pool" (LIP), which is hypothesized to provide iron to the mitochondria and other organelles *(47)*. The exact composition of this iron pool has not yet been determined *(47-49)*. The Fe species in this pool have remained elusive in part because the ligands coordinating this Fe are loosely bound. The labile nature of this Fe pool implies that the Fe species can be easily chelated. In 2001, Petrat, *et al.* studied the intracellular Fe^{2+} by utilizing a fluorescent compound (Phen Green SK) and Fe^{2+} chelators *(50)*. It has been hypothesized that cellular iron exists predominantly in the ferrous state because the reducing environment of the cytosol favors Fe^{2+} rather than Fe^{3+} *(49)*. Schneider, *et al.* showed in 1988 that in aqueous environments of pH ~7.0, Fe^{2+} is soluble (up to 10^{-5} M) while Fe^{3+} is not (over 10^{-12} M) *(24)*. Phen Green SK is fluorescent when it is not bound to divalent transition metals, and the fluorescence quenches when these metals are bound *(50)*. Intact cells were incubated with Phen Green SK, and then with specific Fe^{2+} chelators *(50)*. The concentration of the chelatable Fe^{2+} in the cytosol was measured by quantifying the change in the fluorescence intensity during incubation with and without the Fe^{2+} chelators *(50)*. The concentration of the chelatable cytosolic Fe^{2+} pool was estimated as ~5 – 7 μM *(50)*.

Other studies have also utilized iron-specific fluorescent chelators to investigate the cellular LIP *(24, 51)*. These studies have estimated that the concentration of cytosolic iron is in the range of ~10^{-7} to 10^{-6} M *(24, 49)*. One fundamental problem with this approach is that the intracellular iron must be manipulated (*i.e.*, chelated from its original ligands) to be quantified. When the samples are manipulated in this manner it is possible that the Fe concentrations observed are higher or lower than in untreated cells. In order to address this issue, iron levels *must* be measured using noninvasive, analytical techniques. In this dissertation, cellular iron distributions were studied using noninvasive techniques including Mössbauer and EPR spectroscopies, and ICP-MS was used to determine iron concentrations. Taken together, these methods provide a biophysical and bioanalytical approach to study iron without altering the intracellular environment.

Another important, and yet unidentified, part of iron trafficking in the cytosol pertains to the molecule(s) responsible for transporting iron within the cell. It has been hypothesized that common cellular components such as ATP/ADP *(52)*, inositol phosphates *(53)*, and 2,5-dihydroxybenzoic acid (DHBA) *(54)* are responsible for this. However, these molecules predominantly bind Fe^{3+} rather than Fe^{2+}, which is not consistent with the view that most cytosolic iron is ferrous *(24)*. Alternatively, thiol-containing molecules such as glutathione and cysteine may be responsible for cytosolic iron trafficking *(55)*. It is highly probable that the iron in the cytosol is reduced by glutathione *(24)*. This molecule is responsible for maintaining the reducing cytosolic environment (-320mV) and is present at high concentrations *(55)*. The structures of these potential ligands are shown in Figure 1.1.

Identifying the cytosolic iron trafficking ligands is challenging because 1) "clean" cytosol is difficult to isolate, 2) the iron is most likely loosely bound, and 3) there could be more than one iron trafficking molecule. First, cytosolic fractions are generally obtained by lysing cells in a harsh manner, such as glass beads or sonication. These processes will also damage iron-containing organelles such as mitochondria and vacuoles. Therefore, the iron in the "cytosolic" fractions could also have come from broken organelles. Secondly, because this pool is labile it can be assumed that many cellular components (*i.e.*, polyphosphates in vacuoles and mitochondria) could readily bind this iron when organelles are broken. Finally, there is the possibility that more than one trafficking molecule is utilized in this system. Perhaps many compounds transfer iron between cellular compartments. This uncertainty in the chelation environment of cytosolic iron has led to the utilization of more iron-specific sensing techniques and non-invasive approaches to studying iron in cell biology, such as Mössbauer, EPR, and UV-Visible spectroscopies *(56)*.

Yeast Mitochondrial Iron Trafficking

Once iron has entered the cell it has different "fates", including transport to the mitochondria and vacuoles. The mitochondria are the major hubs of iron metabolism in cells because they house the components used for Fe/S cluster assembly, heme biosynthesis, and components designed to install such iron centers into apoproteins. Mitochondria are composed of an outer mitochondrial membrane (OMM) and an inner mitochondrial membrane (IMM) *(57)*. The space between these two membranes is called

the inner-membrane space (IMS) *(57)*. The area within the IMM is known as the mitochondrial matrix *(57)*.

In yeast, mitochondrial iron is brought in through Mrs3, Mrs4, and Rim2 proteins *(58-63)*. These proteins span the IMM and are specific for iron *(60, 61)*. Mrs3p and Mrs4p are homologous to mitoferrin transporters in human cells, and are responsible for transporting iron into the mitochondrial matrix where it can be utilized for Fe-S cluster and heme biosynthesis *(61, 64)*. Fre5p, a mitochondrial ferric reductase, could be involved in reducing iron prior to import by Mrs3/4 because the IMS of the mitochondria is an oxidizing environment. However, the precise role of Fre5p is unknown *(65)*.

The iron transport role of Mrs3/4p was identified using a triple-deletion strain Δ*mrs3*Δ*mrs4*Δ*yfh1 (60)*. The YFH1 deletion alone resulted in mitochondrial iron overload while the additional deletion of *MRS3* and *MRS4* suppressed this phenotype *(60)*. This indicates that lower levels of iron are imported into the mitochondria in the absence of Mrs3p and Mrs4p. Over-expression of *MRS4* showed an increase in heme biosynthesis and in overall mitochondrial iron levels, which indicates that this protein is involved in mitochondrial Fe import. The deletion of *MRS3* and *MRS4* resulted in a decrease in mitochondrial iron, as well as an increased sensitivity to high medium iron *(58)*. These results suggest that without Mrs3p and Mrs4p Fe can accumulate to toxic levels which are likely localized to the cytosol. The iron-regulon is induced when Mrs3p and Mrs4p are over-expressed, which indicates that the cytosol becomes iron deficient in

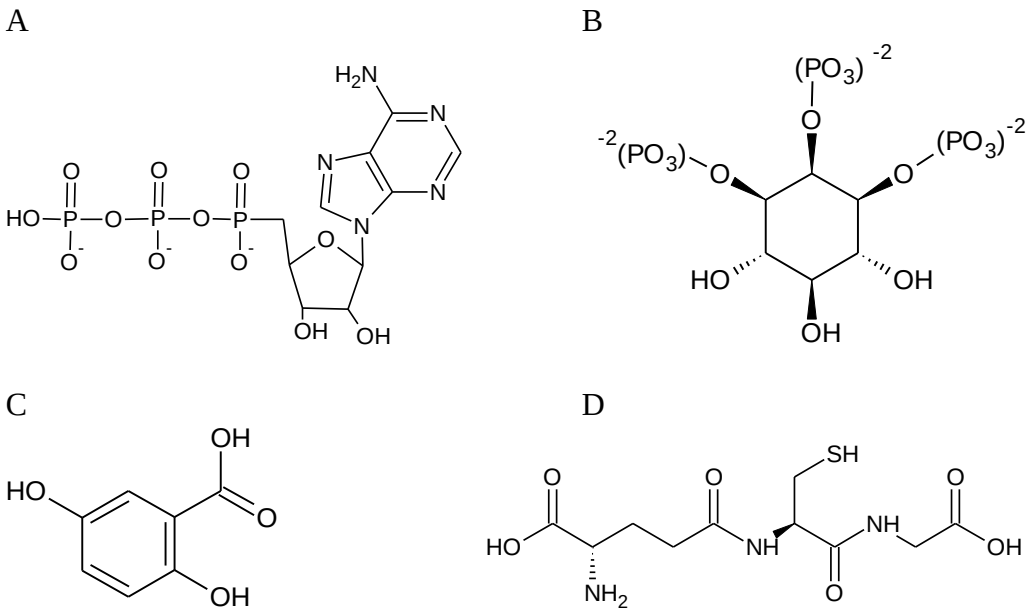

Figure 1.1. Possible ligands for cytosolic iron. A) ATP, B) Myo-Inositol 1,2,3-triphosphate, C) 2,5-Dihydroxybenzoic acid (2,5-DHBA), and D) glutathione (GSH).

these conditions *(58)*. These data support a model in which the mitochondria accumulate Fe from the cytosol via Mrs3p and Mrs4p. It is clear from these studies that Mrs3p and Mrs4p are necessary for mitochondrial iron import and cellular iron homeostasis, but they are not the only pathway for mitochondrial iron import.

Rim2p was recently identified in 2011 as another mitochondrial iron import protein *(62)*. This protein has two separate functions, and was first identified as a pyrimidine nucleotide exchanger in the mitochondria *(66)*. Its role in iron metabolism was discovered when it was found to be up-regulated in Δ*mrs3*Δ*mrs4* cells *(62)*. Other experiments show that expression of *RIM2* in Δ*mrs3*Δ*mrs4*Δ*ccc1* cells can alleviate iron toxicity caused by iron overload in the cytosol *(67)*. Interestingly, when Rim2p is deleted and Mrs3/Mrs4 proteins are intact, iron is not utilized as efficiently as in wild-type cells *(62)*. This suggests that there may be an additional role of Rim2p in iron homeostasis or utilization in the mitochondria, but this role has yet to be identified.

The Labile Iron Pool in Mitochondria

When iron is brought into the mitochondria, but before it is incorporated into iron centers, it may to accumulate in a mitochondrial labile iron pool (MLIP). The first evidence for the existence of this pool was shown in 1980, when isolated mitochondria were incubated with bathophenanthroline sulfonate (BPS) and ~25% of the total iron in the mitochondria was available to be chelated, and was therefore hypothesized to be labile *(68)*. The MLIP was also studied in later experiments utilizing an iron-specific fluorescent chelator which would quench upon iron binding *(69)*. The concentration of

iron in these studies (~15μM) was found to be much lower than the values reported in the previous BPS experiments (>100μM). As previously mentioned, studying LIPs using indirect methods such that the iron must be chelated from its original ligands is not an ideal approach. In 2010, Holmes-Hampton, *et al*. demonstrated that isolated mitochondria contain a pool of non-heme, high spin (NHHS) Fe^{2+} of ~30 μM *(31, 70).* This iron can be chelated when the mitochondria are disrupted but not when the mitochondria are intact, indicating that this NHHS Fe^{2+} is indeed inside the mitochondria *(70).*

Nanoparticle Accumulation in Mitochondria

Another form of iron in the mitochondria accumulates under conditions which model human disease states (*i.e.,* Freidrich's Ataxia). In various strains of yeast (*Δyfh1, Atm1p-deplete, Yah1p-deplete, Aft1-1^{up}*) iron accumulates in the mitochondria as superparamagentic ferric nanoparticles *(71-74).* These nanoparticles apparently are not detected by cells because the cells demonstrate Fe-deficient phenotypes (*ie,* elevated cellular Fe import) even when nanoparticles accumulate in high (mM) concentrations *(71-73).* The composition of nanoparticles was investigated further using TEM elemental analysis and EXAFS *(72, 74).* Electron microscopy images of mitochondria showed insoluble particles accumulating, and further elemental analysis revealed that these particles were composed of iron, phosphorus, and oxygen *(72, 74).* The particles were also found to be devoid of carbon and nitrogen *(72, 74).* Additional EXAFS studies revealed that these "nanoparticles" are composed of iron bound by oxygen in the

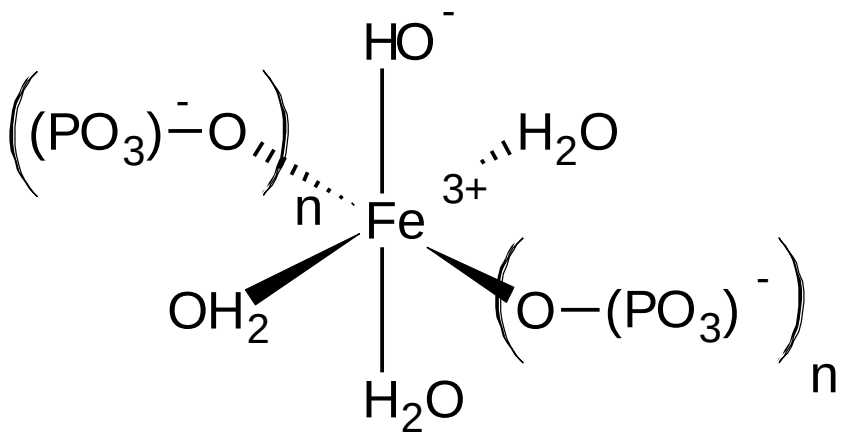

Figure 1.2. Potential structure of nanoparticles found in mitochondria and vacuoles *(72).* Other geometries, as well as protonation states for water and hydroxide ligands, are possible (while maintaining overall charge neutrality).

first coordination sphere and phosphorus in the second, and that iron is coordinated by 4-6 ligands *(72)*.

These studies led to a potential structure for these ferric phosphate nanoparticles, shown in Figure 1.2 *(72)*. Interestingly, although these nanoparticles are redox active (reduced by dithionite) they do not seem to be sensed by the mitochondria. This was demonstrated when nanoparticles were shown to accumulate at high levels but did not necessarily affect levels of other iron-containing mitochondrial proteins *(72)*. Similar ferric phosphate nanoparticles have been found in vacuoles and are discussed in Chapter III.

Mitochondrial Iron-Sulfur Cluster Assembly and Heme Biosynthesis

Perhaps the most commonly known Fe-related functions of the mitochondria are to assemble iron-containing centers such as iron-sulfur clusters and hemes. Iron-sulfur cluster assembly occurs in the mitochondrial matrix *(75)*. This process is complex and not fully understood. The common iron-sulfur cluster centers found in biology are shown in Figure 1.3. The formation of iron-sulfur clusters requires three primary components- iron, sulfur, and reducing equivalents *(75)*. Upon entry through Mrs3/4p iron is bound by Yfh1p and transported to a scaffolding complex on which clusters are formed *(76-79)*. This protein is necessary for iron-sulfur cluster assembly, and mutations in this protein (Frataxin) in humans can lead to the disease Friedreich's ataxia *(80)*. Sulfur is donated to this system through Nfs1p and Isd11p *(75)*. Nfs1p is a cysteine desulfurase which catalyzes the conversion of cysteine to alanine and a

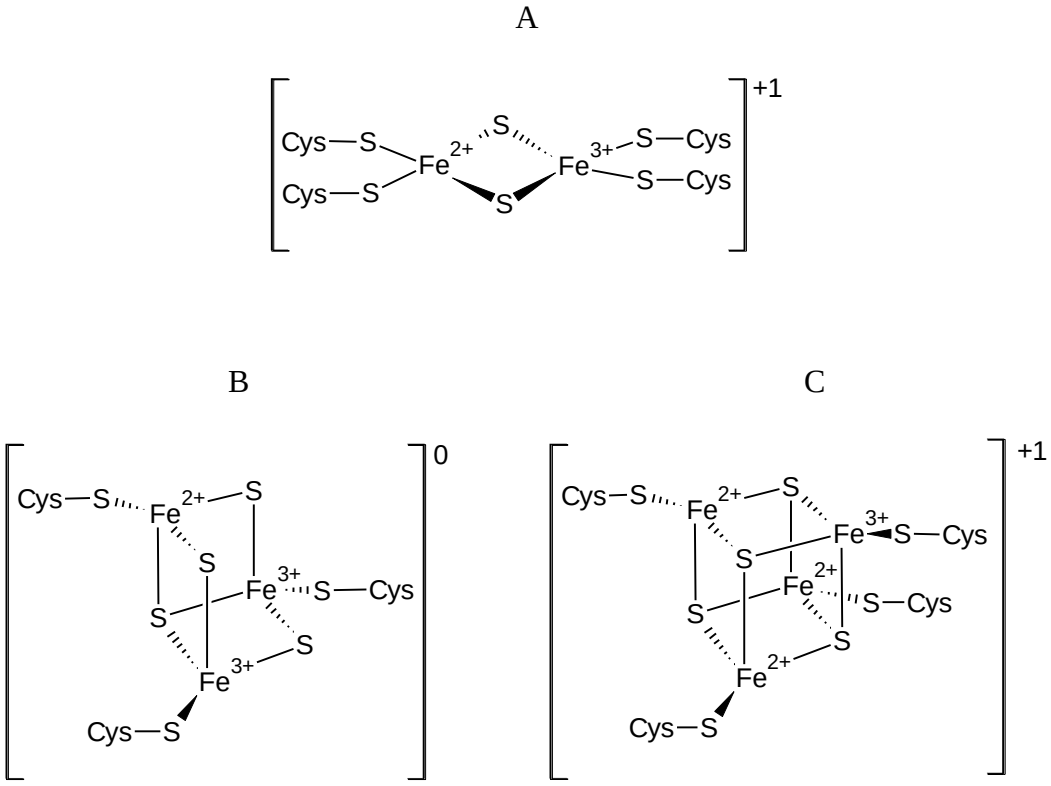

Figure 1.3. Common Iron-Sulfur Clusters in Reduced States. A) $[Fe_2S_2]$ cluster, B) $[Fe_3S_4]$ cluster, and C) $[Fe_4S_4]$ cluster. These clusters can also exist in oxidized states as $[Fe_2S_2]^{2+}$, $[Fe_3S_4]^{1+}$, and $[Fe_4S_4]^{2+}$. The $[Fe_2S_2]$ cluster can also have two N-His ligands in place of two S-Cys lignads, which is known as a Rieske center *(85)*.

persulfide *(81-83)*. Isd11p is necessary for Nfs1p activity and is thought to play a role in stabilizing this protein *(76, 84)*.

Finally, reducing equivalents are provided by an electron transport chain composed of NAD(P)H, ferredoxin (Yah1p) *(86)*, and ferredoxin reductase (Arh1p) *(75, 87, 88)*. These proteins are necessary for iron-sulfur cluster assembly, which implies that a reduction step is essential for cluster formation on Isu1p *(59, 86, 87)*; however, Yah1p has not been shown to interact with other proteins in this system *(75)*. These components are assembled on a scaffolding protein, Isu1p *(89-91)*. This scaffolding protein is highly conserved, from bacteria to humans, and possesses three cysteine residues which are critical for iron-sulfur cluster assembly *(75, 91)*. Once iron-sulfur clusters are assembled they must be transferred and incorporated into apoproteins. This process is facilitated *in vivo* by a number of proteins including Ssq1p, Jac1p, Mge1p, Grx5p, and Atm1p *(75)*. Ssq1p is a Hsp70 chaperone protein and Jac1p is a co-chaperone which associates with Ssq1p *(92)*. Mge1p is a nucleotide exchange factor which is required to replace ADP with ATP at Ssq1p *(93)*. Grx5p is a monothiol glutaredoxin which is necessary for iron-sulfur cluster assembly and transfer from Isu1p, but its precise role in this pathway has not been identified *(75, 94)*.

Heme Biosynthesis in Mitochondria

Other important roles of iron trafficking in mitochondria are heme biosynthesis and incorporation of such centers apoproteins. Heme synthesis begins with the conversion of Succinyl CoA and glycine to δ-aminolevulinic acid (ALA) in the

mitochondria *(95)*. This product is transported to the cytosol where 2 ALA molecules are used to form porphobilinogen *(95)*. Four porphobilinogen molecules are used to form protoporphyrin-IX in a pathway that begins in the cytosol and ends in the mitochondria *(95)*. Finally, Fe^{2+} is inserted into protoporphyrin-IX by Hem15p (homologous to human ferrochelatase) *(96)*. The product of this pathway is heme *b*. Heme *a* and heme *c* are modified from heme *b*. Heme *a* is formed by heme *a* synthase *(97)*, and heme *c* is produced from heme *b* and heme *c* lyase *(98)*. The structures of these heme groups are shown in Figure 1.4.

Iron Trafficking in Yeast Vacuoles

Due to the necessity and potential lethality of iron in the cell, iron must be stored in a form that cannot facilitate ROS formation but still be available as soon as the cell needs. The vacuoles function as a compartment to store iron and other metals safely to avoid ROS damage. Yeast vacuoles are similar to mammalian lysosomes in that these organelles maintain low pH environments (~4.5-5.5) *(99)*. The acidification of vacuoles is vital to maintain its roles in cellular metabolism *(99)*. The process of acidification occurs through the vaculolar H^+-ATPases, which couple ATP hydrolysis and proton transport from the cytosol into the vacuoles *(99)*. Without these H^+-ATPases the vacuoles are unable to efficiently transport metals, such as Fe^{2+}, because metal import is coupled to H^+ export *(99-101)*. Moreover, phosphate and other stored metabolites can be affected by higher vacuolar pHs *(45, 102)*.

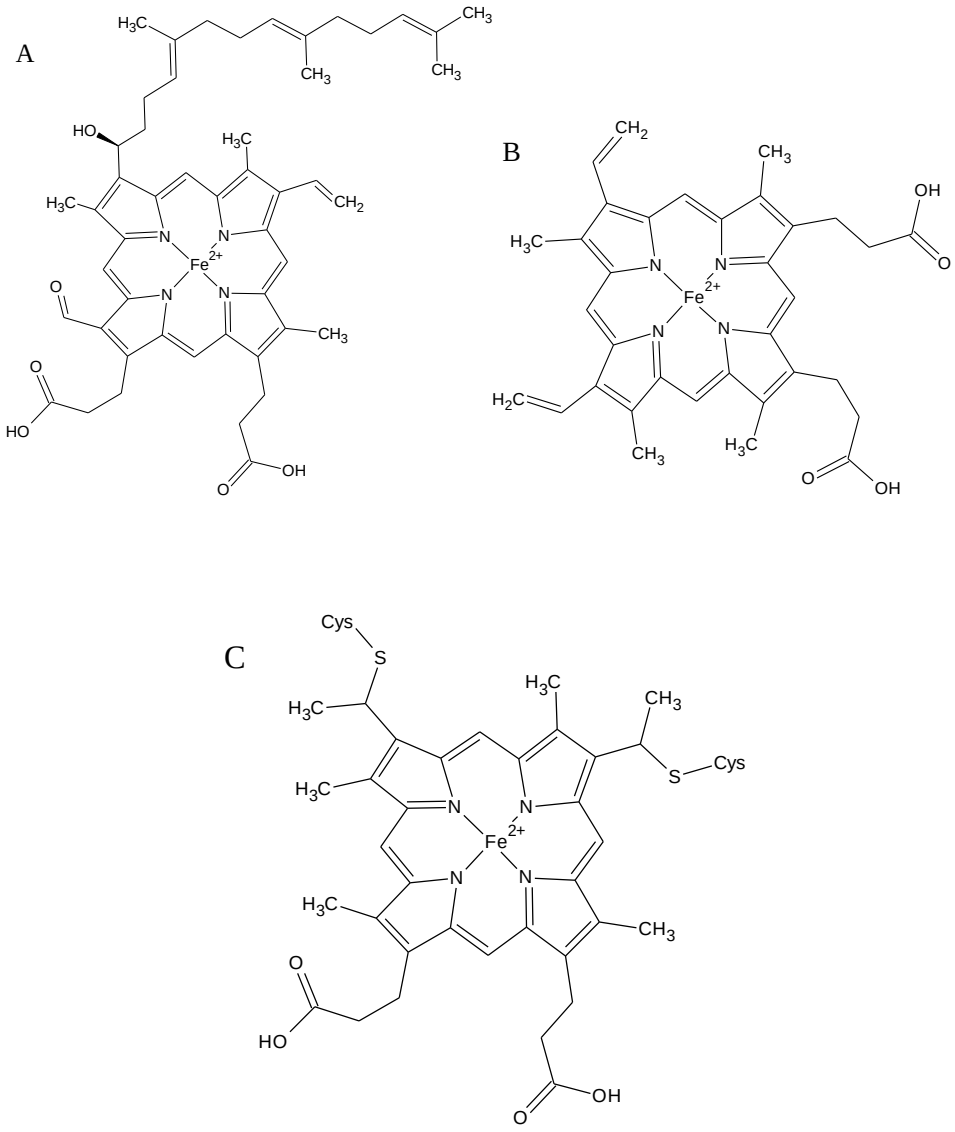

Figure 1.4. Heme centers found in biological systems. A) Heme *a*, B) Heme *b*, C) Heme *c*. These centers can also have a 3+ oxidation state.

Vacuolar Iron Import

Vacuoles are dynamic organelles that can undergo fusion and fission processes *(102)*. Typically these transformations occur in conjunction with import/export processes (endo- or exocytosis) and during cellular stress and cell division when the volume of vacuoles is highly regulated *(102)*. During log-phase growth, vacuoles occupy ~20-30% of the total cell volume, with 2-3 vacuoles per cell *(102)*. Iron is imported from the cytosol into vacuoles through two known pathways. The first is via Ccc1p, a 34-kDa transmembrane protein which reportedly accounts for ~85% of vacuolar iron import *(103)*. The Ccc1 protein is regulated by Yap5p *(104)*. The Yap5 protein is a member of the *YAP* transcription family, and it promotes *CCC1* gene transcription under medium iron conditions *(104)*. Yap5p is localized to the nucleus and is constitutively bound to the *CCC1* promoter *(104)*. This protein also contains two cysteine residues which are required for promoter activity *(104)*.

Iron may facilitate the reduction of these cysteine residues to a disulfide and change the conformation of Yap5p, which results in the promotion of *CCC1* gene transcription *(104)*. When *CCC1* is up-regulated, more iron can be moved from the cytosol into a vacuolar storage form, thereby reducing the concentration of cytosolic iron *(103)*. Ccc1 protein levels are also controlled by Cth2p and Aft1p *(105)*. CTH2 is part of the iron regulon, and encodes a cytosolic protein which is responsible for destabilizing and degrading different mRNA transcripts responsible for reducing cytosolic iron levels *(105)*. Because CTH2 is in the iron regulon it is transcribed during iron deficient conditions by Aft1p *(105)*. This process causes the vacuoles to accumulate

less iron and therefore increase the concentration of cytosolic iron. The second pathway for iron import in vacuoles is endocytosis, which imports reportedly ~15% of vacuolar iron *(103)*.

Phosphate Storage in Vacuoles

Once inside the vacuoles iron can be stored in a non-toxic form which is most likely ligated by polyphosphate (discussed in Chapter III). The concentration of phosphorus in cells is very high (≥ 30 mM) *(106)*. This excessive amount of phosphorus exists in many forms including inorganic phosphate, pyrophosphate, orthophosphate, and polyphosphate *(107)*. Polyphosphate is the primary storage form of phosphate, and is localized primarily to vacuoles *(107, 108)*. Polyphosphate has also been found in nuclei and mitochondria *(107)*. One difference between polyphosphates in vacuoles and other organelles is the chain length *(107)*. In vacuoles, polyphosphate chain lengths are approximately 150 residues, while mitochondria polyphosphate chain lengths are substantially shorter (≤ 15 residues) *(106)*.

Vacuolar polyphosphate can be degraded and supplied to the cytosol under phosphorus-limiting conditions. In the vacuoles polyphosphate is utilized to store metals and other anions *(107)*. The vacuoles can also accumulate phosphorus-containing granules, which have been observed by electron microscopy *(109)* . These granules are precipitated forms of polyphosphate *(109)*. Therefore in vacuoles two forms of polyphosphate can exist: a soluble form and an insoluble form. The ratios of these two forms may depend on culture conditions and the physiological state of the cell. Evidence

is presented in Chapter III that both of these forms of polyphosphate bind iron in vacuoles. Models for changes in these storage forms are proposed in Chapters III and IV.

Export of Iron from Vacuoles

The vacuoles also have mechanisms which can transport iron from the vacuolar lumen to the cytosol *(110, 111).* These pathways are activated when the cytosol is deficient in iron *(110, 111).* The proteins responsible for this iron export are homologous to Fre1p, Fre2p, Fet3p, Ftr1p, Smf1p, and Smf2p on the plasma membrane *(110).* The pathways are similar because the oxidation state of iron in the extracellular environment and the vacuolar lumen is 3+ *(12, 112).* Therefore, the iron must be reduced before it can be transported into the cytosol *(12).* The vacuolar proteins in this pathway consist of a ferric reductase Fre6p *(113, 114),* and a high-affinity and low-affinity transport pathway.

Fre6p is homologous to the Fre1 protein on the plasma membrane, which reduces vacuolar iron to Fe^{2+} before it enters the cytosol *(113, 114).* The high-affinity export pathway in vacuoles is composed of a multi-copper oxidase Fet5p and ferric permease Fth1p, which is homologous to the Fet3p/Ftr1p complex on the plasma membrane *(110, 115, 116).* These proteins must be complexed before they are trafficked to the vacuolar membrane, and expression of both is required for the system to operate *(110).* Like those of Fth1/2p, Fet3p, and Ftr1p, the expression levels of vacuolar iron proteins are also regulated by Aft1p *(117-120).*

The low-affinity transport system is composed of Smf3p, an Nramp-family, divalent metal transporter *(43, 111, 121)*. This protein is homologous to Smf1p on the plasma membrane and is regulated by Rox1p *(121)*, Aft1p, and Aft2p *(43, 111)*. Smf3p is expressed in Fe-depleted, anaerobic conditions *(122)*. The anaerobic expression of this protein is probably due to the oxygen-dependent mechanism of iron export from vacuoles via Fet5p/Fth1p *(44, 122)*. Fet5p activity requires oxygen, so Smf3p becomes the primary iron export pathway when oxygen is unavailable *(43)*.

Also like Fet4p, Smf3p is regulated by Aft1p and Aft2p, as well as another unidentified iron-regulation system *(111)*. The SMF3 gene contains two Aft-like binding sites *(65, 111)*. However, even when these regions are deleted Smf3 transcript levels are still regulated in response to iron availability *(43)*. Smf3 protein levels also change in response to iron levels in Δ*aft1*Δ*aft2* strains *(43)*. These data suggest that another iron-regulation pathway exists, but it has not been identified. The various types of regulation of the vacuolar import and export proteins are essential for controlling cellular iron levels and for understanding iron trafficking.

Iron Regulation in *Saccharomyces cerevisiae* Cells

Although the vacuoles provide a safe environment for iron storage, cells have developed mechanisms which tightly regulate iron levels in the cytosol. The primary iron regulation pathway in *Saccharomyces cerevisiae* is through the low-iron sensing transcription factor Aft1p. Under conditions where cytosolic iron is depleted, Aft1p is found in the nucleus where it binds to DNA and induces the transcription of ~20 genes,

collectively known as the "iron regulon". The genes discussed in this dissertation are shown in Table 1.1.

Under high-iron conditions Aft1p is localized to the cytosol. Several components of the Fe/S cluster biosynthetic pathway in mitochondria are important for cytosolic localization of Aft1p. In cells lacking Yfh1 or Grx5, both of which are essential for mitochondrial Fe/S cluster assembly, Aft1p is not activated *(45, 123, 124)*. When cells lack cytosolic Fe/S cluster assembly machinery Aft1p is activated *(45, 125)*. This demonstrates the involvement of mitochondrial Fe/S cluster assembly in the iron-sensing mechanism of Aft1p. But how does Aft1p sense iron? When Aft1p is inactive it forms a homodimer which contains a Fe_2S_2 cluster *(126)*. Under high intracellular Fe conditions, Fe_2S_2 clusters could bind to Aft1p and facilitate inactivation.

How does Aft1p acquire the Fe2S2 cluster? Aft1p interacts with glutaredoxin proteins (Grx3p and Grx4p), Fra1p, and Fra2p proteins in the cytosol *(45)*. Grx3/4p, Fra1/2p, and glutathione also form a complex in the cytosol, which contains a bridging Fe2S2 cluster. A model of these protein interactions shows that the Fe2S2 cluster transfer to Aft1p is facilitated by the Grx/Fra proteins. The precise mechanism of this transfer has not been established *(102, 127-130)* .

Integrated Biophysical Approach

To better understand how iron assembly and utilization occurs we must study the basic mechanisms of iron trafficking to different organelles. *Saccharomyces cerevisiae* is an excellent model system for these studies because it grows well in large suspension

Gene	Gene Product Localization	Function	Regulation
ARN1	Cell Wall	Siderophore Transporter	Aft1p
ARN2	Cell Wall	Siderophore Transporter	Aft1p
ARN3/SIT1	Cell Wall	Siderophore Transporter	Aft1p
ARN4	Cell Wall	Siderophore Transporter	Aft1p
FRE1	Plasma Membrane	Ferric Reductase	Aft1p
FRE2	Plasma Membrane	Ferric Reductase	Aft1p
FET3	Plasma Membrane	Multicopper Oxidase	Aft1p
FET4	Plasma Membrane	Divalent Metal Transporter	Aft1p, Aft2p, Rox1p, Other
FTR1	Plasma Membrane	Ferric Permease	Aft1p
SMF1	Plasma Membrane	Divalent Metal Transporter	---
SMF2	Plasma Membrane	Divalent Metal Transporter	---
MRS3	Inner Mitochondrial Membrane	Iron Transporter (Fe^{2+})	Aft1p
MRS4	Inner Mitochondrial Membrane	Iron Transporter (Fe^{2+})	Aft1p, Aft2p
FRE5	Inner Mitochondrial Membrane	Ferric Reductase	Aft1p
RIM2	Inner Mitochondrial Membrane	Iron Transporter (Fe^{2+})	---
CCC1	Vacuolar Membrane	Iron Transporter (Fe^{2+})	Yap5p
FRE6	Vacuolar Membrane	Ferric Reductase	Aft1p
FET5	Vacuolar Membrane	Multicopper Oxidase	Aft1p
FTH1	Vacuolar Membrane	Ferric Permease	Aft1p
SMF3	Vacuolar Membrane	Divalent Metal Transporter	Aft1p, Aft2p, Rox1p, Other
CTH2	Cytosol	mRNA Destabilization	Aft1p

Table 1.1. Gene products involved in iron trafficking, discussed in this dissertation. Gene product location, function, and gene regulation are also summarized in this table. This information was collected from *(30, 131, 132).*

cultures, possesses homologous proteins to human cells and effectively incorporates ^{57}Fe into the cells. Mössbauer spectroscopy is the most powerful technique for studying iron, because all the ^{57}Fe in a sample is detected. Mossbauer can also distinguish spin states and oxidation states of iron nuclei. Simulations of this data are performed to give relative percentages of each iron species.

EPR spectroscopy was also utilized because it will detect various the paramagnetic species in sample. Each EPR signal can be quantified to give an absolute concentration value. This, taken with Mossbauer data, allows a more accurate quantification of the iron species in a sample. Finally, ICP-MS is used to accurately determine the concentration of iron in a sample. Using the concentrations found with ICP-MS, absolute concentrations of each iron species in a sample can be obtained. This is unique for a cell biology system, because concentrations are generally reported in ratios (ug Fe/mg protein).

Past studies of iron which have focused on distributions have not been able to distinguish oxidation states and spin states of iron. This information is valuable for determining what iron is in a given part of the cell. These techniques will be discussed further in Chapter II.

The majority of this dissertation is focused on iron trafficking in yeast, and specifically between the vacuoles and cytosol. Chapter III discusses the development of a protocol for isolating large quantities of vacuoles and analyzing the iron content by Mössbauer spectroscopy, EPR spectroscopy, and ICP-MS. In Chapter IV we studied two strains of yeast which alter vacuolar Fe import (Δ*CCC1* and *CCC1-up*). The Fe

distributions in these strains were characterized using the aforementioned techniques. WT cells treated with concanamycin A, a vacuolar H^+-ATPase inhbitior, were also investigated. We determined that two key factors are involved in controlling Fe distributions in vacuoles- redox state and pH. These results led to the development of a model which describes the dynamics of vacuolar Fe distributions. Although the iron trafficking mechanisms in yeast are extremely complex, the changes in various iron levels are becoming clearer with the use of biophysical approaches for solving cell biology questions.

CHAPTER II

MATERIALS AND METHODS

Biophysical Methods Used

In these studies biophysical techniques were employed to approach cell biology questions. These techniques are typically used to study iron compounds, and are often applied to biological systems; however, these techniques are more commonly used for studying isolated proteins rather than entire cell systems. The primary technique used in these studies was Mössbauer spectroscopy, which is specific for ^{57}Fe. Paramagnetic species in these samples were analyzed via EPR spectroscopy, and metal concentrations were determined using ICP-MS. Heme centers in whole cell samples were also analyzed with electron absorption spectroscopy. To investigate metal-containing LMM species an anaerobic in-line SEC-ICP-MS system was used.

Mössbauer Spectroscopy

Mössbauer spectroscopy is the most powerful tool for studying iron containing species. With this technique it is possible to visualize ALL of the ^{57}Fe in a sample, meaning no ^{57}Fe nucleus is invisible when using Mössbauer *(133)*. This technique is somewhat similar to NMR spectroscopy, and can be thought of as "nuclear gamma-ray resonance spectroscopy". As with NMR, Mössbauer involves nuclear transitions. One difference between these techniques is that the energy required for Mössbauer (gamma radiation) is much greater than the energy used in NMR experiments (radio frequency). Mössbauer can be used with other elements, but the majority of Mössbauer experiments

are used to study iron. Gamma radiation is supplied to the samples with a ^{57}Co source; however, few iron centers absorb at this energy (14.4 keV) *(133)*. Therefore, to collect meaningful and interpretable data the energy seen by the sample is modulated by the Doppler Effect *(133)*. The emitting source is mounted on a driver which moves the source towards and away from the sample at a given velocity *(133)*. This allows the sample to be exposed to a range of energies, which induces transitions in different ^{57}Fe nuclei. The resulting data is plotted as percent effect (y-axis) vs. velocity in mm/s (x-axis).

The nuclear transitions in Mössbauer occur between a ground state (for ^{57}Fe, I = 1/2) and the first excited state (I = 3/2). Based on the selection rules for Mössbauer, there are 6 allowed transitions *(133)*. In some conditions some of these transitions are degenerate, and the degeneracy is based on the environment around the ^{57}Fe nucleus *(133)*. For example, a NHHS Fe^{2+} species at low temperature and low field will give rise to a doublet, where only two transitions are observed. A NHHS Fe^{3+} species will produce a paramagnetically split spectrum, where all 6 allowed transitions are observed (Figure 2.1).

Mössbauer data is analyzed using two main parameters- the isomer shift (δ) and quadrupole splitting (ΔE_Q). The isomer shift is reported with respect to a given reference, for ^{57}Fe Mossbauer spectroscopy the δ reported with respected to an iron foil where it is fixed at zero. The δ is dependent on the s-electron density in the nucleus. This parameter provides information about the oxidation state of an iron center. The ΔE_Q is

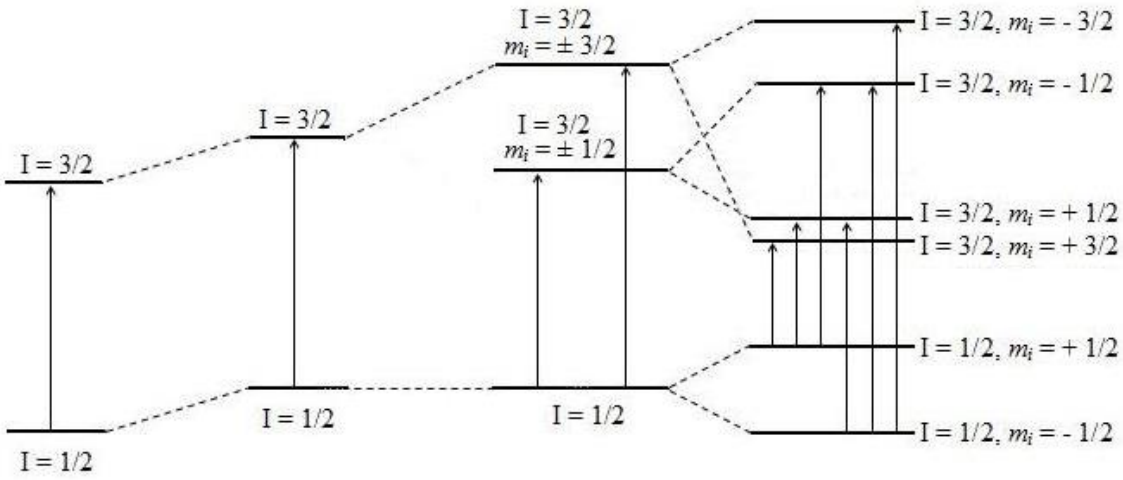

Figure 2.1. Allowed ^{57}Fe nuclear transitions in Mössbauer spectroscopy.

dependent on asymmetry of the electronic field around an iron nucleus. The EFG is affected by the chemical environment of the nucleus. Therefore, different ΔE_Q values are observed depending on the coordination environment of a given ^{57}Fe nucleus. A list of ΔE_Q values which describe biologically relevant Fe centers is shown in Table 2.1.

Because Mössbauer is ^{57}Fe-specific, the contributions of each Fe species in a sample can be directly quantified. Each Fe species is simulated using the WMoss program (See Co, Inc.), and the percent of the spectrum due to each of feature represents the absolute percent of Fe in the sample. When Mössbauer is used in combination with analytical techniques such as ICP-MS, we can determine the absolute concentration of each Fe species in the sample. This is highly advantageous for our studies because whole cells and organelles contain a variety of different Fe nuclei. This combination of techniques allows us to quantify the Fe centers in an analytical fashion, without disrupting the intracellular dynamics through external manipulations.

EPR Spectroscopy

EPR spectroscopy is used for studying paramagnetic species, and detects electronic transitions rather than nuclear transitions. This technique is advantageous for studying many metal species in cells and is not specific for iron. In EPR spectroscopy, half-integer spin systems can be detected. Common Fe-containing proteins which can be identified by EPR include cytochrome c oxidase, succinate dehydrogenase, and others. FeS clusters can be detected as long as the overall spin system is paramagnetic. A list of EPR-active centers found in biological systems is shown in Table 2.1. Because EPR is

Fe Center	Oxidation State	Spin State	δ (mm/sec)	ΔE_Q (mm/sec)	g-value
Mononuclear	HS Fe^{2+}	S = 2	1.0 – 1.4	2.8 – 3.7	≥ 13
Mononuclear	HS Fe^{3+}	S = 5/2	0.4 – 0.6	0.6 – 0.8	4.3
Heme	LS Fe^{2+}	S = 0	0.4 – 0.6	1.0 – 1.1	N/A
Heme	HS Fe^{2+}	S = 2	0.7 – 1.0	2.1 – 2.5	≥ 13
Heme	LS Fe^{3+}	S = 1/2	0.2 – 0.3	~ 2.0	3 – 3.5
Heme	HS Fe^{3+}	S = 5/2	~ 0.4	~ 0.8	~ 6.0
$[Fe_2S_2]$	1^+	S = 1/2	0.4 – 0.6 0.2 – 0.4	2.5 – 3.2 0.4 – 1.0	1.96 – 1.91
$[Fe_2S_2]$	2^+	S = 0	0.2 – 0.4	0.4 – 0.6	N/A
$[Fe_3S_4]$	0	S = 2	0.46 0.49 0.31	1.15 1.46 0.56	≥ 13
$[Fe_3S_4]$	1^+	S = 1/2	0.30	0.66	1.94
$[Fe_4S_4]$	1^+	S = 1/2	0.53	0.80 1.18	1.94
$[Fe_4S_4]$	2^+	S = 0	0.4 – 0.5	0.8 – 1.2	N/A

Table 2.1. Mössbauer and EPR parameters for common biological Fe centers. The specified parameters were collected from *(133)*.

not specific for Fe, other metals having half-integer spins can also be detected, such as copper and manganese. EPR is especially useful for our samples due to its low detection limits (μM). This technique is complementary to Mössbauer spectroscopy because low concentrations of NHHS Fe^{3+} can be more accurately quantified.

The origin of an EPR signal is based on the magnetic moment and spin quantum number of an electron *(133)*. The spin quantum number *s* has magnetic components m_s = + ½ and m_s = - ½. When an external magnetic field is present, the electron's magnetic moment will align parallel (m_s = - ½) or antiparallel (m_s = + ½) to the field *(133)*. Each alignment has a specific energy, and the two spin states have the same energy in the absence of an applied magnetic field. The energy difference between the two spin states increases linearly with increasing magnetic field strength *(133)*. In other words, without the presence of an external magnetic field no transitions will occur, and as the strength of the magnetic field increases so does the energy difference between the electronic spin states.

One factor used to characterize paramagnetic species by EPR is the g-value. This is a proportionality factor which relates the intrinsic magnetic moment of an electron and the magnetic moment arising from the electron orbiting the nucleus *(133)*. The g-value for a free electron is 2.00232. This value will change depending on the environment of the electron *(133)*. Some g-values describing paramagnetic species observed in the biological samples are listed in Table 2.1. EPR spectra are collected by holding the frequency of radiation constant (*i.e.*, 9.5 GHz for these studies) and varying the magnetic field (0-5000 Gauss) *(133)*. When the energy difference between the electronic spin

states is equal to the radiation, absorption occurs. EPR spectra are plotted as a first derivative of the electron absorption *(133)*. The point at which the signal passes through 0 represents the point of maximum absorption *(133)*. By investigating the different paramagnetic species in a sample we can establish a more complete understanding of the Fe-containing species in cells and organelles.

Electron Absorption Spectroscopy

Electron absorption spectroscopy is commonly used to detect hemes and iron-sulfur clusters. Reduced heme centers feature 3 distinct Soret bands (α, β, and γ). The α bands of heme a, b, and c are observed at ~605, ~565, and ~550 nm, respectively. These bands are not present when cytochromes are oxidized. FeS clusters, including Fe_4S_4 and Fe_2S_2, also show features at ~410 and ~430 nm, respectively. These features arise from oxidized clusters, but the intensity of the peaks diminishes when the clusters become reduced.

The extinction coefficients of heme a, b, and c are well established and can be used to determine the concentration of each heme component in a sample *(134)*. This is advantageous for our studies because Mössbauer spectroscopy cannot distinguish between LS hemes and Fe_4S_4 clusters. Moreover, the concentrations of these hemes in whole cell samples are quite low (< 100 μM). Therefore, UV-Vis is a good complementary technique to Mössbauer and EPR spectroscopy which can provide additional information about absolute concentrations of Fe centers in a sample. This analysis also provides information about levels of mitochondria in the cells.

Inductively-Coupled Plasma Mass Spectrometry

ICP-MS is an analytical technique used to determine precise concentrations of metals in a sample, including Fe. This technique ionizes a sample with inductively coupled plasma and uses a mass spectrometry to separate and quantify ions. This method has detection limits as low as one part per trillion (10^{12}). This is advantageous for biological samples which have low concentrations of Fe or other metals. The detection of ICP-MS is based on mass, which means this technique can distinguish different isotopes of a given metal. This allows us to measure the concentrations of ^{56}Fe and ^{57}Fe.

It is important to know the concentrations of each of these isotopes because only ^{57}Fe is detected with Mössbauer. For these studies, samples must be enriched with ^{57}Fe because it is only 2% naturally abundant. By utilizing ICP-MS, we can determine the percent enrichment of ^{57}Fe in Mössbauer samples. Moreover, as discussed previously, simulations of Mössbauer spectra give relative percentages of different ^{57}Fe-containing species in a sample. By determining the overall concentration of ^{57}Fe in a sample by ICP-MS and correlating this with Mössbauer data, we can determine the concentrations of different ^{57}Fe-containing species in a sample. Additionally, ICP-MS can be interfaced with a separations system (*i.e.,* size exclusion chromatography) to separate metal-containing components in a sample. The ICP-MS experiments were conducted using an Agilent ICP-MS (7700x).

Biophysical Studies

MB, EPR, and UV-Vis spectra were collected and analyzed as described *(135)*. MB spectra were collected using a MS4 WRC spectrometer (SEE Co., Edina MN). The instrument was calibrated using a spectrum of α-Fe foil collected at room temperature. Spectra were analyzed and simulations were generated using WMOSS software. EPR spectra were collected on an X-band EMX spectrometer (Bruker Biospin corp., Billerica, MA) equipped with an Oxford Instruments ER910A cryostat. Signals were integrated using a custom Matlab (Mathworks.com) program. Spin concentrations of the observed signals were calculated as described using 1.00 mM $CuSO_4$-EDTA as a standard *(136)*.

Signals were simulated using SpinCount (http://www.chem.cmu.edu/groups/hendrich/facilities/index.html). UV-Vis spectra of whole cells were collected on a Hitachi U3310 spectrometer with a Head-on photomultiplier tube, and then simulated using OriginPro as described *(137)*. Packed cell samples were diluted 3-fold with ddH_2O and analyzed in a 10 mm path length quartz UV-vis cuvette (Precision cells). After collecting MB, isolated mitochondria were thawed anaerobically in a glovebox (≤ 5 ppm O_2, MBraun, Labmaster), diluted 3-fold with SH buffer (0.6 M Sorbitol, 0.02 M HEPES, Fisher Scientific, pH 7.4), and transferred to a 2mm path length quartz UV-vis cuvette (Precision cells). The cuvette was sealed with a rubber septum and brought out of the glovebox. The samples were immediately analyzed by UV-vis.

Yeast Strains and Growth Conditions

Cells were grown and prepared as described *(138)*. WT (W303-1B and DY150) and Δ*CCC1* strains were stored in YPAD medium containing 15% glycerol at -80 °C. *CCC1-up* cells were stored using MM-Leu medium. Frozen cells were removed with a wooden stick and streaked on to YPAD plates (*CCC1-up* cells were maintained on MM-Leu plates). *Saccharomyces cerevisiae* strains W303 (MATα, ura3-1, ade2-1, trp1-1, his3-11,15, leu2-3,112; ATCC) were used for the studies described in Chapter III, and DY150 (MATa, ura3-1, ade2-1, trp1-1, his3-11,15, leu2-3,112; ATCC) were used for the studies described in Chapter IV.

Δ*CCC1* and *CCC1-up S. cerevisiae* cells were a generous gift of Dr. Jerry Kaplan (University of Utah). Both strains were derived from DY150 (isogenic to W303) as described *(139)*. The *CCC1* gene was over-expressed using a *LEU2*-marked multicopy plasmid that contained *CCC1* under its native promoter *(140, 141)*. For this reason, leucine was omitted from the medium used to grow *CCC1-up* cells (called MM-leu). WT and Δ*CCC1* cells were grown in minimal medium supplemented with 10 μM copper sulfate; the resulting medium will be abbreviated MM. Fermenting MM contained 2% w/v glucose (Fisher Scientific), 0.5% w/v ammonium sulfate (Fisher Scientific), 1.7 g/L YNB without ammonium sulfate, ferric citrate, or copper sulfate (MP Biomedicals, LLC #4027-112), 100 mg/L L-leucine (MP Biomedicals, LLC #0219469480), 50 mg/L adenine hemisulfate dehydrate (MP Biomedicals, LLC #0219460790), 20 mg/L L-histidine (MP Biomedicals, LLC #0210195480), and 20 mg/L L ^{57}Ferric citrate (FC).

The ^{57}Fe citrate (40 mM, pH ~5) solution was prepared as described *(138)*. This stock was added to MM to final concentrations of 1, 10, 20, and 40 μM.

Ccc1p overexpression in the *CCC1-up* strain was verified by performing Western blots on vacuoles isolated from WT and *CCC1-up* cells (see figure on p. 86). Vacuoles were isolated as described,*(112)* and 60 μg of protein was used per lane. The Ccc1p antibody, also provided by Dr. Jerry Kaplan, was generated as described *(141)*. The absence of the *CCC1* gene in the Δ*CCC1* strain was verified by PCR, using primers 5' TTTCGGTCTGGACCAATCGC 3' and 5' GCGACCAAATGACGAATTAG 3'. The PCR reaction was performed at two different annealing temperatures (54°C and 58°C). WT and Δ*CCC1* strains produced PCR products of 1.5 kb and 2.5 kb, respectively (see figure on p. 86).

Preparation of Whole Cell Samples

Cells were grown and prepared as described *(138)*. All strains were stored at -80 °C in YAPD medium containing 15% glycerol. Frozen cells were removed with a wooden stick and streaked on to YPAD plates (*CCC1-up* cells were maintained on YPAD-Leu plates). Single colonies were inoculated into 50 mL of MM cultures and grown for 24 hr at 30 °C with shaking. These cells were used to inoculate 1 L of MM cultures which were grown to an OD_{600} = 1.0 (± 0.1) and harvested. Cells were pelleted (4,000×g, 10 min, Sorvall Evolution RC centrifuge, SLC-6000 rotor), washed 1× with 1 mM EGTA, 3× with ddH_2O, and then packed into MB cups or EPR tubes, or resuspended in ddH_2O for UV-vis analysis. Samples were frozen in LN_2 and stored for

subsequent analysis. Whole cell samples were prepared aerobically. Mitochondria and vacuoles were isolated anaerobically and prepared for spectroscopic analysis as described *(135)*.

Isolation of Vacuoles

1L cell cultures (inoculated from 50ml cultures) were grown to an OD_{600} ~ 1, then inoculated into 25L cultures. The 25 L cultures were grown to an OD_{600} of 0.6-0.8 and harvested (6 L at a time) by centrifugation at 4000xg for 5 minutes (Sorvall Evolution RC centrifuge, SLC-6000 rotor). The cell pellet was transferred to a refrigerated argon-atmosphere glovebox (MBraun Labmaster, 6 °C, ~ 2 ppm O_2) where vacuoles were isolated essentially as described *(142)*, except that cells were treated with ~1000 U lyticase/g of wet cell paste for 50-90 min at 30° C (Sigma-Aldrich).

In some batches, TCEP-HCl (Tris(2-carboxyethyl)phosphine, Thermo Scientific, #20491; 5 mM final concentration) was used instead of dithiothreitol (DTT, 10 mM final). Cells were disrupted using 100 µg/ml of diethylaminoethyl dextran (DEAE-Dextran, Sigma-Aldrich) in 15% Ficoll (Fisher Bioreagents) buffer *(143)*. The resulting cell lysate was subjected to density gradient centrifugation (Beckman Coulter Optima L-90K ultracentrifuge, Sw-32 Ti rotor; 110,000 x g, 90 min). The first gradient consisted of cell lysate in 15% Ficoll buffer overlayed with 8% Ficoll buffer and with PS buffer layered on top. The material collected from the PS - 8% interface was diluted with 15% Ficoll buffer and overlayed with 4% Ficoll buffer and with PS buffer layered on top.

Purified vacuoles were collected at the PS - 4% interface. Vacuoles were washed in PS buffer and centrifuged at 38,000×g for 20 min.

Pelleted organelles were resuspended in PS buffer and packed into Delrin Mössbauer cups (12 mm OD × 10 mm) and Suprasil Quartz EPR tubes (Wilmad Labglass; 4 mm OD; 89 mm long) were packed by centrifugation at 10,900×g for 45 min. Cups and tubes were frozen and stored in liquid N_2 for subsequent analysis. Mössbauer and EPR spectra were obtained as described *(135)*. EPR signals were integrated using a program written in Matlab (Mathworks.com) and spin concentrations were calculated as described previously *(136)*. UV-Vis spectra of vacuole suspensions in a 2 mm pathlength quartz cuvette were collected using a Hitachi Model U3310 spectrophotometer with a Head-On photomultiplier tube.

Western Blot Analysis and Electron Microscopy

Protein concentrations were determined using the BCA method *(144)*. Western blots used 60 μg of vacuolar or cell extract protein per lane, and mitochondrial porin (Invitrogen), vacuolar carboxypeptidase Y (CPY) (AbCam), cytosolic 3-phosphoglycerate kinase (PGK) (Invitrogen), and endoplasmic reticular Kar2 (Santa Cruz Biotechnology) proteins were detected. Goat anti-mouse HRP-conjugated secondary antibodies (Invitrogen) were used with Porin and PGK, while goat anti-rabbit HRP-conjugated secondary antibodies (Santa Cruz Biotechnology) were used with CPY and Kar2. Enhanced chemiluminescent western blotting substrate (Thermo Scientific) was added, and images were obtained (FujiFilmLAS-4000mini) with a 10 s standard

exposure and the chemiluminescence setting. Images were analyzed using MultiGauge version 3.1.

For electron micrographs, samples were fixed in 1% acrolein (isolated vacuoles) or 5% acrolein (whole cells) (Sigma-Aldrich) solutions at 4 °C with shaking, then rinsed 4 times with 1% dimethylsulfoxide (DMSO) and stored overnight at 4 °C. The alkaline phosphatase reaction was performed as described *(145, 146)*. Samples were fixed overnight with 1% osmium tetroxide (OsO_4) then dehydrated using a cold methanol series. Samples were infiltrated using three 100% changes of Quetol/Araldite/DDSA resin and polymerized. Ultrathin sections were cut using an Ultracut E microtome (Reichert-Jung), visualized using a transmission electron microscope (JEOL 1200-EX), and photographed using a bottom-mounted 3Kx3K, slow scan, lens-coupled CCD camera (SIA 15C).

Packing Efficiency of Isolated Vacuoles

The packing efficiency of vacuoles was determined as described *(147)*. Briefly, the fractional volume of interstitial buffer in packed vacuoles was calculated using the cell-impermeable fluorescent Compound 5 *(148)*. Vacuoles were isolated from cells grown to OD(600) ~ 0.8, transferred to an EPR tube, and pelleted by centrifugation (10,900×g, 45 min). The volume of the pellet (V_{pel}) was determined from its height in 3.0 mm ID EPR tubes. The pellet was resuspended using 200 μL of buffer containing 0.1 M Compound 5. The vacuoles were pelleted, the supernatant fraction was collected, and its volume determined (V_{sup1}). The concentration of Compound 5 in the supernatant fraction

(C_{sup1}) was determined from a standard curve generated using a fluorescence spectrometer (Koala 90080; ISS Inc.). Fluorescence was detected at 654 nm (fixed) with ten scans per sample. Pellet volumes were assumed to be due exclusively to vacuole and buffer volumes ($V_{\text{pel}} = V_{\text{vac1}} + V_{\text{buf1}}$). The conservation of matter requires that the molar amount of Compound 5 added in the buffer,

$$20\ nmol = C_{\text{sup1}} \cdot V_{\text{sup1}} + C_{\text{sup1}} \cdot V_{buf\,1}$$

Solving for V_{buf1} allowed the packing efficiency of vacuoles, defined as $(V_{pel} - V_{buf\,1}) / V_{pel} \cdot 100$, to be determined. The same steps were repeated with buffer lacking the compound. In this case,

$$C_{\text{sup1}} \cdot V_{\text{buf1}} = C_{\text{sup2}} \cdot V_{\text{sup2}} + C_{\text{sup2}} \cdot V_{\text{buf2}}$$

The equation was solved for V_{buf2} and packing efficiency was defined as $(V_{pel} - V_{buf\,2}) / V_{pel} \cdot 100$. V_{pel} was found to be unchanged with each centrifugation step.

Metal Concentration Determination

Pellets of isolated vacuoles (typically with volumes ranging from 50 – 100 μL) were resuspended in sufficient PS buffer for the suspension volume to total 225 μL. Suspensions were separated into aliquots of 50, 75, and 100 μL using 15 mL plastic screw-top vials. Concentrated (70%) trace-metal grade (TMG) nitric acid (Fisher Chemicals) (100 μL) was added to each vial. Vials were sealed with screw-top caps wrapped tightly with electrical tape, and then incubated at 90 °C for ~ 17 hrs. Aliquots were diluted to 7.9 mL using high purity trace-metal-free double-distilled-deionized

(DDDI) water generated using a Teflon sub-boiling still (Savillex). Samples were analyzed using ICP-MS (Agilent 7700x) utilizing both H_2 reaction mode (^{57}Fe and ^{56}Fe) and He collision modes (Mn, Cu, Zn, and P) to eliminate interferences. Standards were prepared from stock solutions (Inorganic Ventures), concentrated TMG (70%) nitric acid (Fisher Scientific), and DDDI water. Calibration curves with a range of 0 – 1000 ppb were generated for each element, as well as for the two isotopes of Fe.

Redox Activity of Fe in Isolated Vacuoles

After collecting the 7 K low-field Mössbauer spectrum of a preparation of isolated vacuoles (Figure 3.3 Batch 14), the sample was brought into the glove box, thawed, and suspended in PS buffer containing 1% deoxycholate (final concentration). The suspension (200 µL) was transferred to a 2 mm pathlength quartz cuvette, which was sealed with a rubber septum and removed from the box. After collecting the UV-Vis spectrum, the sample was returned to the box, treated with dithionite (400 µM, final concentration) and another UV-Vis spectrum was collected after *ca*. 5 min incubation. The sample was returned to the box, transferred to a Mössbauer cup, and frozen in liquid N_2.

Preparation of Fe Complexes

Sodium phosphate (Dihydrate, Sigma-Aldrich) (50 mM final) and aqueous $^{57}Fe^{3+}$ (5 mM, final) were mixed in an acetate/acetic acid buffer (100 mM, pH ~ 5 final) in an effort to generate Fe^{3+} phosphate. The same approach was used to prepare Fe^{3+}

polyphosphate, except that sodium polyphosphate (Thermo-Fisher) was used. The aqueous $^{57}Fe^{3+}$ stock solution was prepared by dissolving ^{57}Fe metal (Isoflex USA) in concentrated TMG HNO_3 (Fisher Scientific) and concentrated TMG HCl (Thermo-Fisher Scientific) in a 1:1 ratio and then diluted with DDDI H_2O to a final ^{57}Fe concentration of 80 mM and a final acid content of ~0.5%. To ensure complete oxidation, samples were treated using an excess of H_2O_2 (Thermo-Fisher Scientific).

Concanamycin-A and Glucose Treatment

Cells were treated with glucose and ConA as described *(149)*. WT cells were grown in minimal medium (MM) containing 40 μM FC and harvested during late exponential phase (OD_{600} = 1.0 ± 0.1). The wet pellet was washed once with MM, then resuspended and incubated in MM lacking glucose for 10 min at 30 °C. Glucose (50 mM final) and ConA (2 μM final) were then added and the cells were incubated at 30°C for 0, 15, and 60 min. After the given incubation time the cells were packed into MB cups by centrifugation at 4,000xg for 10 minutes then frozen with LN_2. Control experiments were performed without ConA.

CHAPTER III

MÖSSBAUER AND EPR STUDIES OF IRON IN VACUOLES ISOLATED FROM *SACCHAROMYCES CEREVISIAE*[1]

My role in these studies was to grow large cultures of *S. cerevisiae,* to develop the protocol to isolate large quantities of vacuoles, and to harvest the vacuoles from these cells. I was also responsible for collecting and interpreting Mössbauer, EPR, and UV-Visible spectroscopy data. I made the Fe monophosphate and Fe polyphosphate complexes and biophysically characterized these compounds using Mössbauer spectroscopy. Dr. Gregory P. Holmes-Hampton was responsible for maintaining the Mössbauer instruments, for preparing the whole cell samples, and for interpreting these results. Mr. Sean P. McCormick, another graduate student, was responsible for maintaining the ICP-MS, and for collecting the ICP-MS data. Dr. Mrinmoy Chakrabarti provided guidance regarding the biophysical interpretation of the Mössbauer and EPR data, and was responsible for maintaining the high-field Mössbauer instrument and collecting and interpreting these data. All of the authors contributed to discussions regarding the interpretation of these data.

Vacuoles were isolated from fermenting yeast cells grown on minimal medium supplemented with 40 μM ^{57}Fe. Absolute concentrations of Fe, Cu, Zn, Mn, Ca, and P in isolated vacuoles were determined by ICP-MS. Mössbauer spectra of isolated

---

[1] Reprinted with permission from Allison L. Cockrell, Gregory P. Holmes-Hampton, Sean P. McCormick, Mrinmoy Chakrabarti, and Paul A. Lindahl (2011) Mössbauer and EPR Study of Iron in Vacuoles Isolated from *Saccharomyces cerevisiae, Biochemistry 50 (47),* 10275-10283.

vacuoles were dominated by two spectral features; a mononuclear magnetically isolated high-spin (HS) Fe^{3+} species primarily coordinated by hard/ionic (mostly or exclusively oxygen) ligands, and superparamagnetic Fe^{3+} oxyhydroxo nanoparticles. EPR spectra of isolated vacuoles exhibited a g_{ave} ~ 4.3 signal typical of HS Fe^{3+} with E/D ~ 1/3. Chemical reduction of the HS Fe^{3+} species was possible, affording a Mössbauer quadrupole doublet with parameters consistent with N/O ligation. Vacuolar spectral features were present in whole fermenting yeast cells; however, quantitative comparisons indicated that Fe leaches out of vacuoles during isolation. The *in vivo* vacuolar Fe concentration is estimated to be ~1.2 mM while the Fe concentration of isolated vacuoles was ~220 μM. Mössbauer analysis of Fe^{3+} polyphosphate exhibited properties similar to those of vacuolar Fe. At the vacuolar pH of 5, Fe^{3+} polyphosphate was magnetically isolated, while at pH 7, it formed nanoparticles. This pH-dependent conversion was reversible. Fe^{3+} polyphosphate could also be reduced to the Fe^{2+} state, affording similar Mössbauer parameters to that of reduced vacuolar Fe. These results are insufficient to identify the exact coordination environment of the Fe^{3+} species in vacuoles, but they suggest a complex closely related to Fe^{3+} polyphosphate. A model for Fe trafficking into/out of yeast vacuoles is proposed.

Introduction

Yeast vacuoles are major hubs for iron trafficking, and have many Fe-related functions *(102, 142, 150)*. One function is to *sequester* and *detoxify* Fe, so as to restrict the formation of reactive oxygen species that would otherwise be toxic to the cell *(150,*

151). Vacuoles also function as *reservoirs* of Fe, allowing cells to survive in Fe-deficient environments *(131, 150)* and transition from fermenting to respiring metabolism *(152)*. They also *buffer* cytosolic Fe against fluctuations, so as to maintain cellular Fe homeostasis *(131)*.

Raguzzi *et al*. *(152)* and Singh *et al*. *(142)* have proposed that vacuoles contain ferric ions coordinated by hydroxide, phosphate, and/or polyphosphate ions. They suggested the Fe^{3+} oxidation state because the vacuolar lumen is more acidic than the cytosol, which raises the effective electrochemical potential of the glutathione disulfide/glutathione couple. This couple dominates the redox status of the vacuole and cytosol; a higher effective potential translates into diminished reducing power. Phosphate and polyphosphate have been suggested as ligands because of the high concentration of these species in vacuolar lumen *(142, 153)* and the ability of these anions to bind Fe^{3+} ions tightly *(154, 155)*.

Fe is imported into vacuoles through two major pathways, including endocytosis and through Ccc1p, a transporter on the vacuolar membrane *(156, 157)*. The exact species imported is unknown, but the Fe^{2+} state is generally assumed *(131, 150, 158)*. *CCC1* gene expression is responsive to cytosolic Fe concentrations and the *CCC1* mRNA is destabilized under Fe-deficient growth conditions *(129)*. Vacuoles isolated from cells that could not engage in endocytosis were phenotypically normal and contained proportionately more Fe/mg protein than found in Δ*CCC1* vacuoles *(150)*. These results suggest that the Ccc1p pathway is responsible for a larger portion of the Fe imported into the vacuole, relative to the endocytosis pathway *(140)*.

The vacuole membrane contains two Fe export systems, Fth1p/Fet5p *(159)* and Smf3p *(122)*. Fet5p and Fth1p are homologs of the plasma membrane multicopper oxidase Fet3p and permease Ftr1p *(142)*. These two plasma-membrane proteins form a complex that transports Fe^{3+} from the environment into the cytosol, reducing it to the Fe^{2+} state in the process. Fet5p and Fth1p are presumed to function similarly. Fre1p catalyzes the reduction of Fe^{3+} to Fe^{2+} by NADPH prior to delivering this ion to the Ftr1p/Fet3p complex *(19, 20)*. Fre6p catalyzes the analogous reduction during the export of vacuolar Fe *(142, 160)*. The vacuolar membrane protein Smf3p exports Fe (and other divalent metal ions) from the vacuolar lumen to the cytosol under low-Fe growth conditions *(122, 161, 162)*.

In summary, the import of Fe^{2+} from the cytosol to the vacuole appears to be associated with its oxidation to Fe^{3+}, and the export of Fe^{3+} from the vacuole to the cytosol is associated with the reduction of Fe^{3+} back to Fe^{2+}. This scenario is reasonable and well-grounded from a biochemical/genetics perspective, but it has not been examined using biophysical methods. In the study described here, we isolated vacuoles from fermenting WT *S. cerevisiae* cells and characterized their Fe content using Mössbauer, EPR and UV-vis spectroscopies, as well as ICP-MS. We demonstrate that the Fe in this organelle consists predominately of mononuclear nonheme high-spin Fe^{3+} ions, mostly likely as a single complex. A second species consisting of Fe^{3+} oxyhydroxo nanoparticles, is also present. The two species probably interconvert in a pH-dependent fashion.

Results

Bioanalytical Characterization of Isolated Vacuoles

We isolated vacuoles from 23 independent batches of WT yeast cells, each grown under fermenting conditions using minimal medium supplemented with 40 μM ^{57}Fe (or ^{56}Fe) citrate. Each batch could not be analyzed by every method available due to insufficient material; Table 3.1 lists which batches were analyzed by which methods. Purity and membrane integrity were evaluated by electron microscopy (Figure 3.1, top panel) and Western Blot analysis (Figure 3.1, bottom panel). Electron micrographs revealed a dominance of intact vacuolar membranes in the samples. Relative to the cell-extract lane, isolated vacuoles contained 3-fold more CPY, a vacuolar marker protein, 5-fold less KAR2, an ER protein, 16-fold less of mitochondrial Porin, and 4-fold less of the cytosolic protein PGK. Overall, this analysis suggests that our isolated vacuoles were largely intact and purified, with minor contamination of ER, mitochondrial, and cytosolic proteins. We determined the packing efficiency of isolated vacuoles using a fluorescent compound that does not penetrate cellular plasma membranes *(148)*. Neither does this compound appear to penetrate vacuolar membranes, in that samples exposed to it and then washed repeatedly did not exhibit substantial fluorescence beyond that of unexposed samples. The percentage of the volume of packed vacuoles due to the vacuoles themselves, taken as the average of the 6 values was 76% ± 5%. The remainder was assumed to be due to interstitial buffer.

The concentrations of Fe, Cu, Zn, Mn, Ca and P in 18 batches of isolated vacuoles (taking packing efficiency into account) were determined (Table 3.1); averages

± SD in μM were: Fe, 220 ± 100; Cu (low) 30 ± 30; Cu(high) 540 ± 280; Zn, 160 ± 120; Mn, 1.7 ± 0.6; Ca, 190 ± 110; and P, 14,000 ± 8,700. Batch-to-batch variability was significant, with relative errors of *ca*. ± 60% or higher. This suggests that there are unknown and uncontrolled variables in our growth and/or isolation procedures. Cu concentrations were especially scattered, but they bifurcated rather cleanly into low and high groups. The low Cu concentrations are perhaps more reliable, in that they are more consistent with the concentration of Cu in whole cells (see below). Mn concentrations were the least scattered. Phosphorus levels, which almost certainly reflect phosphate and polyphosphate ions, were orders-of-magnitude higher than metal numbers. The $[Fe]_{ave}/[Protein]_{ave}$ ratio of 1.9 μg Fe/mg protein was 10 fold higher than in previous reports *(142, 150),* suggesting that our vacuoles contained more Fe (or less protein, or some combination of the two) than those studied previously. For the 16 batches isolated from cells grown on media enriched in ^{57}Fe, the average level of enrichment was 74 ± 13%. The Fe concentration in a batch of whole WT cells grown on the same media was 380 μM, similar to the value of 440 μM previously reported *(147)*.

Spectroscopic Characterization of Isolated Vacuoles

Figure 3.2 shows the variable field, variable temperature Mössbauer spectra of isolated vacuoles from Batch 15. The 4.3 K, 0.05 T spectrum (Figure 3.2A) is dominated by a paramagnetic species with absorption between -10 to + 10 mm/s. This

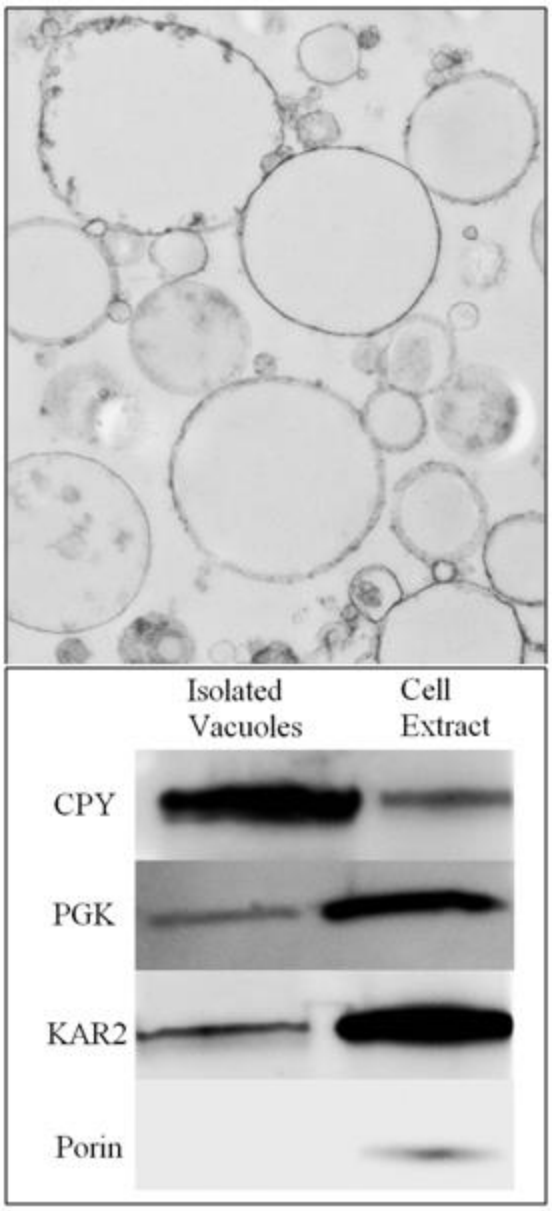

Figure 3.1. TEM images and Western blots of isolated vacuoles. Top panel; images of Batch 6 vacuoles obtained at 10,000× magnification. Bottom panel; isolated vacuoles from Batch 2 (lane 1) were compared with cell extract (lane 2).

Batch	[^{56}Fe]; [^{57}Fe]; % enrichment	$[Fe]_{tot}$	[Cu]	[Zn]	[Mn]	[Ca]	[P]	Protein
1	018; 053; 75	071	007$^{(low)}$	023	0.9	103	07,200	1.2
3	009; 026; 74	035	007$^{(low)}$	023	0.8	093	10,100	7.1
7	061; 200; 77	261	018$^{(low)}$	273	2.3	158	12,200	5.3
8	054; 156; 74	210	352$^{(high)}$	018	1.8	102	08,600	2.9
10	038; 040; 51	078	008$^{(low)}$	039	1.2	097	08,900	2.7
11	049; 053; 52	102	013$^{(low)}$	055	1.5	097	07,600	3.9
12	389; 011;03$^{(un)}$	400	018$^{(low)}$	266	1.6	308	23,500	3.1
13	056; 066;54	122	014$^{(low)}$	072	1.8	098	06,500	---
14	056; 141;72	197	017$^{(low)}$	085	2.0	170	10,700	10.1
15	048; 228; 83	276	016$^{(low)}$	103	2.3	243	15,500	4.8
16	019; 396; 95	415	028$^{(low)}$	416	---	---	---	---
17	074; 243;77	317	022$^{(low)}$	236	3.2	212	14,800	11.5
18	053; 287;84	340	130$^{(low)}$	352	2.1	---	39,500	14.9
19	245; 020;08$^{(un)}$	265	010$^{(low)}$	---	1.0	017$^{(-)}$	---	---
20	080; 206;72	286	960$^{(high)}$	645$^{(-)}$	4.9$^{(-)}$	1290$^{(-)}$	48,500$^{(-)}$	47.2 $^{(-)}$
21	028; 176;86	204	440$^{(high)}$	330	1.8	480	22,900	5.8
22	042; 201;83	243	414$^{(high)}$	299	1.8	284	13,200	8.4
23	019; 287;94	306	070$^{(low)}$	162	1.3	224	10,900	7.0
Ave.	[^{56}Fe] = 50±20 [^{57}Fe]=150±90 74±13% enriched	220 ± 100	30 ± 30$^{(low)}$ 540 ± 280$^{(high)}$	160 ± 120	1.7 ± 0.6	190 ± 110	14,000 ± 8,700	6.3 ±3.8
Whole Cells (#15)	076; 301; 80	380	020	120	2.6	300	20,000	40

Table 3.1. Elemental and protein concentrations of isolated vacuoles. Tabulated values were obtained by multiplying measured concentrations of isolated vacuole solutions by the fold dilution used to resuspend packed pellets (typically ×120), and dividing by the packing efficiency (÷ 0.76). Element concentrations are given in μM, protein concentrations in mg/mL. Abbreviations, (un), unenriched; (low) and (high), batch with low and high concentrations of Cu; (-), not included in average.

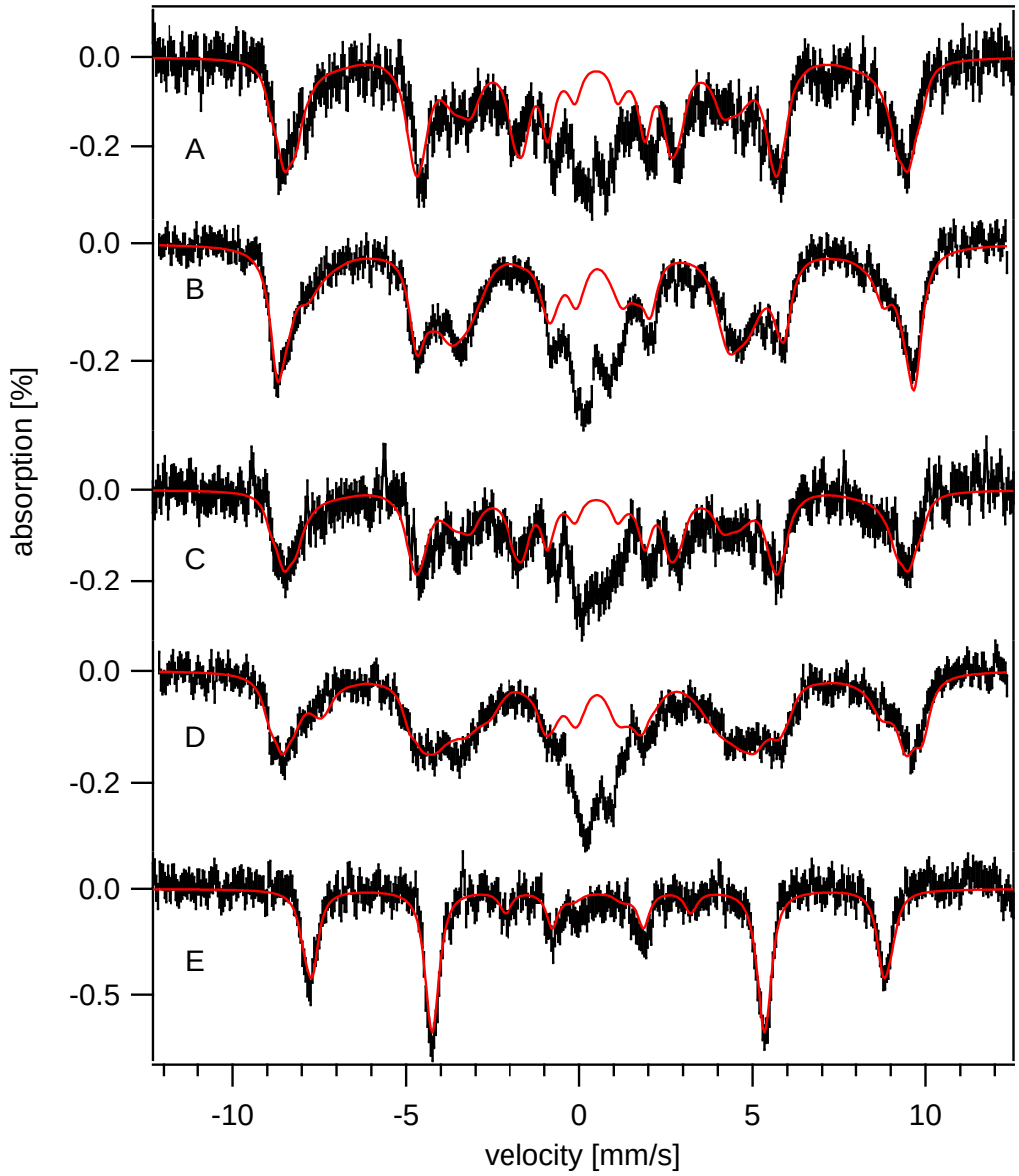

Figure 3.2. Mössbauer spectra of isolated vacuoles. (Batch 15) A, 4.2 K, 0.05 T; B, 7 K, 0.05T; C, 12 K, 0.05T; D, 100 K, 0.05 T; E, 4.2 K, 6 T. Applied fields in A and E were perpendicular to the gamma radiation, while those in B – D were parallel to the radiation. The solid red lines are simulations assuming S = 5/2, D = 0.5 cm^{-1} and E/D = 0.33, $A_o/\gamma_N.\beta_N$ = -230 KG, δ = 0.54 mm/sec, ΔE_Q = 0.39 mm/sec, and η = 2.

spectral feature is typical of a mononuclear high spin Fe^{3+} species and was analyzed with a S= 5/2 spin Hamiltonian

$$\aleph = D(S_z^2 - 35/4) + E(S_x^2 - S_y^2) + \beta S \cdot g \cdot B + S \cdot A \cdot I - g_n \beta_n \cdot B \cdot I + \aleph_Q$$

where *D* and *E* are the axial and rhombic zero-field-splitting parameters, *A* is the ^{57}Fe magnetic hyperfine tensor, and $\aleph_Q$ describes the nuclear quadrupole interactions.

This feature represented 75% of the overall spectral intensity in this batch. Residual intensity was unresolved and centered near 0 mm/s. At 7 K and 0.05 T (Figure 3.2B) the middle doublet ($m_s = \pm 3/2$) of the S = 5/2 spin multiplet has an appreciable population, shown by the strong absorption features in the +4 and -4 mm/sec region. This indicates that *D* is small. Mössbauer and EPR fitting trials suggest that $D = 0.5$ cm^{-1} and $E/D = 0.33$ (rhombic symmetry). The fitted isomer shift and quadruple splitting values suggest a hexacoordinated HS Fe^{3+} species with oxygen/nitrogen donor atoms *(133)*. The isotropic $A_o/\gamma_N \cdot \beta_N = -230$ KG obtained from simulations are also typical of a HS Fe^{3+} species *(133)*.

The spectra of all batches examined by Mössbauer also included a second component in varying relative proportions. The batch just described (Batch 15) exhibited the lowest proportion of this component, while Batch 23 exhibited the highest proportion (Figure 3.4). The spectra of three other batches, with intermediate levels of the second component, are shown in Figure 3.3. In batches showing greater resolution of this second feature, a quadrupole doublet was evident. These parameters were similar to those of Fe^{3+} (phosphorus) oxyhydroxo nanoparticles observed in various genetic strains of yeast *(71, 135, 147, 163)*. The spectral features due to the nanoparticles could be

removed, affording difference spectra (Figure 3.4, C and F) that could be simulated using the same H.S. Fe^{3+} parameters as used above. A somewhat different spectral shape was reported previously *(71, 135, 147, 163)* but in those spectra the field was applied *parallel* to the gamma radiation, affording different selection rules. The magnetic features due to these nanoparticles in Figure 3.4 were broad because the hyperfine coupling tensor A values were widely distributed as is typical of aggregated superparamagnetic materials.

X-band EPR spectra of isolated vacuoles supported this analysis, as all 10 batches examined displayed a dominant feature at g_{ave} ~ 4.3 (Figure 3.5A). Such features are typical of HS Fe^{3+} species with rhombic symmetry (E/D ~ 1/3). However, the quantified intensity of the signal varied considerably, with spin concentrations ranging from 110 to 175 μM in samples of packed isolated vacuoles from 4 separate batches (Batches 14, 16, 17 and 23). When normalized to the [Fe], and to the fraction of Fe Figure 3.4 associated with the six-line pattern in the Mössbauer spectra (measured to be 56% and 85% in Batches 23 and 14, respectively; and assumed to be midway between these percentages in Batches 17 and 16), the ratio of [spin]/[HS Fe^{3+}] was 0.9, 0.7, 0.8 and 0.6**,** respectively.[1] No Cu^{2+}-based EPR signals were observed, even in the 4 batches examined that had high Cu concentrations (Batches 8, 20, 21 and 22). Cu ions in this organelle may be in the cuprous state, which is counterintuitive given the oxidizing environment of the vacuolar lumen. They may also be in the cupric state and EPR-silent for other reasons, e.g., involving spin-coupling.

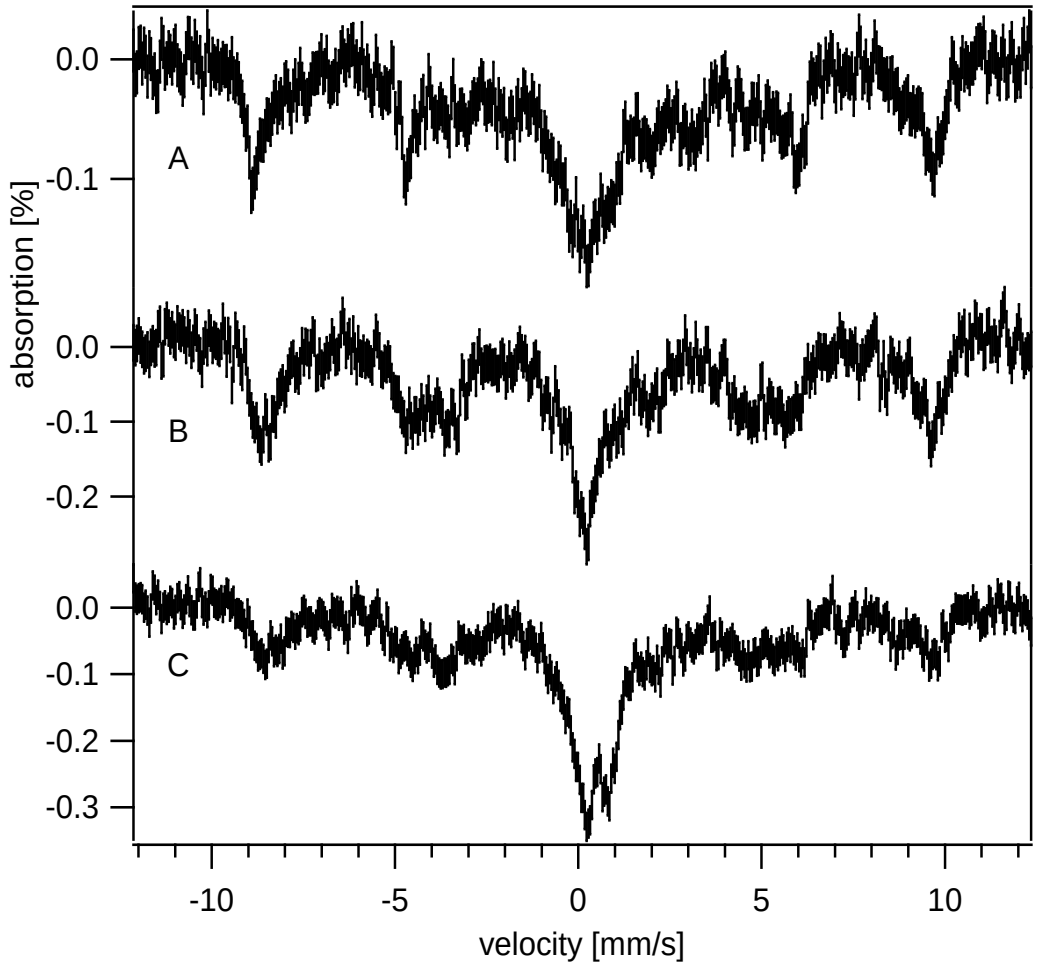

Figure 3.3. Additional 6 K, 0.05T Mössbauer spectra of isolated vacuoles. A, Batch 7; B, Batch 14; C, Batch 11. Applied fields were parallel to the gamma radiation.

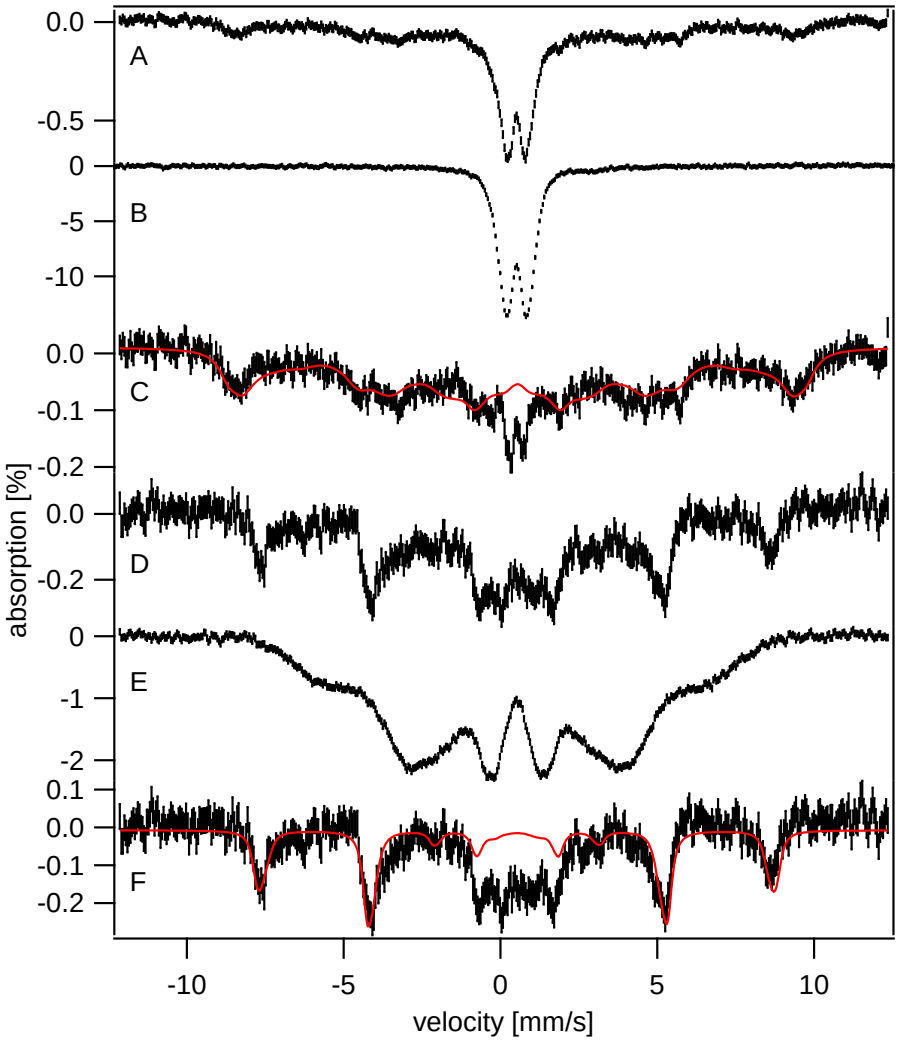

Figure 3.4. Mössbauer spectra of isolated vacuoles and mitochondria isolated from a genetic strain (Aft1-1^{up}) known to contain Fe^{3+} (phosphate) nanoparticles. Vacuoles were from Batch 23, and nanoparticle spectra were shown in *(147)*. A, vacuoles at 7 K and 0.05 T; B, mitochondria at 4.3 K and 0.05 T; C, same as A after spectrum B was subtracted at the 40% level. The solid red line is a simulation assuming the parameters specified in Figure 3.2; D, vacuoles at 4.2 K and 6 T; E, mitochondria at 4.2 K and 6 T. F, same as D after spectrum E was subtracted at the 40% level. The solid line is a simulation assuming the same parameters as in C except that the applied field was 6T. In D and E, applied fields were perpendicular to the gamma radiation. In A and B, applied fields were parallel to the radiation.

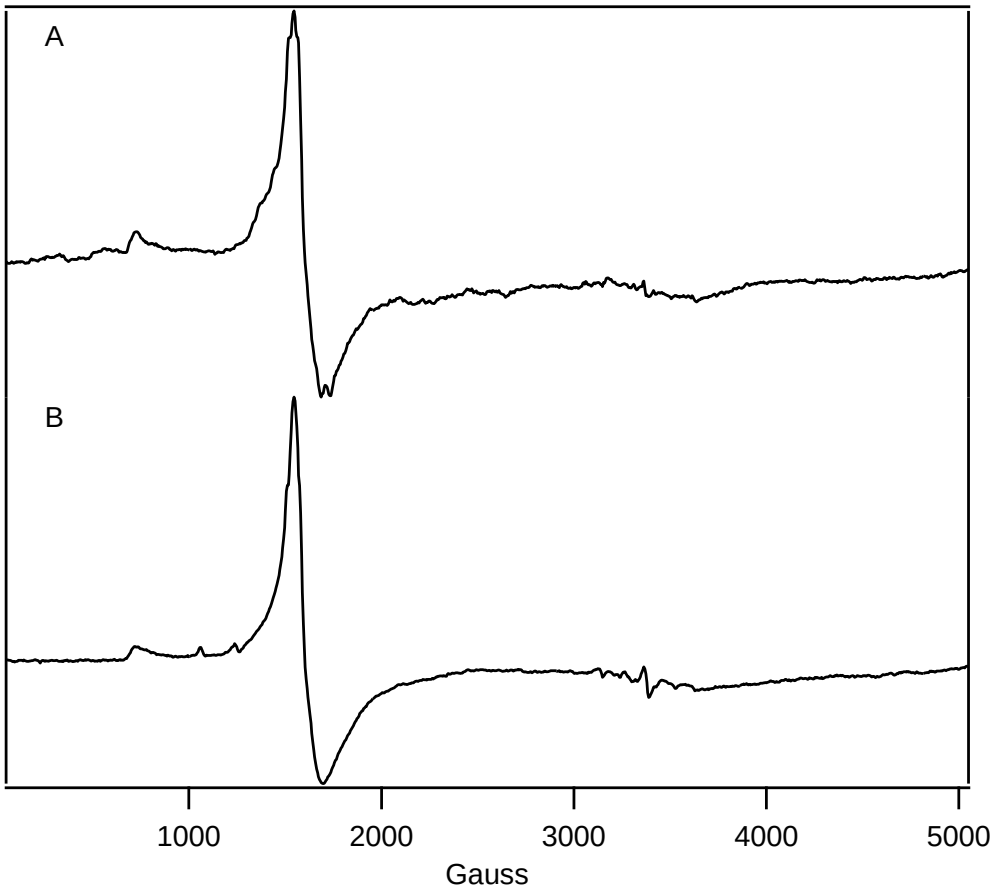

Figure 3.5. EPR of isolated vacuoles and whole cells. A, Batch 23; temperature, 4 K; microwave frequency, 9.46 GHz; microwave power 0.08 mW; B, Temperature, 10 K; microwave frequency, 9.46 GHz; microwave power 0.2 mW. The whole-cell spectrum includes low-intensity features at g = 6.4 and 5.4, and signals in the g = 2 region which are absent or of diminished intensity in the spectrum of isolated vacuoles. These features originate from mitochondria *(135, 164)*. The whole-cell spectrum includes low-intensity features at g = 6.4 and 5.4 *(135, 164)*. The low-field features probably arise from cytochrome c oxidase while the high-field features arise from other respiration-related proteins.

When suspended in buffer, solutions of isolated vacuoles were milky white, and have electronic absorption spectra dominated by the effects of light scattering (Figure 3.6, top panel). We considered that the low-intensity feature at ~ 410 nm was due to the HS Fe^{3+} species evidenced by Mössbauer and EPR spectra, as it reminded us of the broad low-intensity transition at 470 nm from diferric transferrin *(165)*. However, subsequent treatment with dithionite had no effect on this feature (Figure 3.6, top panel). The effectiveness of dithionite in reducing the HS Fe^{3+} species was evidenced by the quadrupole doublet generated in the Mössbauer spectrum of the treated sample (Figure 3.6, bottom panel). We conclude that the dominant HS Fe^{3+} species in as-isolated vacuoles is redox-active, and can be reduced to the Fe^{2+} state. However, neither redox state is associated with the observable electronic absorption feature. The Mössbauer parameters associated with the Fe^{2+} doublet suggest that this species is primarily coordinated by oxygen and/or nitrogen donor ligands. Whether the exchange of one oxygen- or nitrogen- dominating ligand set for another accompanied reduction remains undetermined.

Related Fe^{3+} Compounds

We attempted to reproduce the mononuclear HS Fe^{3+} species in vacuoles by adding phosphate and polyphosphate ions to hex(aqua/hydroxo) Fe^{3+} ions in pH 5 buffer. This pH was used to mimic the vacuolar lumen, which has pH between 4.8 and 5.4 *(166)*. Presuming that the intended complexes formed, the 6 K and 0.05 T Mössbauer

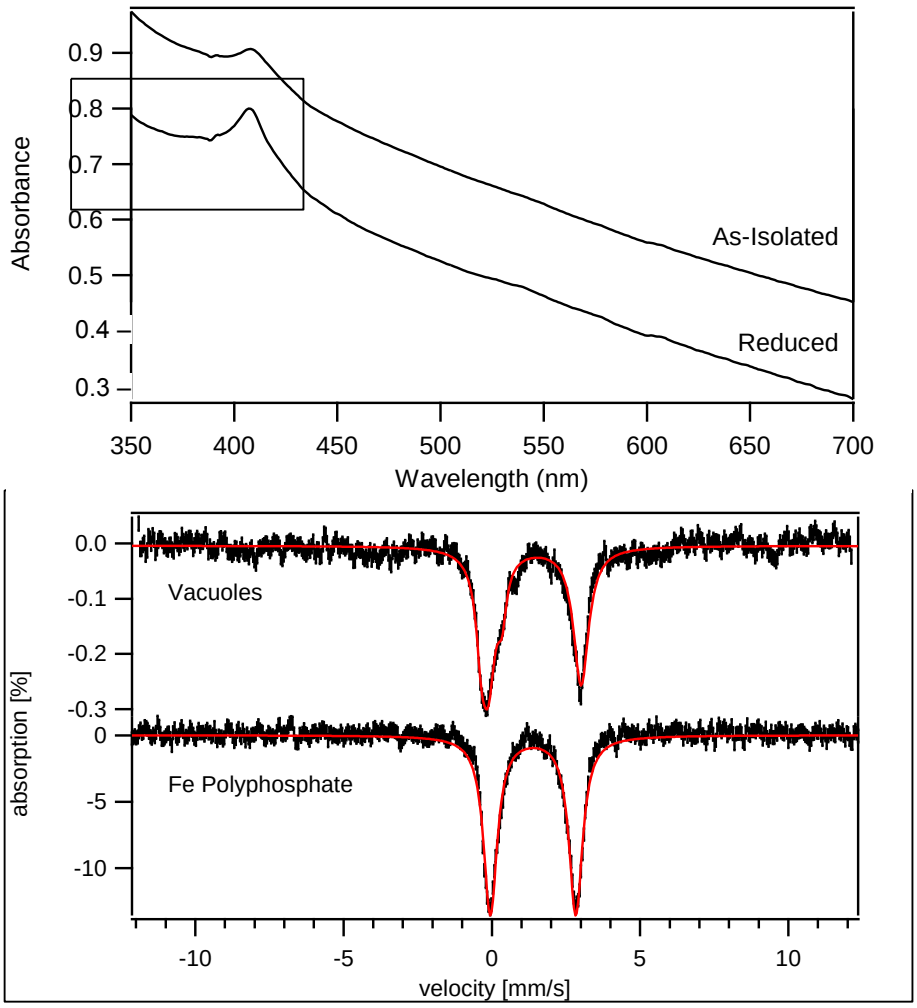

Figure 3.6. Electronic absorption spectra of isolated vacuoles, before and after treatment with a reductant (upper panel), and Mössbauer spectrum of the same after treatment with a reductant (lower panel). Vacuoles were isolated from Batch 15. The corresponding Mössbauer spectrum prior to adding the reductant is shown in Figure 3.3, spectrum B. The 6 K, 0.05 T Mössbauer spectrum of Fe^{3+} polyphosphate (pH 7) after treatment with dithionite is also shown in the lower panel. The red lines are simulations assuming (vacuoles) δ = 1.41 mm/s and ΔE_Q = 3.15 mm/s and ($^{57}Fe^{3+}$ polyphosphate) δ = 1.39 mm/s and ΔE_Q = 2.88 mm/s.

spectrum of Fe^{3+} phosphate (Figure 3.7A) and Fe^{3+} hex(aqua/hydroxo) species (data not shown) exhibited features typical of Fe^{3+} oxyhydroxo nanoparticles. In contrast, the spectrum of Fe^{3+} polyphosphate (Figure 3.7B) exhibited features associated with mononuclear HS Fe^{3+} ions with similar parameters to those used to fit the equivalent spectrum in Figure 3.2B. After data collection, the Fe^{3+} polyphosphate sample was thawed, adjusted to pH = 7, and refrozen. The resulting Mössbauer spectrum (Figure 3.7C) indicated the presence of both nanoparticles and HS Fe^{3+} ions. This suggests that mononuclear HS Fe^{3+} polyphosphate can convert to Fe^{3+} nanoparticles simply by raising the pH. The nanoparticle-forming reaction was reversible, in that thawing the pH-7-adjusted sample, lowering its pH to 4, and refreezing it resulted in a Mössbauer spectrum again indicating the mononuclear HS Fe^{3+} state. In contrast, the Fe^{3+} (phosphate) nanoparticles at pH 5 could not be converted into the mononuclear HS Fe^{3+} state by lowering the pH to 3, 2 and finally 1. Similar to the Fe species in vacuoles, the Fe^{3+} polyphosphate sample could be reduced by dithionite, resulting in a quadrupole doublet (Figure 3.5, bottom panel) with parameters very similar to that observed when the HS Fe^{3+} complex in vacuoles was reduced.

Whole Cells

We calculated the concentration of Fe (and other metal ions) within fermenting yeast cells grown in the same medium used to grow the cells from which vacuoles were isolated. Measured values using packed cells were normalized using the previously determined packing efficiency *(167)*. Low-temperature Mössbauer spectra of whole cells

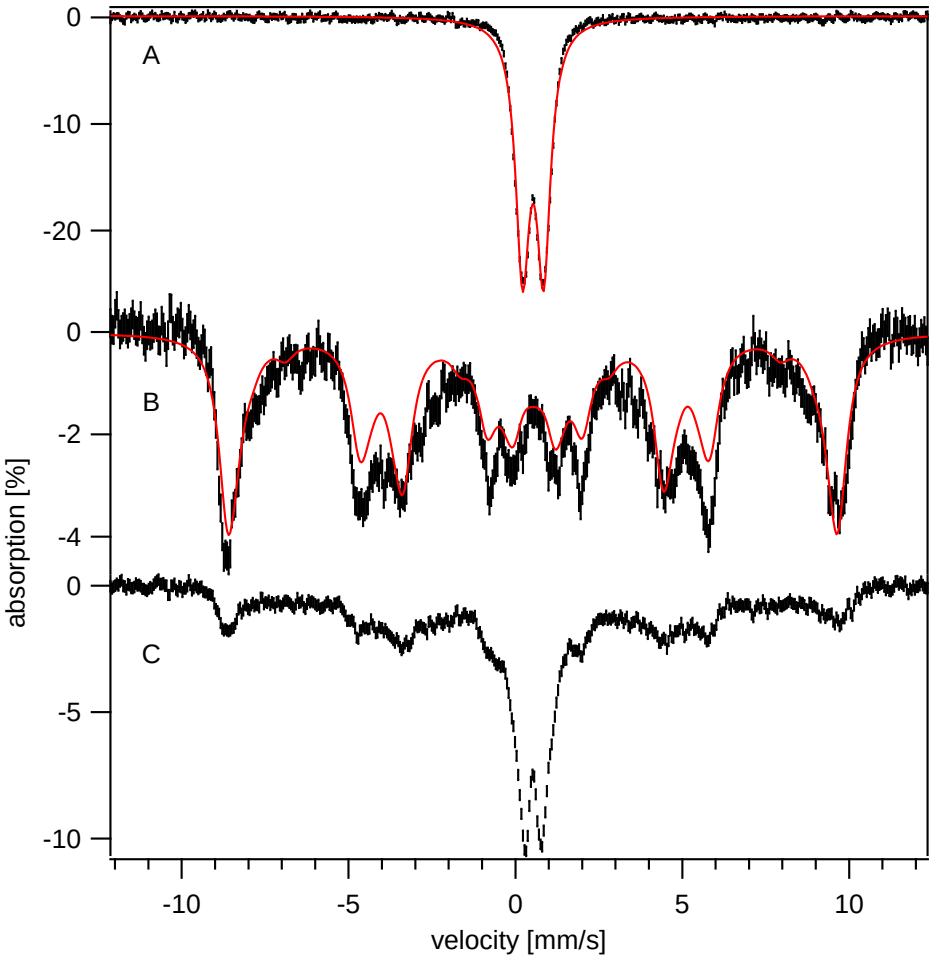

Figure 3.7. 6 K and 0.05 T Mössbauer spectra of $^{57}Fe^{3+}$ phosphate and $^{57}Fe^{3+}$ polyphosphate at different pH values. A, $^{57}Fe^{3+}$ phosphate at pH 5; B, $^{57}Fe^{3+}$ polyphosphate at pH 5; C, $^{57}Fe^{3+}$ polyphosphate at pH 7. Applied fields were parallel to the gamma radiation. Samples were prepared in 0.1 M acetate/acetic acid buffer (pH 5) and excess H_2O_2 was added to each sample obtain an oxidizing environment. The solid line in A is a simulation assuming δ = 0.53 mm/s and ΔE_Q = 0.63 mm/s. The solid line in B is a simulation assuming S = 5/2, D = 0.5 cm^{-1}, E/D = 0.33, $A_o/\gamma_N \cdot \beta_N$ = -238 KG, δ = 0.54 mm/s, ΔE_Q = 0.39 mm/s, and η = 3.

(Figure 3.8) were dominated by the same pattern that was observed in spectra of isolated vacuoles; i.e. typical of a mononuclear HS Fe^{3+} species. EPR spectra of same whole cells from which the vacuoles of Figure 3.5A were isolated were dominated by a $g_{ave} = 4.3$ signal (Figure 3.5B), essentially indistinguishable from that of isolated vacuoles.

Discussion and Conclusions

Two Types of Fe in Vacuoles

Our results indicate that vacuoles isolated from Fe-sufficient fermenting yeast cells contain two major types of Fe species. One is a mononuclear, magnetically isolated (i.e. soluble) high-spin Fe^{3+} complex; the other is magnetically interacting (i.e. insoluble) Fe^{3+} oxyhydroxo nanoparticles. The nanoparticles contained in Yah1p-depleted, Atm1p-depeleted, Yfh1p-depleted and Aft1-1^{up} mitochondria have similar Mössbauer properties, and in the three cases investigated, phosphorus, presumed to be in the form of phosphate, was found to be associated with this material *(71, 135, 147, 163)*.

The composition and structure(s) of the Fe^{3+} nanoparticles in vacuoles is unknown, including whether phosphate or a phosphate-related species is associated. We suspect that these nanoparticles are related to ferrihydrite, a metastable iron oxyhydroxo generated by titrating $Fe^{3+}(NO_3)_3$ with hydroxide ions to pH ~ 7.5 *(168)*. Ferrihydrite contains both octahedrally and tetrahedrally coordinated Fe^{3+} ions *(169)*. When present, phosphate ions and other oxyanions coprecipitate with Fe^{3+} *(170-172)*. This alters the structure, crystallinity and superparamagnetic properties of the resulting nanoparticles *(173-175)*.

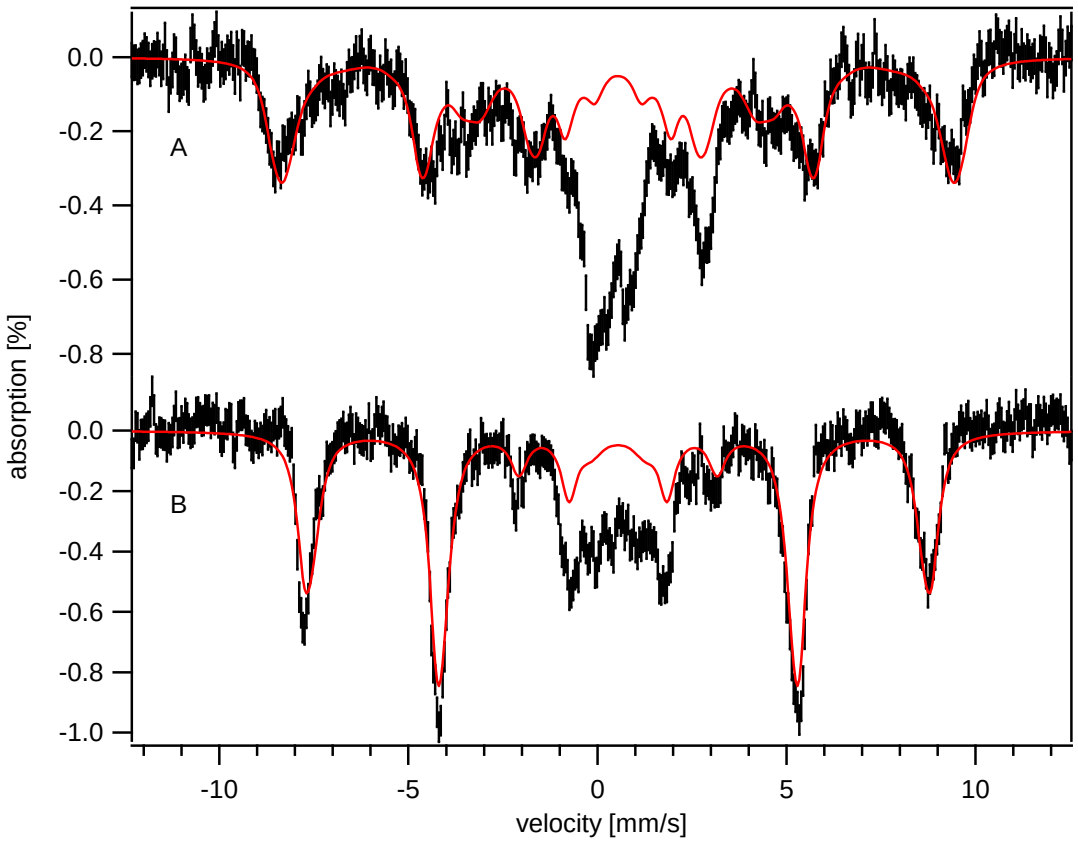

Figure 3.8. Mössbauer spectra of WT whole cells. A, 4.2 K and 0.05 T; B, 4.2 K and 6 T; Applied fields were perpendicular to the gamma radiation. The solid red lines are simulations assuming the parameters specified in *Figure 3.2*.

We propose that the two major forms of Fe in vacuoles interconvert by reactions promoted by a simple change in pH. As illustrated in the model of Figure 3.9, low pH (protonation) favors the mononuclear species while high pH (deprotonation) favors nanoparticles. Deprotonation of a ligand (e.g. water, phosphate, or polyphosphate group) on one isolated HS Fe^{3+} molecular species, and dissociation of a ligand on a neighboring species (to create an open coordinate site) might be sufficient to promote an association between the two, ultimately generating nanoparticles. At the normal pH of vacuoles (pH ~ 5) we would expect that the majority of the Fe would be present as the mononuclear HS Fe^{3+} species, as is observed in whole cells and in most batches of isolated vacuoles. Nanoparticles probably form when the pH of the vacuole lumen is somewhat higher than 5. Perhaps the pH of the vacuoles increases slightly during isolation, or the ratio of phosphate:polyphosphate in the vacuoles is altered. Studies are currently underway to test these hypotheses.

Our results are insufficient to unambiguously identify the coordination environment of the HS Fe^{3+} species, but they are consistent with an Fe^{3+} polyphosphate complex and inconsistent with an Fe^{3+} phosphate complex or with hex(aqua/hydroxo) Fe^{3+}. Of these three possibilities, only the Fe^{3+} polyphosphate complex was present as a HS mononuclear species at the pH of the vacuolar lumen (pH ~ 5); the Fe^{3+} phosphate and hex(aqua/hydroxo) complexes were present as nanoparticles. Fe^{3+} phosphate remained as nanoparticles at pH's as low as 1 (the behavior of the hex(aqua/hydroxo) complex was not evaluated at lower pHs). Our results indicate that the HS Fe^{3+} complex

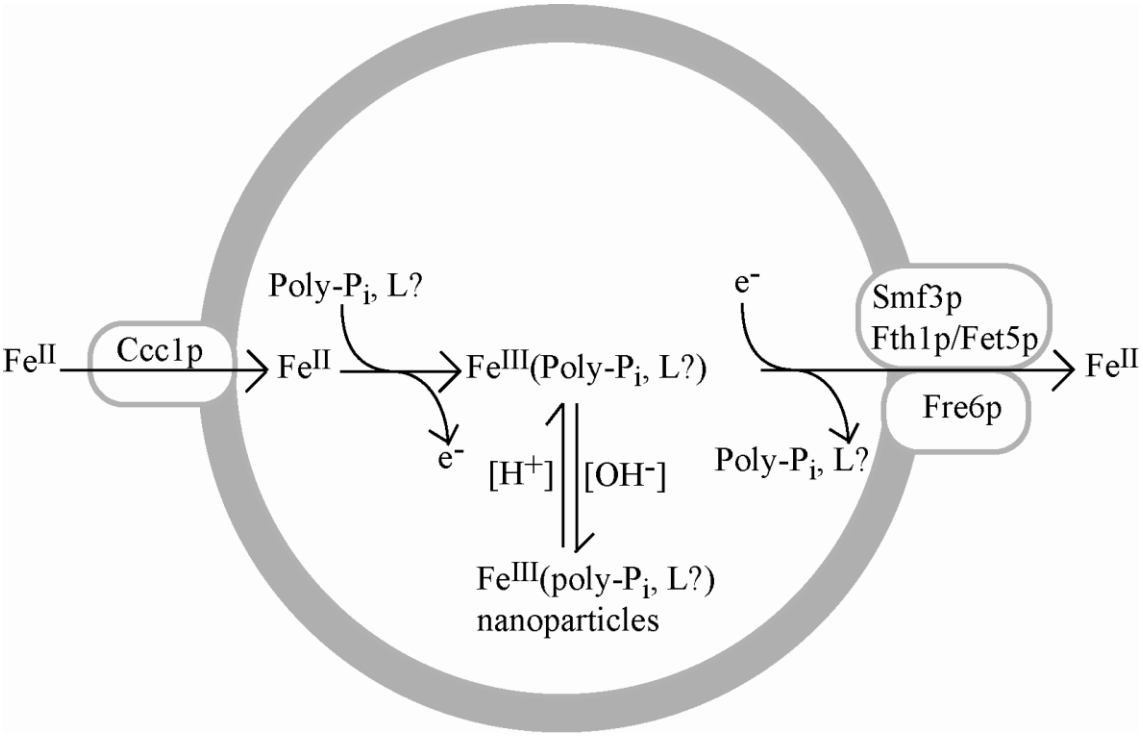

Figure 3.9. Model showing the dynamics of Fe import and export in yeast vacuoles. An unknown ferrous species enters the vacuole via Ccc1p. Associated with this import is the exchange of ligands and oxidation to HS Fe^{3+}. Polyphosphate is suggested as a possible coordinated ligand, but further studies are required to establish this. Upon export, the HS Fe^{3+} species is reduced to Fe^{2+} and ligands are again exchanged. At pH > *ca*. 5, some or all of the species precipitates in the form or Fe^{3+} (phosphate-based) oxyhydroxo nanoparticles perhaps associated with polyphosphate.

in vacuoles is closely related to an Fe^{3+} polyphosphate complex, consistent with earlier and quite perceptive proposals by Lesuisse, Crichton, and Kosman that vacuolar Fe is bound by polyphosphate *(142, 152)*. However, further studies are required to unambiguously identify the HS Fe^{3+} complex in vacuoles.

Vacuolar Metal Concentrations

We report here the first absolute (μM) concentrations of the metal content of vacuoles; previously only *ratios* of metal concentrations divided by protein concentrations (or dry weight) had been reported. Such ratios cannot be used in mass-balance equations and are difficult to interpret because differences might arise from changes in either protein concentration or metal concentration (or some combination of the two). For example, in the current study, metal-to-protein ratios were found to be ~10-fold higher than previously reported *(142, 150)*. Whether this is due to higher Fe concentrations or lower protein concentrations (or both) in our vacuoles cannot be determined.

We suspect that we achieved higher concentrations of Fe in isolated vacuoles than have been obtained previously, due to our use of TCEP rather than DTT to prepare the cell wall for digestion by lyticase. Raguzzi, *et al. (152)* reported that adding a chelator and reductant mobilizes vacuolar Fe stores, and DTT is a membrane-permeable reducing agent. TCEP is a membrane-impermeable reducing agent. EGTA was also excluded from our isolation buffers to avoid loss of vacuolar Fe, whereas EGTA is

commonly added to buffer solutions to remove loosely-bound Fe from membranes.

Loss of Fe from Vacuoles During Isolation

Vacuoles isolated from cells grown under fermenting conditions and in the presence of 40 μM Fe contained an average of ~ 220 μM Fe, with 56% - 85% present as a HS Fe^{3+} species. Whole cells grown under the same conditions contained 380 μM Fe with ~ 75% of the Mössbauer spectral intensity due to what appears to be the same HS Fe^{3+} species. Assuming that it is the same species and that it is located exclusively in vacuoles (which occupy ~ 25% of cell volume) suggests that the concentration of this species in vacuoles in whole cells is *ca*. 1.2 mM. This is *ca*. 5-times higher than found in our isolated vacuole preps, implying that the majority of Fe in the vacuole is lost during isolation. Other groups have suggested that Fe leaches from vacuoles during isolation *(150)*. Given their function in the cell (dynamic storage and release of Fe as needed), it is not surprising that Fe can be easily mobilized from this organelle.

The export of Fe has been associated with its reduction *(142)*. Our results show that there is no build up of HS Fe^{2+} in the vacuole even though the Fe^{3+} contained in the organelle is redox active (reducible by dithionite). We have not observed by Mössbauer spectroscopy any Fe^{2+} in isolated vacuoles, suggesting that reduction of Fe^{3+} to Fe^{2+} is slower than export from the vacuoles. Essentially, the Fe^{3+} species is *trapped* in vacuoles, escaping immediately once it is reduced.

In the future, we hope to identify the mononuclear HS Fe^{3+} species present in vacuoles. We also hope to use our biophysical methods, in conjunction with genetic and

biochemical investigations, to explore the mechanisms of vacuolar Fe import and export and the regulation of these processes. Since vacuoles are a major hub of iron trafficking, understanding how they store and release iron is a prerequisite to better understanding cellular Fe metabolism.

CHAPTER IV

INSIGHTS INTO VACUOLAR IRON TRAFFICKING USING MÖSSBAUER SPECTROSCOPY AND Δ*CCC1* AND *CCC1-UP SACCHAROMYCES CEREVISIAE*

My contribution to this project was to grow Δ*CCC1*, WT, and *CCC1-up* whole cells under various conditions, to prepare these cells for Mössbauer, EPR, UV-Visible, and ICP-MS analyses, and to interpret these data. Another graduate student, Mike Moore, harvested mitochondria from the Δ*CCC1* strain and collected the Mössbauer data. I fit and interpreted this Mössbauer data, and prepared the Δ*CCC1* mitochondria for ICP-MS and UV-Vis analyses. Sean McCormick, another graduate student, was responsible for maintaining the ICP-MS instrument and for collecting the ICP-MS data. Dr. Mrinmoy Chakrabarti, a post-doctoral fellow in the Lindahl group, was responsible for maintaining the Mössbauer and EPR instruments, and for assisting in the interpretation of the Mössbauer and EPR results. All of these authors contributed in group discussions regarding these results.

Saccharomyces cerevisiae strains lacking or over-expressing *CCC1* were characterized using Mössbauer and EPR spectroscopies, and using ICP-MS. Ccc1p is the only known vacuolar Fe import protein. Δ*CCC1* cells contained ~ 20% less Fe than equivalently grown WT cells and the Fe was distributed differently, with more non-heme high spin (NHHS) Fe^{2+} and less vacuolar high-spin (HS) Fe^{3+} and less Fe^{3+} oxyhydroxide nanoparticles (NP). The concentrations of vacuolar Fe^{3+} and NHHS Fe^{2+} increased with increasing medium [Fe]. Mitochondria isolated from Δ*CCC1* cells contained more NHHS Fe^{2+} than WT mitochondria, but this did not account for most of

the NHHS Fe^{2+} observed in whole-cell spectra. The concentration of Fe in *CCC1-up* cells was much higher than in WT cells, with most extra Fe present as NHHS Fe^{2+} and NP. The majority of Fe in isolated vacuoles was Fe^{3+} nanoparticles, with little NHHS Fe^{3+} and no NHHS Fe^{2+}. As the concentration of medium [Fe] was increased from 1 to 40 μM, the NHHS Fe^{2+} accumulated before the vacuolar NHHS Fe^{3+} and NP. Supplementing the medium with additional adenine caused a decline of NHHS Fe^{2+}. Inhibition of the V^{+}-ATPase with concanamycin A (ConA) promoted Fe accumulation as NP in WT cells, consistent with an increased vacuolar pH.

Introduction

Iron is a critical component of biological systems where it is found in various forms, including hemes and other mononuclear centers, iron-sulfur clusters (ISCs) and diiron centers *(7, 12)*. Mitochondria are perhaps the major site of Fe metabolism, as both ISCs and heme biosynthesis occurring in this organelle and Fe-rich respiratory complexes housed within this structure *(75)*. In yeast, vacuoles are another major site of Fe metabolism, but their role is less understood. Vacuoles are acidic organelles that sequester Fe and other cellular metabolites. Fe is imported into vacuoles under Fe-replete growth conditions and exported under Fe-deficient conditions *(122, 140, 142, 159)*. Most of this Fe enters the vacuole through Ccc1p, a protein that localizes on the vacuolar membrane *(140)*. Some Fe enters this organelle through endocytosis *(140, 176)*.

Ccc1p is tightly regulated through a number of mechanisms (Scheme 4.1), one of which involves the Yap5p protein *(141)*. This Fe-sensing transcription factor is

constitutively bound to the *CCC1* promoter which induces transcription of the *CCC1* gene under high-Fe conditions *(141)*. This promotes the import of Fe into the vacuole under Fe-replete conditions. Ccc1p expression is also regulated by Cth2p *(105)*. CTH2 is a member of the Fe regulon, a collection of > 20 genes involved in Fe metabolism *(177)*. Under low-Fe conditions Cth2p binds and destabilizes *CCC1* mRNA, causing its degradation which prevents Cccp1 biosynthesis and Cccp1-dependent Fe import into vacuoles *(105)*. Cth2p expression is controlled by Aft1p, an Fe-sensitive transcription factor *(105)*. Under high-Fe conditions Aft1p localizes to the cytosol where it is inactive. Under low-Fe conditions, Aft1p localizes to the nucleus where it promotes the expression of the Fe regulon, including Cth2p *(131)*. These mechanisms collectively regulate Ccc1p-dependent entry of Fe into the vacuole.

Under Fe-sufficient growth conditions (> 10 μM Fe in minimal medium), ~ 75% of Fe in WT cells is located in vacuoles *(112)*. The majority is stored as one or more mononuclear, high-spin (HS) Fe^{3+} complexes, most likely coordinated by polyphosphate-related ligands *(112)*. Depending on growth or isolation conditions, vacuoles can also contain aggregates of Fe^{3+} oxyhydroxide (phosphate or polyphosphate-related) nanoparticles (NP) *(112, 178)*. Vacuoles export Fe to the cytosol in times of Fe deprivation. The proteins involved in this process are homologous to Fe import proteins on the plasma membrane. Just prior to export, vacuolar nonheme high-spin (NHHS) Fe^{3+} is reduced by Fre6p, a ferric reductase *(142)*.

The reduced Fe^{2+} can be exported from the vacuole by the Fet5p/Fth1p complex

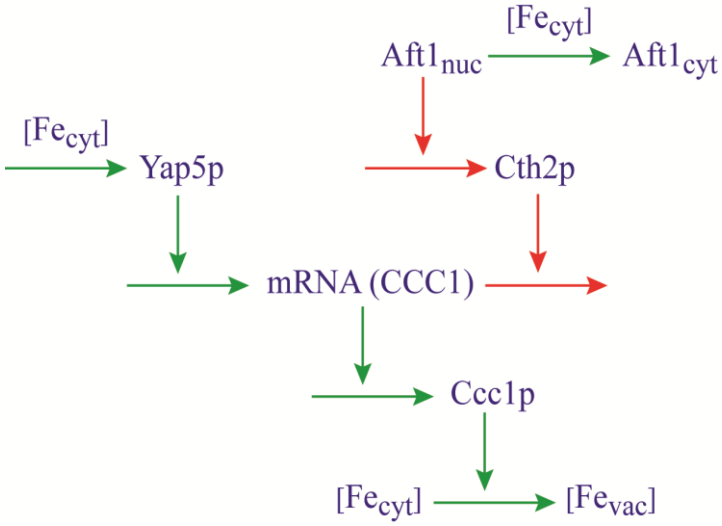

Scheme 4.1. Regulation of Ccc1p. Ccc1p is regulated via two primary pathways: Yap5p and Aft1p. Yap5p is constitutively bound to the *CCC1* promoter. In high cytosolic Fe conditions Yap5p up-regulates *CCC1* transcription which leads to high Ccc1p levels. In low cytosolic Fe conditions Aft1p is active. Aft1p negatively regulates Ccc1p expression through Cth2p. Cth2p causes the destabilization and degradation of *CCC1* mRNA, which results in low levels of Ccc1p expression. This information was collected from *(103)* and *(104)*.

and by Smf3p, both of which are vacuolar membrane-bound proteins *(122, 159)*. Fet5p, a multicopper oxidase, and Fth1p, a ferric permease, comprise the high-affinity export system *(159)*. The low-affinity system is composed of Smf3p, a divalent metal transport protein which is not specific for Fe *(122)*. High-affinity Fe transporters allow cells to grow on media containing low concentrations of Fe (< ~ 1 μM) *(139, 179, 180)*. Fre6p, Fet5p, and Fth1p are regulated by Aft1p *(131, 132)* whereas Smf3p is regulated by Aft2p, a homolog to Aft1p *(122, 161)*. When intracellular Fe levels decrease, these vacuolar Fe export proteins are up-regulated by Aft1p and Aft2p *(130, 131, 159)*. This causes Fe to efflux from the vacuoles and move into the cytosol, probably in the Fe^{2+} redox state.

Vacuoles isolated from cells in which *CCC1* is deleted (*ΔCCC1*) only contain ~20% of the Fe concentration typical of WT vacuoles *(140)*. The residual Fe level in Δ*CCC1* vacuoles is due to Fe uptake via *END4*-associated endocytosis *(103)*. The vacuolar Fe concentration in Δ*END4* vacuoles (containing functional *CCC1*) is ~ 60% of WT levels *(103)*. Thus, Ccc1p appears to import 60% - 80% of vacuolar Fe *(103)*.

Δ*CCC1* cells have difficulty growing in medium containing > 3 mM Fe *(140)*. Kaplan has proposed that the cytosolic Fe concentration is high in these cells because Fe import from the cytosol into vacuoles is largely blocked *(103, 181)*. Accordingly, the high concentrations of cytosolic Fe would promote ROS formation, leading to cell death when the concentration of this species becomes sufficiently high *(140)*. Conversely, when Ccc1p is constitutively over-expressed, vacuolar and cellular Fe levels are 3 – 4 times higher than in WT cells *(140, 142)*. Kaplan has hypothesized that in this strain,

excessive cytosolic Fe is transported to vacuoles, leaving the cytosol Fe-deficient *(103)*. This induces the Fe regulon which up-regulates Fe-import proteins on the plasma membrane which increases cellular Fe import. This import process would continue until the sensed Fe species in the cytosol exceeds some threshold concentration.

Kaplan has hypothesized further that a common Fe pool is shared between the mitochondria and vacuoles *(181)*. Deleting the genes which encode the mitochondrial Fe import proteins, *MRS3* and *MRS4*, impedes mitochondrial Fe import and promotes vacuolar Fe import *(58, 181)*. When *CCC1* is deleted, the total cellular Fe concentration declines *(181)*. The decline in total cellular Fe implies that Fe import levels are also decreased *(182)*. A decline in Fe import is often associated with inactivation of Aft1p *(132)*. Aft1p is inactivated when cytosolic Fe levels are high *(183)*. Therefore, the decline in total cellular Fe indicates that cytosolic Fe levels are elevated in Δ*CCC1* cells compared with WT cells *(181)*. These data suggest that the concentration of a common cytosolic Fe pool is dictated by competing fluxes of Fe into vacuoles and mitochondria along with Aft1-based regulation of cellular Fe import proteins.

In this study, Mössbauer (MB), EPR, and UV-Vis spectroscopies, as well as ICP-MS, were used to study the Fe content of *CCC1-up* and Δ*CCC1* cells grown under various conditions. Our results support and extend Kaplan's hypotheses. They suggest that the shared pool of cytosolic Fe is a mononuclear nonheme high-spin Fe^{2+} complex coordinated predominately by O and N donor ligands. We present circumstantial evidence that this species accumulates in cytosol of Δ*CCC1* cells grown in medium supplemented with high concentrations of Fe, and is sensed by the machinery used to

regulate Fe import into the cell. It has been proposed that intracellular Fe is sensed via Fe-S clusters *(184)*. If this is the case, this implies that the accumulated form of Fe which we observe can be utilized for Fe-S cluster biogenesis. We further suggest that *CCC1-up* cells contain a similar species that is not sensed, either because it's a different complex or because it is sequestered in a noncytosolic compartment such as the vacuoles. The forms of Fe present in vacuoles appear to be controlled by the redox status and pH of these organelles.

We used Mössbauer (MB), EPR and UV-visible spectroscopy to characterize the Fe content of two genetic strains of *S. cerevisiae*, namely Δ*CCC1* and Cccp1-up. Δ*CCC1* cells lack the Cccp1 transporter on the vacuolar membrane, whereas Cccp1-up cells contain an abundance of this vacuolar Fe importer, relative to in WT cells. As hypothesized by Kaplan, Δ*CCC1* cells should contain unusually high concentrations of cytosolic Fe, since such Fe should be largely unable to move into vacuoles *(140)*. Thus, we expected to observe a diminished percentage of the HS Fe^{3+} sextet in the MB spectrum of these cells. We also anticipated an increase in a new spectral feature due to cytosolic Fe. In previous studies, assigning MB features of whole yeast spectra to cytosolic Fe has been hampered by the low concentration of such Fe in WT cells. Likewise, Ccc1-up cells should contain more vacuolar HS Fe^{3+} and less cytosolic Fe. Our initial objective was to evaluate these expectations and if so to spectroscopically characterize cytosolic Fe in a yeast cell.

Results

DY150 WT Cells

We have described the Fe composition of W303-1B WT cells previously*(138)* but we briefly summarize it here to provide a baseline against which the other strains investigated in this study (derived from the same WT strain) can be compared. Notable differences between the current strain (DY150) and the previous strain (W303-1B, a generous gift from Roland Lill, Philipps Universität, Marburg Germany) were observed.

The Fe concentrations of both WT strains, when grown on MM supplemented with 40 μM FC, were similar (Table 4.1, and Table 1 from *(138)*); however, the distribution and speciation of Fe were not. The low-temperature (6 ± 1 K), low-field (0.05 T) MB spectrum of DY150 cells shown in Figure 4.1A was dominated by a sextet due to one or more mononuclear nonheme high-spin (NHHS) Fe^{3+} species located in the vacuoles *(112)*. This feature was simulated by the orange line above the spectrum. The cellular concentration of Fe associated with these species (~270 μM) was lower than that in W303-1B cells (~380 μM) *(112)*. Other components of the DY150 spectrum were more intense, including a broad quadrupole doublet arising from superparamagnetic Fe^{3+} oxyhydroxide nanoparticles (NP), and a doublet arising from one or more NHHS Fe^{2+} species. The NP doublet (with parameters δ = 0.53 mm/s and ΔE_Q = 0.45 mm/s, simulated by the green line) was 4.5× more intense than the corresponding doublet in the W303-1B spectrum. The NHHS Fe^{2+} doublet (with parameters δ = 1.3 mm/s and ΔE_Q = 3.0 mm/s, simulated by the blue line) was 1.4× more intense. The intensity of the so-

Sample	Total [Fe] (ICP-MS)	NHHS Fe^{2+} (MB)	HS Fe^{2+} Hemes (MB)	CD (MB)	Nanoparticles (MB)	NHHS Fe^{3+} (MB)	Fe^{2+} Hemes (UV-vis)	g = 4.3 (EPR)
WT1	170 ± 45 (6)	25% (43 μM)	5% (9 μM)	60% (103 μM)	< 5% (< 9 μM)	0%	44 ± 1	0
WT40	490 ± 140 (8)	13% (64 μM)	3% (15 μM)	8% (39 μM)	18% (88 μM)	55% (269 μM)	55 ± 3	152
D1	148 ± 64 (8)	15% (22 μM)	10% (15 μM)	57% (85 μM)	< 5% (< 7 μM)	0%	46 ± 2	< 1
D10	209 ± 8 (2)	26% (54 μM)	7% (15 μM)	39% (82 μM)	5% (11 μM)	23% (48 μM)	ND	ND
D20	285 ± 5 (2)	35% (100 μM)	5% (14 μM)	27% (77 μM)	8% (23 μM)	28% (80 μM)	ND	ND
D40	360 ± 100 (7)	30% (107 μM)	5% (18 μM)	19% (69 μM)	17% (61 μM)	30% (108 μM)	43 ± 4	73
UP1	250 ± 60 (3)	51% (130 μM)	3% (10 μM)	10% (30 μM)	19% (50 μM)	18% (50 μM)	32 ± 3	30
UP10	565 ± 10 (2)	53% (300 μM)	2% (11 μM)	5% (28 μM)	25% (141 μM)	18% (102 μM)	ND	ND
UP20	979 ± 24 (2)	39% (382 μM)	≤ 1% (≤ 10 μM)	3% (29 μM)	39% (382 μM)	17% (167 μM)	ND	ND
UP40	1839 ± 750 (5)	38% (700 μM)	≤ 1% (≤ 18 μM)	2% (37 μM)	24% (441 μM)	17% (313 μM)	31 ± 6	372

Table 4.1. Summary of Fe percentages and concentrations determined by biophysical methods. Mössbauer percentages and corresponding concentrations are ± 3%. Concentrations of Fe^{2+} hemes (UV-vis) are the sum of individual heme components (hemes a, b, and c), which were simulated as described *(137)*. The g = 4.3 EPR signals were quantified from individual samples (Table 4.2), using the equation described *(136)*. Sample concentrations were corrected for packing efficiencies which are 73% for whole cells, 75% for isolated vacuoles, and 78% for isolated mitochondria *(185-187)*. ND = not determined

Sample	Total [Fe] (ICP-MS)	NHHS Fe^{2+} (MB)	HS Fe^{2+} Hemes (MB)	CD (MB)	Nanoparticles (MB)	NHHS Fe^{3+} (MB)	Fe^{2+} Hemes (UV-vis)	g = 4.3 (EPR)
D40, Mitochondria	854 ± 102 (2)	37% (316 μM)	5% (43 μM)	32% (273 μM)	23% (197 μM)	0%	364 ± 9	ND
UP1+A	385 ± 68 (3)	70% (270 μM)	2% (8 μM)	7% (27 μM)	11% (42 μM)	10% (39 μM)	29 ± 3	39
UP40+A	1040 ± 108 (4)	18% (187 μM)	2% (21 μM)	4% (42 μM)	29% (301 μM)	45% (468 μM)	40 ± 4	415
WT40 – glucose + ConA, 0m	1014 (1)	38% (385 μM)	2% (20 μM)	4% (40 μM)	17% (172 μM)	20% (203 μM)	ND	ND
WT40 - ConA, 15m	990 (1)	60% (594 μM)	2% (20 μM)	4% (40 μM)	7% (70 μM)	23% (230 μM)	ND	ND
WT40 + ConA, 15m	1060 (1)	39% (414 μM)	3% (32 μM)	4% (43 μM)	19% (202 μM)	20% (213 μM)	ND	ND

Table 4.1 Continued.

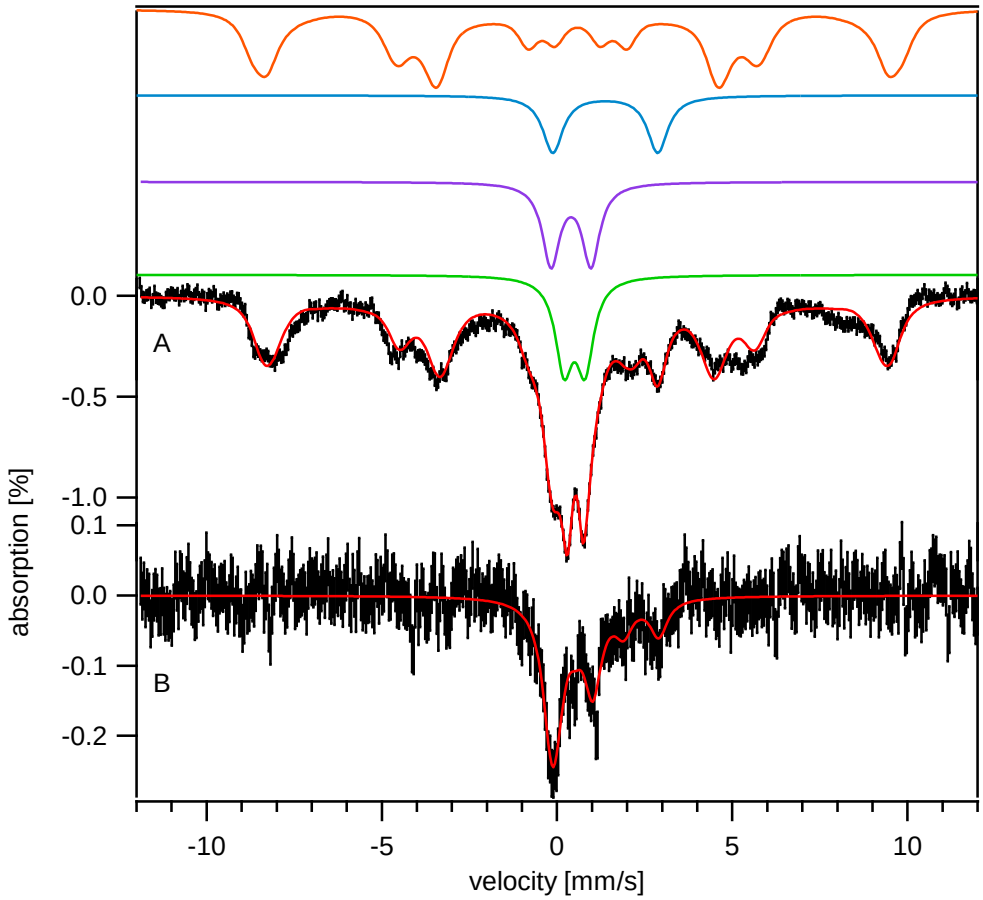

Figure 4.1. Mössbauer spectra of DY150 WT whole cells. WT cells grown with 40μM FC (A) and 1μM FC (B). The orange simulation shows NHHS Fe3+ with the parameters D = 0.5, E/D = 0.33, A = -228, and η = -3.0. The blue simulation shows NHHS Fe2+ with the parameters δ = 1.35 and ΔEQ = 3.05. The green simulation shows ferric phosphate nanoparticles with parameters δ = 0.53 and ΔEQ = 0.50. The purple simulation shows the Central Doublet, which is composed of Fe4S4 clusters and LS Hemes, with the parameters δ = 0.45 and ΔEQ = 1.14. The red simulations contain all of these features, and the respective percentages are outlined in Table 4.1.

called "central doublet" (CD), which originates from S = 0 $[Fe_4S_4]^{2+}$ clusters and LS Fe^{2+} heme centers (the two types of centers cannot be distinguished by MB), was similar to that obtained previously.[25] The purple line above the spectrum, which simulates the CD, was generated using the parameters δ = 0.45 mm/s and ΔE_Q = 1.14 mm/s at 8% intensity). The simplest interpretation of these differences is that *ca*. 100 μM of the vacuolar NHHS Fe^{3+} species in W303-1B cells were replaced by *ca.* 60 μM of nanoparticles and *ca.* 40 μM of NHHS Fe^{2+} in DY150 cells. We will argue below that this arises because vacuoles in DY150 cells are slightly less acidic (higher pH) than those in W303-1B cells.

The EPR spectrum of DY150 cells grown on MM40 (to be called WT40 cells) was dominated by a g = 4.3 signal (Figure 4.2E) which arose from a mononuclear, NHHS Fe^{3+} S = 5/2 center with rhombic symmetry (E/D ~ 1/3).[16] The spin concentration associated with this signal was ~ 130 μM (Table 4.1). This concentration was divided by the cellular Fe concentration (~350 μM in this sample) and the fraction of the NHHS Fe^{3+} sextet in the MB spectrum (0.55) to yield a [spin]/[HS Fe^{3+}] ratio of 0.8. Given the large uncertainties associated with these determinations, we regard this ratio as acceptably close to 1. The g = 2 region was dominated by a Mn^{2+}-based hyperfine split signal (see below), but it also included low intensity (2 - 5 μM) free-radical (g = 2.00) and g_{ave} = 1.94 signals.

DY150 cells grown on MM containing 1 μM ^{57}FC (called WT1 cells) contained less Fe than WT40 cells (Table 4.1). The low-temperature low-field MB spectrum of

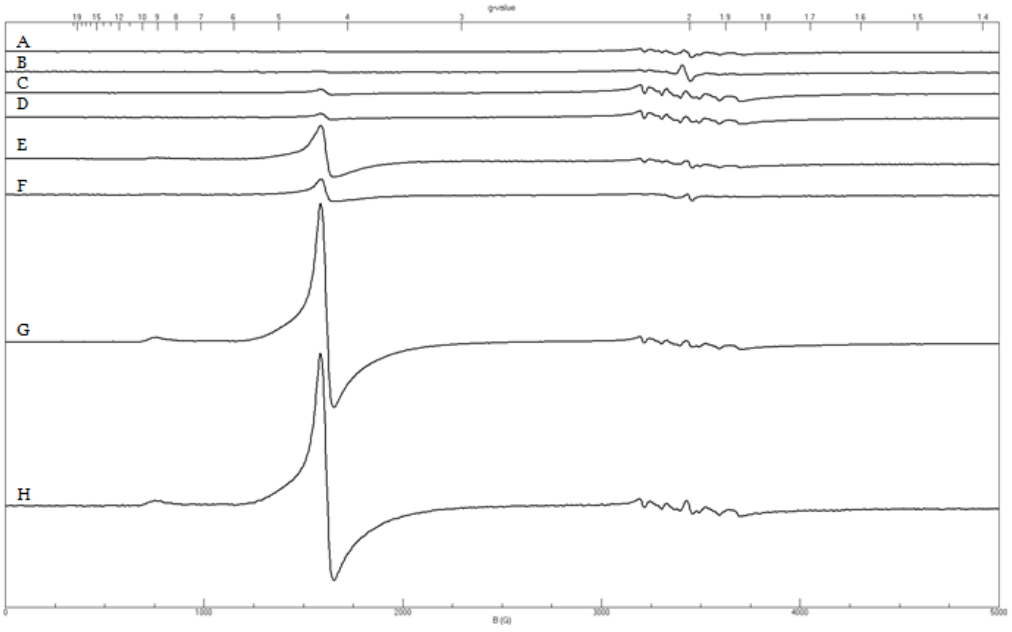

Figure 4.2. EPR of WT, ΔCCC1, and *CCC1-up* whole cells. A, WT1 cells; B, D1 cells; C, UP1 cells; D, UP1+A cells; E, WT40 cells; F, D40 cells; G, UP40 cells; H, UP40+A cells. Spectra were collected at temperature 4K, microwave frequency 9.63 GHz, and microwave power 0.2 mW.

WT1 cells (Figure 4.1B) was dominated by the CD. A NHHS Fe^{2+} doublet and HS Fe^{2+} hemes were also strong. Minor amounts of nanoparticles and HS Fe^{2+} hemes were also evident. WT1 cells did not exhibit a g = 4.3 EPR signal (Figure 4.2A), suggesting the absence of NHHS Fe^{3+} associated with vacuoles. The corresponding MB spectrum (Figure 4.1B) was noisy and there was no evidence for a NHHS Fe^{3+} sextet. These results confirm that WT1 cells do not accumulate significant Fe in the vacuoles under Fe-deficient growth conditions *(138).*

UV-vis spectroscopy was used to determine the concentrations of hemes *a*, *b*, and *c* in WT1 and WT40 cells (Figure 4.3, A and B; Table 4.1). The concentrations of the heme features did not change significantly as the medium FC concentration was increased. The total Fe content of yeast cells was decomposed into vacuolar Fe and mitochondrial Fe *(112, 187).* This suggests that the majority of heme centers in a yeast cell are probably mitochondrial. Similarly, the CD and HS Fe^{2+} heme concentrations determined by MB and ICP-MS also did not show significant changes in these features, which are also probably associated with the mitochondria. Viewed collectively, these results strongly suggest that the concentration of mitochondria in WT1 and WT40 cells was similar. The differences in intracellular Fe concentrations (170 *vs.* 490 μM) were largely due to differences in the Fe levels in the vacuoles (empty in WT1 cells; *ca.* 300 μM Fe in WT40 cells).

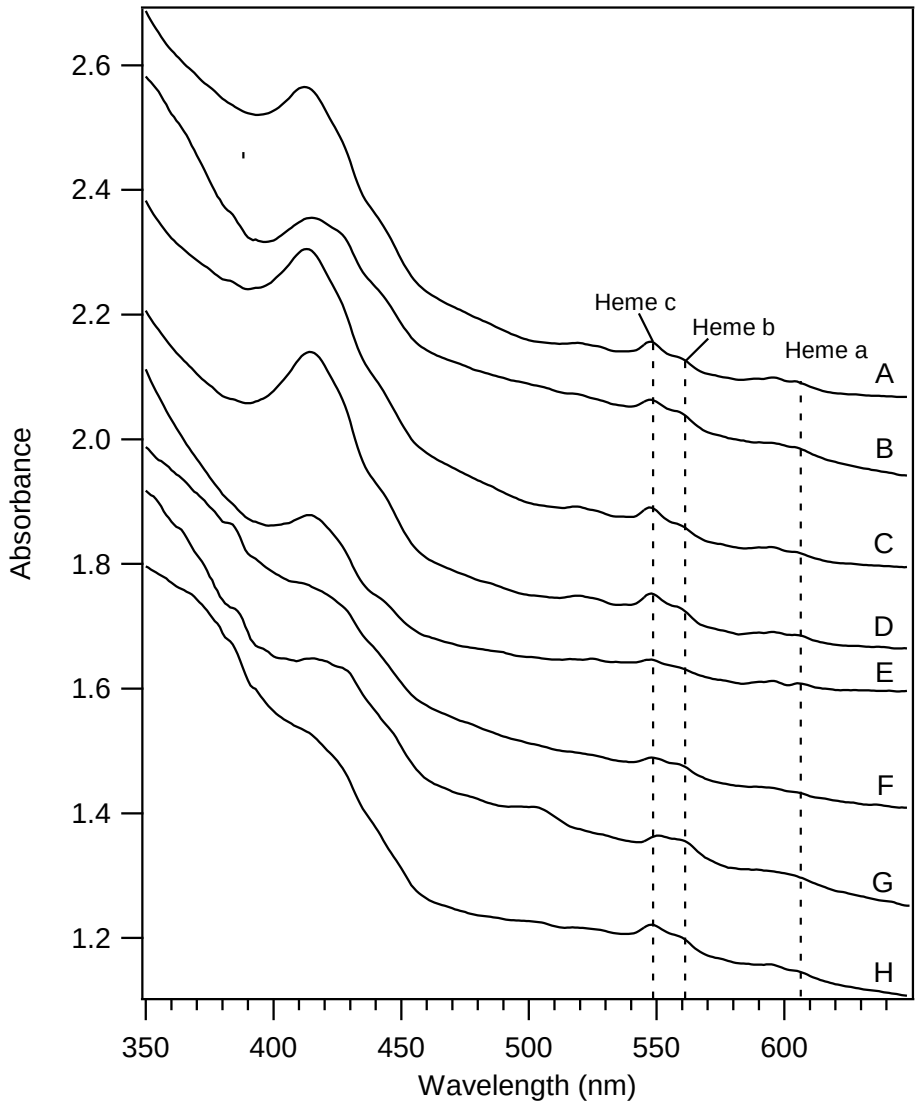

Figure 4.3. Electronic absorption spectroscopy of WT, ΔCCC1, and *CCC1-up* whole cells. A, WT1; B, WT40; C, D1; D, D40; E, UP1; F, UP40; G, UP1+A; H, UP40+A. Cells were grown to OD_{600} = 1.0, washed 1x with EDTA and 2x with ddH_2O, then diluted 1:3 with ddH_2O.

Δ*CCC1 Cells*

The absence of *CCC1* in this strain was verified by PCR (Figure 4.4, B). Δ*CCC1* cells grown on MM that were supplemented with 1, 10, 20 and 40 μM Fe will be referred to as Δ1, Δ10, Δ20 and Δ40 cells, respectively. The Fe concentrations in these cells were ~20% less than in the corresponding WT cells (Table 4.1). The low-temperature low-field MB spectrum of Δ1 cells (Figure 4.5A) was dominated by the CD. Although the spectrum was noisy, doublets due to NHHS Fe^{2+} and HS Fe^{2+} Hemes could be discerned; the red line is a composite simulation, using percentages given in Table 4.1. EPR of Δ1 cells exhibited a very low intensity g = 4.3 signal, consistent with the MB spectrum devoid of a sextet. UV-vis spectra of Δ1 cells (Figure 4.4C) showed that the concentrations of reduced hemes in Δ1 cells were similar to those in WT1 cells. These results indicate that *the absence of CCC1 under low-Fe conditions has no significant effect on cellular Fe content, relative to WT cells grown under similar conditions*. This makes sense because vacuoles do not store Fe under low-Fe conditions and so the absence of the vacuolar Fe import will not be evident under these conditions. The MB spectrum of Δ10, Δ20, and Δ40 cells (Figure 4.5, B, C and D) exhibited less CD on a percentage basis than did the Δ1 spectrum (Figure 4.5A), but the absolute concentration of CD-associated Fe in Δ*CCC1* cells grown in media containing increasing concentrations of Fe was similar to that of Δ1 cells (Table 4.1). The concentrations of HS Fe^{2+} hemes also remained relatively constant as the FC concentration increased. The concentrations of reduced hemes in Δ1 and Δ40 cells, as monitored by UV-vis (Figure

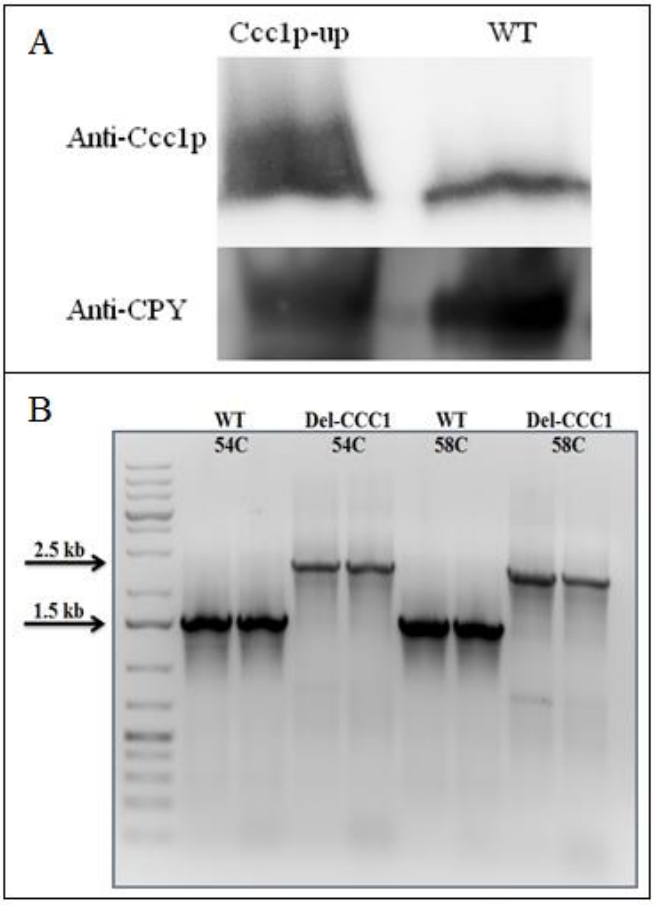

Figure 4.4. Verification of *CCC1-up* and Δ*CCC1* strains. A, Western Blot of vacuoles isolated from UP40 and WT40 fermenting cells (40μg of protein per lane). B, PCR of WT40 and D40 fermenting cells grown with 40 μM Fe in the medium. The bands at 1.5kb correspond to the PCR product of WT DNA (CCC1) and the bands at 2.5kb correspond to the PCR product of Δ*CCC1* DNA. The PCR reaction was conducted at 54°C and 58°C, and even-numbered lanes were loaded with twice as much DNA compared with odd-numbered lanes. (These different conditions were run because we were unsure of the annealing temp of the primers and wanted to ensure there was a sufficient concentration of DNA to show a PCR product.)

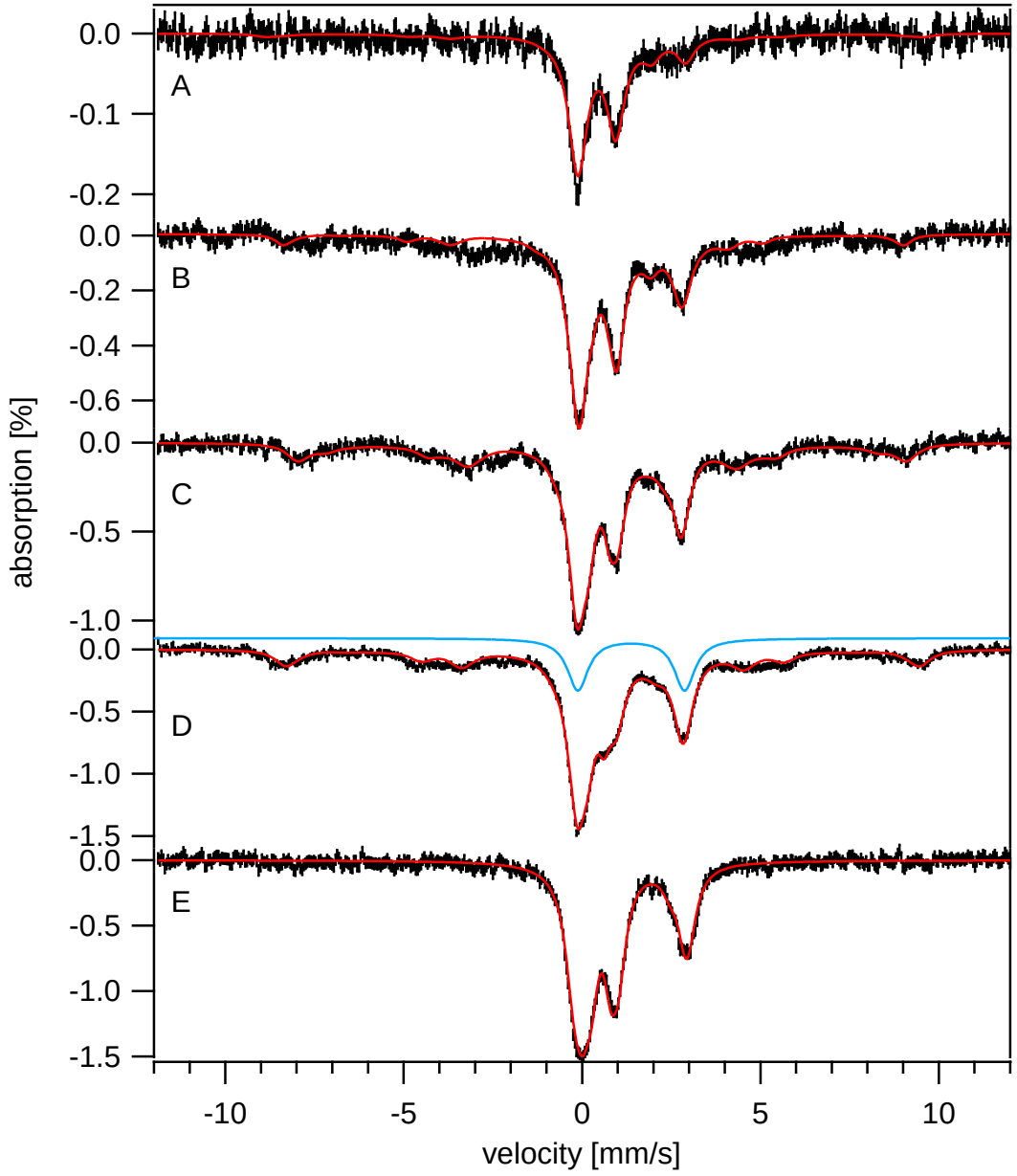

Figure 4.5. 5 K, 0.05 T Mössbauer spectra of Δ*CCC1* cells and isolated mitochondria. A, D1; B, D10; C, D20; D, D40; E, Mitochondria isolated from D40 cells. The red lines are simulations of the entire spectrum using the percentages of each feature given in Table 4.1. The blue line is a simulation of the NHHS Fe^{2+} feature with parameters specified in Figure 1.

4.3C) were similar to each other and to the analogous concentrations in WT1 cells (Figure 4.3A) – 40 – 50 μM for each condition. Collectively, these data indicate that *the concentration of Fe-containing centers in the mitochondria of ΔCCC1 cells was similar to that in WT cells and was largely unaffected by changes in the medium Fe concentration.*

The major changes occurring in the MB spectra of Δ*CCC1* cells prepared in MM with increasing Fe concentration were increases in the sextet that reflects vacuolar NHHS Fe^{3+} and a NHHS Fe^{2+} doublet (Figure 4.5, B – D, and Table 4.1). The concentration of the vacuolar Fe increased from 0 → 110 μM; the latter value was less than half of the concentration observed with WT cells at the same (40 uM) Fe concentration in the medium. Δ40 cells exhibited a g = 4.3 EPR signal (Figure 4.2F) that was also about half as intense as the signal exhibited by equivalent WT cells. These results show that vacuolar NHHS Fe^{3+} in Δ40 declined to about 40% of WT levels. This indicates that ca. 60% of the Fe that is imported into vacuoles enters via Ccc1p; the remaining vacuolar Fe (which we observed here) enters via other pathways (e.g. END4). This result agrees with the previous estimate of Kaplan, *et. al. (103)*. Regardless of import pathway, the resulting vacuolar Fe exhibits the same spectroscopic signature suggesting the same structure (i.e. a mononuclear NHHS Fe^{3+} complex).

The most interesting spectral feature was the NHHS Fe^{2+} doublet. The concentration of this feature increased from 20 → 110 μM as the Fe concentration in Δ*CCC1* growth medium increased. This represents about twice the concentration observed in corresponding WT cells (compare the blue doublet line shown in Figure

4.5D to that in 1A). This species accumulates in the range of concentrations normally associated with the import of vacuolar Fe. This behavior is remarkably analogous to that hypothesized by Kaplan regarding the cytosolic Fe species. For this reason we propose that *the NHHS Fe^{2+} complex giving rise to the doublet in MB spectra of ΔCCC1 cells is the cytosolic Fe complex that normally (in WT cells) enters into the vacuole via the Ccc1p-dependent import pathway*. Since the Fe concentration in Δ*CCC1* cells is ~ 20% less than in equivalent WT cells, we further propose that *this cytosolic Fe complex is sensed by the system that regulates Fe import into the cell*. Accordingly, the higher concentration of this species would down-regulate Fe import, as observed. Finally, we found that Δ40 cells suffered ~ 4 times more oxidative damage than comparable WT cells (Figure 4.6). We propose that the cytosolic NHHS Fe^{2+} complex promotes Fenton chemistry which is responsible for the increased extent of oxidative damage. Further studies are of course required to test these proposals.

ΔCCC1 Mitochondria

The Fe concentration in mitochondria isolated from Δ40 cells (~860 μM) was slightly higher than the W303-1B mitochondria (~710 μM) *(137, 138, 187)*. However, the same primary features were observed in MB spectra of Δ*CCC1* mitochondria, including the CD, a NHHS Fe^{2+} doublet, a NP doublet, and a doublet due to HS Fe^{2+} hemes (Figure 4.5E). The percentage intensities were similar to those of WT mitochondria except that the NHHS Fe^{2+} doublet was more intense (37%, 316 μM). The increased concentration

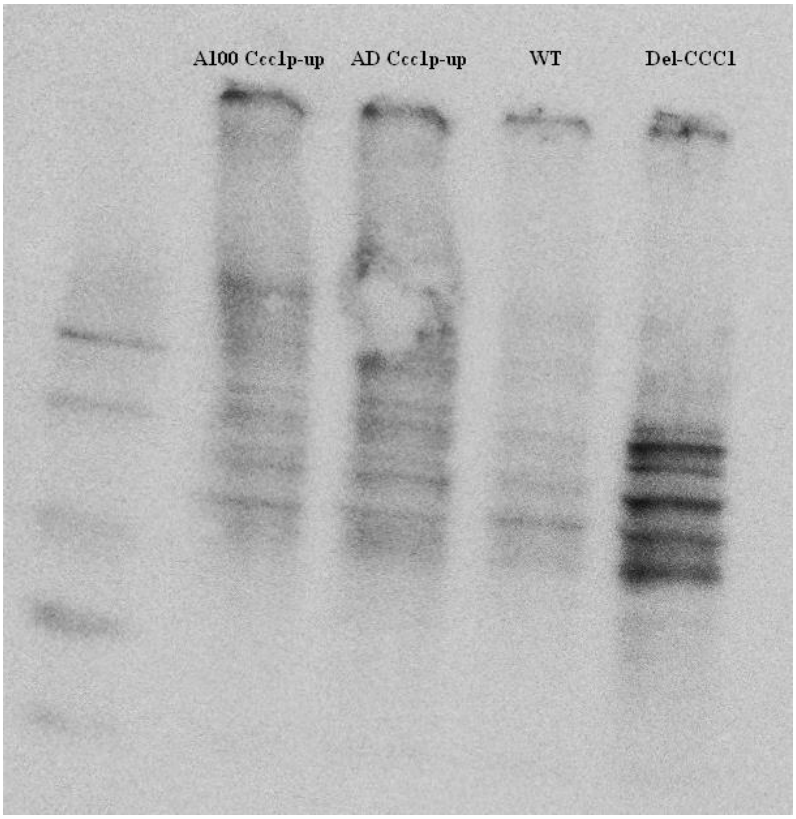

Figure 4.6. Oxyblot of WT40, D40, UP40, and UP2x40 cells. Lane 1: MW Standard, Lane 2: UP2x40, Lane 3: UP40, Lane 4: WT40, Lane 5: D40. This experiment was performed twice.

of NHHS Fe^{2+} in Δ*CCC1* mitochondria might have arisen from a higher level of mitochondrial Fe import due to the higher concentration of cytosolic Fe. This increased import could be due to a faster import rate, or to elevated levels of mitochondrial Fe import proteins in these conditions.

CCC1-up Cells

In this strain, *CCC1* was overexpressed using a *LEU2*-marked multicopy plasmid that contained *CCC1* under its native promoter; thus, *CCC1-up* cells were grown on MM lacking leucine. Western blot analysis of vacuoles isolated from *CCC1-up* cells grown on this medium and with 40 μM FC (abbreviated UP40 cells) indicated that these vacuoles contained approximately twice the normal concentration of Ccc1p compared to WT40 vacuoles (Figure 4.4).

The concentration of Fe in *CCC1-up* cells grown with 1 μM FC in the medium ("UP1 cells") was substantially higher than in WT1 cells (Table 4.1). The low-temperature low-field MB spectrum of UP1 cells was dominated by a NHHS Fe^{2+} doublet (Figure 4.7A). This feature was 2 – 4 times more intense than the corresponding feature in spectra of WT1 or Δ1 cells, corresponding to absolute concentrations of 130 μM in UP1 vs. 43 μM in WT1 and 22 μM in Δ1. A sextet and doublet due to NHHS Fe^{3+} and NP species, respectively, were also more intense relative to in WT1 (4.1B) and Δ1 (Figure 4.1A) spectra. Consistent with this, the intensity of the g = 4.3 EPR signal exhibited by UP1 cells was also higher (compare Figure 4.2, C vs. A or B; also see Table 4.1). The dominance of the NHHS Fe^{2+} doublet in the MB spectrum of UP1 cells

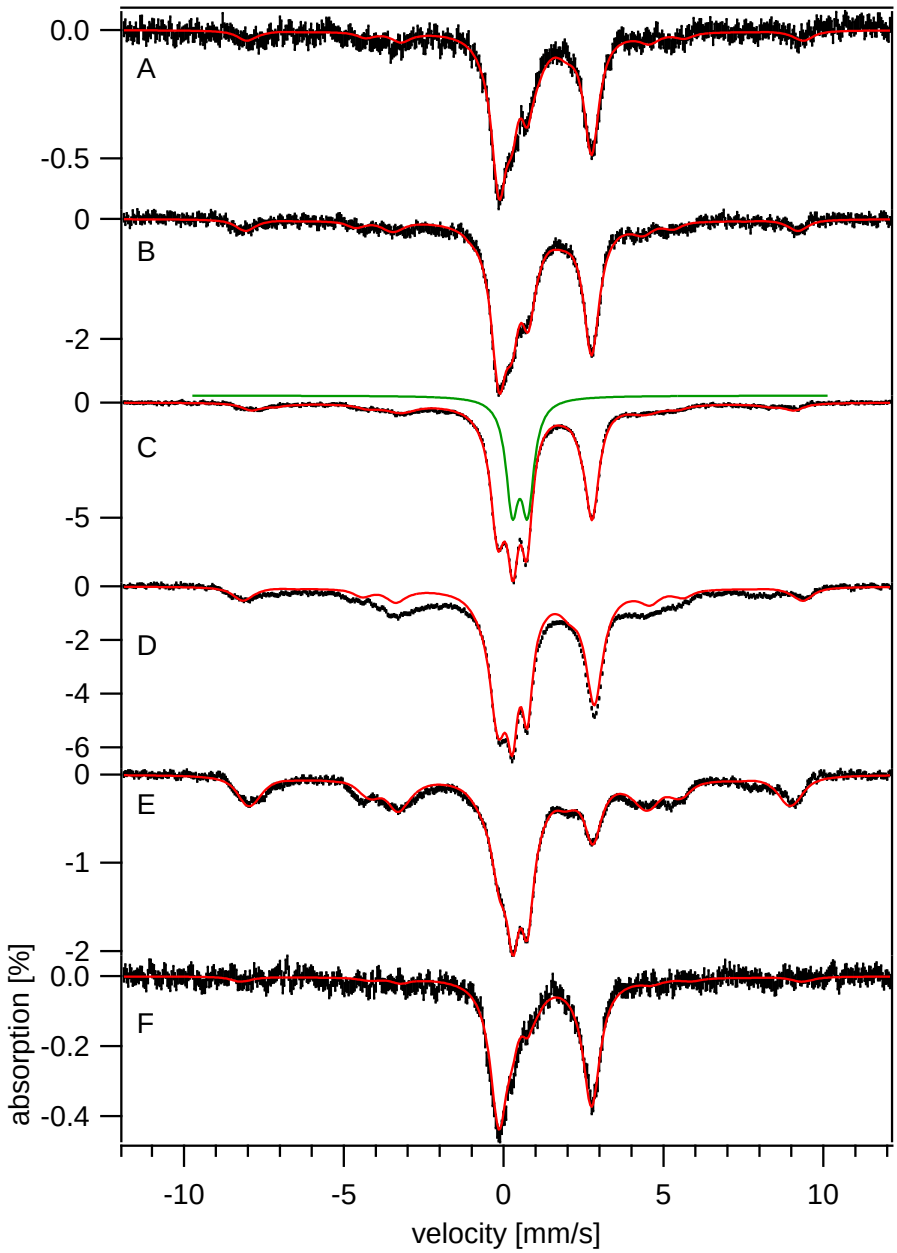

Figure 4.7. Mössbauer spectra of *CCC1-up* cells grown at various FC concentrations. A, UP1; B, UP10; C, UP20; D, UP40; E, UP1+A; F, UP40+A. The red lines are simulations of the entire spectrum using the percentages of each feature given in Table 4.1, and the green line is a simulation of the NP feature using the parameters specified in Figure 4.1.

diminished our ability to quantify the intensity of the CD. However, after removing the contributions of the three major components (the NHHS Fe^{2+} doublet, the NHHS Fe^{3+} sextet, and the NP doublet) little intensity remained that could fit to the CD. Consistent with this, the UV-vis spectrum of UP1 cells indicated a lower concentration of Fe^{2+} hemes in UP1 cells, relative to in WT1 or Δ1 cells.

Collectively, these results indicate that the concentration of mitochondria was lower in UP1 cells than in WT1 or Δ1 cells, while the concentration of vacuolar HS Fe^{3+} species was higher. The concentration of NHHS Fe^{2+} species was much higher in UP1 cells than in WT1 or Δ1 cells, but the location(s) of these species is uncertain.

The concentration of Fe in UP10 cells was about twice that in UP1 cells. The low-temperature low-field MB spectrum of these cells (Figure 4.7B) was similar to that of UP1 cells, with the NHHS Fe^{2+} doublet again dominating. The NHHS Fe^{3+} sextet was evident, as was a shoulder on the low-energy doublet line, due to a NP doublet. The intensity of the CD was again low, corresponding an Fe concentration of ~ 30 μM. This was similar to the concentration associated with the CD in UP1, UP20, and UP40 cells.

The Fe concentration in UP20 cells was nearly twice that in UP10 cells, and the corresponding MB spectrum (Figure 4.7C) was correspondingly more intense. The NHHS Fe^{2+} doublet remained intense, but not as high (percentage-wise) as in spectra of UP1 or UP10 cells. The absolute concentration of this species was slightly higher but other features changed to a far greater extent. The major spectral change was an increase in the intensity of the NP doublet. The concentration of Fe associated with NPs more

than doubled in UP20 cells, relative to in UP10 cells. The concentration of the NHHS Fe^{3+} species also increased (Table 4.1).

The Fe concentration of UP40 cells was nearly twice that in UP20 cells (Table 4.1). Such a proportional increase in the cellular Fe concentration of UP cells with increasing Fe concentration in the medium (intracellular Fe concentrations doubling from 10 μM → 20 μM Fe in the medium, and doubling again from 20 μM → 40 μM) is unusual. It indicates that the import of Fe into these cells is effectively unregulated. This could arise if the regulatory system was defective in *CCC1-up* cells or that the concentration of the sensed Fe species used in regulating Fe import was consistently below the threshold concentration in *CCC1-up* cells. We will argue below for the latter explanation.

The low-temperature low-field MB spectrum of U40 cells was again dominated by the NHHS Fe2+ doublet (Figure 4.7D). In fact, the NHHS Fe^{2+} concentration in UP40 cells was the highest observed in this study. Curiously, Oxyblot analysis revealed that these cells exhibited less ROS damage than in Δ*CCC1* cells (Figure 4.6). This raised the possibility that the majority of this NHHS Fe^{2+} might be sequestered in a manner that somehow avoids ROS formation.

A strong NP doublet was also present, similar to the spectrum of UP20 cells (Figure 4.7C). The major difference between the UP40 and UP20 spectra was a more intense NHHS Fe3+ sextet. Consistent with this, EPR of UP40 cells showed an intense g = 4.3 signal representing ~415 μM HS Fe^{3+} ([spin]/[HS Fe^{3+}] ~0.93; Figure 4.2G and Table 4.2).

Little intensity remained after the three dominant features were subtracted from this spectrum. The remaining intensity (~ 5%) fit to the CD and HS Fe^{2+} hemes (Table 4.1). UV-vis analysis revealed that the levels of Fe^{2+} hemes were similar in UP1 and UP40 cells (Figure 4.3, E and F, respectively, and Table 4.1). These data indicate that mitochondrial Fe levels are lower in UP cells, regardless of the elevated intracellular Fe concentrations. We conclude that when *CCC1* is overexpressed, less than the normal amount of Fe is trafficked into mitochondria. This indicates that there is some level of competition for cytosolic Fe between the mitochondria and the vacuoles. When vacuolar Fe import is elevated, the mitochondrial Fe levels decline.

The MB spectrum of UP40 cells also exhibited a broad, magnetic feature that accounted for ~15% of the spectral intensity (~275 μM). At high temperatures (100K) this feature was absent and the signals in the central region of the MB spectrum increased, (data not shown). This feature overlayed with the NP feature which was present at low and high temperatures, resulting in a ~1.8x increase in this signal (45%). Variable temperature EPR of UP40 cells showed the appearance of a broad signal in the g = 2 region which displayed anti-Curie Law behavior; it was 5-times more intense at 78K (Figure 4.8, black line) that it was at 10 K (red line). In these spectra, the g = 4.3 signal intensity, which follows the Curie Law, served as a control. A similar though slightly broader signal has been observed in other samples which displayed a broad magnetic feature by MB (Park, *et al.*, submitted). Broad g = 2 signals displaying anti-Curie Law behavior have been observed in samples which contained high concentrations of NP *(74, 178)*.

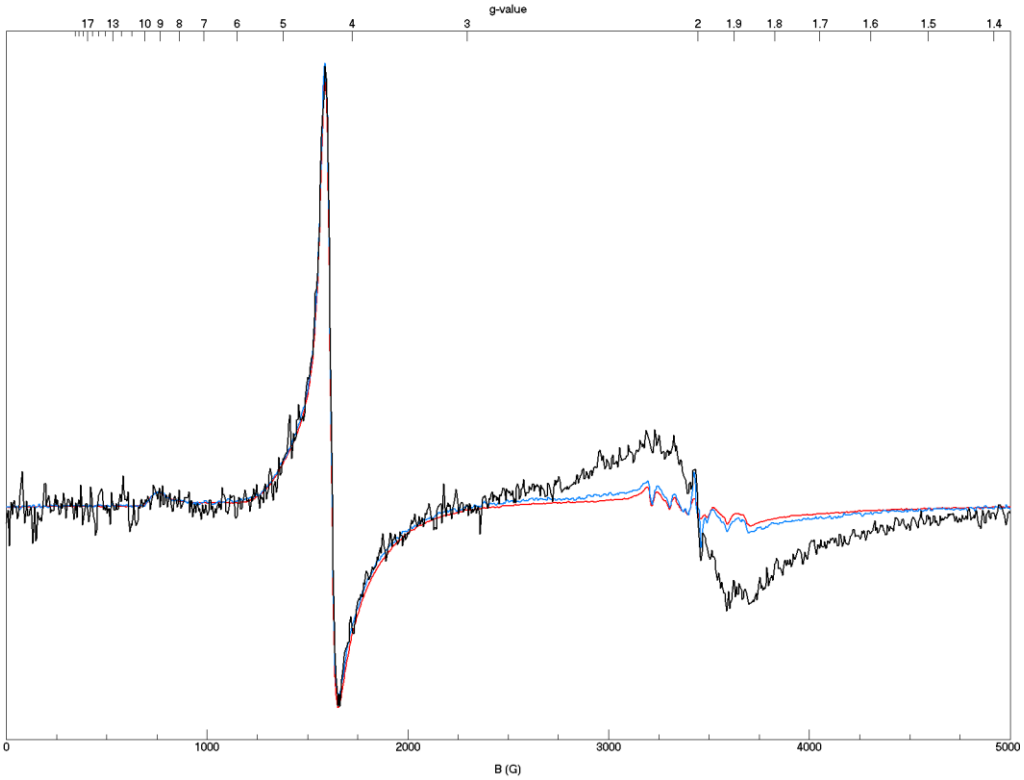

Figure 4.8. Variable temperature EPR spectra of UP40 cells. The red spectrum was collected at 10K; the blue line was collected at 22K; the black line was collected at 79K. Spectra were collected at microwave frequency 9.63 GHz, and microwave power 0.2 mW. Spectra were normalized and plotted using SpinCount.

Adenine Deficiency of CCC1-up Cells

As UP cells (UP1 → UP40) reached an OD_{600} ~1.0, a pink color was observed, which indicated an adenine deficiency *(188).* The pink color is caused by the accumulation of an oxidized red adenine precursor (AIR) in yeast vacuoles. Standard MM, containing 50 mg L^{-1} of adenine is sufficient to suppress this phenotype in WT cells.

Reducing this concentration 8-fold results in an adenine deficiency in WT cells (Park, *et al.*, submitted). The Fe in adenine deficient WT cells is dominated by NHHS Fe^{2+} (J. Park, *et al.*, submitted). We concluded that the vacuoles in adenine deficient cells are more reducing than in WT cells, causing vacuolar NHHS Fe^{3+} ions to be reduced to the Fe^{2+} state. The pink color and high concentration of NHHS Fe^{3+} in UP40 cells indicates that these cells are adenine deficient despite having been grown in medium containing the normal concentrations of adenine that is sufficient to prevent adenine deficiency in WT cells. This made us concerned that some (or all) of the phenotype that we would otherwise associate directly with the overexpression of Ccc1p might instead be associated with the adenine deficiency.

To deconvolute these effects, we attempted to relieve the adenine deficiency in *CCC1-up* cells by growing them on MM medium containing twice the normal adenine concentration (100 mg/L). The resulting UP1+A cells did not turn pink. The concentration of Fe in UP1+A cells was slightly higher than in UP1 cells, but the MB spectra (Figure 4.7, E and A) were similar –dominated by a NHHS Fe^{2+} doublet. EPR and UV-vis spectra were also similar (Figures 4.2D and 4.3G). These results indicate

that under low-Fe growth conditions, the observed buildup of NHHS Fe^{2+} species is not due to an adenine deficiency in *CCC1-up* cells.

The situation was somewhat different with UP40+A cells. They also did not develop a pink color, indicating the absence of an adenine deficiency. However, UP40+A cells contained about half as much total Fe as found in UP40 cells (Table 4.1), and the Fe was distributed differently. Relative to UP40 cells, the proportion of Fe due to NHHS Fe^{2+} species in UP40+A cells was lower while the proportions due to NHHS Fe^{3+} and NP were higher. This afforded a MB spectrum (Figure 4.7F) that was reminiscent of the WT40 spectrum (Figure 4.1A). The concentrations of Fe species associated with mitochondria, including the CD (Figure 4.7F) and heme centers (Figure 4.4H) were not noticeably affected by relieving the adenine deficiency.

Like UP40 cells, UP40+A cells also exhibited a broad g = 2 feature by EPR which displayed anti-Curie law behavior. Despite having a lower cellular Fe concentration, UP40+A cells exhibited a g = 4.3 EPR signal (Figure 4.3H) with greater intensity than that exhibited by UP40 cells. This confirms the shift from mononuclear NHHS Fe^{2+} to Fe^{3+} as UP40 cells were relieved of their adenine deficiency. This means that ~75% of the NHHS Fe^{2+} observed in UP40 cells was due to the adenine deficiency (not due to the overexpression of Ccc1p). Interestingly, the loss of this NHHS Fe2+ resulted in a decline in the concentration of cellular Fe. If that NHHS Fe2+ were the sensed form of Fe in the cytosol, we would expect that its decline would be associated with an *increase* in cellular Fe. Since the opposite happened, we propose that some

(perhaps most) of the NHHS Fe^{2+} species present in *CCC1-up* cells are NOT being sensed by the system that regulates the import of Fe into the cell.

Effect of Concanamycin A (ConA)

Previous studies have shown a connection between the Fe content and pH of vacuoles *(149, 189, 190)*, so we wondered whether some of the observed changes in the Fe distribution of the cell upon deleting or overexpression Ccc1p might be related to changes in vacuolar pH. ConA increases the pH of the vacuoles by inhibiting the vacuolar H^+-ATPase following glucose-deprivation *(149, 191)*. Depriving WT40 cells of glucose and then adding glucose back 10 min later, as prescribed by the protocol, resulted in a decline in the vacuolar NHHS Fe^{3+} sextet and an increase in the NHHS Fe2+ doublet (Figure 4.9A). All of the samples treated in this way contained ~2-fold higher Fe compared with WT40 whole cells, suggesting that the glucose deprivation/loading protocol was responsible for the elevated Fe levels. We don't understand this effect on the molecular level, but it served as our control nonetheless (moreover, it highlights the redox sensitivity of vacuolar Fe to perturbations in cellular metabolism).

The MB spectrum of the ConA treated sample (Figure 4.9C) exhibited more of the NP doublet and less of the NHHS Fe^{2+} than the sample treated with glucose alone (Figure 4.9B). This shift is highlighted by the difference spectrum shown in Figure 4.9D.

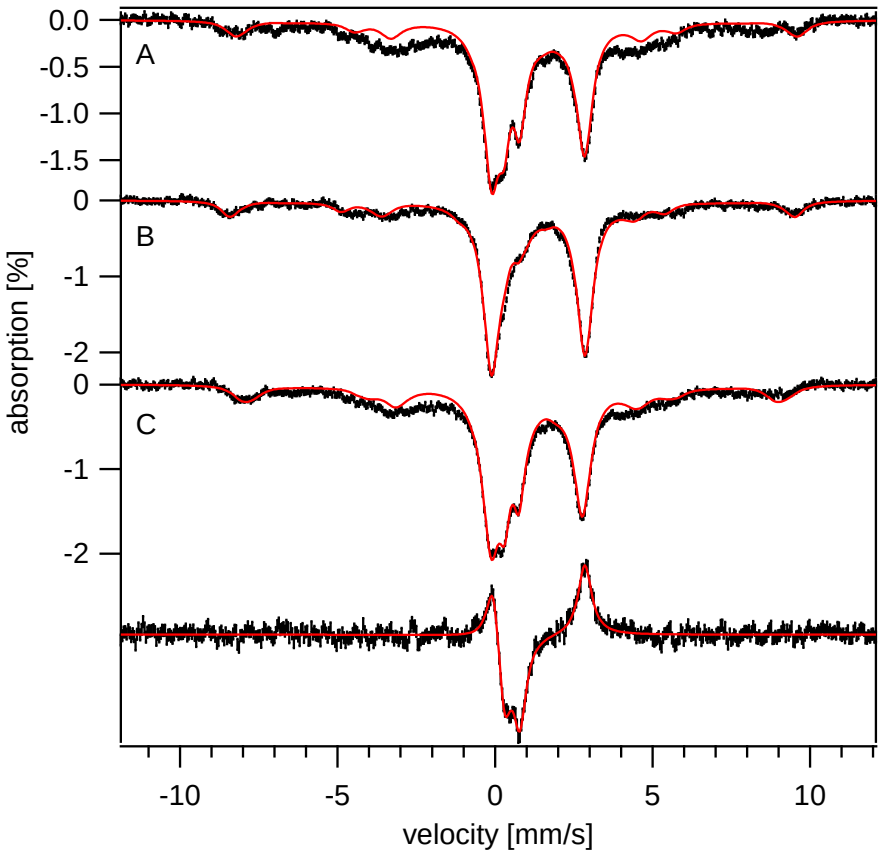

Figure 4.9. Mössbauer spectra of cells that were resuspended in MM containing 40μM FC and deprived of glucose for 10 minutes. A, ConA and glucose were added to the cell suspension which was immediately packed into a MB cup and frozen; B, same as A, but without ConA and frozen after 15 min of incubation; C, same as A but frozen after 15 min incubation; D, difference spectrum of B and C. The red lines are simulations of the entire spectrum, and the percentages of each feature are shown in Table 4.1.

We conclude that rendering the vacuoles less acidic causes some intracellular NHHS Fe^{2+} to convert into NP. This process involved oxidation and probably ligand exchange. This suggests that at least some of the NHHS Fe2+ species in *CCC1-up* cells are either located in vacuoles (or are closely associated with vacuolar NHHS Fe^{3+}).

Parenthetically, a broad magnetically-interacting form of Fe was evident in the low-temperature MB (~15%, 160 μM) of ConA-treated cells (Figure 4.9C; notice the discrepancy between the simulation and the data in the central region of the spectrum). At high temperatures (100 K) this material collapsed into an unresolved doublet with parameters typical of nanoparticles appeared (data not shown). An Fe species which behaved in a similar manner was also observed in AD *CCC1-up* cells (280 μM), which also contained high levels (> 1 mM) of intracellular Fe. A similar feature has also been observed in WT samples which grew for 5 days on MM supplemented with high levels of Fe (Park, *et al*. 2013, submitted).

Manganese Homeostasis

Although not the focus of this paper, some effects involving Mn seem relevant to our understanding of the effects of ΔCC1 and *CCC1-up* on Fe metabolism. The g = 2 regions of the WT1 and WT40 EPR spectra (Figure 4.3, A and D) were dominated by a Mn^{2+}-based hyperfine split signal, quantifying to a spin concentration of ~35 μM in both spectra. This concentration was normalized to the cellular Mn concentration (~35 ± 5 μM), yielding a [spin]/[Mn] ratio of ~ 0.9 (Table 4.2). This confirms a previous report that the vast majority of the Mn in yeast cells is EPR active *(138)*, and demonstrates that

Strain	[Fe] ICP-MS; [NHHS Fe^{3+}] (μM)	[Fe^{3+}] (EPR)	[spin]/[Fe^{3+}]	[Mn] ICP-MS (μM)	[Mn^{2+}] (EPR)	[spin]/[Mn^{2+}]
WT1	163 (0)	0	-	32	29	0.91
WT40	349 (170)	152	0.79	37	36	0.97
D1	123 (0)	< 1	-	16	< 10	-
D40	263 (84)	73	0.87	17	< 10	-
UP1	395 (35)	30	0.86	64	61	0.95
UP40	2428 (413)	372	0.90	71	67	0.94
UP1+A	395 (40)	39	0.98	83	76	0.91
Up40+A	976 (439)	415	0.95	85	75	0.88

Table 4.2. Fe^{3+} and Mn^{2+} concentrations and spin quantitations of cells studied in these experiments. These signals were quantified as described in Table 4.1.

the cellular Mn concentration is not significantly affected by the concentration of Fe in the growth medium.

The spin concentration of the Mn^{2+} based signal exhibited by Δ*CCC1* cells were lower (< 10 μM), reflecting a lower Mn concentration in these cells (~16 μM, Table 4.2). Besides transporting Fe into vacuoles, Ccc1p also transports Mn^{2+} *(103, 157)*. Therefore, when Ccc1p is absent, cytosolic Mn^{2+} may be unable to enter into vacuoles and the buildup of cytosolic Mn^{2+} which may inhibit further Mn import into the cell.

The concentration of Mn in *CCC1-up* cells (including UP1, UP40, UP1+A, and UP40+A) was ca. 76 μM, which is double the concentration of Mn in WT cells and about 5 times the concentration in Δ*CCC1* cells. These results are consistent with reports that cellular Mn is elevated when Ccc1p is overexpressed *(103)*. The intensity of the Mn^{2+} signal in the EPR spectrum of UP1 cells was also greater than in WT1 or D1 cells, affording a [spin]/[Mn] ratio of ~ 0.9. Again, this indicates that the vast majority of the Mn in UP1 cells is EPR-active Mn^{2+} species. The Mn^{2+} signal intensities exhibited by UP1, UP40 and UP40+A cells were similar (Tables 4.1 and 4.3). This indicates that the Mn^{2+} levels were not affected by adenine supplementation or the Fe concentration in the medium.

Discussion and Conclusions

Synopsis

Ccc1p is a vacuolar Fe importer in yeast. Δ*CCC1* and Cccp1 overexpression (UP) strains were evaluated by Mossbauer, EPR, UV-vis and ICP-MS. The objective of

the study was to detect the cytosolic Fe that is imported by Ccc1p into vacuoles, and the vacuolar Fe that resulted from this importation. Cells were grown on minimal medium containing 1 → 40 μM Fe. Δ*CCC1* cells contained ~20% less Fe than WT cells. The absence of *CCC1* under low-Fe conditions did not affect cellular Fe content, relative to WT cells, probably because vacuoles do not store Fe under low-Fe conditions.

Most of the Fe in Δ1 cells (grown with 1 μM Fe) was mitochondrial but some nonheme high-spin (NHHS) Fe^{2+} was evident. The concentration of Fe centers in Δ*CCC1* mitochondria was independent of the Fe concentration in the medium (1 → 40 μM), and was similar to that in WT cells. Most of the changes in the Fe content of Δ*CCC1* cells occurred when the concentration of Fe in the growth medium was in the range in which vacuoles load Fe in WT cells (i.e. 10 → 40 μM). In this range, the concentration of vacuolar Fe^{3+} in Δ*CCC1* cells increased as the medium Fe concentration increased, but only to 60% of the level observed in WT cells; this represents the percentage of Fe imported into WT vacuoles via Ccc1p. Regardless of import pathway, the resulting vacuolar Fe exhibits the same spectroscopic signature suggesting the same or related structure; i.e. a mononuclear NHHS Fe^{3+} complex.

The concentration of NHHS Fe^{2+} also increased in Δ*CCC1* cells as the Fe concentration in the growth medium increased within the vacuolar Fe-loading range. The concentration of NHHS Fe^{2+} in Δ*CCC1* cells grown with 40 μM Fe was about twice that observed in corresponding WT cells. The combined concentration of NHHS Fe^{2+} and Fe^{3+} in Δ40 cells was about the same as the NHHS Fe^{3+} level in WT40 vacuoles. The NHHS Fe^{2+} species in Δ*CCC1* cells is proposed to be the cytosolic Fe complex that in

WT cells enters the vacuoles via Ccc1p. The same Fe^{2+} species is proposed to be sensed by the system that regulates Fe import into cells (Aft1p). Aft1p is active when cytosolic Fe levels are low, but is inactive when cytosolic Fe is high. As the medium Fe concentration is raised from 1 → 40 μM, less Fe is imported in Δ*CCC1* cells than in WT cells. These results suggest that the accumulated NHHS Fe^{2+} species in Δ*CCC1* cells is sensed (either directly or indirectly) by Aft1p. When Aft1p senses high-Fe levels, Fe import decreases. Moreover, Δ40 cells suffered ~ 4 times more oxidative damage than comparable WT cells, suggesting that the cytosolic NHHS Fe^{2+} complex may promote Fenton chemistry.

The same NHHS Fe^{2+} species is probably imported into mitochondria. Mitochondria isolated from Δ40 cells contained slightly more Fe than WT40 mitochondria, with higher levels of NHHS Fe^{2+} which might have arisen from a higher level of mitochondrial Fe import, due in turn to the higher concentration of cytosolic Fe. The concentration of Fe in UP1 cells was substantially higher than in WT1 or Δ1 cells. Most of the Fe was present as NHHS Fe^{2+}; NHHS Fe^{3+} and NP species were also abundant. The concentration of mitochondrial Fe in Cccp1-up cells was low relative to in WT or Δ*CCC1* cells, perhaps because these organelles cannot import sufficient cytosolic Fe (due to a deficiency in this species).

As the concentration of Fe in the medium increased 4 fold (10 → 20 → 40 μM), the Fe concentration in the cell increased proportionately, suggesting that the import of Fe into *CCC1-up* cells is effectively unregulated, perhaps because the concentration of the sensed Fe used in regulating Fe import was consistently below a threshold

concentration. UP40 cells contained the highest NHHS Fe^{2+} concentration measured but exhibited less ROS damage than Δ*CCC1* cells. Some of the NHHS Fe^{2+} in these cells might be sequestered in a manner that avoids ROS formation. The concentration of Fe due to NP's (and NHHS Fe^{3+}) increased in the range of medium Fe concentrations associated with vacuolar Fe loading in WT cells.

A new type of NP was observed in UP40 cells. Ccc1-up cells were adenine deficient when grown on normal MM, but this deficiency could be removed by growing them on MM that contained twice the normal adenine concentration. Vacuoles are reducing under adenine deficient conditions, such that some NHHS Fe^{3+} is converted to NHHS Fe^{2+}. Adenine sufficient Cccp1-up cells contained about half as much NHHS Fe^{2+} as adenine deficient UP cells, suggesting that about half of the Fe buildup in UP40 cells (and half of the NHHS Fe^{2+} observed) was associated with an adenine deficiency rather than Ccc1p overexpression.

UP40 cells shifted from mononuclear NHHS Fe^{2+} to Fe^{3+} when the adenine deficiency was relieved. The decline in cellular Fe concentration along with the loss of NHHS Fe^{2+} (as adenine deficiency was relieved) suggested that the NHHS Fe^{2+} was not the sensed form of Fe in the cytosol. Instead, these results suggest that the NHHS Fe^{2+} accumulation is related to adenine deficiency. Adenine deficiency leads to the accumulation of a glutathione conjugate in in the vacuoles, which causes the vacuoles to be more reducing *(192)*. This could promote the accumulation of NHHS Fe^{2+}. Increasing the pH of vacuoles in WT40 cells caused NP levels to increase and NHHS Fe^{2+} levels to decrease. At least some of the NHHS Fe^{2+} species in *CCC1-up* cells are located in

vacuoles or are closely associated with vacuolar NHHS Fe^{3+}. Virtually all of the Mn in the cell was EPR-active Mn^{2+}. Δ*CCC1* cells contained about half the Mn concentration of WT cells, and WT cells contained about half the Mn concentration of UP cells. This can be explained, since *CCC1* also imports Mn from the cytosol to the vacuole. Deletion of *CCC1* might increase the cytosolic Mn concentration which would inhibit Mn import into the cell. Ccc1p overexpression would cause greater Mn import into the vacuole, creating a deficiency of Mn in the cytosol which would upregulate Mn import into the cell.

Vacuoles and Mitochondria Share a Common Fe Pool

The Fe content of yeast cells can roughly be divided into two groups; vacuolar and mitochondrial. In WT40 cells, about 75% of cellular Fe is located in vacuoles while approximately 20% is located in mitochondria. Other forms of Fe (in other locations) are undoubtedly present, but they cannot be observed by MB spectroscopy because the collective concentration of such species is less than ca. 10% of spectral intensity.

Although we and others have hypothesized the presence of cytosolic Fe, direct evidence for this form of Fe (e.g. by MB spectroscopy) is lacking. Kaplan has reported extensively on this issue, and have provided strong (albeit circumstantial) evidence that a single form of cytosolic Fe is imported into both mitochondria and vacuoles, and that the two organelles essentially compete for this form of Fe. Thus, deletion of the mitochondrial Fe importers *MRS3*/4 is thought to lead to an increase of cytosolic and vacuolar Fe. Similarly, deletion of the vacuolar Fe importer Ccc1p is thought to increase

the level of cytosolic and mitochondrial Fe. Correspondingly, overexpression of Ccc1p would be expected to cause a *decrease* of cytosolic Fe (and a decrease in mitochondrial Fe). These hypotheses motivated the current study, as they provide a strategy to detect (and ultimately identify) cytosolic Fe.

WT Fe Distributions are Different in W303-1B and DY150 Cells

We compared the DY150 and W303-1B cells to establish the WT background for these studies. DY150 cells showed higher ratios of NP to NHHS Fe^{3+} than W303-1B cells. Both NP and NHHS Fe^{3+} have been observed in vacuoles, and we have proposed that a higher vacuolar pH could cause a shift from NHHS Fe^{3+} to NP *(112)*. These data showed that WT strains which were derived from the same background (W303) and are isogenic can have slightly different intracellular Fe distributions. NP accumulation has been observed in cells which have Fe overload phenotypes (*i.e.*, Aft1-1^{up}), and in isolated vacuoles *(74, 112, 178)*. In DY150 cells the overall Fe concentration was similar to W303-1B cells, which shows that the NP accumulation was not due to increased Fe uptake. Therefore, the differences in WT DY150 and W303-1B cells could be due to a slightly less acidic vacuolar environment in DY150 cells.

ΔCCC1 Cells are Fe-Replete

The regulation of Fe import into yeast has been well studied, and both high- and low-affinity transporters on the plasma membrane have been identified *(19, 33-35, 44, 159)*. Also, the major Fe-sensitive transcription factor involved (Aft1p) and the

mechanism by which it activated the Fe regulon genes has been well documented *(35, 123, 126, 182, 183)*. Aft1 toggles between the cytosol and the nucleus in an Fe-dependent fashion *(126, 183)*.

What remains unknown is the particular form and location of the Fe species that serves as a sensor in this regulation. In principle, the homeostatic regulatory process would sense the concentration of this species and compare it to some threshold concentration. When the sensor concentration exceeds the threshold concentration, the rate of Fe import would decrease; when it was less than the threshold, the Fe import rate would increase. In the simplest situation, the sensor would be located in the cytosol (but other scenarios are possible).

In the most basic scenario, the same cytosolic Fe species that is imported into vacuoles and mitochondria would also be sensed by the regulatory system. In this case, a buildup of cytosolic Fe would be expected to *lower* the cellular Fe concentration, while a deficiency in cytosolic Fe would be expected to *raise* the cellular Fe concentration. This is essentially the behavior that we observed. The Δ*CCC1* strain exhibited somewhat lower Fe concentrations than WT cells, consistent with a buildup of the sensed molecule.

NHHS Fe^{2+} in ΔCCC1 Cells is the Cytosolic LIP

Our studies of Δ*CCC1* fully supports the Kaplan hypothesis in that we indeed observed a decline in vacuolar NHHS Fe^{3+} and the formation of a new form of Fe - NHHS Fe^{2+}- which we propose is the long-sought-after cytosolic Fe. Although further studies will be required to isolate and characterize this(these) species, the current study

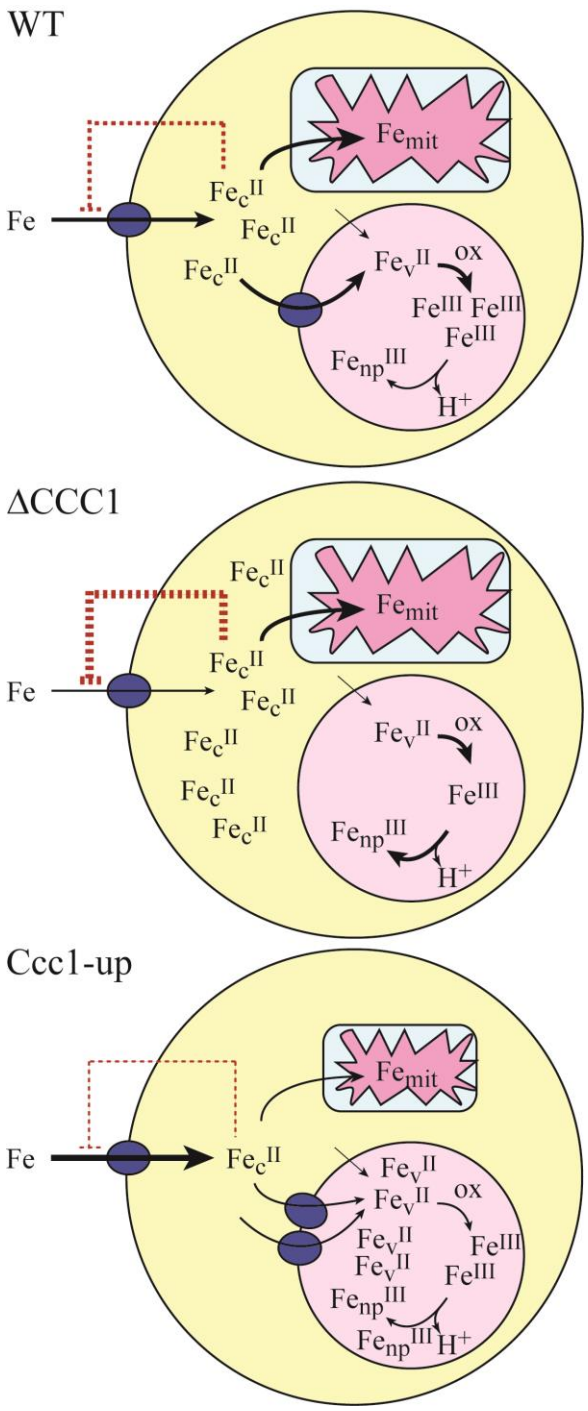

Figure 4.10. Model for Fe Trafficking in WT, ΔCCC1, and *CCC1-up* cells. These models are based on the effects that we have observed in these studies, and that have been previously proposed in the Kaplan hypothesis.

allowed quantification of this species under various circumstances. The NHHS Fe^{2+} nature of this species fits well with our expectations that it is involved in cellular Fe trafficking into vacuoles and mitochondria. High spin complexes are generally correlated with weak/labile coordinating ligands. Fe involved in trafficking would be expected to have weak and labile ligands, as the ligand environment of the trafficking Fe would likely change as the Fe reaches its final destination in the cell. Tightly bound ligands, which might give rise to low-spin configurations, might not dissociate as needed. These same types of NHHS Fe^{2+} complexes would also be expected to participate in Fenton chemistry and be associated with an increase in ROS damage. In agreement with this expectation, Δ*CCC1* cells exhibited substantially higher ROS damage than equivalently grown WT cells. A model of Fe trafficking in Δ*CCC1* cells is proposed in Figure 4.10.

CCC1-up Cells Accumulate an Un-sensed form of NHHS Fe^{2+}

The Cccp1-up strain accumulated Fe, consistent with a deficiency in the sensed Fe. One ***apparent*** inconsistency with this model and our results is that the *CCC1-up* strain contained a high concentration of NHHS Fe^{2+}. By MB spectroscopy, the parameters of the doublet associated with this species were indistinguishable from those associated with the NHHS Fe^{2+} species in Δ*CCC1* cells. Thus, one might regard the two species as the same, e.g. both cytosolic, sensing, and used for import into vacuoles and mitochondria.

However, we argue that these represent different species, with only the NHHS Fe^{2+} species in Δ*CCC1* cells being sensed in the cytosol and used for import into

vacuoles and mitochondria. The NHHS Fe^{2+} species in CCC1up cells, we argue, is not sensed or used for import into these organelles. Either it is sequestered in the vacuoles, or it is cytosolic but is bound in a way that cannot be sensed. Sensing ultimately would involve binding recognition and thus the structure of the NHHS Fe^{2+} complex would be critical.

What is our evidence for this? First, Fe accumulates in CCC1-up cells, which indicates that these cells "feel" Fe deficient. This means that the concentration of the sensed form of Fe is much greater than the threshold concentration. The concentration of Fe in this strain was nearly directly proportional to the concentration of Fe in the medium (see Table 4.1), which indicates that Fe import is not regulated in *CCC1-up* cells under these conditions. This lack of regulation could result if the concentration of the sensed Fe were substantially lower than threshold throughout this medium concentration range.

The second line of evidence is that as the NHHS Fe^{2+} concentration of Ccc1-up cells declined (e.g., UP40 to UP1), the total cellular iron concentration also declined. If the NHHS Fe^{2+} was the sensed species in Cccp1-up cells, then lowering its concentration should cause the Fe concentration in the cell to increase – opposite of what was observed. A model of Fe trafficking in *CCC1-up* cells is proposed in Figure 4.10.

Reducing Conditions and Increased Vacuolar pH Promote NHHS Fe^{2+} Accumulation

Most of the effects that we observe are due to changes in vacuolar Fe. We can rationalize these changes by assuming a thermodynamic box in which the Fe contents of

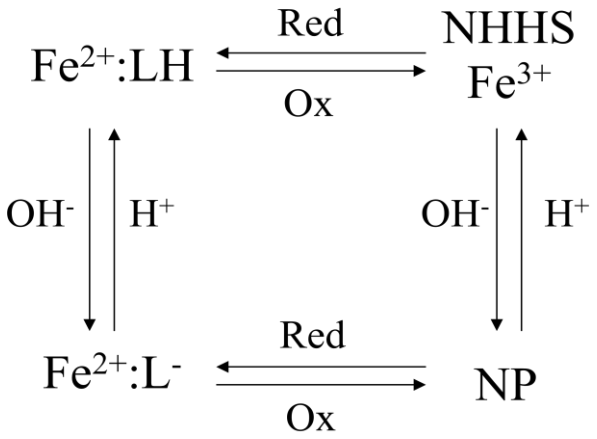

Scheme 4.2. Thermodynamic Box Model of Vacuolar Fe Distributions. The ratios of these species change based on the redox environment and pH conditions of the vacuoles.

the vacuole is controlled by redox status and pH (Scheme 4.2). This model proposes that the vacuolar Fe can exist in four different states. In oxidized conditions the vacuolar Fe will exist in the 3+ oxidation state. The vacuolar pH then determines if the Fe^{3+} is present as NHHS Fe^{3+} (e.g., W303-1B WT) or as NP (e.g., DY150 WT). In reduced conditions the vacuolar Fe is in the ferrous (2+) form. The ligands which chelate this Fe could be protonated (LH) or deprotonated (L^-) based on the pH.

According to this model, low pH conditions would favor NHHS Fe^{2+}:LH and NHHS Fe^{3+} will be dominant, while NHHS Fe^{2+}:L^- and NP are favored at higher pH. Cells treated with ConA (a specific V^+-ATPase inhibitor) have higher vacuolar pH's than untreated cells *(101, 193, 194)*. Here, we observed accumulation of NHHS Fe^{2+} and

NP in ConA-treated cells (Figure 4.9). Similar Fe distributions were also observed in UP40 cells. Based on our model, we hypothesize that the vacuolar pH is higher and more reducing in UP40 cells than in WT cells. The vacuolar pH could increase as a result of excess H^+ export during Ccc1p-mediated Fe^{2+} import *(195)*.

The addition of excess adenine to UP40 cells showed lower NHHS Fe^{2+} and more NP. According to the thermodynamic model, NP formation is favored in oxidizing and high pH conditions. This would suggest that adenine deficiency leads to a more reducing vacuolar environment, as predicted in Park, *et al.* (submitted). The pH in these cells would be higher due to Ccc1p overexpression and elevated Fe^{2+} import.

CHAPTER V

CONCLUSIONS

The overall goal of these studies was to determine the form of Fe in vacuoles and how these organelles are involved in cellular Fe homeostasis. The initial studies were focused on isolating large quantities of purified intact vacuoles which could be studied with biophysical and bioanalytical techniques. In previous work with whole cells, Dr. Greg Holmes-Hampton showed that the dominant Fe species was NHHS Fe^{3+} (~75%). When mitochondria were isolated, this feature was not present. Therefore, the goal of this project was to determine if isolated vacuoles contained the major NHHS Fe^{3+} species observed in whole cells but not in isolated mitochondria.

Chapter III discusses the process of isolating sufficient quantities of vacuoles for biophysical analysis, and the form of stored Fe in isolated vacuoles grown with 40 μM FC in the medium. The isolated vacuoles did not contain as much Fe as we expected based on whole cell calculations (~300 μM vs. ~1 mM). The vacuoles are extremely delicate organelles, and any disruption during the isolation procedure could induce Fe loss. EM showed that vacuoles were intact, which implies that Fe could be lost through protein-mediated export.

Biophysical analyses of isolated vacuoles showed that Fe exists primarily in two forms: NHHS Fe^{3+} and NP. The ratios of these two forms varied between ~20 different WT preps, with 60-85% NHHS Fe^{3+} and 15-40% NP. Model compounds of Fe^{3+} polyphosphate, Fe^{3+} monophosphate, and Fe^{3+} hexaaqua were made in order to determine if these are possible ligands involved in Fe storage. At pH 5.0 (the average

vacuolar pH), Fe^{3+} polyphosphate showed a sextet with the same Mössbauer parameters as vacuolar NHHS Fe^{3+}. Fe^{3+} monophosphate gave a quadrupole doublet with similar parameters to NP. When the pH was raised to 7.0, Fe^{3+} polyphosphate was redistributed to give NHHS Fe^{3+} and NP. From these studies, we concluded that vacuolar Fe is stored as NHHS Fe^{3+} with a polyphosphate-like ligand in low pH conditions. An increase in the vacuolar pH induces a shift from NHHS Fe^{3+} to NP.

We also investigated strains where the vacuolar Fe import protein, Ccc1p, was deleted or was overexpressed (Chapter IV). These strains were made in DY150 cells, which have a W303 background. The DY150 strain contained more NP than W303-1B cells, which could result from a slightly higher vacuolar pH in DY150 cells.

Kaplan, et al., proposed that there is a common pool of cytosolic Fe that is shared between the mitochondria and the vacuoles (Li, 2004). In conditions where Ccc1p is absent (ΔCCC1) this cytosolic Fe pool accumulates and vacuolar Fe declines. We observed that Δ*CCC1* cells contained more NHHS Fe^{2+} and less vacuolar NHHS Fe^{3+} than WT cells.

MB of mitochondria isolated from Δ*CCC1* cells showed overall higher Fe concentrations and ~2x higher levels of NHHS Fe^{2+} compared with WT, which suggested that accumulation of cytosolic Fe promotes mitochondrial Fe accumulation. This was consistent with the Kaplan hypothesis that the mitochondria and vacuoles share a common Fe pool. We proposed that the NHHS Fe^{2+} which accumulates in Δ*CCC1* cells is cytosolic.

The Ccc1p-overexpression strain was also investigated in Chapter IV. *CCC1-up* cells showed increased levels of NHHS Fe^{3+} and NP compared with WT cells. Both NHHS Fe^{3+} and NP were previously observed in isolated vacuoles, which indicated that the vacuolar Fe was elevated with Ccc1p overexpression. Vacuoles isolated from *CCC1-up* cells primarily contained NP (> 80%), which indicated that the vacuolar pH was lower in *CCC1-up* cells than in WT cells. We proposed that the vacuolar pH increases in this strain due to excess Fe import and H^+ export.

The *CCC1-up* cells also showed a surprisingly high concentration of NHHS Fe^{2+}. Δ*CCC1* cells also showed an accumulation of NHHS Fe^{2+}, but the overall Fe concentration was lower than WT, which indicated that this Fe was sensed by the cell. *CCC1-up* cells accumulated ~3x more total Fe and ~10x more NHHS Fe^{2+} than WT, which suggested that the Fe import was not shut down in this case. We proposed that the NHHS Fe^{2+} that accumulated in *CCC1-up* cells was sequestered such that it was not sensed by Aft1p.

CCC1-up cells also demonstrated an adenine deficient (AD) phenotype, which leads to the accumulation of a red pigment in the vacuoles. Previous studies on AD WT cells have been conducted by Mr. Jinkyu Park, a graduate student in the Lindahl lab. In low-adenine grown WT cells an accumulation of NHHS Fe^{2+} was also observed. In *CCC1-up* cells, when the medium adenine concentration was raised 2-fold (UP2x40) the *CCC1-up* cells contained less NHHS Fe^{2+} than normal-adenine *CCC1-up* cells. This showed that the accumulation of NHHS Fe^{2+} was most likely related to adenine

deficiency, which could promote a more reducing vacuolar environment. The mechanism for this process was summarized in the model proposed in Chapter IV.

We also hypothesized that the accumulation of NP in *CCC1-up* cells could be related to elevated vacuolar pH. To investigate this, WT cells were treated with ConA to inhibit the V^{+}-ATPase. WT cells treated in this manner showed a Fe distribution very similar to *CCC1-up* cells. This indicated that maintaining a low vacuolar pH influences NHHS Fe^{3+} levels, and that disrupting this system results in the formation of NHHS Fe^{2+} and NP. These experiments led us to develop a predictive mathematical model, which summarizes the effects of vacuolar pH and redox status on intracellular Fe distributions. Overall, these studies demonstrated that the vacuoles play an important role in cellular Fe homeostasis. The pH and redox environments of these cellular compartments must be maintained in order to properly utilize, traffic, and store intracellular Fe.

CHAPTER VI

FUTURE WORK

Vacuoles are central in maintaining intracellular Fe homeostasis, and the studies presented here have demonstrated that changes in the vacuolar environment leads to a disruption of intracellular Fe distributions. In Chapter IV, cells were treated with concanamycin A to inhibit the V^+-ATPase and to study changes in intracellular Fe distributions. It would be interesting to investigate how Fe distributions change in mutants which are deficient in vacuolar acidification (*i.e., vma* mutants). The Vma proteins are essential for proper V^+-ATPase assembly and function, and have shown alterations in Fe homeostasis *(149, 189, 190)*. These cells sense Fe deficiency and activate Aft1p, which elevates cellular Fe import. It would be interesting to determine if these cells show similar Fe distributions to other strains which have been investigated-particularly *CCC1-up*. We expect the *vma* and *CCC1-up* cells to be similar based on the ConA studies presented in Chapter IV of this dissertation. These studies could reveal information about how intracellular Fe distributions change when the vacuolar pH is disrupted, and may provide further support for the model proposed in Chapter IV.

The form(s) of Fe which is(are) transported via Ccc1p into the vacuoles has(have) not been identified, but some groups suggest that molecules like glutathione or 2,5-DHBA could be responsible for intracellular Fe trafficking *(24)*. It would be interesting to incubate isolated vacuoles with these different Fe-bound molecules to determine if Fe could accumulate in isolated vacuoles. Because ICP-MS is able to detect different isotopes, this could be done using ^{56}Fe and ^{57}Fe, which are readily available in

the Lindahl laboratory. These studies could provide some information about the specificity of Ccc1p and potentially give information about the components of the cytosolic LIP. These studies could also be performed with isolated mitochondria, to determine if the same species taken up by vacuoles could be brought in to the mitochondria. If one (or more) of these species are transported into the mitochondria and the vacuoles, this would provide further evidence that the vacuoles and the mitochondria share a common pool of Fe in the cytosol.

The composition of the cytosolic LIP must be determined in order to fully understand intracellular Fe trafficking. Currently, LC-ICP-MS studies are being conducted with the WT and Δ*CCC1* strains. At this time, the lack of reproducibility of the Fe traces in these experiments has revealed the complications involved in isolating *labile* Fe trafficking complexes. In the studies presented in this dissertation, we have suggested that redox and pH effects can alter the distribution of intracellular Fe complexes which may or may not be involved in trafficking. LC-ICP-MS separations experiments could be used to determine if the concentrations of Fe species in whole cells change with various redox or pH conditions.

Additional experiments could also be used to determine the composition of the cytosolic LIP. For example, a protocol to isolate cytosol (mostly free of vacuolar components) could be developed. Current protocols in which "cytosol" is isolated involve harsh lysis procedures with glass beads or sonication. These techniques result in soluble lysate fractions, but are most likely contaminated with vacuolar and/or mitochondrial material which could be released during lysis. We have shown in Chapter

III that the vacuoles are very delicate organelles that must be isolated with a gentle lysis procedure. Therefore, to obtain a more purified cytosolic fraction a gentler lysis method could be employed. For example, mammalian cells are typically lysed using N_2 cavitation. This technique is used for isolating mammalian lysosomes, which are structurally and functionally similar to the yeast vacuoles *(102)*. Isolating these delicate organelles in this manner demonstrates a possible way to isolate cytosol from yeast cells. The yeast cells could be treated to form spheroplasts, resuspended in a minimal amount of buffer, and lysed with N_2 cavitation. The resulting lysate fraction would most likely contain intact organelles, which could be separated from the cytosolic fraction by differential centrifugation.

Iron metabolism is related to many cellular processes, and there are various studies which have provided genetic, molecular, biochemical, and biophysical information about intracellular Fe trafficking. The studies presented here have provided insight into vacuolar Fe dynamics and metabolism which had not been previously observed. There are many questions that remain, but the information gained from these studies has provided a more complete picture of vacuolar Fe distributions and trafficking.

REFERENCES

1. Kobayashi, T., and Nishizawa, N. K. (2012) Iron uptake, translocation, and regulation in higher plants, *Annu Rev Plant Biol 63*, 131-152.
2. Beinert, H. (2002) Spectroscopy of succinate dehydrogenases, a historical perspective, *Biochim Biophys Acta 1553*, 7-22.
3. Raha, S., McEachern, G. E., Myint, A. T., and Robinson, B. H. (2000) Superoxides from mitochondrial complex III: the role of manganese superoxide dismutase, *Free Radic Biol Med 29*, 170-180.
4. Zitomer, R. S., Montgomery, D. L., Nichols, D. L., and Hall, B. D. (1979) Transcriptional regulation of the yeast cytochrome c gene, *Proc Natl Acad Sci U S A 76*, 3627-3631.
5. Beinert, H., and Kennedy, M. C. (1993) Aconitase, a two-faced protein: enzyme and iron regulatory factor, *Faseb J 7*, 1442-1449.
6. Beinert, H., Kennedy, M. C., and Stout, C. D. (1996) Aconitase as iron-sulfur protein, enzyme, and iron-regulatory protein, *Chem Rev 96*, 2335-2374.
7. Flint, D. H., and Allen, R. M. (1996) Iron-sulfur proteins with nonredox functions, *Chem Rev 96*, 2315-2334.
8. Alseth, I., Eide, L., Pirovano, M., Rognes, T., Seeberg, E., and Bjoras, M. (1999) The *Saccharomyces cerevisiae* homologues of endonuclease III from *Escherichia coli*, Ntg1 and Ntg2, are both required for efficient repair of spontaneous and induced oxidative DNA damage in yeast, *Mol Cell Biol 19*, 3779-3787.

9. Boal, A. K., Yavin, E., and Barton, J. K. (2007) DNA repair glycosylases with a [4Fe-4S] cluster: a redox cofactor for DNA-mediated charge transport?, *J Inorg Biochem 101*, 1913-1921.

10. Klinge, S., Hirst, J., Maman, J. D., Krude, T., and Pellegrini, L. (2007) An iron-sulfur domain of the eukaryotic primase is essential for RNA primer synthesis, *Nat Struct Mol Biol 14*, 875-877.

11. Lukianova, O. A., and David, S. S. (2005) A role for iron-sulfur clusters in DNA repair, *Curr Opin Chem Biol 9*, 145-151.

12. Crichton, R. R., and Pierre, J. L. (2001) Old iron, young copper: from Mars to Venus, *Biometals 14*, 99-112.

13. Fenton, H. J. H. (1902) Oxidation in presence of iron, *P Camb Philos Soc 11*, 358-374.

14. Drake, I. M., Mapstone, N. P., Schorah, C. J., White, K. L., Chalmers, D. M., Dixon, M. F., and Axon, A. T. (1998) Reactive oxygen species activity and lipid peroxidation in *Helicobacter pylori* associated gastritis: relation to gastric mucosal ascorbic acid concentrations and effect of *H. pylori* eradication, *Gut 42*, 768-771.

15. Irazusta, V., Moreno-Cermeno, A., Cabiscol, E., Ros, J., and Tamarit, J. (2008) Major targets of iron-induced protein oxidative damage in frataxin-deficient yeasts are magnesium-binding proteins, *Free Radic Biol Med 44*, 1712-1723.

16. Wiseman, H., and Halliwell, B. (1996) Damage to DNA by reactive oxygen and nitrogen species: role in inflammatory disease and progression to cancer, *Biochem J 313 (Pt 1)*, 17-29.

17. Lin, Y., Epstein, D. L., and Liton, P. B. (2010) Intralysosomal iron induces lysosomal membrane permeabilization and cathepsin D-mediated cell death in trabecular meshwork cells exposed to oxidative stress, *Invest Ophthalmol Vis Sci 51*, 6483-6495.

18. Dixon, S. J., Lemberg, K. M., Lamprecht, M. R., Skouta, R., Zaitsev, E. M., Gleason, C. E., Patel, D. N., Bauer, A. J., Cantley, A. M., Yang, W. S., Morrison, B., 3rd, and Stockwell, B. R. (2012) Ferroptosis: an iron-dependent form of nonapoptotic cell death, *Cell 149*, 1060-1072.

19. Askwith, C., Eide, D., Van Ho, A., Bernard, P. S., Li, L., Davis-Kaplan, S., Sipe, D. M., and Kaplan, J. (1994) The FET3 gene of *S. cerevisiae* encodes a multicopper oxidase required for ferrous iron uptake, *Cell 76*, 403-410.

20. Stearman, R., Yuan, D. S., Yamaguchi-Iwai, Y., Klausner, R. D., and Dancis, A. (1996) A permease-oxidase complex involved in high-affinity iron uptake in yeast, *Science 271*, 1552-1557.

21. Haas, H. (2003) Molecular genetics of fungal siderophore biosynthesis and uptake: the role of siderophores in iron uptake and storage, *Appl Microbiol Biotechnol 62*, 316-330.

22. Tomai, F., Pesarini, G., Castriota, F., Reimers, B., De Luca, L., De Persio, G., Sparta, D., Aurigemma, C., Pacchioni, A., Spagnolo, B., Cremonesi, A., and

Ribichini, F. (2011) Early and long-term outcomes after combined percutaneous revascularization in patients with carotid and coronary artery stenoses, *JACC Cardiovasc Interv 4*, 560-568.

23. Johnson, L. (2008) Iron and siderophores in fungal-host interactions, *Mycological Research 112*, 170-183.

24. Hider, R. C., and Kong, X. (2013) Iron speciation in the cytosol: an overview, *Dalton transactions 42*, 3220-3229.

25. Martins, L. J., Jensen, L. T., Simon, J. R., Keller, G. L., and Winge, D. R. (1998) Metalloregulation of FRE1 and FRE2 homologs in *Saccharomyces cerevisiae*, *J Biol Chem 273*, 23716-23721.

26. Shi, X., Stoj, C., Romeo, A., Kosman, D. J., and Zhu, Z. (2003) Fre1p Cu2+ reduction and Fet3p Cu1+ oxidation modulate copper toxicity in *Saccharomyces cerevisiae*, *J Biol Chem 278*, 50309-50315.

27. Lesuisse, E., Raguzzi, F., and Crichton, R. R. (1987) Iron uptake by the yeast *Saccharomyces cerevisiae*: involvement of a reduction step, *J Gen Microbiol 133*, 3229-3236.

28. Wang, T. P., Quintanar, L., Severance, S., Solomon, E. I., and Kosman, D. J. (2003) Targeted suppression of the ferroxidase and iron trafficking activities of the multicopper oxidase Fet3p from Saccharomyces cerevisiae, *J Biol Inorg Chem 8*, 611-620.

29. Ehmann, W. C., Dancis, A., Ferziger, R., and Karpatkin, S. (1990) Posttransfusion purpura: conversion of PLA1-negative platelets to the PLA1-

positive phenotype by stored plasma is not due to the presence of soluble PLA1 antigen, *Proc Soc Exp Biol Med 195*, 192-196.

30. Philpott, C. C. (2006) Iron uptake in fungi: a system for every source, *Biochim Biophys Acta 1763*, 636-645.

31. Holmes-Hampton, G. P., Jhurry, N. D., McCormick, S. P., and Lindahl, P. A. (2013) Iron content of *Saccharomyces cerevisiae* cells grown under iron-deficient and iron-overload conditions, *Biochemistry-Us 52*, 105-114.

32. Felice, M. R., De Domenico, I., Li, L., Ward, D. M., Bartok, B., Musci, G., and Kaplan, J. (2005) Post-transcriptional regulation of the yeast high affinity iron transport system, *J Biol Chem 280*, 22181-22190.

33. Kwok, E. Y., Severance, S., and Kosman, D. J. (2006) Evidence for iron channeling in the Fet3p-Ftr1p high-affinity iron uptake complex in the yeast plasma membrane, *Biochemistry-Us 45*, 6317-6327.

34. Severance, S., Chakraborty, S., and Kosman, D. J. (2004) The Ftr1p iron permease in the yeast plasma membrane: orientation, topology and structure-function relationships, *Biochemical Journal 380*, 487-496.

35. Singh, A., Severance, S., Kaur, N., Wiltsie, W., and Kosman, D. J. (2006) Assembly, activation, and trafficking of the Fet3p.Ftr1p high affinity iron permease complex in Saccharomyces cerevisiae, *J Biol Chem 281*, 13355-13364.

36. Waters, B. M., and Eide, D. J. (2002) Combinatorial control of yeast FET4 gene expression by iron, zinc, and oxygen, *J Biol Chem 277*, 33749-33757.

37. Jensen, L. T., and Culotta, V. C. (2002) Regulation of *Saccharomyces cerevisiae* FET4 by oxygen and iron, *Journal of molecular biology 318*, 251-260.

38. Chen, X. Z., Peng, J. B., Cohen, A., Nelson, H., Nelson, N., and Hediger, M. A. (1999) Yeast SMF1 mediates H(+)-coupled iron uptake with concomitant uncoupled cation currents, *J Biol Chem 274*, 35089-35094.

39. Cohen, A., Nelson, H., and Nelson, N. (2000) The family of SMF metal ion transporters in yeast cells, *J Biol Chem 275*, 33388-33394.

40. Portnoy, M. E., Liu, X. F., and Culotta, V. C. (2000) *Saccharomyces cerevisiae* expresses three functionally distinct homologues of the nramp family of metal transporters, *Molecular and Cellular Biology 20*, 7893-7902.

41. Skordis-Worrall, J., Pace, N., Bapat, U., Das, S., More, N. S., Joshi, W., Pulkki-Brannstrom, A. M., and Osrin, D. (2011) Maternal and neonatal health expenditure in Mumbai slums (India): a cross sectional study, *BMC Public Health 11*, 150.

42. Kmetik, K. S., O'Toole, M. F., Bossley, H., Brutico, C. A., Fischer, G., Grund, S. L., Gulotta, B. M., Hennessey, M., Kahn, S., Murphy, K. M., Pacheco, T., Pawlson, L. G., Schaeffer, J., Schwamberger, P. A., Scholle, S. H., and Wozniak, G. (2011) Exceptions to outpatient quality measures for coronary artery disease in electronic health records, *Ann Intern Med 154*, 227-234.

43. Ramirez, A., Pacchia, C. F., Sanders, N. A., Wasmund, S. L., and Hamdan, M. H. (2012) The effects of radio-frequency ablation on blood pressure control in

patients with atrial fibrillation and hypertension, *J Interv Card Electrophysiol 35*, 285-291; discussion 291.

44. Jensen, L. T., and Culotta, V. C. (2002) Regulation of *Saccharomyces cerevisiae* FET4 by oxygen and iron, *J Mol Biol 318*, 251-260.

45. Cyert, M. S., and Philpott, C. C. (2013) Regulation of Cation Balance in *Saccharomyces cerevisiae*, *Genetics 193*, 677-713.

46. Yamaguchi-Iwai, Y., Dancis, A., and Klausner, R. D. (1995) AFT1: a mediator of iron regulated transcriptional control in *Saccharomyces cerevisiae*, *Embo J 14*, 1231-1239.

47. Hassett, R. F., Romeo, A. M., and Kosman, D. J. (1998) Regulation of high affinity iron uptake in the yeast *Saccharomyces cerevisiae*. Role of dioxygen and Fe, *J Biol Chem 273*, 7628-7636.

48. Jacobs, A. (1977) Low molecular weight intracellular iron transport compounds, *Blood 50*, 433-439.

49. Williams, R. J. (1982) Free manganese (II) and iron (II) cations can act as intracellular cell controls, *FEBS Lett 140*, 3-10.

50. Petrat, F., de Groot, H., and Rauen, U. (2001) Subcellular distribution of chelatable iron: a laser scanning microscopic study in isolated hepatocytes and liver endothelial cells, *Biochemical Journal 356*, 61-69.

51. Egyed, A., and Saltman, P. (1984) Iron is maintained as Fe(II) under aerobic conditions in erythroid cells, *Biological Trace Element Research 6*, 357-364.

52. Weaver, J., Pollack, S., and Zhan, H. (1989) Low molecular weight iron from guinea pig reticulocytes isolated by Sephadex G-25 chromatography, *Eur J Haematol 43*, 321-327.

53. Veiga, N., Torres, J., Mansell, D., Freeman, S., Dominguez, S., Barker, C. J., Diaz, A., and Kremer, C. (2009) "Chelatable iron pool": inositol 1,2,3-trisphosphate fulfils the conditions required to be a safe cellular iron ligand, *J Biol Inorg Chem 14*, 51-59.

54. Devireddy, L. R., Hart, D. O., Goetz, D. H., and Green, M. R. (2010) A mammalian siderophore synthesized by an enzyme with a bacterial homolog involved in enterobactin production, *Cell 141*, 1006-1017.

55. Hider, R. C., and Kong, X. L. (2011) Glutathione: a key component of the cytoplasmic labile iron pool, *Biometals 24*, 1179-1187.

56. Que, E. L., Domaille, D. W., and Chang, C. J. (2008) Metals in neurobiology: Probing their chemistry and biology with molecular imaging (vol 108, pg 1517, 2008), *Chem Rev 108*, 4328-4328.

57. Okamoto, K., and Shaw, J. M. (2005) Mitochondrial morphology and dynamics in yeast and multicellular eukaryotes, *Annu Rev Genet 39*, 503-536.

58. Foury, F., and Roganti, T. (2002) Deletion of the mitochondrial carrier genes MRS3 and MRS4 suppresses mitochondrial iron accumulation in a yeast frataxin-deficient strain, *J Biol Chem 277*, 24475-24483.

59. Muhlenhoff, U., Stadler, J. A., Richhardt, N., Seubert, A., Eickhorst, T., Schweyen, R. J., Lill, R., and Wiesenberger, G. (2003) A specific role of the

yeast mitochondrial carriers MRS3/4p in mitochondrial iron acquisition under iron-limiting conditions, *J Biol Chem 278*, 40612-40620.

60. Zhang, Y., Lyver, E. R., Knight, S. A., Pain, D., Lesuisse, E., and Dancis, A. (2006) Mrs3p, Mrs4p, and frataxin provide iron for Fe-S cluster synthesis in mitochondria, *J Biol Chem 281*, 22493-22502.

61. Froschauer, E. M., Schweyen, R. J., and Wiesenberger, G. (2009) The yeast mitochondrial carrier proteins Mrs3p/Mrs4p mediate iron transport across the inner mitochondrial membrane, *Biochim Biophys Acta 1788*, 1044-1050.

62. Yoon, H., Zhang, Y., Pain, J., Lyver, E. R., Lesuisse, E., Pain, D., and Dancis, A. (2011) Rim2, a pyrimidine nucleotide exchanger, is needed for iron utilization in mitochondria, *Biochem J 440*, 137-146.

63. Lange, H., Kispal, G., and Lill, R. (1999) Mechanism of iron transport to the site of heme synthesis inside yeast mitochondria, *J Biol Chem 274*, 18989-18996.

64. Shaw, G. C., Cope, J. J., Li, L., Corson, K., Hersey, C., Ackermann, G. E., Gwynn, B., Lambert, A. J., Wingert, R. A., Traver, D., Trede, N. S., Barut, B. A., Zhou, Y., Minet, E., Donovan, A., Brownlie, A., Balzan, R., Weiss, M. J., Peters, L. L., Kaplan, J., Zon, L. I., and Paw, B. H. (2006) Mitoferrin is essential for erythroid iron assimilation, *Nature 440*, 96-100.

65. Hill, J. S., Pace, T. M., and Robbins, R. R. (2010) Decolonizing personality assessment and honoring indigenous voices: a critical examination of the MMPI-2, *Cultur Divers Ethnic Minor Psychol 16*, 16-25.

66. Marobbio, C. M., Di Noia, M. A., and Palmieri, F. (2006) Identification of a mitochondrial transporter for pyrimidine nucleotides in *Saccharomyces cerevisiae*: bacterial expression, reconstitution and functional characterization, *Biochem J 393*, 441-446.

67. Lin, H., Li, L., Jia, X., Ward, D. M., and Kaplan, J. (2011) Genetic and biochemical analysis of high iron toxicity in yeast: iron toxicity is due to the accumulation of cytosolic iron and occurs under both aerobic and anaerobic conditions, *J Biol Chem 286*, 3851-3862.

68. Tangeras, A., Flatmark, T., Backstrom, D., and Ehrenberg, A. (1980) Mitochondrial iron not bound in heme and iron-sulfur centers. Estimation, compartmentation and redox state, *Biochim Biophys Acta 589*, 162-175.

69. Petrat, F., de Groot, H., Sustmann, R., and Rauen, U. (2002) The chelatable iron pool in living cells: a methodically defined quantity, *Biol Chem 383*, 489-502.

70. Holmes-Hampton, G. P., Miao, R., Garber Morales, J., Guo, Y., Munck, E., and Lindahl, P. A. (2010) A nonheme high-spin ferrous pool in mitochondria isolated from fermenting *Saccharomyces cerevisiae*, *Biochemistry-Us 49*, 4227-4234.

71. Lesuisse, E., Santos, R., Matzanke, B. F., Knight, S. A., Camadro, J. M., and Dancis, A. (2003) Iron use for haeme synthesis is under control of the yeast frataxin homologue (Yfh1), *Hum Mol Genet 12*, 879-889.

72. Miao, R., Kim, H., Koppolu, U. M., Ellis, E. A., Scott, R. A., and Lindahl, P. A. (2009) Biophysical characterization of the iron in mitochondria from Atm1p-depleted *Saccharomyces cerevisiae*, *Biochemistry-Us 48*, 9556-9568.

73. Miao, R., Holmes-Hampton, G. P., and Lindahl, P. A. (2011) Biophysical investigation of the iron in Aft1-1(up) and Gal-YAH1 *Saccharomyces cerevisiae*, *Biochemistry-Us 50*, 2660-2671.

74. Miao, R., Martinho, M., Morales, J. G., Kim, H., Ellis, E. A., Lill, R., Hendrich, M. P., Munck, E., and Lindahl, P. A. (2008) EPR and Mossbauer spectroscopy of intact mitochondria isolated from Yah1p-depleted *Saccharomyces cerevisiae*, *Biochemistry-Us 47*, 9888-9899.

75. Lill, R., Hoffmann, B., Molik, S., Pierik, A. J., Rietzschel, N., Stehling, O., Uzarska, M. A., Webert, H., Wilbrecht, C., and Muhlenhoff, U. (2012) The role of mitochondria in cellular iron-sulfur protein biogenesis and iron metabolism, *Biochim Biophys Acta 1823*, 1491-1508.

76. Tsai, C. L., and Barondeau, D. P. (2010) Human frataxin is an allosteric switch that activates the Fe-S cluster biosynthetic complex, *Biochemistry-Us 49*, 9132-9139.

77. Wang, T., and Craig, E. A. (2008) Binding of yeast frataxin to the scaffold for Fe-S cluster biogenesis, Isu, *J Biol Chem 283*, 12674-12679.

78. Bencze, K. Z., Kondapalli, K. C., Cook, J. D., McMahon, S., Millan-Pacheco, C., Pastor, N., and Stemmler, T. L. (2006) The structure and function of frataxin, *Crit Rev Biochem Mol Biol 41*, 269-291.

79. Gerber, J., Muhlenhoff, U., and Lill, R. (2003) An interaction between frataxin and Isu1/Nfs1 that is crucial for Fe/S cluster synthesis on Isu1, *EMBO Rep 4*, 906-911.

80. Babcock, M., de Silva, D., Oaks, R., Davis-Kaplan, S., Jiralerspong, S., Montermini, L., Pandolfo, M., and Kaplan, J. (1997) Regulation of mitochondrial iron accumulation by Yfh1p, a putative homolog of frataxin, *Science 276*, 1709-1712.

81. Beinert, H., Holm, R. H., and Munck, E. (1997) Iron-sulfur clusters: nature's modular, multipurpose structures, *Science 277*, 653-659.

82. Zheng, L., White, R. H., Cash, V. L., and Dean, D. R. (1994) Mechanism for the desulfurization of L-cysteine catalyzed by the nifS gene product, *Biochemistry-Us 33*, 4714-4720.

83. Kaiser, J. T., Clausen, T., Bourenkow, G. P., Bartunik, H. D., Steinbacher, S., and Huber, R. (2000) Crystal structure of a NifS-like protein from Thermotoga maritima: implications for iron sulphur cluster assembly, *J Mol Biol 297*, 451-464.

84. Pandey, A., Yoon, H., Lyver, E. R., Dancis, A., and Pain, D. (2011) Isd11p protein activates the mitochondrial cysteine desulfurase Nfs1p protein, *J Biol Chem 286*, 38242-38252.

85. Coleman, R., Wharton, D., and Rieske, J. S. (1964) Effects of P-Chloromercuriphenyl Sulfonate on Isolated Nonheme Iron-Protein from Beef Heart Mitochondria, *Fed Proc 23*, 323-&.

86. Lange, H., Kaut, A., Kispal, G., and Lill, R. (2000) A mitochondrial ferredoxin is essential for biogenesis of cellular iron-sulfur proteins, *Proc Natl Acad Sci U S A 97*, 1050-1055.

87. Li, J., Saxena, S., Pain, D., and Dancis, A. (2001) Adrenodoxin reductase homolog (Arh1p) of yeast mitochondria required for iron homeostasis, *J Biol Chem 276*, 1503-1509.

88. Manzella, L., Barros, M. H., and Nobrega, F. G. (1998) ARH1 of *Saccharomyces cerevisiae*: a new essential gene that codes for a protein homologous to the human adrenodoxin reductase, *Yeast 14*, 839-846.

89. Schilke, B., Voisine, C., Beinert, H., and Craig, E. (1999) Evidence for a conserved system for iron metabolism in the mitochondria of *Saccharomyces cerevisiae*, *Proc Natl Acad Sci U S A 96*, 10206-10211.

90. Muhlenhoff, U., Gerber, J., Richhardt, N., and Lill, R. (2003) Components involved in assembly and dislocation of iron-sulfur clusters on the scaffold protein Isu1p, *Embo J 22*, 4815-4825.

91. Garland, S. A., Hoff, K., Vickery, L. E., and Culotta, V. C. (1999) *Saccharomyces cerevisiae* ISU1 and ISU2: members of a well-conserved gene family for iron-sulfur cluster assembly, *J Mol Biol 294*, 897-907.

92. Dutkiewicz, R., Marszalek, J., Schilke, B., Craig, E. A., Lill, R., and Muhlenhoff, U. (2006) The Hsp70 chaperone Ssq1p is dispensable for iron-sulfur cluster formation on the scaffold protein Isu1p, *J Biol Chem 281*, 7801-7808.

93. Ikeda, E., Yoshida, S., Mitsuzawa, H., Uno, I., and Toh-e, A. (1994) YGE1 is a yeast homologue of Escherichia coli grpE and is required for maintenance of mitochondrial functions, *Febs Lett 339*, 265-268.

94. Rodriguez-Manzaneque, M. T., Tamarit, J., Belli, G., Ros, J., and Herrero, E. (2002) Grx5 is a mitochondrial glutaredoxin required for the activity of iron/sulfur enzymes, *Mol Biol Cell 13*, 1109-1121.

95. Atamna, H. (2004) Heme, iron, and the mitochondrial decay of ageing, *Ageing Res Rev 3*, 303-318.

96. Camadro, J. M., and Labbe, P. (1988) Purification and properties of ferrochelatase from the yeast *Saccharomyces cerevisiae*. Evidence for a precursor form of the protein, *J Biol Chem 263*, 11675-11682.

97. Mogi, T., Saiki, K., and Anraku, Y. (1994) Biosynthesis and functional role of haem O and haem A, *Mol Microbiol 14*, 391-398.

98. Dumont, M. E., Cardillo, T. S., Hayes, M. K., and Sherman, F. (1991) Role of cytochrome c heme lyase in mitochondrial import and accumulation of cytochrome c in *Saccharomyces cerevisiae*, *Mol Cell Biol 11*, 5487-5496.

99. Li, S. C., and Kane, P. M. (2009) The yeast lysosome-like vacuole: endpoint and crossroads, *Biochim Biophys Acta 1793*, 650-663.

100. Plant, P. J., Manolson, M. F., Grinstein, S., and Demaurex, N. (1999) Alternative mechanisms of vacuolar acidification in H(+)-ATPase-deficient yeast, *J Biol Chem 274*, 37270-37279.

101. Martinez-Munoz, G. A., and Kane, P. (2008) Vacuolar and plasma membrane proton pumps collaborate to achieve cytosolic pH homeostasis in yeast, *J Biol Chem 283*, 20309-20319.

102. Li, S. C., and Kane, P. M. (2009) The yeast lysosome-like vacuole: Endpoint and crossroads, *Bba-Mol Cell Res 1793*, 650-663.

103. Li, L., Chen, O. S., McVey Ward, D., and Kaplan, J. (2001) CCC1 is a transporter that mediates vacuolar iron storage in yeast, *J Biol Chem 276*, 29515-29519.

104. Li, L., Bagley, D., Ward, D. M., and Kaplan, J. (2008) Yap5 is an iron-responsive transcriptional activator that regulates vacuolar iron storage in yeast, *Mol Cell Biol 28*, 1326-1337.

105. Puig, S., Askeland, E., and Thiele, D. J. (2005) Coordinated remodeling of cellular metabolism during iron deficiency through targeted mRNA degradation, *Cell 120*, 99-110.

106. Moreno, S. N. J., and Docampo, R. (2013) Polyphosphate and its diverse Functions in Host Cells and Pathogens, *Plos Pathogens 9*, 1-3.

107. Kornberg, A., Rao, N. N., and Ault-Riche, D. (1999) Inorganic polyphosphate: A molecule of many functions, *Annu Rev Biochem 68*, 89-125.

108. Urech, K., Durr, M., Boller, T., Wiemken, A., and Schwencke, J. (1978) Localization of polyphosphate in vacuoles of *Saccharomyces cerevisiae*, *Arch Microbiol 116*, 275-278.

109. Wiame, J. M. (1947) The metachromatic reaction of hexametaphosphate, *J Am Chem Soc 69*, 3146-3147.

110. Urbanowski, J. L., and Piper, R. C. (1999) The iron transporter Fth1p forms a complex with the Fet5 iron oxidase and resides on the vacuolar membrane, *J Biol Chem 274*, 38061-38070.

111. Portnoy, M. E., Liu, X. F., and Culotta, V. C. (2000) *Saccharomyces cerevisiae* expresses three functionally distinct homologues of the nramp family of metal transporters, *Mol Cell Biol 20*, 7893-7902.

112. Cockrell, A. L., Holmes-Hampton, G. P., McCormick, S. P., Chakrabarti, M., and Lindahl, P. A. (2011) Mossbauer and EPR study of iron in vacuoles from fermenting *Saccharomyces cerevisiae*, *Biochemistry-Us 50*, 10275-10283.

113. V, M., A, T. D., Jm, H., Pa, N., and Bl, S. (2013) Lifestyle factors and the risk of a Second Breast Diagnosis after DCIS in the Wisconsin In Situ Cohort, *Cancer Epidemiol Biomarkers Prev 22*, 472.

114. Wilde, B., Thewissen, M., Damoiseaux, J., Knippenberg, S., Hilhorst, M., van Paassen, P., Witzke, O., and Cohen Tervaert, J. W. (2013) Regulatory B cells in ANCA-associated vasculitis, *Ann Rheum Dis*.

115. Pacheco, J. M., Gao, F., Bumb, C., Ellis, M. J., and Ma, C. X. (2013) Racial differences in outcomes of triple-negative breast cancer, *Breast Cancer Res Treat 138*, 281-289.

116. Rossi, I. A., Rousson, V., and Paccaud, F. (2013) The contribution of rectangularization to the secular increase of life expectancy: an empirical study, *Int J Epidemiol 42*, 250-258.

117. Rana, M. M., Huhtala, H., Apter, D., Eriksson, T., Luostarinen, T., Natunen, K., Paavonen, J., Pukkala, E., and Lehtinen, M. (2013) Understanding long-term protection of human papillomavirus vaccination against cervical carcinoma: Cancer registry-based follow-up, *Int J Cancer 132*, 2833-2838.

118. De la Torre, A., Pacepavicius, G., Martinez, M. A., Darling, C., Muir, D., Sherry, J., McMaster, M., and Alaee, M. (2013) Polybrominated diphenyl ethers and their methoxylated and hydroxylated analogs in Brown Bullhead (Ameiurus nebulosus) plasma from Lake Ontario, *Chemosphere 90*, 1644-1651.

119. Mossman, J. A., Pearson, J. T., Moore, H. D., and Pacey, A. A. (2013) Variation in mean human sperm length is linked with semen characteristics, *Hum Reprod 28*, 22-32.

120. Hawley, K. A., Pabon, S., Hoschar, A. P., and Sindwani, R. (2013) The presentation and clinical significance of sinonasal respiratory epithelial adenomatoid hamartoma (REAH), *Int Forum Allergy Rhinol 3*, 248-253.

121. Salminen-Tuomaala, M., Astedt-Kurki, P., Rekiaro, M., and Paavilainen, E. (2013) Spouses' coping alongside myocardial infarction patients, *Eur J Cardiovasc Nurs 12*, 242-251.

122. Portnoy, M. E., Liu, X. F., and Culotta, V. C. (2000) *Saccharomyces cerevisiae* expresses three functionally distinct homologues of the Nramp family of metal transporters, *Mol Cell Biol 20*, 7893-7902.

123. Ueta, R., Fujiwara, N., Iwai, K., and Yamaguchi-Iwai, Y. (2012) Iron-Induced Dissociation of the Aft1p Transcriptional Regulator from Target Gene Promoters

Is an Initial Event in Iron-Dependent Gene Suppression, *Mol Cell Biol 32*, 4998-5008.

124. Vilella, F., Alves, R., Rodriguez-Manzaneque, M. T., Belli, G., Swaminathan, S., Sunnerhagen, P., and Herrero, E. (2004) Evolution and cellular function of monothiol glutaredoxins: involvement in iron-sulphur cluster assembly, *Comp Funct Genom 5*, 328-341.

125. Lill, R., and Muhlenhoff, U. (2008) Maturation of iron-sulfur proteins in eukaryotes: Mechanisms, connected processes, and diseases, *Annu Rev Biochem 77*, 669-700.

126. Ueta, R., Fujiwara, N., Iwai, K., and Yamaguchi-Iwai, Y. (2007) Mechanism underlying the iron-dependent nuclear export of the iron-responsive transcription factor Aft1p in *Saccharomyces cerevisiae*, *Mol Biol Cell 18*, 2980-2990.

127. Ojeda, L., Keller, G., Muhlenhoff, U., Rutherford, J. C., Lill, R., and Winge, D. R. (2006) Role of glutaredoxin-3 and glutaredoxin-4 in the iron regulation of the Aft1 transcriptional activator in *Saccharomyces cerevisiae*, *J Biol Chem 281*, 17661-17669.

128. Pujol-Carrion, N., Belli, G., Herrero, E., Nogues, A., and de la Torre-Ruiz, M. A. (2006) Glutaredoxins Grx3 and Grx4 regulate nuclear localisation of Aft1 and the oxidative stress response in *Saccharomyces cerevisiae*, *J Cell Sci 119*, 4554-4564.

129. Kumanovics, A., Chen, O. S., Li, L. T., Bagley, D., Adkins, E. M., Lin, H. L., Dingra, N. N., Outten, C. E., Keller, G., Winge, D., Ward, D. M., and Kaplan, J.

(2008) Identification of FRA1 and FRA2 as genes involved in regulating the yeast iron regulon in response to decreased mitochondrial iron-sulfur cluster synthesis, *J Biol Chem 283*, 10276-10286.

130. Philpott, C. C. (2012) Coming into view: eukaryotic iron chaperones and intracellular iron delivery, *J Biol Chem 287*, 13518-13523.

131. Kaplan, C. D., and Kaplan, J. (2009) Iron Acquisition and Transcriptional Regulation, *Chem Rev 109*, 4536-4552.

132. Philpott, C. C., and Protchenko, O. (2008) Response to iron deprivation in *Saccharomyces cerevisiae*, *Eukaryotic Cell 7*, 20-27.

133. Que, L. (2000) *Physical methods in bioinorganic chemistry : spectroscopy and magnetism*, University Science Books, Sausalito, Calif.

134. Berry, E. A., and Trumpower, B. L. (1987) Simultaneous Determination of Hemes-a, Hemes-B, and Hemes-C from Pyridine Hemochrome Spectra, *Anal Biochem 161*, 1-15.

135. Lindahl, P. A., Morales, J. G., Miao, R., and Holmes-Hampton, G. (2009) Isolation of *Saccharomyces cerevisiae* Mitochondria for Mossbauer, EPR, and Electronic Absorption Spectroscopic Analyses, *Method Enzymol 456*, 267-285.

136. Orme-Johnson, N. R., and Orme-Johnson, W. H. (1978) Detection and quantitation of free cytochrome P-450 and cytochrome P-450 complexes by EPR spectroscopy, *Methods Enzymol 52*, 252-257.

137. Morales, J. G., Holmes-Hampton, G. P., Miao, R., Guo, Y. S., Munck, E., and Lindahl, P. A. (2010) Biophysical characterization of iron in mitochondria isolated from respiring and fermenting yeast, *Biochemistry-Us 49*, 5436-5444.

138. Holmes-Hampton, G. P., Jhurry, N. D., McCormick, S. P., and Lindahl, P. A. (2013) Iron content of *Saccharomyces cerevisiae* cells grown under iron-deficient and iron-overload conditions, *Biochemistry 52*, 105-114.

139. Askwith, C., Eide, D., Vanho, A., Bernard, P. S., Li, L. T., Daviskaplan, S., Sipe, D. M., and Kaplan, J. (1994) The Fet3 gene of *Saccharomyces cerevisiae* encodes a multicopper oxidase required for ferrous iron uptake, *Cell 76*, 403-410.

140. Li, L. T., Chen, O. S., Ward, D. M., and Kaplan, J. (2001) CCC1 is a transporter that mediates vacuolar iron storage in yeast, *J Biol Chem 276*, 29515-29519.

141. Li, L., Bagley, D., Ward, D. A., and Kaplan, J. (2008) Yap5 is an iron-responsive transcriptional activator that regulates vacuolar iron storage in yeast, *Mol Cell Biol 28*, 1326-1337.

142. Singh, A., Kaur, N., and Kosman, D. J. (2007) The metalloreductase Fre6p in Fe-Efflux from the yeast vacuole, *J Biol Chem 282*, 28619-28626.

143. Dürr, M., Boller, T., and Wiemken, A. (1975) Polybase induced lysis of yeast spheroplasts - new gentle method for preparation of vacuoles, *Arch Microbiol 105*, 319-327.

144. Smith, P. K., Krohn, R. I., Hermanson, G. T., Mallia, A. K., Gartner, F. H., Provenzano, M. D., Fujimoto, E. K., Goeke, N. M., Olson, B. J., and Klenk, D.

C. (1985) Measurement of protein using bicinchoninic acid, *Anal Biochem 150*, 76-85.

145. Kobayashi, T., Seguchi, H., and Robinson, J. M. (1991) Localization of alkaline-phosphatase activity in human neutrophils, *J Electron Microsc 40*, 208-208.

146. Robinson, J. M. (1985) Improved localization of intracellular sites of phosphatases using cerium and cell permeabilization, *J Histochem Cytochem 33*, 749-754.

147. Kamat, S. S., Bagaria, A., Kumaran, D., Holmes-Hampton, G., Fan, H., Sali, A., Sauder, J. M., Burley, S. K., Lindahl, P. A., Swaminathan, S., and Raushel, F. M. (2011) Catalytic mechanism and three-dimensional structure of adenine deaminase, *Biochemistry 50*, 1917-1927.

148. Jose, J., Loudet, A., Ueno, Y., Barhoumi, R., Burghardt, R. C., and Burgess, K. (2010) Intracellular imaging of organelles with new water-soluble benzophenoxazine dyes, *Org Biomol Chem 8*, 2052-2059.

149. Diab, H. I., and Kane, P. M. (2013) Loss of vacuolar H+-ATPase (V-ATPase) activity in yeast generates an iron deprivation signal that is moderated by induction of the peroxiredoxin TSA2, *Journal of Biological Chemistry 288*, 11366-11377.

150. Li, L. T., Chen, O. S., Ward, D. M., and Kaplan, J. (2001) A yeast vacuolar membrane transporter CCC1 facilitates iron storage, *Mol Biol Cell 12*, 206a-206a.

151. Corson, L. B., Folmer, J., Strain, J. J., Culotta, V. C., and Cleveland, D. W. (1999) Oxidative stress and iron are implicated in fragmenting vacuoles of *Saccharomyces cerevisiae* lacking Cu,Zn-superoxide dismutase, *J Biol Chem 274*, 27590-27596.

152. Raguzzi, F., Lesuisse, E., and Crichton, R. R. (1988) Iron storage in *Saccharomyces cerevisiae*, *Febs Lett 231*, 253-258.

153. Paz, Y., Shimoni, E., Weiss, M., and Pick, U. (2007) Effects of iron deficiency on iron binding and internalization into acidic vacuoles in *Dunaliella salina*, *Plant Physiol 144*, 1407-1415.

154. Pan, B. J., Wu, J., Lv, L., Zhang, W. M., Xiao, L. L., Wang, X. S., Tao, X. C., Zheng, S. R., and Pan, B. C. (2009) Development of polymer-based nanosized hydrated ferric oxides (HFOs) for enhanced phosphate removal from waste effluents, *Water Res 43*, 4421-4429.

155. Rachmilovich-Calis, S., Masarwa, A., Meyerstein, N., and Meyerstein, D. (2011) The effect of pyrophosphate, tripolyphosphate and ATP on the rate of the Fenton reaction, *J Inorg Biochem 105*, 669-674.

156. Fu, D. D., Beeler, T., and Dunn, T. (1994) Sequence, Mapping and disruption of Ccc1, a gene that cross-complements the Ca2+-sensitive phenotype of Csg1 mutants, *Yeast 10*, 515-521.

157. Lapinskas, P. J., Lin, S. J., and Culotta, V. C. (1996) The role of the *Saccharomyces cerevisiae* CCC1 gene in the homeostasis of manganese ions, *Mol Microbiol 21*, 519-528.

158. Lin, H. L., Burton, D., Li, L. T., Warner, D. E., Phillips, J. D., Ward, D. M., and Kaplan, J. (2009) Gain-of-function mutations identify amino acids within transmembrane domains of the yeast vacuolar transporter Zrc1 that determine metal specificity, *Biochemical Journal 422*, 273-283.

159. Urbanowski, J. L., and Piper, R. C. (1999) The iron transporter fth1p forms a complex with the Fet5 iron oxidase and resides on the vacuolar membrane, *J Biol Chem 274*, 38061-38070.

160. Rees, E. M., and Thiele, D. J. (2007) Identification of a vacuole-associated metalloreductase and its role in Ctr2-mediated intracellular copper mobilization, *J Biol Chem 282*, 21629-21638.

161. Cohen, A., Nelson, H., and Nelson, N. (2000) The family of SMF metal ion transporters in yeast cells, *J Biol Chem 275*, 33388-33394.

162. Nelson, N. (1999) Metal ion transporters and homeostasis, *Embo J 18*, 4361-4371.

163. Miao, R., Martinho, M., Morales, J. G., Kim, H., Ellis, E. A., Lill, R., Hendrich, M. P., Münck, E., and Lindahl, P. A. (2008) EPR and Mössbauer spectroscopy of intact mitochondria isolated from Yah1p-depleted *Saccharomyces cerevisiae*, *Biochemistry-Us 47*, 9888-9899.

164. Hudder, B. N., Morales, J. G., Stubna, A., Münck, E., Hendrich, M. P., and Lindahl, P. A. (2007) Electron paramagnetic resonance and Mössbauer spectroscopy of intact mitochondria from respiring *Saccharomyces cerevisiae*, *J Biol Inorg Chem 12*, 1029-1053.

165. Nowalk, A. J., Tencza, S. B., and Mietzner, T. A. (1994) Coordination of Iron by the Ferric Iron-Binding Protein of Pathogenic Neisseria Is Homologous to the Transferrins, *Biochemistry-Us 33*, 12769-12775.

166. Brett, C. L., Kallay, L., Hua, Z. L., Green, R., Chyou, A., Zhang, Y. Q., Graham, T. R., Donowitz, M., and Rao, R. (2011) Genome-Wide Analysis Reveals the Vacuolar pH-Stat of *Saccharomyces cerevisiae*, *Plos One 6*, 1-9.

167. Holmes-Hampton, G. P., Miao, R., Morales, J. G., Guo, Y. S., Münck, E., and Lindahl, P. A. (2010) A Nonheme High-Spin Ferrous Pool in Mitochondria Isolated from Fermenting *Saccharomyces cerevisiae*, *Biochemistry-Us 49*, 4227-4234.

168. Debnath, S., Hausner, D. B., Strongin, D. R., and Kubicki, J. (2010) Reductive dissolution of ferrihydrite by ascorbic acid and the inhibiting effect of phospholipid, *J Colloid Interface Sci 341*, 215-223.

169. Michel, F. M., Ehm, L., Antao, S. M., Lee, P. L., Chupas, P. J., Liu, G., Strongin, D. R., Schoonen, M. A. A., Phillips, B. L., and Parise, J. B. (2007) The structure of ferrihydrite, a nanocrystalline material, *Science 316*, 1726-1729.

170. Arai, Y., and Sparks, D. L. (2001) ATR-FTIR spectroscopic investigation on phosphate adsorption mechanisms at the ferrihydrite-water interface, *J Colloid Interf Sci 241*, 317-326.

171. Khare, N., Martin, J. D., and Hesterberg, D. (2007) Phosphate bonding configuration on ferrihydrite based on molecular orbital calculations and XANES fingerprinting, *Geochim Cosmochim Ac 71*, 4405-4415.

172. Rhoton, F. E., and Bigham, J. M. (2005) Phosphate adsorption by ferrihydrite-amended soils, *J Environ Qual 34*, 890-896.

173. Thibault, P. J., Evans, R. J., Dutrizac, J. E., and Rancourt, D. G. (2009) Mineralogical confirmation of a near-P:Fe=1:2 limiting stoichiometric ratio in colloidal P-bearing ferrihydrite-like hydrous ferric oxide, *Geochim Cosmochim Ac 73*, 364-376.

174. Rancourt, D. G., Thibault, P. J., Evans, R. J., and Dutrizac, J. E. (2009) Mineralogical confirmation of a near-P:Fe=1:2 limiting stoichiometric ratio in colloidal P-bearing ferrihydrite-like hydrous ferric oxide, *Geochim Cosmochim Ac 73*, 364-376.

175. Larese-Casanova, P., Haderlein, S. B., and Kappler, A. (2010) Biomineralization of lepidocrocite and goethite by nitrate-reducing Fe(II)-oxidizing bacteria: Effect of pH, bicarbonate, phosphate, and humic acids, *Geochim Cosmochim Ac 74*, 3721-3734.

176. Shvartsman, M., and Cabantchik, Z. I. (2012) Intracellular iron trafficking: role of cytosolic ligands, *Biometals 25*, 711-723.

177. Yamaguchiiwai, Y., Dancis, A., and Klausner, R. D. (1995) Aft1 - a Mediator of iron-regulated transcriptional control in *Saccharomyces cerevisiae*, *Embo J 14*, 1231-1239.

178. Miao, R., Kim, H., Koppolu, U. M. K., Ellis, E. A., Scott, R. A., and Lindahl, P. A. (2009) Biophysical characterization of the iron in mitochondria from Atm1p-depleted *Saccharomyces cerevisiae*, *Biochemistry-Us 48*, 9556-9568.

179. Spizzo, T., Byersdorfer, C., Duesterhoeft, S., and Eide, D. (1997) The yeast FET5 gene encodes a FET3-related multicopper oxidase implicated in iron transport, *Mol Gen Genet 256*, 547-556.

180. Desilva, D. M., Askwith, C. C., Eide, D., and Kaplan, J. (1995) The Fet3 gene-product required for high-affinity iron transport in yeast is a cell-surface ferroxidase, *J Biol Chem 270*, 1098-1101.

181. Li, L. T., and Kaplan, J. (2004) A mitochondrial-vacuolar signaling pathway in yeast that affects iron and copper metabolism, *J Biol Chem 279*, 33653-33661.

182. Outten, C. E., and Albetel, A. N. (2013) Iron sensing and regulation in *Saccharomyces cerevisiae*: Ironing out the mechanistic details, *Curr Opin Microbiol*.

183. Yamaguchiiwai, Y., Yuan, D. S., Dancis, A., and Klausner, R. D. (1995) Aft1 - activator of ferrous transport regulates iron uptake transcriptionally in *Saccharomyces cerevisiae*, *Journal of Cellular Biochemistry*, 251-251.

184. Li, H. R., Mapolelo, D. T., Dingra, N. N., Naik, S. G., Lees, N. S., Hoffman, B. M., Riggs-Gelasco, P. J., Huynh, B. H., Johnson, M. K., and Outten, C. E. (2009) The Yeast Iron Regulatory Proteins Grx3/4 and Fra2 Form Heterodimeric Complexes Containing a [2Fe-2S] Cluster with Cysteinyl and Histidyl Ligation, *Biochemistry-Us 48*, 9569-9581.

185. Cockrell, A. L., Holmes-Hampton, G. P., McCormick, S. P., Chakrabarti, M., and Lindahl, P. A. (2011) Mossbauer and EPR study of iron in vacuoles from fermenting *Saccharomyces cerevisiae*, *Biochemistry-Us 50*, 10275-10283.

186. Garber Morales, J., Holmes-Hampton, G. P., Miao, R., Guo, Y., Munck, E., and Lindahl, P. A. (2010) Biophysical characterization of iron in mitochondria isolated from respiring and fermenting yeast, *Biochemistry-Us 49*, 5436-5444.

187. Holmes-Hampton, G. P., Miao, R., Morales, J. G., Guo, Y. S., Munck, E., and Lindahl, P. A. (2010) A Nonheme High-Spin Ferrous Pool in Mitochondria Isolated from Fermenting *Saccharomyces cerevisiae*, *Biochemistry-Us 49*, 4227-4234.

188. Sharma, K. G., Kaur, R., and Bachhawat, A. K. (2003) The glutathione-mediated detoxification pathway in yeast: an analysis using the red pigment that accumulates in certain adenine biosynthetic mutants of yeasts reveals the involvement of novel genes, *Arch Microbiol 180*, 108-117.

189. Davis-Kaplan, S. R., Ward, D. M., Shiflett, S. L., and Kaplan, J. (2004) Genome-wide analysis of iron-dependent growth reveals a novel yeast gene required for vacuolar acidification, *Journal of Biological Chemistry 279*, 4322-4329.

190. Serrano, R., Bernal, D., Simon, E., and Arino, J. (2004) Copper and iron are the limiting factors for growth of the yeast *Saccharomyces cerevisiae* in an alkaline environment, *Journal of Biological Chemistry 279*, 19698-19704.

191. Parra, K. J., and Kane, P. M. (1998) Reversible association between the V-1 and V-0 domains of yeast vacuolar H+-ATPase is an unconventional glucose-induced effect, *Mol Cell Biol 18*, 7064-7074.

192. Sharma, K. G., Kaur, R., and Bachhawat, A. K. (2003) The glutathione-mediated detoxification pathway in yeast: an analysis using the red pigment that

accumulates in certain adenine biosynthetic mutants of yeasts reveals the involvement of novel genes, *Archives of Microbiology 180*, 108-117.

193. Sambade, M., Alba, M., Smardon, A. M., West, R. W., and Kane, P. M. (2005) Genomic screen for yeast vacuolar membrane ATPase mutants, *Genetics 170*, 1539-1551.

194. Drose, S., Bindseil, K. U., Bowman, E. J., Siebers, A., Zeeck, A., and Altendorf, K. (1993) Inhibitory Effect of Modified Bafilomycins and Concanamycins on P-Type and V-Type Adenosine-Triphosphatases, *Biochemistry-Us 32*, 3902-3906.

195. Martinoia, E., Maeshima, M., and Neuhaus, H. E. (2007) Vacuolar transporters and their essential role in plant metabolism, *J Exp Bot 58*, 83-102.

APPENDIX A

IRON TRAFFICKING IN MAMMALIAN SYSTEMS

The studies presented in Appendices A, B, and C were performed as a group effort with Dr. Lora Lindahl, Dr. Mrinmoy Chakrabarti, Dr. Gregory Holmes-Hampton, Mr. Sean McCormick, and Mr. Jinkyu Park. The goal of these projects was to analyze the Fe distributions in mouse brains using biophysical and bioanalytical techniques. My role in these projects was to care for the animals, perform organ dissections, prepare samples for the appropriate studies, and participate in discussions to analyze and understand these systems.

Iron Uptake in Mammalian Systems

The second portion of this dissertation focuses on the importance of iron in mammalian systems, specifically in the brain. Iron delivery in mammalian systems (ie, mice, humans) is more complex than in *S. cerevisiae*, although there are some similarities between the systems. In mammals iron is absorbed from the diet by enterocytes in the duodenum as either heme or nonheme iron. Heme iron (ie, from meats) is transported by heme carrier protein 1 (HCP1). Nonheme iron (ie, from vegetables) absorption is facilitated by a reductase (DCytb1) and divalent metal transport protein (DMT1). DMT1 is a member of the Nramp-family of metal transporters, which also includes Smf proteins in yeast, and will transport divalent metals including Fe^{2+}, Cu^{2+}, Mn^{2+}, Zn^{2+}, Co^{2+}, Cd^{2+}, and Pb^{2+} (*1*). While this protein is not specific for iron, it is highly expressed under low-iron conditions. Because extracellular iron exists as Fe^{3+}

it must be reduced before it is transported by DMT1. The DCytb1 protein is co-expressed with DMT1 in enterocytes, and appears to be an ascorbate-dependent reductase (*1*).

After absorption iron is transported across enterocytes and into the blood. The export of iron from enterocytes and into the circulation is facilitated by ferroportin (FPN) and hephaestin. FPN is the only identified exporter protein in cells, and transports ferrous iron into the blood stream. This protein is regulated by Hepcidin, which is a peptide hormone secreted by the liver. Under high iron-conditions hepcidin binds to FPN, resulting in the internalization and consequent degradation of FPN in the lysosome. Also, Fe^{2+} must be bound to FPN before it is internalized (*1*). The regulation of hepcidin is controlled in part by CCAAT/Enhancer-binding protein α (C/EBPα). This protein is indicated as an iron-mediated transcriptional regulator of hepcidin mRNA. Under high-iron conditions C/EBPα is up-regulated, and mice devoid of C/EBPα have low levels of hepcidin. The exact mechanism by which C/EBPα may sense iron and regulate hepcidin mRNA is unclear. Other regulatory factors are possibly involved in hepcidin expression levels as well, (ie, hepatocyte nuclear factor 4 and signal transducer and activator of transcription- STAT- proteins) but defined mechanisms remain to be identified.

In order for iron to be trafficked throughout the blood it must be oxidized to Fe^{3+}. Therefore, FPN is associated with ferroxidase proteins like ceruloplasmin (Cp) and hephaestin (Heph). Cp and Heph share 50% sequence similarity and contain types I-III Cu binding sites. Iron accumulates in the cell upon disruption of these proteins,

indicating they are necessary for efficient cellular iron export (*1*). The expression of Cp or Heph is dependent on the cell type; for example, Heph is expressed in intestinal cells while Cp is found in liver, heart, and brain (astrocytes). The purpose of Heph and Cp is to catalyze the oxidation of Fe^{2+} to Fe^{3+}, which allows transferrin (Tf) to bind iron and deliver it to different tissues.

Tf is circulated throughout the body and is responsible for binding and transferring iron to non-intestinal cells. This protein is recognized by Transferrin protein receptors (TfR) located on cell surfaces and iron is imported via receptor-mediated endocytosis. Upon acidification in the endosome iron is released from Tf, reduced by a vesicular reductase (Steap3), and subsequently transported into the cytosol by the ferrous transporter DMT1. The Tf-TfR complex is then recycled to the plasma membrane where Tf is released into the circulation. Tf is produced by hepatocytes and secreted by the liver to the plasma. There are two homologous amino acid domains in Tf which bind one Fe^{3+} atom each. When Tf is endocytosed, the release of bound iron is facilitated by a decrease in pH, which induces a conformational change in the iron-binding domains and allows iron release from Tf. There are two different receptors- TfR1 and TfR2- which bind $Tf[Fe^{3+}]_2$. TfR1 is found in many cell types and is relatively abundant in organs; whereas TfR2 is primarily localized to hepatocytes, and enterocytes in the duodenum. The TfRs exist as homodimers, each binding one $Tf[Fe^{3+}]_2$. Therefore, 4 iron atoms are imported by each TfR dimer. These two receptors seem to serve different purposes based on their regulation. Expression of TfR1 is regulated by IRP1, IRP2, which are discussed in more detail later in this chapter. IRP1 and IRP2 regulate protein

expression at a translational level in response to iron concentrations in the cytosol. TfR1 is also regulated at a transcriptional level by hypoxia-responsive element (HRE), where TfR1 expression is up-regulated under hypoxic conditions.(*1*) Finally, TfR1 is regulated by hereditary hemachromatosis protein, HFE. This protein is expressed in intestinal cells and is hypothesized to act as a competitive inhibitor of Tf on TfR1. On the other hand, TfR2 has a lower affinity for $Tf[Fe^{3+}]_2$ than TfR1, is not regulated by IRP1, IRP2, or HFE, and its expression does not appear to change with iron levels. Deletion of this protein results in phenotypes associated with hereditary hemachromatosis (HH). The deletion of this protein in mice having type 3 HH results in a severe disruption in iron metabolism. This indicates that TfR2 plays an important role in iron metabolism, but the mechanism of regulation and iron sensing is unclear.(*1*)

Iron Storage in Mammalian Systems

Once iron has entered the cell it can be trafficked to different organelles or to ferritin. Ferritin exists in the blood plasma and within cells in the nucleus, cytosol, and mitochondria. This multimeric protein is responsible for storing up to 4,500 iron atoms. It replaces the role of vacuoles in yeast cells by sequestering and storing iron safely. This protein is composed of 24 subunits of heavy (H) and light (L) chains, which assemble to form a hollow shell in which iron is stored. The H subunit acts as a ferroxidase, which oxidizes iron for storage as a precipitated ferric-oxide form while the L subunits stabilize the protein shell structure and facilitate iron uptake into the protein. The ratios of H to L chains are tissue, cell, and organelle dependent. For example,

mitochondrial ferritin is H-rich while serum ferritin is rich in L-chains. Iron is transported from the cytosol to ferritin via poly(rC) binding proteins (PCBP1 and PCBP2). These proteins were found to be involved in iron transport to ferritin, although it is unclear whether or not PCBP1 and PCBP2 are responsible for iron transport to other iron centers as well (REF).

Under conditions where cytosolic iron levels are decreased due to the addition of a chelator, bacterial infection, or amino acid starvation ferritin is degraded through a lysosomal autophagy mechanism in order to recycle iron from ferritin to the cytosol. Under low-iron growth conditions Ferritin is monoubiquitinated and degraded via a proteosome-mediated pathway. Further studies are needed to understand this mechanism and to distinguish the different triggers for lysosome- and proteosome-mediated degradation pathways.

Ferritin is regulated via IRP1 and IRP2, although the deletion of IRP2 has a greater effect on Ferritin levels than IRP1 indicating IRP2 is the more prominent regulator for Ferritin expression. Due to the ability of ferritin to sequester iron and thereby prevent ROS formation, Ferritin can also be thought of as an antioxidant protein. The ferritin gene contains an antioxidant-responsive element (ARE), which responds to oxidative stress signals and up-regulates transcription of ferritin.

Mammalian Mitochondrial Iron Trafficking

As stated earlier, mitochondria are the major hubs of iron metabolism and iron plays a crucial role in metabolic pathways. Iron metabolism in mammalian cells is

extremely similar to iron metabolism in yeast. For example, iron enters the mitochondria through mitoferrin proteins 1 and 2 (Mfrn1p and Mfrn2p), which are homologous to Mrs3p and Mrs4p in yeast. The oxidation state and ligand environment of transported iron is unclear, but it has been hypothesized that the molecule is an iron-glutathione complex, or an organic ligand or peptide which can bind iron. The concentrations of iron, citrate, and GSH are higher in the mitochondrial matrix than in the cytosol, but again this has not been shown conclusively. The main difference in iron homeostasis in mammalian and yeast mitochondria is that mammalian mitochondria also contain ferritin, which is rich in H chains, as mentioned previously.

De novo Fe-S cluster biosynthesis is also an extremely important function of the mitochondria, and is conducted in a similar pathway as in yeast. The primary proteins involved include Frataxin (Yfh1p in yeast), IscU (Isu1 in yeast), and Ferredoxin (Yah1 in yeast). Frataxin acts as an iron trafficking protein which binds Fe^{2+} and may assemble [2Fe-2S] clusters on IscU. Nfs1 serves as a cysteine desulfurase which donates sulfur to IscU. Heme biosynthesis in human cells is also reliant on Frataxin, just as heme synthesis in yeast depends on Yfh1p. The protoporphyrin-IX ring is assembled as in yeast (see earlier section) and frataxin is hypothesized to deliver Fe^{2+} to ferrochelatase which inserts Fe^{2+} into protoporphyrin-IX. In this dissertation Appendix X discusses the process of isolating mitochondria from mouse brains and investigating the distribution of iron by Mössbauer, EPR, and UV-vis spectroscopy. This research shows that the iron distributions in mitochondria are conserved across organisms. Moreover, the

mitochondria in these organelles show a NHHS Fe^{2+} species which could represent the MLIP.

Iron Trafficking to the Brain

While iron trafficking to cells is the same for most tissues, the transport of iron into some tissues is more complex. Iron is necessary for brain function, such as respiration, production of neurotransmitters, and myelinogenesis.(*1*) Just as in other systems, iron overload can have detrimental effects. In the brain these effects can be extremely detrimental, often resulting in neurodegenerative diseases including Alzheimer's disease and Parkinson's disease. Iron entry in the brain is tightly controlled because of the potentially fatal effects. The first level of iron control in the brain is a physical barrier known as the blood-brain barrier (BBB). In the systemic circulation iron is transported through the blood by Tf, but because the central nervous system (CNS) is physically separated from the systemic circulation, iron must be transported into the cerebrospinal fluid (CSF) from the blood before it can be transported into brain cells.

The BBB consists of endothelial cells of capillaries and epithelial cells from the choroid plexus. The choroid plexus is composed of tight-junction epithelial cells which surrounds each of the four ventricles of the brain. This structure is responsible for producing CSF and acts as a kind of filtration system which is responsible for maintaining the extracellular environment in the brain. The barrier between the choroid plexus and CSF is known as the blood-CSF barrier, which iron and other nutrients must

cross to be accessible to brain cells. CSF plays a major role in delivering and maintaining brain iron levels as brain Tf is found in this fluid (*2*). The proteins responsible for transporting iron to and from the CSF are the same as (or very similar to) those expressed in cells exposed to serum Tf, including DMT1, FPN, Cp, Heph, TfR1, and Dcytb (*2*).

Iron Regulation by IRP1 and IRP2

Iron must be tightly regulated in mammalian cells in order to maintain the delicate balance between necessity and toxicity. There are many stages at which iron is regulated. For example, iron uptake and release into the circulation is regulated by hepcidin and hypoxia inducible factor 2α (HIF2α) (*2*). Hepcidin is a hormone secreted by the liver in response to inflammation or iron overload (*2*). HIF2α is a transcription factor which responds to hypoxia by regulating the transcription of DMT1 and Dcytb (*3, 4*).

Iron is also regulated within cells by two iron regulatory proteins: IRP1 and IRP2. These proteins bind to mRNA to regulate protein expression under iron deficient conditions. When iron is abundant IRP1 acquires a 4Fe-4S cluster and acts as a cytosolic aconitase protein. In these conditions the IRP2 protein is degraded by the proteasome. The degradation of IRP2 is induced by FBXL5, which has an iron-sensing mechanism. FBXL5 contains an iron-binding hemerythrin domain which regulates the protein stability. If iron is bound, FBXL5 will become more stable and bind to IRP2, but when iron is not bound FBXL5 is degraded and ultimately results in the expression of

IRPP2. It must be noted that FBXL5 favors Fe^{2+} rather than Fe^{3+}, which indicates that cytosolic iron is most likely ferrous.

In these studies iron distributions in mice brains were investigated using biophysical approaches (Mössbauer, EPR, UV-Vis) and bioanalytical techniques (LC-ICP-MS). One problem in studying brain iron is that most of the samples are prepared and analyzed in an aerobic environment, which allows any labile or reduced iron to be oxidized. Moreover, many imaging techniques (ie, Perl staining) visualize iron aggregates and cannot detect iron at low levels. In the following studies the isolation conditions were tightly controlled by using an anaerobic environment for organ dissections and sample preparation. By applying the biophysical and bioanalytical techniques described in Appendices B and C it was possible to detect low levels of iron which have not previously been visualized. Therefore, by taking advantage of these biophysical methods in conjunction with molecular biology and genetic approaches reported previously it is possible to observe changes in iron-containing components in the brain.

APPENDIX B

CHANGING IRON CONTENT OF THE MOUSE BRAIN DURING DEVELOPMENT[2]

Abstract

Iron is crucial to many processes in the brain yet the percentages of the major iron-containing species contained therein, and how these percentages change during development, have not been reliably determined. To do this, C57BL/6 mice were enriched in ^{57}Fe and their brains were examined by Mössbauer, EPR, and electronic absorption spectroscopy; Fe concentrations were evaluated using ICP-MS. Excluding the contribution of residual blood hemoglobin, the three major categories of brain Fe included ferritin (an iron storage protein), mitochondrial iron (consisting primarily of Fe/S clusters and hemes), and mononuclear nonheme high-spin (NHHS) Fe^{II} and Fe^{III} species. Brains from prenatal and one-week old mice were dominated by ferritin and were deficient in mitochondrial Fe. During the next few weeks of life, the brain grew and experienced a burst of mitochondriogenesis. Overall brain Fe concentration and the concentration of ferritin declined during this burst phase, suggesting that the rate of Fe incorporation was insufficient to accommodate these changes. The slow rate of Fe import and export to/from the brain, relative to other organs, was verified by an isotopic labeling study. Iron levels and ferritin stores replenished in young adult mice. NHHS

---

[2] Holmes-Hampton, GP; Chakrabarti, M; Cockrell, AL; McCormick, SP; Abbott, LC; Lindahl, LS; Lindahl, PA. (2012) Changing Iron Content of the Mouse Brain During Development. *Metallomics 4*, 761-770. http://pubs.rsc.org/en/Content/ArticleLanding/2012/MT/c2mt20086d#!divAbstract. Reproduced by permission of The Royal Society of Chemistry.

Fe^{II} species were observed in substantial levels in brains of several ages. A stable free-radical species that increased with age was observed by EPR spectroscopy. Brains from mice raised on an Fe-deficient diet showed depleted ferritin iron but normal mitochondrial iron levels.

Introduction

Iron plays a major role in generating the chemical energy required for neurological activity, in that Fe/S clusters and heme groups are abundant in mitochondrial respiratory complexes (*5*). This transition metal is found at the active sites of numerous metalloenzymes in the brain (*6*) and is required for myelin biosynthesis (*7*). Over a billion people worldwide suffer from anemia (*8*), and Fe deficiency affects neonatal brain development and cell-mediated immunity (*9*). An overabundance of Fe is also problematic, as certain forms of iron, particularly NHHS Fe^{II} complexes, promote Fenton chemistry that generates reactive oxygen species (ROS). The brain may be particularly sensitive to ROS damage because of its high rate of O_2 consumption (*10*) and limited ability of neuronal cells to be repaired or replaced (*11*). Moreover, Fe accumulates with age and neurodegeneration (*12*).

Iron traveling into the brain passes through the blood-brain barrier (BBB) (*13*). Fe^{III}-bound transferrin in the blood binds to receptors on the luminal side of the endothelial cells associated with this barrier (*14*). Once inside neurons and other cells of the brain, a portion of the Fe is trafficked to mitochondria, where hemes and iron-sulfur clusters are assembled. Another portion is stored as ferritin, a spherically shaped protein

complex with a hollow core into which large amounts of Fe can be deposited in the form of magnetically-interacting Fe^{III} oxyhydroxide material (*15*). Ferritin helps regulate cytosolic Fe concentrations and sequester Fe that might otherwise generate ROS. Similar forms of Fe are found in hemosiderin (*16*), a degradation product of ferritin, neuromelanin (*17*), and perhaps mitochondrial ferritin (*18*).

X-ray fluorescence (*19*), high-field magnetic resonance imaging (*20*) and high-resolution histological staining (*21*) have revealed an inhomogeneous spatial distribution of Fe in the brain. The globus pallidus, putamen, substantia nigra pars reticulata, red nucleus, cerebral dentate nucleus, the nucleus accumbens and portions of the hippocampus contain high concentrations of Fe; white matter and the cerebrospinal fluid contain lesser amounts. The distribution of brain Fe follows the distribution of ferritin whereas the distribution of transferrin is more homogeneous (*22*), reflecting the dominance of ferritin Fe in the brain.

These imaging methods provide excellent *spatial* resolution of brain Fe but their ability to resolve different *types* of Fe-containing species is limited. Mössbauer spectroscopy can distinguish different types of Fe (*23*), but it has barely been applied to the brain, perhaps due to the insensitivity of the technique, the low concentration of Fe in the brain, and the ability of Mössbauer to detect only ^{57}Fe (2% natural abundance).

We have used Mössbauer spectroscopy, in conjunction with EPR and UV-vis spectroscopies, and ICP-MS, to assess the Fe content of yeast mitochondria, vacuoles and whole cells (*24-26*). Our objective in those studies was to evaluate the types and relative amounts of Fe present in these organelles and cells. In yeast, the two dominant

Fe "traffic hubs" include vacuoles, which store Fe, and mitochondria, which use it to obtain cellular energy.

Here we apply the same methods to study the iron content of intact ^{57}Fe-enriched mouse brains. Previous Mössbauer studies of the brain have focused on particular Fe-rich subcomponents of unenriched human brains. These studies found that virtually all Fe in these regions consists of magnetically interacting, superparamagnetic ferric species, including ferritin and neuromelanin (*12, 15-18*) curiously, mitochondrial Fe, *e.g.* Fe/S clusters and heme groups were not observed. This is difficult to rationalize, given the enormous role of mitochondria in brain function, and the substantial proportion of yeast Fe due to this organelle. We show here that, besides ferritin-like species, the brains of mice contain substantial amounts of Fe/S clusters, much of it arising from mitochondria. Also detected were nonheme high-spin (NHHS) Fe^{II} and Fe^{III} species. A portion of these mononuclear species may constitute the labile iron pool (LIP) and which may participate in ROS-generating reactions.

Experimental Procedures

Animal Care and Dissections

C57BL/6 mice were raised and manipulated in accordance with the TAMU Animal Care and Use committee (AUP 2010-226). Mice were housed in disposable plastic cages (Innovive Innocage Static Short) with all-plastic water bottles and plastic feeders with zinc electroplated reinforcements. Mice were fed Fe-deficient chow (Harlan

Laboratories, Inc. Teklad ID TD.80396.PWD) supplemented as follows. For experiments involving ^{56}Fe or^{57}Fe, the chow was supplemented with 50 μg/g of either natural abundance Fe citrate or ^{57}Fe citrate (IsoFlex USA) prepared as described (*26*). For each kg of chow, 22 mL of a 40 mM stock solution of Fe citrate (adjusted to pH 7) was added. The chow was further moistened with *ca.* 45 mL of double-distilled water containing 0.6 ng Fe/g water. The chow was compressed into pellets, heated at 100 °C for 20 min, and then stored at −20 °C in zip-locked plastic bags. Samples of the 7 batches of this chow examined contained an average of 33 ± 2 μg Fe/g chow as determined by ICP-MS.

Fe-deficient pups were born to a mother that was fed the Fe-sufficient diet until ~3 days prior to birth when her diet was switched to Fe-deficient (1.2 μg Fe/g chow). Fe-deficient animals received water that was house-distilled, deionized using ion-exchange columns (Thermo Scientific 09-034-3), and distilled again using a sub-boiling still (Savillex DST-1000). The resulting sub-boiling distilled water contained 0.02 ng Fe/g water.

Each cage contained *ca.* 200 g of synthetic bedding (Ketchum Omega Dry) with 1.5 μg ^{56}Fe/g. Nestlets (Ancare) that were included in the cages of pregnant females weighed ~10 g and contained 20 μg ^{56}Fe/g. Nitrile gloves were worn when mice, chow, water, bedding, *etc.* were handled. So-called "^{56}Fe-enriched" mice were treated equivalently but were raised on chow supplemented with natural-abundance Fe citrate.

Mice were euthanized by an IP injection of a solution that provided 3 mg ketamine and 0.5 mg xylazine per 20 g body wt. Immediately after breathing ceased and

the heart stopped beating, animals were imported into a refrigerated (5–10 °C) argon-atmosphere glove box (MBraun Labmaster) containing between 2–20 ppm O_2, where all dissections and tissue manipulations were performed. The “hands” of a pair of standard butyl rubber gloves on the box were cut off and replaced with tight-fitting surgical gloves using custom-designed plastic cuffs. The open end of each surgical glove was stretched over one end of a cuff and secured with two O-rings that fit into grooves on the cuff. The other end of the cuff was attached similarly to a butyl rubber glove, the other end of which was secured on the box glove port in standard fashion.

Unless noted otherwise, animals were perfused with Ringer's buffer (155 mM NaCl, 5 mM KCl, 2 mM $CaCl_2$, 1 mM $MgCl_2$, 2 mM NaH_2PO_4, 10 mM HEPES, 10 mM glucose, and ~10 U heparin/mL). A 27 gauge 1/2” long stainless-steel needle was inserted into the left ventricle of the heart, and buffer was pumped at *ca.* 0.7 mL min^{-1}. After ensuring proper placement of the needle, the caudal vena cava was severed, and pumping continued for an additional 1–2 min until blanching of the liver appeared complete. For some dissections, blood diluted with Ringer's buffer was collected.

Immediately after perfusion, brains and other organs were isolated by dissection using stainless steel and/or titanium instruments. The Fe concentration of a 50 mL solution of Ringer's buffer into which the stainless steel instruments were immersed for 30 min increased by 190 nM. This is far longer than animals contacted the instruments. Thus, an insignificant amount of Fe was leached from these instruments during dissections and none of the Fe-associated features observed in the spectra originated from them.

Densities

Masses of dissected brains were determined using an analytical balance (Toledo Mettler Model AB104) in the glove box. Volumes were measured using a 10 mL graduated cylinder into which a Delrin screen, supported by a thin plastic line, was submersed in buffer. Brains were submersed into the cylinder and the displaced volumes were measured. Densities were determined for 6 samples; an average value of 1.17 g mL^{-1} was obtained, similar to the reported value of 1.06 g mL^{-1} (*27*). The latter value was used for all calculations.

Mössbauer Spectroscopy

Whole brains were anaerobically loaded into Delrin Mössbauer cups and frozen as described (*28*). Low-field spectra were collected using a model MS4 WRC spectrometer (SEE Co., Edina MN). High-field (6 T) and low-field spectra were collected at 4.3 K using a model L:He-6T spectrometer. Spectra were analyzed using WMOSS software. Parameters are reported relative to α-Fe foil at room temperature.

EPR and UV-visible Spectroscopy

Following Mössbauer analysis, brains were transferred to disposable plastic 15 mL tubes containing an equal volume of Ringer's buffer. Samples were homogenized for 1 min using a plastic rotary knife inserted into a tissue grinder (Omni TH). For EPR measurements, homogenates were packed (4000 × g, 10 min) and frozen in custom quartz tubes as described.[24] Spectra were collected on an X-band spectrometer (EMX,

Bruker Biospin Corp., Billerica MA) with an Oxford Instruments ER910 cryostat. Signals were quantified using a 1.00 mM CuEDTA standard and Spincount (http://www.chem.cmu.edu/groups/hendrich) software. For UV-Vis measurements, samples were transferred to a 2 mm pathlength custom-designed quartz cuvette (NSG Precision Cells), sealed anaerobically with a septum. RT UV-vis spectra were collected on a Hitachi 4400U spectrophotometer with a head-on photomultiplier tube. Spectra were analyzed as described for specific heme *a*, heme *b*, and heme *c* content as described (*24*).

The contributions of blood from the UV-vis spectra of brain homogenates were removed, based on the percentage contribution of deoxyhemoglobin present in corresponding Mössbauer spectra of the same brain sample. This percentage was multiplied by the concentration of Fe in the sample, affording the concentration of hemoglobin (typically ~20 μM). The UV-vis spectrum of 100-fold diluted blood was determined (data not shown), as was the Fe concentration of undiluted blood (7.6 mM Fe). The spectral absorbance was scaled based on the ratios of Fe concentrations in blood *vs.* in the brain samples, and the scaled spectra were subtracted from the raw UV-vis spectra of the corresponding brain homogenate.

ICP-MS

Homogenized brain samples were transferred to plastic tubes containing 350 μL of concentrated trace-metal-grade nitric acid (Fisher). After overnight digestion at 90 °C,

samples were diluted with 6.5 mL of H_2O and analyzed by ICP-MS (Agilent model 7700x). The H_2O used was sub-boiling distilled as described above.

Results

^{57}Fe-Enrichment.

The concentration of Fe in the mouse brain was so low (Table B1) that ^{57}Fe enrichment was required for Mössbauer studies. To evaluate enrichment rates, mice born to an ^{56}Fe-enriched mother were fed ^{57}Fe-supplemented chow immediately after weaning. Their brains enriched slowly such that only partial ^{57}Fe-enrichment was achieved after 58 wks on the ^{57}Fe-supplemented diet (Figure B1). Other organs, including liver, spleen, heart, and kidney enriched faster and to a greater extent than the brain, with the duodenum enriching fastest (data not shown). The slow incorporation of ^{57}Fe into the brain was probably due to the blood-brain barrier (*13*). Cu, Mn, Zn, Mo and P concentrations in these organs were also determined (data not shown).

The rate of Fe enrichment was biphasic, with the transition from fast to slow phase occurring 4–6 wks postnatal. During the fast-enrichment period, the total nanomoles of ^{56}Fe in the brain declined rapidly while that of ^{57}Fe increased gradually (Figure B1). The overall concentration of Fe in the brain *declined* during the fast-enrichment phase, followed by a gradual recovery in the slow-enrichment phase. Brain mass increased rapidly during the fast-enrichment phase and slowed thereafter. The concentration of ^{57}Fe in the brain increased with each generation raised under ^{57}Fe-enrichment conditions, maximizing at ~80% after about 3 generations. Thus, Mössbauer

spectra were typically collected from animals raised under ^{57}Fe-enrichment conditions for ≥ 2 generations.

Brains from three-week-old mice

The low-temperature, low-field Mössbauer spectrum of a 3-wk-old brain exhibited 4 discernible features. A sextet typical of ferritin-bound Fe^{III} ions dominated (Figure B2, A); the blue line is a simulation with δ = 0.5 mm s^{-1}, ΔE_Q = −0.3 mm s^{-1} and Γ = 0.6 mm s^{-1}, and H_{eff} = 480 kG. At 70 K, this feature collapsed into a doublet (δ = 0.5 mm s^{-1} and ΔE_Q = 0.7 mm s^{-1}) (Figure B2, B), similar to the behavior of authentic ferritin (*16*). The baseline of the 70 K spectrum did *not* reveal underlying features. When a 6 T field was applied at 4.3 K, the resulting pattern (Figure C2, C) associated with this feature was again indistinguishable from that of ferritin. We conclude that this feature arises from ferritin, but other magnetically interacting Fe^{III} ions such as Fe-bound haemosiderin (*16*), neuromelanin (*17*)or mitochondrial ferritin (*18*) could have contributed.

Another major feature in the spectrum was a quadrupole doublet with δ = 0.45 mm s^{-1} and ΔE_Q = 1.15 mm s^{-1}; these values are typical of S = 0 $[Fe_4S_4]^{2+}$ clusters and low-spin Fe^{II} heme centers. At 6 T, the splitting pattern observed for this so-called *Central Doublet* (CD) was simulated (Figure B2, C, purple line) confirming the expected diamagnetism. A doublet with identical parameters in spectra of isolated mitochondria from yeast (*24*) arises primarily from respiratory complexes, and so we assign the majority of the CD intensity in brain to mitochondrial respiratory complexes.

Animal ID	F053PNP	F016P	F019P	F019P	F020P (Fe def)	F050P F019P	M013 M014	M001
Age (wks)	-1	1	2	3	3	4	24	60
Comments	Not Perfused				Iron Deficient			
Number and Sex	6 (sex not determined)	7F 2M	1F 2M	0F 3M	1F 8M	1F 3M	0F 2M	0F 1M
Average (SD) brain mass (mg)	52 ± 6	200 ± 30	350 ± 4	310 ± 40	350 ± 10	390 ± 30	377 ± 2	456
Num. used for element, protein analysis	6	4	2	3	3	2	2	1
[Protein] (mg/mL)	21	30	29	40	32	40	28	33
[Cu] (μM)	33	15	10	7	28	16	26	42
[Mn] (μM)	21	3	6	6	26	11	5	6
[Zn] (μM)	123	210	179	205	167	197	172	206
[Fe] (μM)	270	121	195	199	149	182	212	322
% ^{57}Fe	60	72	66	73	57	85	83	58
Hemoglobin Doublet subtracted (%)	37	3	5	10	11	14	11	18
Effective [Fe] in brain (μM)	170	117	185	179	132	157	188	264
Ferritin-like Fe (% of effective Fe)	67	54	51	57	19	42	57	56
Central Doublet (% of effective Fe)	19	27	37	31	57	42	30	33
Ferritin-like/CD ratio	3.5	2.0	1.4	1.8	0.33	1.0	1.9	1.7
HS Fe^{II} hemes (% of effective Fe)	~ 0	13	8	6	13	9	7	9
HS Fe^{II} nonheme (% of effective Fe)	10	6	~ 4	6	10	8	6	~ 2

Table B1. **Summary of Results.** The concentration of heme *b* in the prenatal brain (*) was not quantified. Values obtained by EPR, UV-vis, ICP-MS and protein analyses have an estimated relative uncertainty of ± 20%. Values derived from Mössbauer analyses have an absolute uncertainty of ± 4%.

[Fe^{II} heme *a*] (μM)	~ 0	~ 0	4	15	15	18	18	18
[Fe^{II} heme *b*] (μM)	*	~ 0	6	15	12	18	18	18
[Fe^{II} heme *c*] (μM)	~ 0	~ 4	12	23	25	32	32	35
g_{ave} = 4.3 (μM); HS Fe^{III} nonheme	0.1	0.1	0.1	0.1	0.1	0.1	0.1	0.1
g = 1.90 (μM); Rieske $[Fe_2S_2]^{1+}$	0	0.9	1.2	1.5	1.5	2.7	2.4	1.7
g = 1.94 (μM); SDH $[Fe_2S_2]^{1+}$	0	1	1.2	1.5	1.5	2.4	2.1	1.5
g = 2.00 (μM); organic radical	0.1	0.1	0.1	0.3	0.3	0.2	0.3	0.7

Table B1 Continued.

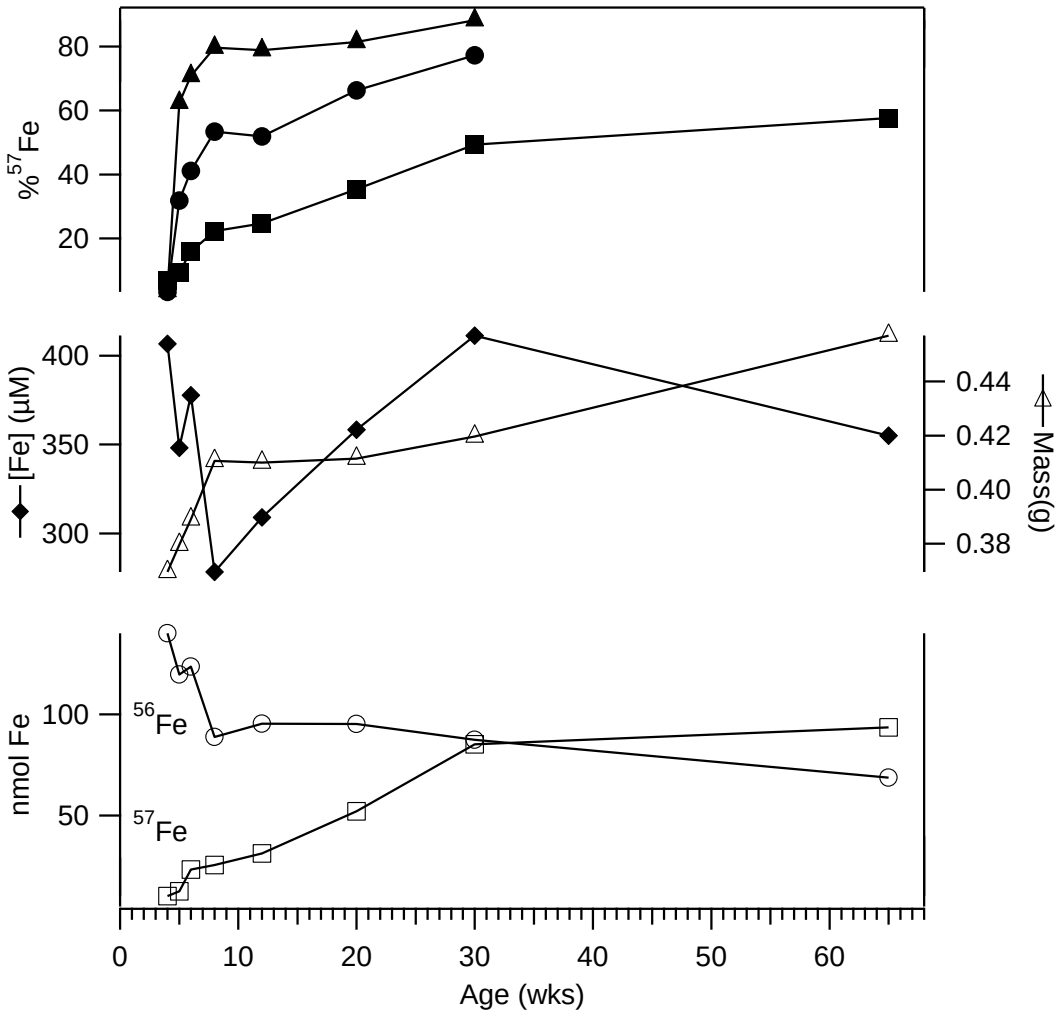

Figure B1. Enrichment of ^{57}Fe into ^{56}Fe-enriched mice raised on ^{57}Fe-enriched chow for different durations after weaning. Upper plots refer to the % ^{57}Fe scale, including solid triangles (duodenum), solid circles (average of liver, kidney, heart and spleen) and solid squares (brain). Solid diamonds in the middle group of plots refer to total [Fe] in the brain whereas open triangles refer to brain mass. In the lower group, open circles and squared refer to nmoles of ^{56}Fe and ^{57}Fe in the brain, respectively.

The 70 K, low-field spectrum also exhibited a quadrupole doublet with $\delta \sim 1.4$ mm s^{-1}, $\Delta E_Q \sim 3.3$ mm s^{-1} arising from one or more NHHS Fe^{II} species. This is simulated by the green line in Figure B2, B. These parameters are typical of such complexes with 5–6 O/N donor ligands. Most evident in the 70 K spectrum was the doublet from HS Fe^{II} heme centers (Figure B2, B, yellow line), with $\delta = 0.96$ mm s^{-1} and $\Delta E_Q = 2.3$ mm s^{-1}.

UV-vis spectra of corresponding brain homogenate (Figure B3, D) revealed the Soret, α and β bands indicating reduced hemes. These features were similar to those of yeast mitochondria (*24*); their concentrations were quantified and are listed in Table B1.

Low-temperature EPR spectra of packed 4-wk mouse brain homogenates (Figure B4) were virtually identical to those of a 3-wk old animal but were slightly more intense. The spectra exhibited overlapping signals in the $g = 2$ region. Resonances at $g = 1.93$ and 1.86 probably arose from the $S = ½$ $[Fe_2S_2]^{1+}$ cluster of succinate dehydrogenase and the reduced Rieske $S = ½$ $[Fe_2S_2]^{1+}$ cluster associated with cytochrome bc_1, respectively (*24*). Also evident was an isotropic signal at $g = 2.00$, probably from an organic radical. The weak signal at $g = 4.3$ undoubtedly arose from mononuclear HS Fe^{III} species with rhombic symmetry. The origin of the derivative-like feature at $g = 2.16$ is uncertain. Spin quantifications are listed in Table B1.

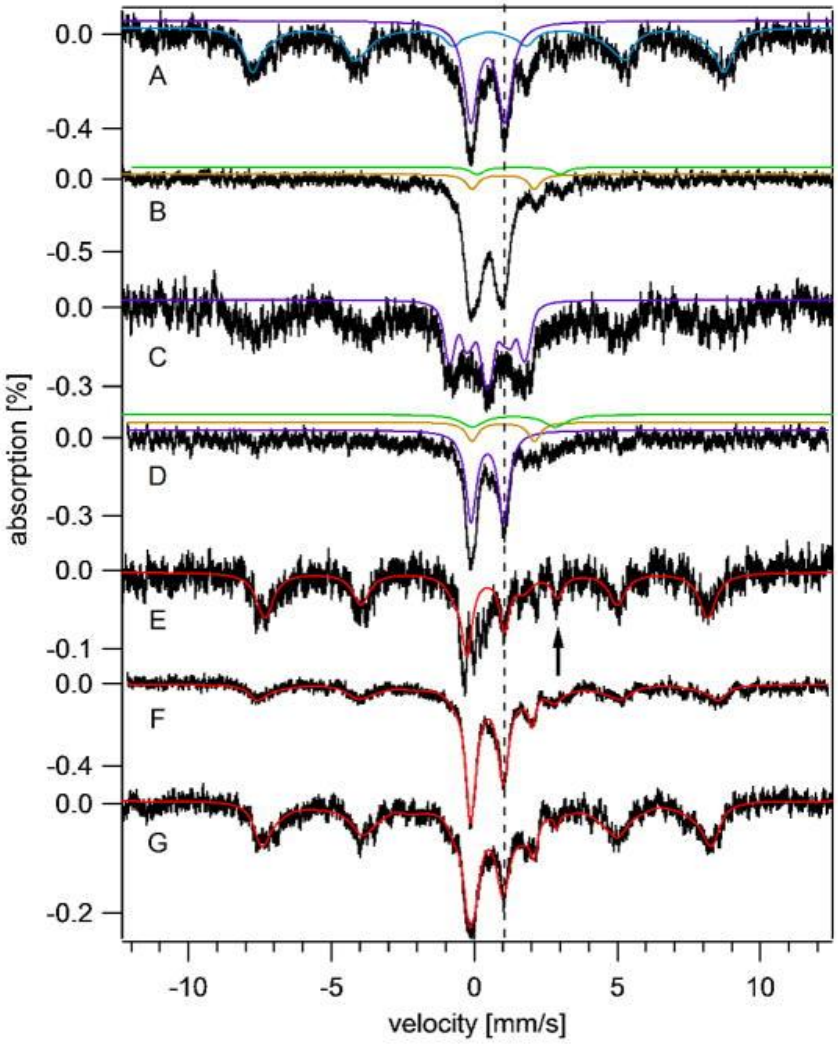

Figure B2. Mössbauer spectra of brains isolated at different ages. Spectra were collected at 6 K and with a 0.05 T field applied parallel to the radiation unless otherwise noted. A, 3 wk brain; B, same as A but at 70 K; C, same as A but at 4.3 K and 6 T field applied perpendicular to the radiation; D, 3wk Fe-deficient brain; E, −1wk brain; F, 4 wk brain; G, 58 wk brain. Red lines are composite simulations for E – G. Simulations assumed parameters mentioned in the text and percentages in Table B1. The vertical dashed line shows the position of the high-energy line of the central doublet. The arrow in E shows the position of the NHHS Fe^{II} feature. H_{int} values associated with the ferritin sextet ranged from 480 – 506 kG, perhaps reflecting subtle differences in the ferritin core structure.

Brains from iron-deficient mice

A pregnant ^{57}Fe-enriched mouse was switched to Fe-deficient chow 3 days prior to giving birth, and her offspring were euthanized 3 wks later at which time they displayed alopecia (image not shown), an indicator of Fe-deficiency (*29*). Also, the average Fe concentration in their livers (260 μM) was nearly 6-fold lower than in Fe-replete livers. Beard *et al*. found a 4-fold decline of liver Fe in mice fed an Fe-deficient diet for 8 wks (*30*). The average Fe concentration in their brains (Table 1) was also less than in Fe-sufficient brains, but the fold change was less dramatic. Mössbauer spectra (Figure B2, D) exhibited less of the ferritin sextet relative to Fe-sufficient brains, while, unexpectedly, the CD (purple line) was *more* intense. Also surprisingly was that the *absolute* concentration of the CD Fe in these brains was slightly *higher* than that in comparable Fe-sufficient brains (75 μM *vs.* 55 μM). A minor NHHS Fe^{II} feature was evident (Figure B2, D, green line). EPR and UV-vis spectra of Fe-deficient brains exhibited the same suite of signals and comparable intensities as were observed in spectra from brains of Fe-sufficient mice.

Brains from prenatal mice

Prenatal mice could not be perfused, such that the quadrupole doublet due to hemoglobin in the corresponding Mössbauer spectra was more intense than in the 3-wk brain spectra. The exact position of the heme doublet (δ = 0.96 mm s^{-1}, ΔE_Q = 2.35 mm s^{-1}) was also shifted slightly relative to that in other spectra, due to the presence of *fetal* hemoglobin in prenatal brains (*31*).

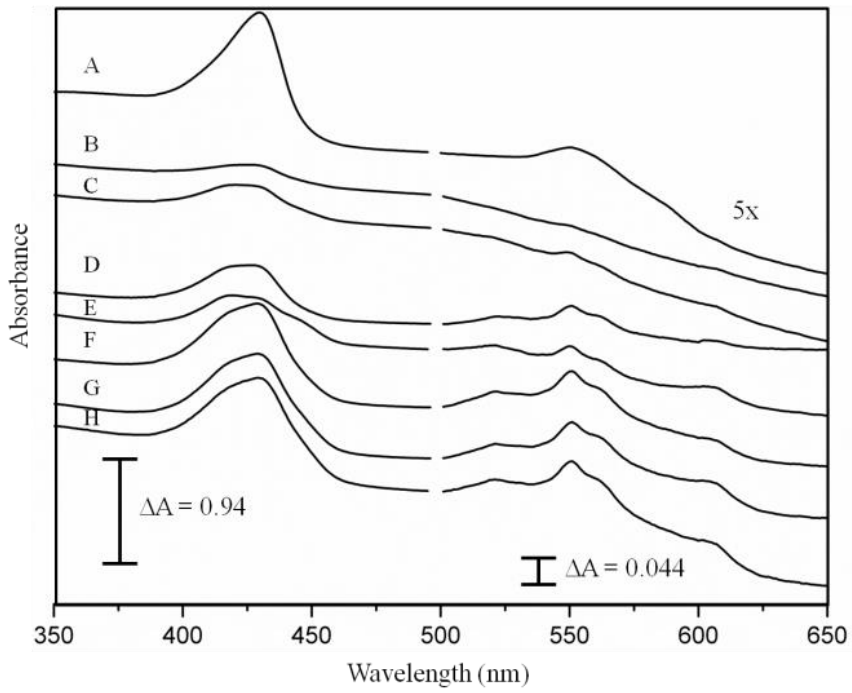

Figure B3. UV-vis spectra of brains isolated at different ages. a, -1 wk; **b**, 1 wk; **c**, 2 wks; **d**, 3 wks; **e**, 3 wks, Fe-deficient; **f**, 4 wks; **g**, 24 wks; and **h**, 60 wks. Intensities at wavelengths longer than 500 nm were multiplied by 5. Spectra shown are prior to subtracting the contributions due to hemoglobin.

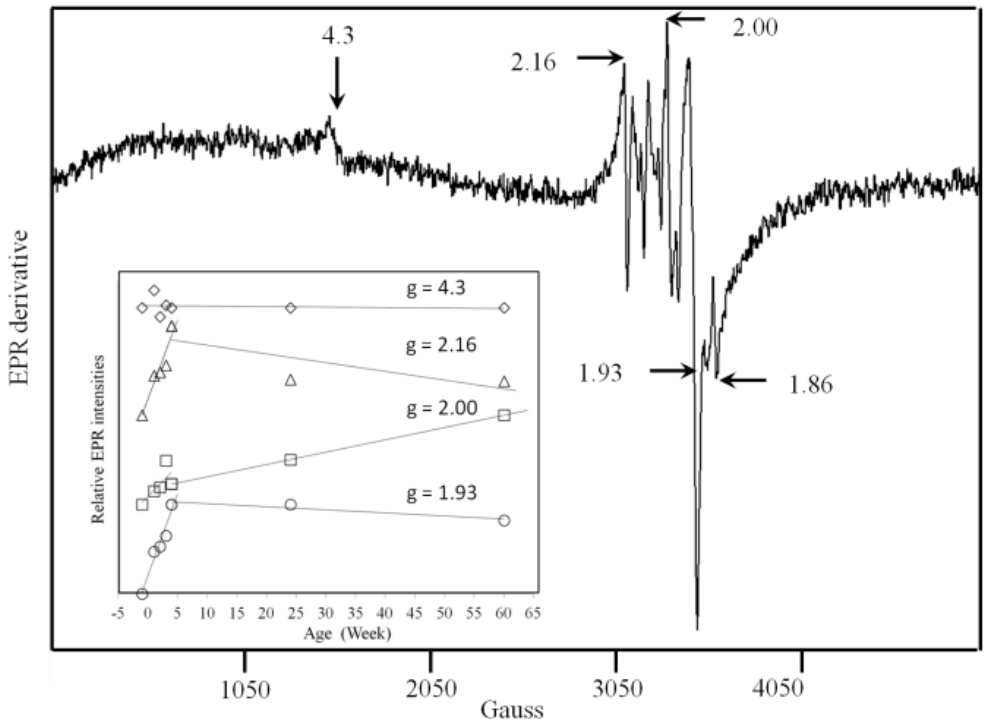

Figure B4. EPR spectrum of 3 wk brains. Highlighted signals are indicated by arrows. Conditions: temperature, 4 K; microwave frequency, 9.43 GHz; microwave power, 0.2 mW; modulation amplitude, 10 G; sweep time, 335 sec; time constant, 164 msec. The average of 10 scans is shown. The inset shows the relative intensity of highlighted features as a function of age. Plots are offset by arbitrary amounts.

The average Fe concentration in the prenatal brains (Table B1) included a significant contribution from blood (~100 μM). Since the concentration of Fe in undiluted blood was 7.8 mM (data not shown), we calculate that ~1.3% of the dissected prenatal brain volume was occupied by blood. This underestimates the value in living animals, as some blood exited the tissue during dissection. Apart from the blood contribution, the Mössbauer spectrum of prenatal brains was dominated by the ferritin sextet, with only a minor percentage due to the CD (Figure B2, E, Table B1). A NHHS Fe^{II} doublet was evident (arrow), with intensity comparable to that of the 3 wk brain spectrum. The UV-vis spectrum of prenatal brain homogenate (Figure B3, A) was dominated by features due to fetal hemoglobin; other heme-based species (*e.g.* mitochondrial cytochromes) could not be discerned. Intensities of EPR signals from the prenatal brain homogenate were diminished relative to those in other spectra (Figure S4A). These results indicate that ***prenatal brains were deficient in mitochondria***, with most Fe present as ferritin or ferritin-like species.

Brains from mice of various ages

Mössbauer spectra of brains from mice of different ages (Figure B2, E–G) showed an age-dependent *increase* in the percentages of the CD and a relative *decrease* in the ferritin-like sextet. This is indicated most reliably by the ferritin:CD intensity ratios (Table B1) which was highest for prenatal brains and lowest at 4 wks. Mössbauer spectra of the 24 and 58 wk brains exhibited age-dependent increases in the percentage of the ferritin-like sextet and decreases in the CD. UV-vis

spectra also showed an age-dependent increase in cytochromes at early ages (Figure B3). EPR spectra exhibited increasing intensities of the signals in the $g = 2$ region (data not shown), including features that likely originate from mitochondria. The radical signal at $g = 2.00$ also increased with age, while the $g = 4.3$ signal intensity was age-invariant.

Discussion

During the 150 year history of studying Fe in the brain, the vast majority of imaging studies have involved staining the brain with Fe chelators, *e.g.* using Perls' stain (*32*). This gives useful, albeit qualitative, estimates of the distribution of Fe. Quantitative estimates of brain Fe concentrations have been obtained by analytical methods (*e.g.* AA and ICP). Since the mid 1980's, the distribution of brain Fe has been monitored using NMR spectroscopy (*33*). With this technique, Fe is detected indirectly, in that ferritin and other magnetic forms of Fe shorten T_2 relaxation times (*34*). Magnetic susceptibility contrast measurements have also been used as a reporter of brain Fe in MRI studies (*35*). These are very powerful techniques, but they also have limitations. They can only detect magnetic forms of Fe, such that diamagnetic Fe forms are not detected. Non-iron paramagnetic metal ions will also affect NMR-based measurements, which complicate analyses (*36*).

X-ray absorption spectroscopy does not suffer from these problems, and has also been used to evaluate the spatial distribution of brain Fe (*36, 37*). This method measures Fe directly, regardless of magnetic properties, and has some ability to distinguish oxidation states. XAS methods have shown that the brain contains both Fe^{II} and

Fe^{III} ions, with the Fe^{III} state dominating (*37*). Wang *et al.* (*38*) and Pushie *et al.* (*19*) used synchrotron X-ray fluorescence spectroscopy to map the distribution of Fe and other metals in the mouse brain. However, the type of Fe centers, including oxidation states and coordination environments, could not be determined.

Mössbauer spectroscopy can play a complementary role to these other spectroscopic method, as it has unique strengths and weaknesses. The low-sensitivity of standard Mössbauer spectroscopy precludes its use in spatially resolving brain Fe, and the requirement for ^{57}Fe-enrichment limits the technique (for practical reasons) to the study of rodent brains. Although it might be possible to study micro-dissected regions of a mouse or rat brain, this would take many animals and thus we have focused in this initial study on whole intact mouse brains. Thus, our results reflect the *average of all of the ^{57}Fe nuclei distributed inside the brain, without any spatial resolution*. Mössbauer spectroscopy also has distinct and powerful advantages, relative to these other spectroscopic methods, in its ability to resolve different types of Fe centers in the brain and to determine precisely the percentage of each type of Fe present. No other method can compete with Mössbauer spectroscopy in this regard.

Comparison to Previous Mössbauer Studies

The only type of Fe observed in previous Mössbauer studies of the brain was a sextet due to ferritin or ferritin-like Fe (*15, 39, 40*). The Mössbauer spectra presented here are significantly different in that other types of Fe were observed. Why none of the previously published spectra of brain displayed the CD, a heme quadrupole doublet, or

NHHS Fe^{II} species is puzzling but perhaps rationalizable. Previous studies utilized human brains which were unenriched in ^{57}Fe; this diminished the spectral quality greatly such that minor species, *e.g.* NHHS Fe^{II}, could have gone undetected. That does not explain why intense features, like those originating from heme centers or the CD, would not have been observed. We suspect that blood would have been drained from postmortem human samples, explaining the absence of spectral features due to hemoglobin. Previous spectra were exclusively obtained on Fe-rich regions of the brain (*e.g.* the substantia nigra), which may be dominated by ferritin Fe. The averaged Fe content of the entire brain may not be dominated by ferritin to this extent. More speculatively, the human donors were generally at the end of their natural lifespan, and older brains may possibly contain more ferritin than younger and middle-aged ones, the age periods we have studied here (*41*). Finally, the concentration of Fe in the average human diet may be higher, relatively speaking, than in our mouse chow, which could translate into relatively more ferritin and less CD in the human brain. Further studies are required to examine each of these possibilities.

Incorporation of Fe into the Brain

In this study, we found that young mouse brains exchanged Fe rapidly during the rapid growth phase, including the *export* of Fe. This resulted in an overall *decline* in the concentration of Fe in the brain. During this period, the brain appears to grow faster than could be maintained by the rate of Fe import, such that ferritin stores were activated. With age, the dynamic exchange of Fe slows, brain growth slows, and the concentration

of Fe in the brain recovers. During the first month of life, the proportion of stored Fe declines while the proportion of mitochondrial Fe increases. As the animals become adults, the proportion of stored Fe increases again. In our study, the concentration of mitochondria did not decline noticeably up to 58 wks; we are currently investigating whether mitochondrial levels decline towards the end of the animal's natural lifespan, as has been reported (*11*).

A decline of Fe concentration in the brain immediately after birth has been reported (*42-44*). Keen and Hurley measured age-dependent brain Fe concentrations in hybrid mice (*45*). At birth, Fe concentrations were 17.3 μg Fe/gm brain wet wt (which corresponds to 330 μM using the same density assumed here). By days 5–8, the brain contained 8.6 μg Fe/gm (160 μM). By day 60, [Fe] returned to newborn levels.

Burst of Mitochondriogenesis

In yeast cells, the Mössbauer CD and HS heme doublet, the g = 1.93 and 1.86 EPR signals and the heme *a*, *b*, and *c* UV-vis signals arise primarily from the mitochondrial respiratory complexes (*24*), and so we have assigned the analogous features in brain spectra similarly. The intensity of these signals, considered collectively, undoubtedly reflects the concentration of mitochondria in the brain. The ferritin-like sextet in the Mössbauer spectrum reflects brain Fe that is stored. These assignments are supported by a recent study of the ironome of human Jurkat cells and their isolated mitochondria (*46*).

Our results show that most of the Fe in the brain of prenatal and newborn mice is stored, and that during the first month of life, the proportion of stored Fe declines while the proportion of mitochondrial Fe increases. As the animals move into adulthood, the proportion of stored Fe in the brain increases again. We did not detect an overall decline in the concentration of mitochondria with age up to 58 wks; further studies are underway to determine whether mitochondrial levels decline towards the end of the animal's natural lifespan. Mitochondrial levels have been reported to decline with age due to mitophagy (*11*).

These results, in conjunction with those of the ^{57}Fe incorporation study, suggest a connection between this burst of mitochondriogenesis and an increase in brain activity (Figure B5). Before birth and immediately thereafter, the level of brain activity is low and so might be the demand for energy. During this period, Fe is slowly imported into the brain where most of it is stored as ferritin or ferritin-like material. During the first few weeks of life, there is an increased level of brain activity as the animal's eyes open and they explore their environment. The increased brain activity increases the demand for more chemical energy, prompting a burst of mitochondriogenesis. This demand for Fe is beyond that at which Fe can be imported into the brain. Thus, the brain draws upon its Fe stores to build the requisite Fe/S clusters and heme centers. The scarcity of Fe is exacerbated by the rapid increase of brain volume during the same period, resulting in the overall decline in the Fe concentration in the brain. Eventually, the burst of mitochondriogenesis slows, as does the rate of brain growth. The brain replenishes its Fe

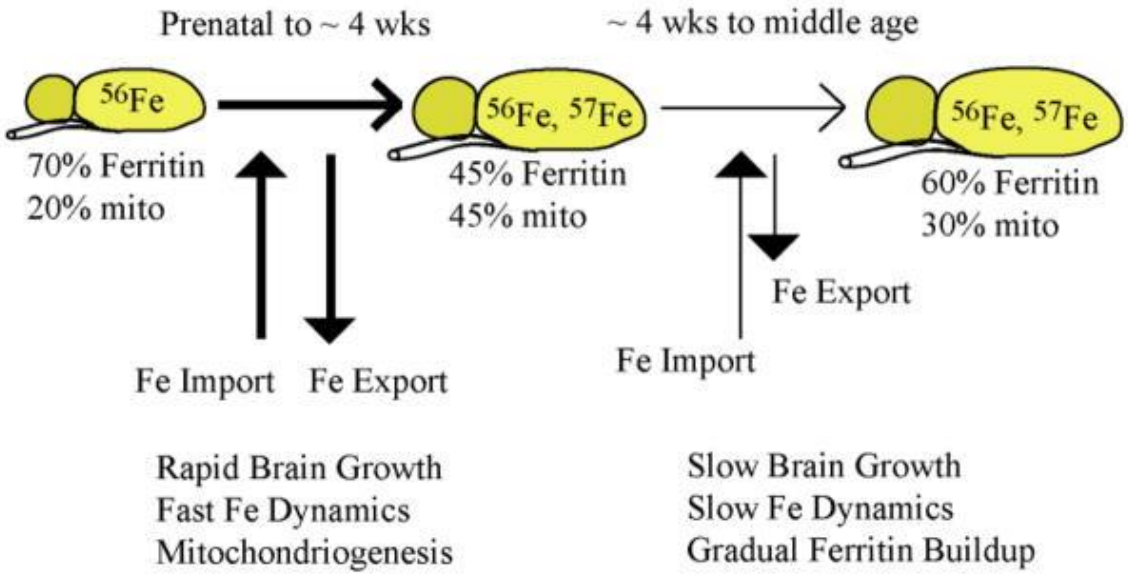

Figure B5. Mössbauer spectra of brains isolated at different ages. a, -1 wk; **b**, 1 wk; **c**, 2 wks; **d**, 4 wks; **e**, 24 wks; **f**, 60 wks. All samples were collected at 6 K, 0.05 T, and applied fields were parallel to the gamma radiation. The vertical dashed line shows the position of the high-energy line of the central doublet. The arrow shows the position of the nonheme HS Fe^{II} feature.

stores, *via* the slow import of Fe from the blood, and it reestablishes a higher overall Fe concentration.

This model is consistent with previous results. Pysh and co-workers used electron microscopy to determine the proportion of rat cell volume (in the inferior colliculus) due to mitochondria during different stages of development (*47*). The mitochondrial profile number was relatively low during the first few postnatal days but increased rapidly thereafter, leveling off at *ca.* 25 days postnatal. The mitochondrial volume fraction increased 6-fold, reaching 9% of tissue volume in adults. Interestingly, there was no correlation of mitochondria with synapse *concentrations*; rather, the rate of mitochondriogenesis correlated with increased levels of synaptic *activity*.

Effect of Iron Deficiency

Our results indicate that the regulation of brain Fe is sensitive to dietary changes. The brain responds to Fe deficiency by reducing levels of stored ferritin Fe while maintaining normal mitochondria levels. Ten-day old rats fed an Fe-deficient diet for 28 days showed a 27% decline in non-heme brain Fe,(*48*) similar to the 25% decline that we observed. Interestingly, in our study, the concentration of mitochondria in Fe-deficient brains was actually *higher*than observed in Fe-sufficient animals at any developmental stage examined. Explaining this counterintuitive result will require further study, but Fe regulation in the brain is undoubtedly complex, and the brain is probably protected from organism-level Fe deficiencies. In other studies, levels of the brain Fe-containing proteins tyrosine hydroxlase, tryptophan hydroxylase, monoamine

oxidase, succinate hydroxylase and cytochrome *c* in Fe deficient animals were also normal (*49*). Mackler *et al.* (*50*) reported that the levels of cytochromes *a* and *c* were normal under Fe deficient conditions, and that the level of cytochrome *b* was only slightly reduced relative to that in Fe-sufficient mitochondria. Neurological problems may only arise if the Fe deficiency is so severe that all storage forms of Fe in the animal have been exhausted and the brain can no longer be protected from the deficiency.

Mononuclear Nonheme High-spin Ferrous and Ferric Species

Our results indicate the presence of substantial amounts of NHHS Fe^{II} in the mouse brain. NHHS Fe^{II} complexes are generally less tightly coordinated than LS complexes and they exhibit more rapid ligand-exchange. Such properties would be expected for trafficking Fe and for complexes that undergo Fenton chemistry. Three of our Mössbauer spectra clearly indicate the presence of substantial concentrations of NHHS Fe^{II} species in the brain (−1 wk, 3 wks, and Fe-deficient). In these cases, the concentration of all NHHS Fe^{II} species in the mouse brain was ~20 μM. The NHHS Fe^{II} doublets were broad, suggesting that many NHHS Fe^{II} species contribute. The NHHS Fe^{II} doublet in the other brain Mössbauer spectra were present but less well resolved.

The g = 4.3 EPR signal was present in every brain homogenate examined; this indicates the presence of HS Fe^{III} ions with rhombic symmetry in the brain. The quantified intensity of this signal indicates that these Fe^{III} species are present at a combined concentration of ~100 nM. A portion of these species are undoubtedly

Fe^{II} and Fe^{III} ions bound tightly in the active site of enzymes in the brain; perhaps some is present as Fe^{III} transferrin (*51*). Another portion may be involved in trafficking and/or the Labile Iron Pool (LIP) (*52-54*). Such species have not been observed in previous Mössbauer and EPR studies of the brain (*55*).

Other groups have reported the presence "chelatable", "free", "labile" or "loosely-bound" Fe in the brain. These pools of Fe are defined operationally, *i.e.* as the Fe in supernatant fractions of brain extracts treated with Fe chelators and then spun by centrifugation. Sohal *et al.* (*56*) measured bleomycin-chelated and ferrozine-chelated (called nonheme) Fe in the mouse brain, and observed an age-dependent increase of nonheme Fe but not bleomycin-chelatable Fe. Magaki *et al.* (*57*) measured "loosely bound iron" and "non-heme iron", defined operationally, in 6, 12, and 24 week old mouse brains. They found that loosely bound Fe represented 20%–30% of non-heme Fe, with the latter type of Fe increasing with age and the former decreasing slightly or remaining constant. Using chelator induced calcein-quenching, Kaur *et al.* (*58*) found that an operationally defined LIP in mouse brain increased with age. Other LIPs are defined by staining the brain directly. Using high-resolution histological staining methods, Meguro *et al.* (*21*) reported substantial amounts of (again, operationally defined) nonheme Fe^{II} and Fe^{III} species distributed heterogeneously throughout the rat brain. They determined that the levels of these species increase with the age of the animal.

All of these previously reported LIPs, defined by their chelation ability, differ fundamentally from the mononuclear HS Fe^{II} and Fe^{III} species observed here. The

species we observed are defined solely by their spectroscopic properties, not by their chelation properties. Comparing the two will require establishing the chelation properties of the species we observe and the spectroscopic properties of the chelatable Fe species reported previously.

Spin Radical Species

The radical species detected here may be physiologically relevant since samples were prepared in the absence of O_2 which minimizes the possibility of generating artifactual radical signals during sample preparation. Transient radicals in the brain have been detected using spin-probes (*59*) but the radical detected here is fundamentally different because it is stable in the absence of such probes (radical probes trap unstable radicals). Radical species are cleared from the brain faster in young mice than in old, suggesting that the reducing capacity of the brain may decrease with age (*60*). These changes may be related to the age-dependent increase in the stable radical species that we observed by EPR. Most theories of aging involve the age-dependent accumulation of ROS (*61*), which could be responsible for the gradual build-up of the stable radical.

Conclusions

Our study provides new insights into Fe metabolism, trafficking and homeostasis in the brain. We have enriched mice with ^{57}Fe and have used Mössbauer spectroscopy, along with EPR, UV-vis, and ICP-MS, as biophysical probes of the types of Fe centers contained in the mouse brain at different stages of development. We quantified the rates

of Fe incorporation into the brain, and found that Fe is imported slowly, relative to the rate of import into other organs. The slow rate of Fe incorporation into the brain is probably due to the tight regulation at the BBB. The rate of Fe incorporation is biphasic, with a rapid phase occurring in very young animals and a slower phase occurring in adult animals. During the rapid Fe-incorporation phase, the brain grows rapidly, and the level of brain activity increases. As such, ATP-generating mitochondria are being generated rapidly. This creates a high demand for Fe. This demand cannot be met solely with newly imported Fe. As a result, the concentration of Fe in the brain declines and some ferritin-stored Fe is released and used for mitochondriogenesis. As brain growth and mitochondriogenesis slow, the Fe import rate becomes sufficient to allow some of the imported Fe to be stored once again.

The brain contains substantial concentrations of NHHS Fe^{II} and Fe^{III} species a portion of which may be used in trafficking and homeostasis. Iron in this category is known to undergo the Fenton reaction to generate reactive oxygen species which is associated with aging. Further studies are required to determine whether the detected Fe species actually participate in such reactions. We observed a stable organic radical EPR signal which increased with age, consistent with the ROS theory of aging. Only ferritin-like Fe was observed in previous Mössbauer studies of the human brain, possibly because only Fe-rich regions were examined, and/or because of differences in the age and/or diets of the mice *vs.* human involved. We demonstrated that the Fe content of the brain is sensitive to diet, in that stored Fe was preferentially utilized when mice were Fe-deficient.

The methods developed here are widely applicable, and could be applied to any and all mouse organs, including those found in transgenic animals with various Fe-associated disorders. This approach may reveal differences in Fe metabolism, trafficking and/or regulatory homeostasis, and thus significantly impact the mechanistic study of Fe-related diseases.

APPENDIX C

LOW-MOLECULAR-MASS METAL COMPLEXES IN THE MOUSE BRAIN[3]

Abstract

The presence of labile low-molecular-mass (LMM, defined as < 10 kDa) metal complexes in cells and super-cellular structures such as the brain has been inferred from chelation studies, but direct evidence is lacking. To evaluate the presence of LMM metal complexes in the brain, supernatant fractions of fresh mouse brain homogenates were passed through a 10 kDa cutoff membrane and subjected to size-exclusion liquid chromatography under anaerobic refrigerated conditions. Fractions were monitored for Mn, Fe, Co, Cu, Zn, Mo, S and P using an on-line ICP-MS. At least 30 different LMM metal complexes were detected along with numerous P- and S- containing species. Reproducibility was assessed by performing the experiment 13 times, using different buffers, and by examining whether complexes changed with time. Co exhibited 11 LMM complexes with molecular masses < 4 kDa; Fe and Mn each exhibited 2 - 3 such complexes. Mo contained the molybdopterin cofactor and another LMM complex. No Cu or Zn complexes in this very low mass range were observed. These two metals were present in what appeared to be protein-bound complexes with masses ranging from 4 – 20 kDa. Co was the only metal for which the "free" or aqueous complex was reproducibly observed. Aqueous Co may be sufficiently stable in this environment due

[3] McCormick, SP; Chakarabarti, M; Cockrell, AL; Park, J; Lindahl, LS; Lindahl, PA. (2013) Low-molecular-mass metal complexes in the mouse brain. *Metallomics 5*, 232-241. http://pubs.rsc.org/en/Content/ArticleLanding/2013/MT/c3mt00009e#!divAbstract.Reproduced by permission of The Royal Society of Chemistry.

to its relatively slow water-exchange kinetics. Attempts were made to assign some of these complexes, but further efforts will be required to identify them unambiguously and to determine their functions.

Introduction

Transition metals such as iron, copper, manganese, molybdenum, and cobalt are critical components of cells and super-cellular structures like the brain. They tend to be redox-active and have excellent catalytic properties that render them common residents in the active-sites of enzymes. However, many of those same properties can be deleterious to the cell, especially when their ligands are coordinated weakly. Labile Fe^{II} and Cu^{I} complexes in particular can react with H_2O_2 to generate •OH via the Fenton reaction (*62*, *63*). Hydroxyl radicals and other reactive oxygen species (ROS) can damage DNA, proteins and membranes. Thus, trafficking newly-imported metal ions from the plasma membrane to various apo-protein targets requires chaperones that bind these metal ions weakly enough so that they can be transferred from one species to the next while simultaneously avoiding dangerous side-reactions. Substantial progress has been made in understanding how this happens in cells, but many molecular-level details, e.g. the specific metal trafficking species involved and their exact cellular functions, remain unknown (*64*). Nowhere is metal ion trafficking more important than in the brain, since many neurodegenerative diseases are associated with metal ion accumulation (*65*, *66*).

The concentration of Fe in the brains of mice fed standard (50 mg Fe/kg) chow is *ca*. 350 μM, with ~ 50% present as ferritin, ~ 40% as Fe/S clusters and heme centers,

and 5% - 9% as mononuclear nonheme high-spin (NHHS) Fe^{II} and Fe^{III} species.(*67*) Ferritin is a protein complex that stores Fe in cells. Most Fe/S clusters and heme centers reside in mitochondrial respiratory complexes where they help provide chemical energy for the brain. Some NHHS Fe^{II} ions are found in the active sites of enzymes while others may be involved in trafficking. NHHS Fe^{II} complexes often have weakly-coordinating ligands and engage in Fenton chemistry. Fe in the brain is heterogeneously distributed (*21*). The reasons for this are unknown, but spatially-dependent differences in traffic patterns or flows are implied. The concentration of Fe in the *Substantia Nigra* (SN) increases in Parkinson's Disease (PD), in association with the loss of mitochondrial function and damage to dopaminergic neurons (*68*).

Trafficking of metals involves protein chaperones that bind metal ions in one location of the cell and release them in another, e.g. to an apo-protein binding site during folding and maturation (*69*). Whether trafficking also involves low-molecular-mass (LMM) metal complexes is less certain. Such species may exist in aqueous regions of a cell, where they might interact with protein chaperones and/or pass through membrane-bound transporters. For example, Mrs3p/Mrs4p are membrane-bound mitochondrial proteins that transport Fe from the cytosol to the mitochondrial matrix (*70*). Although the structures of these two proteins are unknown, homologous structures suggest that the channels that pass through them are too small to accommodate a protein (*70*). This suggests that LMM Fe complexes, consisting of the metal ion coordinated by small organic or inorganic ligands, and/or by waters, pass through these transporters.

If LMM metal complexes are involved in trafficking, they should have weakly coordinating ligands that can be displaced by strong chelating agents. However, this form of Fe is also likely to engage in Fenton chemistry. Pamp *et al*.(*71*) concluded that labile Fe constitutes 0.2 – 3% of overall cellular Fe. In human cells containing 400 μM Fe,(*46*) this corresponds to a collective labile Fe concentration of 1-10 μM. Using fluorescence sensors, Petrat *et al.* found that the concentration of chelatable iron in the cytosol of intact hepatocytes was in the same range, namely 5.8 ± 2.6 μM.(*54*) According to Rauen *et al.* about 1% of cellular Fe exists in a pool that is not bound to ferritin or other proteins.(*72*) They estimate that the concentration of chelatable Fe in liver mitochondria and in the cytosol is 12 μM(*73*) and 6 μM(*54*), respectively. Using chelators of different Fe affinities had no effect on the estimated size of the mitochondrial chelatable Fe pool, suggesting that the determined pool concentration (16 ± 2 μM) represents its "true" size. These estimates are substantially less than the concentration of NHHS Fe^{II} ions present within respiring yeast mitochondria (*ca*. 150 μM), as quantified by Mössbauer spectroscopy.(*74*) Some Mössbauer-detectable NHHS Fe^{II} species may be protein-bound and not labile. Differences may also arise from the different organisms probed and/or different cellular metabolic growth modes. The Mössbauer-detected NHHS Fe^{II} ions are chelated by 1,10-phenantroline (Phen),(*74*) which attenuates Fe/S cluster synthesis,(*75*) strongly suggesting that these ions serve as feedstock for this process.

In most cases, the exact roles of LMM Fe complexes in cells and the brain are unknown. However, patterns are emerging suggesting involvement in development,

aging and neurodegenerative diseases. Kaur *et al.*(*58*) found an increase in the labile iron pool (LIP) in the brains of older mice, suggesting that such ions might be involved in aging. Wypijewska *et al*.(*76*) found increased LIP in the SN of PD patients. Sohal *et al.*(*56*) and Magaki *et al*.(*57*) reported that 20% - 30% of nonheme Fe in the developing mouse brain was labile. Meguro *et al.*(*21*) found that chelatable nonheme Fe^{II} and Fe^{III} species were distributed heterogeneously throughout the rat brain and that the concentration of these species increased with age. Huang *et al.*(*77*) reported that psychological stress (generated using electric shock) expands the LMM Fe^{III} and Fe^{II} pools in the cerebral cortex, hippocampus and striatum, as detected by Perl's and Turnbull's stains, respectively. Nothing is known regarding the particular complexes involved in these effects.

Zn is not formally a transition metal, but this redox-inactive divalent metal ion also plays critical roles in brain metabolism.(*78*) The concentration of Zn in the mouse brain is *ca*. 320 μM,(*67*) most of which is bound to metalloproteins. Metallothioneins are the primary intracellular Zn-buffering proteins. Metallothionein III in the brain has a molecular mass (MM) of *ca*. 7 kDa and contains 8-11 Zn binding sites.(*79*) Zn is also found in aggregated amyloid beta protein filaments in Alzheimer's Disease (AD), and is associated with amyotrophic lateral sclerosis, epilepsy, strokes, depression, and schizophrenia.(*80*) Protein-based and non-protein-based fluorescent probes have been used to image mobile Zn ions in cells and tissues.(*81, 82*) Palmer and coworkers targeted protein-based FRET fluorescence sensors to the mitochondria, ER and Golgi of HeLa cells, and estimated the presence of such pools at low pM concentrations.(*83, 84*) The

detected concentration of cytosolic Zn was also extremely low, namely 80 pM. In contrast, high concentrations of Zn (estimated to be mM levels) are found in synaptic vesicles within neurons that use glutamate as a neurotransmitter.(*85*) The synaptic Zn pool has been detected by Zn-specific fluorescent dyes.(*86, 87*) These vesicles are located primarily in the cerebral cortex and limbic structures. Labile Zn ions enter these vesicles via the membrane-bound protein ZnT3 and are released upon synaptic activation.(*88*) This pool modulates the overall excitability of the brain, and is involved in signal transduction, memory and learning.

Copper is present in the mouse brain at low concentrations (~ 5 μM)(*67*) but it is no less important than Fe or Zn. Cu plays essential roles in respiration, oxidative stress response, and other enzymatic activities.(*89*) Cu ions in the brain parenchyma are involved in the metabolism of neurotransmitters and myelination.(*90*)

Numerous proteins are known to be involved in Cu trafficking. Ctr1 is a transporter on the plasma membrane that brings Cu into the cell.(*91*) Once in the cell, Cu can be stored in metallothionein, transported to mitochondria, incorporated into apo-Cu/Zn SOD, or transported to the Golgi apparatus for export from the cell.(*90*) Cu-containing ceruloplasmin helps distribute and metabolize Cu, and it may help Fe efflux from the brain.(*92*) Cox17 is an 8.0 kDa protein that transfers cytosolic Cu to mitochondria for incorporation into apo-cytochrome c oxidase.(*93*) CCS1 is a trimer with 9 kDa subunits which functions to insert Cu into apo-Cu/Zn SOD.(*94, 95*) The concentration of CCS1 is sensitive to intracellular levels of Cu. Atx1 is an 8.2 kDa copper-binding chaperone that transports Cu to the Cu-ATPases in the trans-Golgi

network. These proteins, Atp7a and Atp7b, deliver Cu for incorporation into proteins.(*96*) When intracellular Cu concentration exceeds some setpoint value, they export Cu from the cell.

The presence of a labile Cu pool is less certain than that for Fe or Zn. Using highly selective ratiometric fluorescent reporters for Cu^{I} ions, Domaille *et al*. found an ascorbate-induced increase in the labile Cu^{I} pool in HEK 293T cells.(*97*) Hirayama *et al*. used a fluorescent sensor to visualize labile Cu^{I} pools in mice.(*98*)

The mouse brain contains ~14 μM Mn, ~ 400 nM Mo, and ~ 30 nM Co, respectively.(*67*) Some Mn is incorporated into mitochondrial superoxide dismutase (SOD2) which functions to diminish oxidative stress.(*99*) Mn levels in the brain are elevated in patients with AD and Prion disease.(*100*) Mo is coordinated to the molybdopterin cofactor in the active site of various molybdenum hydroxylases.(*101*) A deficiency of the molybdopterin cofactor causes seizures and death in newborns.(*102, 103*) Cobalt metabolism in the brain includes lipid biosynthesis and one-carbon metabolism.(*104, 105*) Co is present in coenzyme B_{12} bound in methionine synthase.(*106*) This enzyme functions in methionine metabolism, which includes methyl group transfer reactions involving choline, folate and S-adenosyl-methionine.(*107*)

In this study, we have evaluated the presence of LMM metal complexes in the mouse brain. Rather than using specific chelators to detect such species, we have detected them using anaerobic liquid chromatography with an on-line ICP-MS. We report here that the brain contains a limited number of LMM Fe, Co, Mn, Mo, Cu and Zn

complexes. These complexes were enumerated and characterized in terms of concentration and approximate MM. A few species were tentatively assigned.

Experimental Procedures

Chemicals and Standards

The water used was house-distilled, deionized using ion-exchange columns (Thermo Scientific 09-034-3), and then distilled again using a sub-boiling still (Savillex DST-1000). Cytochrome c (*Saccharomyces cerevisiae*), aprotinin (bovine lung), ATP, ADP, AMP, and cyanocobalamin were from Fisher Scientific (Pittsburgh, PA, USA). Inositol hexaphosphate (IP_6), oxidized and reduced glutathione, sodium molybdate, and sodium phosphate were from Sigma Aldrich (St. Louis, Mo, USA). The molybdopterin cofactor was isolated as described(*108*) from xanthine oxidase. The sample buffer was 20 mM Tris (Fisher) pH 7.4.

Animal Care and Dissections

ICR (Imprinting Control Region) outbred mice were raised and manipulated in accordance with the TAMU Animal Care and Use committee (AUP 2010-226). Mice were housed in disposable plastic cages (Innovive Innocage Static Short) with all-plastic water bottles and plastic feeders with zinc electroplated reinforcements. Mice were fed Fe-deficient chow (Harlan Laboratories, Inc. Teklad ID TD.80396.PWD) supplemented with 50 mg/Kg of Fe citrate. Mice were euthanized by an intraperitoneal injection of ketamine and xylazine as described.(*67*) Immediately after breathing ceased and the

heart stopped beating, animals were imported into a refrigerated (5–10 °C) Ar-atmosphere glove box (MBraun Labmaster) containing 2–20 ppm O_2, as monitored by a Teledyne O_2 analyzer (Model 310). From this point forward, all sample manipulations were performed in a glove box unless mentioned otherwise.

Preparation of LMM Brain Extracts

Animals were perfused with heparinized Ringer's buffer at 1.0 mL/min for 0.5 min/g mouse, and then dissected as described.(*67*) Immediately after isolation, 3 - 4 brains were added to a known volume (2 – 3 mL) of degassed 20 mM Tris buffer (pH 7.4). The solution was homogenized for 1 min using a plastic rotary knife inserted into a tissue grinder (Omni TH). The resulting homogenate was disrupted by nitrogen cavitation (model 4639, Parr Instruments) at 800 psi for 10 min. The resulting extract was treated with Triton X-100 and Sodium deoxycholate (final concentrations of 1% (v/v) and 1% (w/v), respectively) for 10 min. The sample was removed from the box in an O-ring-sealed centrifuge bottle and spun at 110,000×g for 30 min. The bottle was returned to the box and the resulting supernatant fraction (~ 3 mL) was transferred to a stirred cell concentrator (Amicon Model 8003, Millipore) fitted with a 10 kDa cutoff membrane (YM-10, Millipore). The supernatant was passed through the membrane with a head pressure of 90 psi Ar, and ~ 2 mL of the flow-through solution (FTS) was collected in a plastic screw-top tube. The tube was sealed with electrical tape, placed inside of a second container that was then sealed, removed from the box, and immediately imported into a second glovebox that contained the LC. In one experiment,

the FTS was split into two aliquots, one of which was spiked with 100 µL of 180 nM stock solutions (prepared in 20 mM Tris pH 7.4) of $FeSO_4$, $CuCl_2$, $MnCl_2$, $CoCl_2$, $ZnCl_2$ and Na_2MoO_4. After 3 hrs, aliquots were injected, one after the other, into the LC-ICP-MS system.

Elemental Concentrations in Flow-Through Solutions

Aliquots (150 µL) of the FTS for each run were placed into 15 mL plastic screw-top tubes (BD Falcon) containing 100 µL of concentrated trace-metal-grade (TMG) nitric acid (6.4 M final concentration). After ~ 12 hr at 90 ºC, samples were diluted with 9.75 mL of distilled-and-deionized water, affording a final acid concentration of 0.14 M. Calibration curves were prepared from standard solutions containing P, S, Co, Cu, Zn, Fe, Mn, and Mo (Inorganic Ventures, Christiansburg Virginia, USA) at known concentrations, prepared in trace-metal-grade nitric acid and diluted using distilled-and-deionized water. Data were collected in He collision mode using ICP-MS (model 7700x, Agilent Technologies, Tokyo, Japan). Elemental concentrations were determined using the calibration curve. Values obtained were adjusted for dilution factors.

Chromatography and Instrumentation

HPLC separations were carried out in a refrigerated Ar-atmosphere glove box (Labmaster, Mbraun USA) using an Agilent 1200 Bioinert LC composed of a metal-free Infinity 1260 Quaternary Pump equipped with a manual injection valve fitted with a 500 µL PEEK injection loop. Two size-exclusion Superdex Peptide GL 10/300 columns (300

× 10 mm, GE Life Science, USA) were combined in series using a male-to-male union connector. The mobile phase was 20 mM Tris buffer (pH 7.4). Post-column eluent flow (0.35 mL/min) was mixed in real-time with a solution of 4% trace-metal-grade nitric acid plus 100 μg/L ^{116}In, diluting the eluent 2-fold. The resulting solution flowed into an on-line inductively coupled plasma mass spectrometer (ICP-MS) (7700x, Agilent Technologies, Tokyo Japan), and ^{31}P, ^{34}S , ^{55}Mn, ^{35}Cu, ^{59}Co, ^{65}Zn, ^{95}Mo, $^{56/57}$Fe, and ^{116}In were detected. Indium was used as an internal standard to monitor plasma suppression. Other ICP-MS conditions: RF power, 1500 W; Ar flow rate, 15 L/min; collision cell He flow rate, 4.3 mL/min; sampling/skimmer cones, Pt, Pt; dwell time, 0.2 sec; internal standard pump rate, 0.35 mL/min.

The column was cleaned after each run using 10 column volumes (CVs) of a chelator cocktail at a flow rate of 150 μL/min and then regenerated with the elution buffer (20 mM Tris, pH 7.4). The chelator cocktail was composed of 20 mM Tris pH 8.0 plus 10 μM each of ethylenediaminetetraacetic acid (EDTA), ethylene glycol tetraacetic acid, tetrakis-(2-pyridylmethyl)ethylenediamine (TPEN), Phen and 2,2'-bipyridine.

Molecular Mass Calibration

The MM associated with each chromatographic peak was calculated using a standard curve constructed from 14 known species (data not shown). Standard stock solutions were prepared in 20 mM Tris pH 7.4, affording concentrations ranging from 1 - 200 μM. Each solution was injected individually onto the column. Elution volumes V_e were assigned based either on ICP-MS detector response or on UV-vis spectral intensity.

In cases where multiple forms were evident (GSH, GSSG, ATP, ADP, and AMP), the peak with the MM nearest to the known mass of the species was assigned to that species. Void volume V_0 was determined using Blue Dextran (MM 2000 kDa). The logarithm of the MM was plotted *vs*. the ratio V_e/V_0 (Data not shown). The best-fit linear regression curve was constructed through the data points.

Results

The objective of this study was to determine whether the mouse brain contained LMM transition metal complexes detectable by LC-ICP-MS. We avoided oxidizing Fe^{II}-containing species due to concern that endogenous ligands might dissociate upon oxidation and be replaced by waters, rendering insoluble aqueous Fe^{III} ions that would adhere to the column. Once animals were euthanized, all procedures involving samples were performed in a refrigerated Ar-atmosphere glove box. In each experiment, isolated brains were homogenized and centrifuged, and then supernatants were passed through a 10 kDa cut-off membrane. Because such complexes could potentially be highly dynamic and unstable, samples were prepared for the LC as fast as possible; FTSs were injected onto the LC column *ca*. 3 hrs after animals were euthanized. Experiments were performed 13 times to assess reproducibility.

Elemental concentrations in the FTSs were determined and corrected for dilution, affording estimates for the collective concentrations of all the LMM species for these elements in the brain. The results were (in μM): Co, 0.06 ± 0.01; Mo, 0.3 ± 0.1; Mn, 0.8 ± 0.1; Cu, 4.2 ± 0.2; Fe, 18 ± 1; Zn, 44 ± 7; S, 1500 ± 70; and P, 11,000 ± 1000.

Assuming the total metal concentrations in the brain mentioned in the Introduction (except for Co, which was found in the current study to be present in the brain at 88 ± 5 nM), the percentages of these elements in the brain that passed through the LMM membrane are: Co, 66 ± 10; Mo, 67 ± 25; Mn, 6 ± 1, Cu, 84 ± 12; Fe, 5 ± 0.4; Zn, 14 ± 2; S, 9 ± 2; P, 12 ± 3. Thus, LMM species represent large percentages of total Co, Mo and Cu ions in the brain, but small percentages of Mn, Fe, Zn, S and P. For Fe in particular, the calculated percentage is comparable to previous chelation-based determinations in human cells (see Introduction).

Given the potential lability of these metal complexes, we evaluated the percentage of the metals that eluted from the column, normalized to the amount loaded. The averages of three runs were: Mo, 74 ± 12; Mn, 93 ± 4; Fe, 89 ± 7; Co, 93 ± 4; Cu, 84 ± 6; Zn, 92 ± 3; P, 91 ± 3 and S, 92 ± 6, respectively. These values indicate that the majority of the metal-containing species in the FLSs eluted from the column. The small percentage of each metal that did not elute demonstrates the importance of washing the column extensively between runs.

A total of 13 runs were performed; of these, 11 were analyzed. The two excluded runs had peak linewidths 2 - 3 fold greater than the others (suggesting a problem with the column). Thus, our analyses were essentially free of subjective bias. Reproducibility was acceptable but there were noticeable variations. P and S chromatograms were the most reproducible, in that the same sets of peaks, with similar relative area-ratios, were observed in each run. The V_e associated with each peak were not perfectly matched from one chromatogram to another, and so small shifts in the volume dimension,

corresponding to no more than 0.24 mL, were allowed to align S and P peaks to the greatest extent possible. The identical alignment offsets were used for the corresponding Mo, Mn, Co, Fe, Cu and Zn chromatograms generated in the same run. In this way, the S and P chromatograms served as an internal calibration to align the metal-based chromatograms. Data sets were not adjusted further.

We considered that some peaks might arise from degradation products of the brain, despite using freshly prepared FTS and working quickly. To examine this, a FTS was left for 13 days in a refrigerated box prior to passage through the column. The resulting chromatograms, compared to those obtained using fresh FTS, revealed virtually no change in relative peak areas and distributions (data not shown). We conclude that our samples did not degrade on the time scale of the experiment.

We also considered that our results might depend on the FTS buffer employed. To examine this, the buffer was switched from Tris to HEPES (both 20 mM at pH 7.4). The resulting chromatograms revealed no significant differences (data not shown). Remaining run-to-run variations probably arose from animal-to-animal differences. To minimize these, mice were euthanized at approximately the same time of day (10 am – 12 noon). Age and gender differences were considered as variational factors, but no correlations were obvious. In analyzing datasets, we assumed that any peak observed in $\geq$ 50% of the metal-matched datasets represented a real species in the brain. Peaks observed in 25% - 50% of chromatograms were viewed as probably reflecting real species. Peaks observed in < 25% of chromatograms were considered artifacts and were not included in downstream analyses. Averages for peaks that were reproducibly present,

according to these criteria, are summarized in Table 1. MMs for each species were estimated from V_e and the best-fit linear regression standard-curve line.

Representative chromatograms of the FLS for each element, along with various standard compounds, are shown in Figures C1 – 9. The P chromatogram (Figure C1) exhibited two major regions of peaks. The high-molecular-mass (HMM) region corresponds to P-containing compounds with MMs between *ca*. 13 - 6 kDa (21 – 25 mL). P-compounds with MMs between 4 - 0.2 kDa (27– 41 mL) are included in the low-molecular-mass (LMM) region. The intermediate-molecular-mass (IMM) region between 4 – 6 kDa was effectively devoid of peaks.

The ill-resolved shape of the HMM region suggested that multiple overlapping species contributed, and we did not attempt to decompose it. In contrast, the peaks in the LMM region were better resolved. These were simulated using the equation

$$I_V = I_0 + I_{\max} e^{-\left(\frac{V-V_0}{\omega}\right)^2} \qquad (1)$$

where ω is the width of the peak and I_V, I_0, and I_{max} are the detector responses at any volume V, at volume $V = 0$, and at the volume corresponding to the peak maximum, respectively. We integrated the total area under the chromatogram along with the relative areas under the individual LMM peaks such that the percentage of the total eluent P due to each LMM peak ($f_{cpd\text{-}i}$) could be determined. The concentration of each P-containing species represented by the LMM peaks in the brain ([Cpd_i]) was calculated using the equation

$$[Cpd_i] = f_{cpd-i} \cdot [P]_{fts} \cdot FD \qquad (2)$$

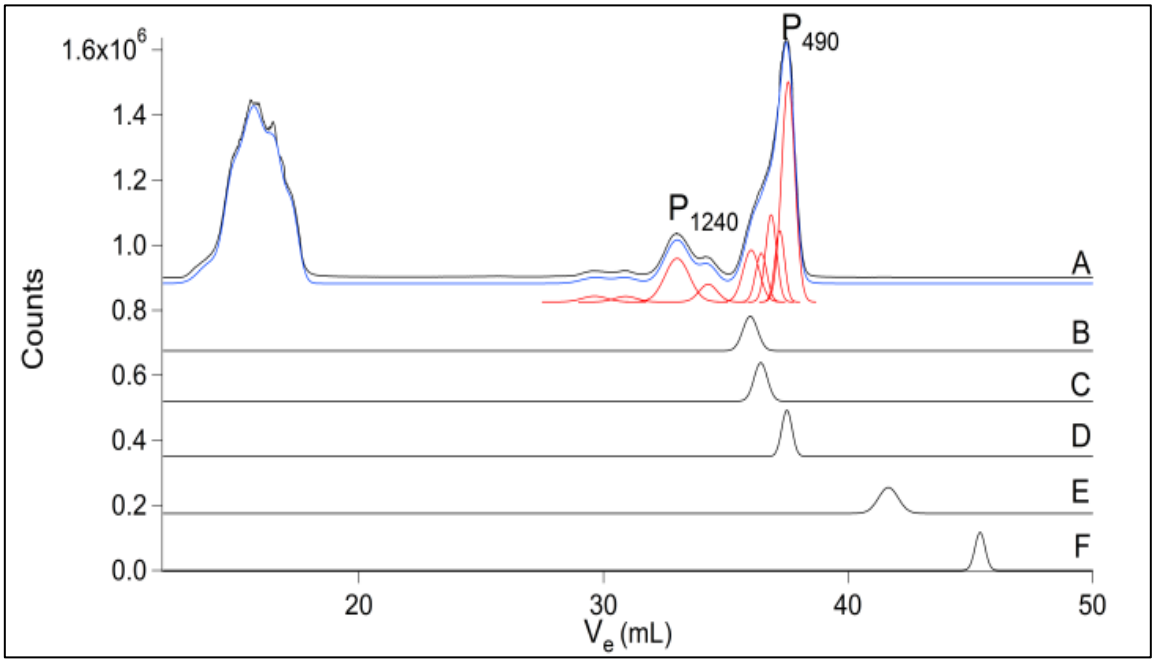

Figure C1. Phosphorus chromatograms of brain FTS and various phosphorus-containing compounds. A, brain FTS; B, IP_6; C, ATP; D, ADP; E, AMP, and F, HPO_4^{2-}. Red lines in Figures C1 - 8 are simulations representing the LMM species listed in Table C1. The blue line is the overall simulation.

Assigned Name	Peak Center (mL)	Peak Width (mL)	Molecular Mass (Da)	Area (%)	$[Metal]_{Brain}$ (μM)	Confidence (%)
P_{HMM}	V < 18 mL	N/A	24,000 – 48,000	43 ± 14	4600 ± 1500	100
P_{2490}	29.5 ± 0.3	0.6 ± 0.2	2490 ± 150	0.8 ± 0.5	90 ± 50	67
P_{1950}	30.7 ± 0.6	1.0 ± 0.5	1950 ± 240	1.2 ± 1	130 ± 110	92
P_{1240}	32.9 ± 0.4	0.7 ± 0.1	1240 ± 100	7 ± 3	760 ± 320	100
P_{1060}	33.7 ± 0.2	0.5 ± 0.1	1060 ± 40	4 ± 3	430 ± 320	41
P_{900}	34.5 ± 0.3	0.4 ± 0.1	900 ± 60	3 ± 2	320 ± 220	92
P_{630}	36.2 ± 0.2	0.5 ± 0.2	630 ± 30	19 ± 13	2000 ± 1400	83
P_{570}	36.7 ± 0.2	0.5 ± 0.2	570 ± 20	15 ± 11	1600 ± 1200	67
P_{530}	37.1 ± 0.1	0.5 ± 0.1	530 ± 10	14 ± 10	1500 ± 1100	50
P_{490}	37.5 ± 0.1	0.5 ± 0.2	490 ± 10	13 ± 13	1400 ± 1400	58
S_{HMM}	V < 18 mL	n/a	24,000 - 48,000	54 ± 10	800 ± 150	100
S_{1540}	31.8 ± 0.2	0.6 ± 0.1	1540 ± 76	2.4 ± 1	35 ± 15	100
S_{940}	34.3 ± 0.4	0.8 ± 0.4	940 ± 73	1.4 ± 1	21 ± 15	100
S_{570}	36.7 ± 0.1	0.4 ± 0.1	570 ± 5	22 ± 13	320 ± 190	92
S_{520}	37.1 ± 0.1	0.5 ± 0.1	520 ± 7	17 ± 11	250 ± 160	100
S_{370}	38.8 ± 0.2	0.7 ± 0.2	370 ± 14	5 ± 1	74 ± 74	100
Co_{HMM}	V < 18 mL	n/a	24,000 - 48,000	8 ± 7	0.005 ± 0.004	100
Co_{1640}	31.5 ± 0.8	0.5 ± 0.1	1640 ± 250	38 ± 16	0.020 ±0.009	100
Co_{1380}	32.4 ± 0.3	0.8 ± 0.3	1380 ± 80	18 ± 8	0.010 ± 0.004	100
Co_{1130}	33.4 ± 0.6	0.9 ± 0.5	1130 ± 140	15 ± 11	0.009 ± 0.006	100
Co_{920}	34.4 ± 0.5	0.5 ± 0.2	920 ± 90	3 ± 2	0.002 ± 0.001	92
Co_{900}	34.5 ± 0.3	1 ± 1	900 ± 60	2 ± 1	0.001 ± 0.0005	50
Co_{630}	36.2 ± 0.3	1 ± 1	630 ± 40	5 ± 5	0.003 ± 0.003	75
Co_{500}	37.4 ± 0.3	1 ± 1	500 ± 30	3 ± 3	0.002 ± 0.002	75
Co_{400}	38.4 ± 0.3	0.7 ± 0.7	400 ± 20	2 ± 2	0.001 ± 0.001	58
Co_{300}	39.7 ± 0.5	0.8 ± 0.5	310 ± 30	1 ± 1	0.0008 ± 0.0004	75
Co_{210}	41.6 ± 0.5	1.1 ± 0.9	210 ± 20	2 ± 2	0.001 ± 0.001	85
Co_{aq}	43.9 ± 0.5	1.0 ± 1.3	< 200	3 ± 3	0.002 ± 0.002	50

Table C1. Low-Molecular-Mass Metal Complexes in the Mouse Brain. Confidence was defined as the number of chromatograms for a given element in which the peak was present divided by the total number of chromatograms for that element, multiplied by 100.

Assigned Name	Peak Center (mL)	Peak Width (mL)	Molecular Mass (Da)	Area (%)	$[Metal]_{Brain}$ (μM)	Confidence (%)
Cu_{HMM}	V < 19.4 mL	n/a	24,000 – 48,000	60 ±16	2.6 ± 0.7	100
Cu_{19390}	19.5 ± 0.1	0.8 ± 0.6	19390 ± 440	23 ± 12	1.0 ± 0.5	100
Cu_{15670}	20 ± 0.2	0.6 ± 0.1	15670 ± 610	13 ± 5	0.6 ± 0.2	100
Cu_{8650}	23.4 ± 0.3	1.0 ± 0.2	8650 ± 500	2 ± 0.7	0.08 ± 0.03	100
Cu_{5680}	25.5 ± 0.2	0.6 ± 0.2	5680 ± 280	0.5 ± 0.3	0.02 ± 0.01	100
Cu_{4230}	26.9 ± 0.4	0.7 ± 0.3	4230 ± 350	0.5 ± 0.2	0.02 ± 0.01	100
Cu_{1020}	33.9 ± 0.7	0.4 ± 0.2	1020 ± 140	0.2 ± 0.6	0.01 ± 0.03	92
Cu_{370}	38.9 ± 0.2	0.6 ± 0.2	370 ± 20	0.8 ± 0.8	0.03 ± 0.03	100
Zn_{HMM}	V < 18 mL	n/a	24,000 – 48,000	86 ± 3	38 ± 1	100
Zn_{19630}	19.4 ± 0.4	0.6 ± 0.2	19630 ± 1610	8.5 ± 4	3.75 ± 2	100
Zn_{16000}	20.4 ± 0.5	0.8 ± 0.4	16000 ± 1640	5 ± 2	2.2 ± 0.9	92
Zn_{1760}	31.2 ± 0.5	0.6 ± 0.5	1760 ± 180	0.4 ± 0.2	0.18 ± 0.09	42
Zn_{400}	38.5 ± 0.1	0.4 ± 0.1	400 ± 8	0.2 ± 0.1	0.09 ± 0.04	67
Fe_{HMM}	V < 18 mL	n/a	24,000 - 48,000	98 ± 2	17.4 ± 0.4	100
Fe_{3320}	28.1 ± 0.4	0.6 ± 0.5	3320 ± 270	1.4 ± 1.2	0.2 ± 0.2	58
Fe_{1720}	31.3 ± 0.1	0.6 ± 0.2	1720 ± 40	0.3 ± 0.2	0.05 ± 0.03	58
Fe_{510}	37.3 ± 0.3	0.6 ± 0.4	510 ± 30	0.5 ± 0.3	0.09 ± 0.05	75
Mn_{HMM}	V < 18 mL	n/a	24,000 - 48,000	77 ± 22	0.6 ± 0.2	100
Mn_{3810}	27.4 ± 0.2	0.6 ± 0.1	3810 ± 190	3 ± 1	0.025 ± 0.008	50
Mn_{2710}	29.1 ± 0.5	0.7 ± 0.2	2710 ± 300	3 ± 2	0.025 ± 0.017	85
Mn_{2040}	30.5 ± 0.8	1.4 ± 0.9	2040 ± 320	11 ± 5	0.09 ± 0.04	58
Mn_{1680}	31.4 ± 0.3	0.7 ± 0.4	1680 ± 100	17 ± 9	0.14 ± 0.08	50
Mn_{1270}	32.8 ± 1.3	1 ± 1	1270 ± 340	8 ± 7	0.07 ± 0.06	50
Mo_{HMM}	V < 18 mL	n/a	20,000 - 48,000	80 ± 10	0.22 ± 0.03	100
Mo_{940}	34.3 ± 0.5	0.5 ± 0.2	940 ± 100	2 ± 2	0.005 ± 0.004	50
Mo_{410}	38.4 ± 0.6	1.2 ± 0.7	410 ± 50	5 ± 3	0.01 ± 0.008	58
Mo_{350}	39.1 ± 0.7	0.9 ± 0.4	350 ± 50	9 ± 5	0.02 ± 0.013	67
Mo_{240}	41.0 ± 0.6	1.6 ± 0.7	240 ± 30	4 ± 3	0.01 ± 0.008	67

Table C1. Low-Molecular-Mass Metal Complexes in the Mouse Brain. Confidence was defined as the number of chromatograms for a given element in which the peak was present divided by the total number of chromatograms for that element, multiplied by 100.

where $[P]_{fts}$ is the concentration of P in the FTS and *FD* is the fold-dilution used to prepare the FTS starting from the intact brain. Similar equations were used to estimate the concentrations of all LMM metal and S compounds. Equation [2] assumes that the same proportion of each P compound was retained by the column. Maximum and minimum concentrations for each compound (Table 1) were estimated by assuming that the P retained by the column was exclusively either the P species of interest, or other P-containing species, respectively.

Eight species were used to simulate the LMM region of the P chromatogram (Figure C1, Table C1). Each was designated by the element followed by a subscript indicating its approximate MM. The dominant P peak (P_{490}) comigrated with ADP and was assigned as such. Authentic ATP migrated at a slightly smaller V_e and its peak fit in the HMM shoulder of P_{490} as long as the linewidth was increased. Alternatively, the peak for ATP and another species could both fit into this shoulder if narrower linewidths were assumed. IP_6 binds Fe in cells and is thought to be involved in trafficking.(*109*) However, no Fe peaks comigrated with Fe-bound IP_6. The remaining P peaks were not assigned. Curiously, no peaks comigrated with AMP or orthophosphate.

Peaks in the representative S chromatogram (Figure C2) again segregated into HMM, IMM and LMM regions. Again, there were few, if any, S-containing species present in the IMM region. As with P, the S-containing species in the HMM region were poorly resolved and only the overall response in this region was determined by simulation. The LMM region contained 4 major resolved peaks. The dominant peak

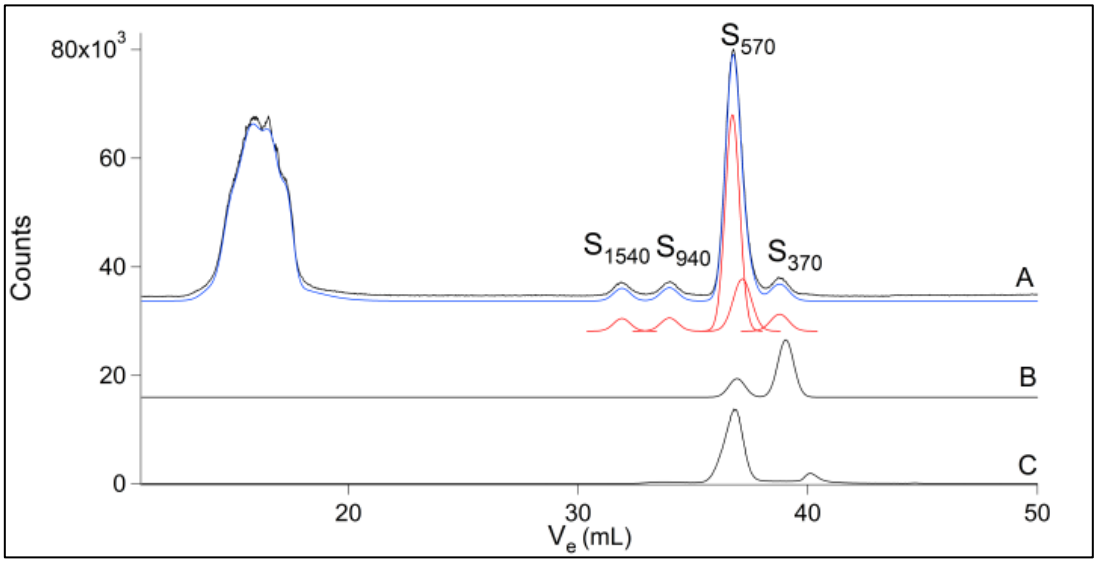

Figure C2. Sulfur chromatograms of brain FTS and various S-containing compounds. A, brain FTS; B, glutathione, GSH; C, oxidized glutathione, GSSG. The authentic glutathione solution contained some GSSG, while the GSSG solution contained a contaminant.

(S_{570}) comigrated with GSSG. However, its broad linewidth suggested that GSSG and another S species with a similar MM contributed. Another peak (S_{370}) nearly comigrated with GSH, and was assigned as such. The remaining two species, S_{1540} and S_{940} were not assigned. The ratio of peak areas for the oxidized and reduced glutathione species was *ca*. 4:1 GSSG:GSH, assuming that one of the two species that contributed to S_{570} was GSSG. This suggests a molar ratio of *ca*. 2:1 which is reasonably close to previously reported molar ratios for brain samples.(*110*)

The Co chromatogram (Figure C3) displayed numerous species in the LMM region, some HMM peak intensity, and little if any peaks in the IMM region. Of all metals detected, Co exhibited the greatest number of LMM species. Cyanocobalamin migrated just slightly slower than the dominant Co peak (Co_{1640}), suggesting that Co_{1640} might arise from a related complex (e.g. adenosylcobalamin). Aqueous Co^{II} ions migrated as multiple species, consistent with rapid ligand/proton exchange reactions.

The representative Cu chromatogram (Figure C4) indicated a HMM region containing *ca.* 5 – 6 reasonably resolved peaks, with MMs between 19 and 48 kDa. The IMM region was devoid of peaks, and the LMM region contained only *ca*. 2 peaks. Although the trace in Figure C4 suggests a miniscule amount of aqueous Cu, this feature was not reliably present in other traces.

The Zn chromatogram (Figure C5) showed a well-resolved HMM region that included *ca*. 5 species. The IMM and LMM regions were virtually devoid of peaks.

The Fe chromatogram (Figure C6) showed a poorly resolved HMM region and an IMM region largely devoid of peaks. The LMM region included two significant peaks

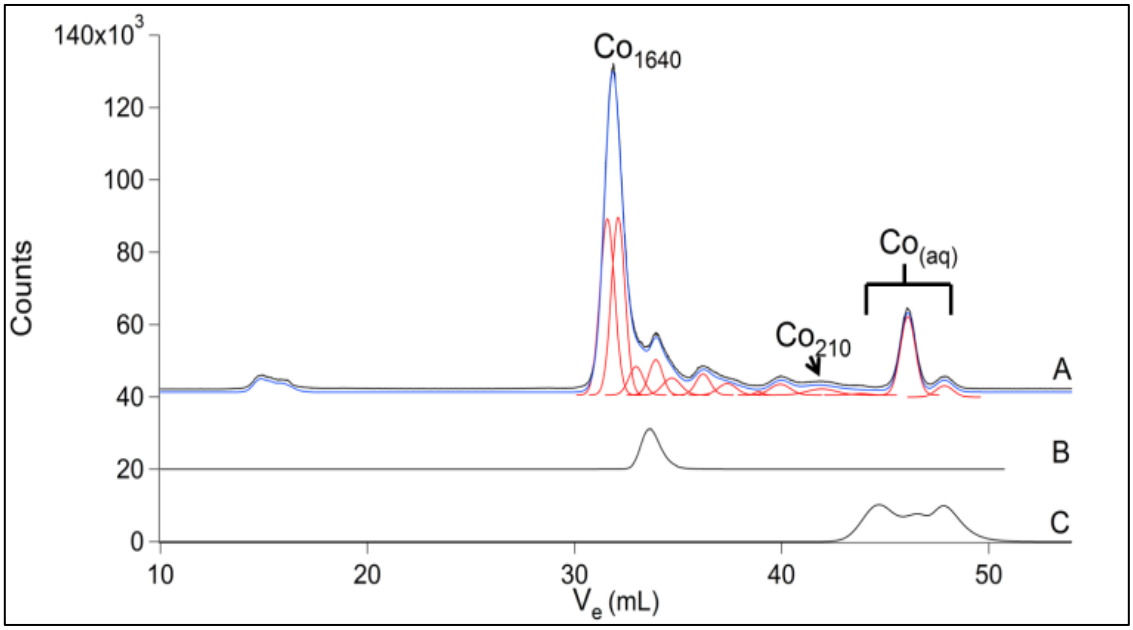

Figure C3. Cobalt chromatograms of brain FTS and other Co species. A, brain FTS; B, cyanocobalamin; and C, aqueous Co. The three lowest MM simulations in the figure are considered a single species (Co_{aq}) in Table C1.

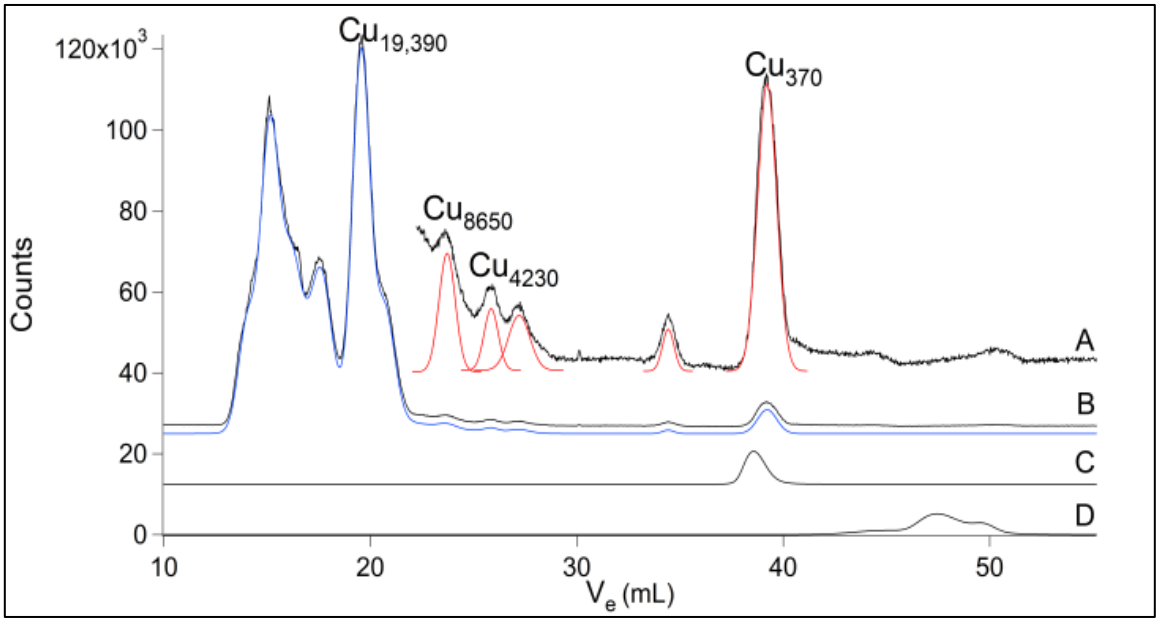

Figure C4. Copper chromatograms of brain FTS and other Cu species. A, brain FTS ×15; B, brain FTS ×1; C, Cu^{II}(EDTA); and D, aqueous Cu.

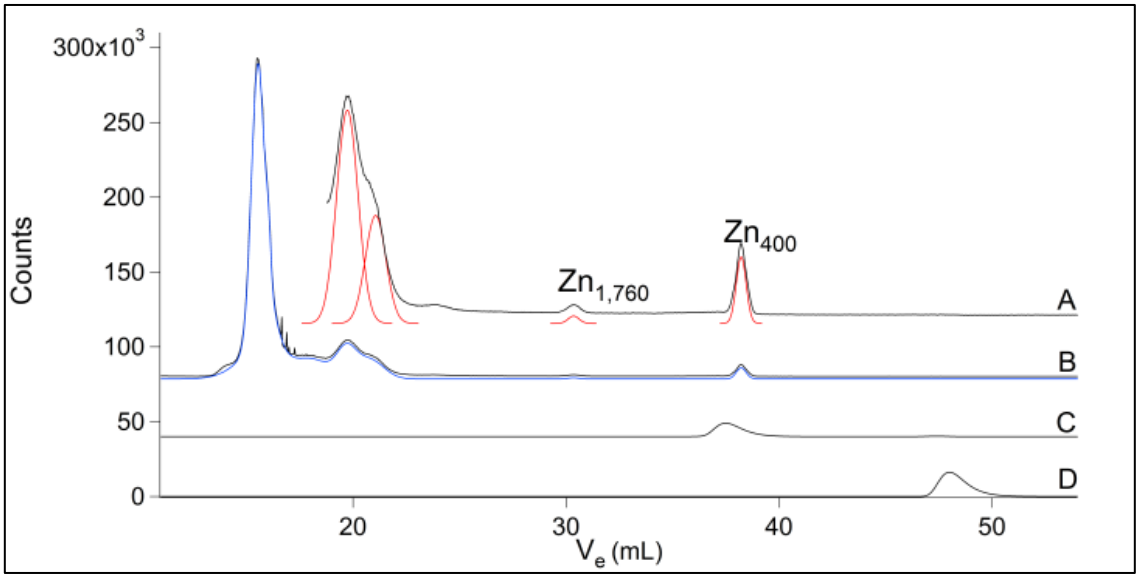

Figure C5. Zinc chromatograms of brain FTS. A, brain FTS ×16; B, brain FTS ×1; C, Zn^{II}(TPEN); and D, aqueous Zn.

(Fe_{1720} and Fe_{510}), but these were only observed in 58% and 75% of the chromatograms, respectively. In general, there was more variability in the Fe (and Mn) chromatograms than in chromatograms from the other metals. In most traces, the ultra LMM region was devoid of features (the trace shown in Figure C6 shows such a feature, but it was not routinely observed).

The Mn chromatogram (Figure C7) included poorly resolved features in the HMM region, no features in the IMM region, and a few peaks in the LMM region. Mn_{1270} and the broad feature centered at *ca.* 28 mL were present in about half of the traces. The Mo chromatogram (Figure C8) exhibited peaks in the HMM and LMM regions, while the IMM region was largely devoid of peaks. The major LMM peak (Mo_{350}) comigrated with molybdopterin isolated from xanthine oxidase, suggesting that these peaks arise from the same or a closely related species.

Discussion and Conclusions

The objective of this study was to determine whether the mouse brain contains LMM metal complexes, defined as Mo, Mn, Fe, Co, Cu and Zn complexes possessing MMs < 10 kDa. Rather than using chelators, our approach was to detect such species directly, using ICP-MS to monitor metals eluting from our LMM size-exclusion chromatography column. We were careful to avoid oxidation of any redox-active complexes, by working in an inert-atmosphere glovebox.

We attempted to limit ligand substitution reactions by minimizing the time between euthanizing the animals and loading the LC column, and by running the column

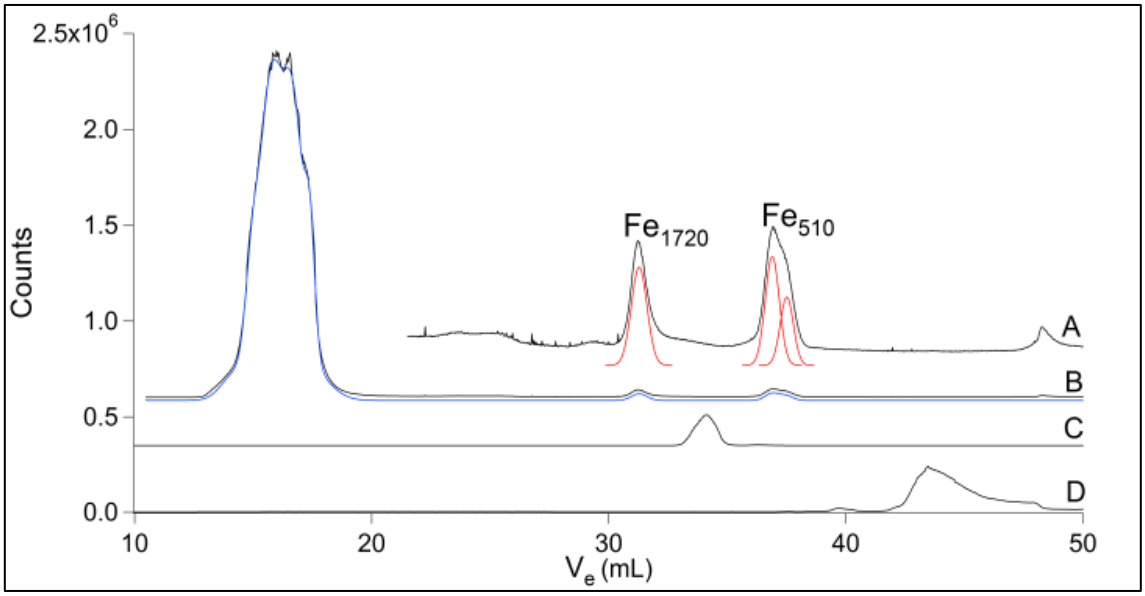

Figure C6. Iron chromatograms of brain FTS. A, brain FTS ×15; B, brain FTS ×1; C, Fe^{II}(ATP); and D, aqueous Fe.

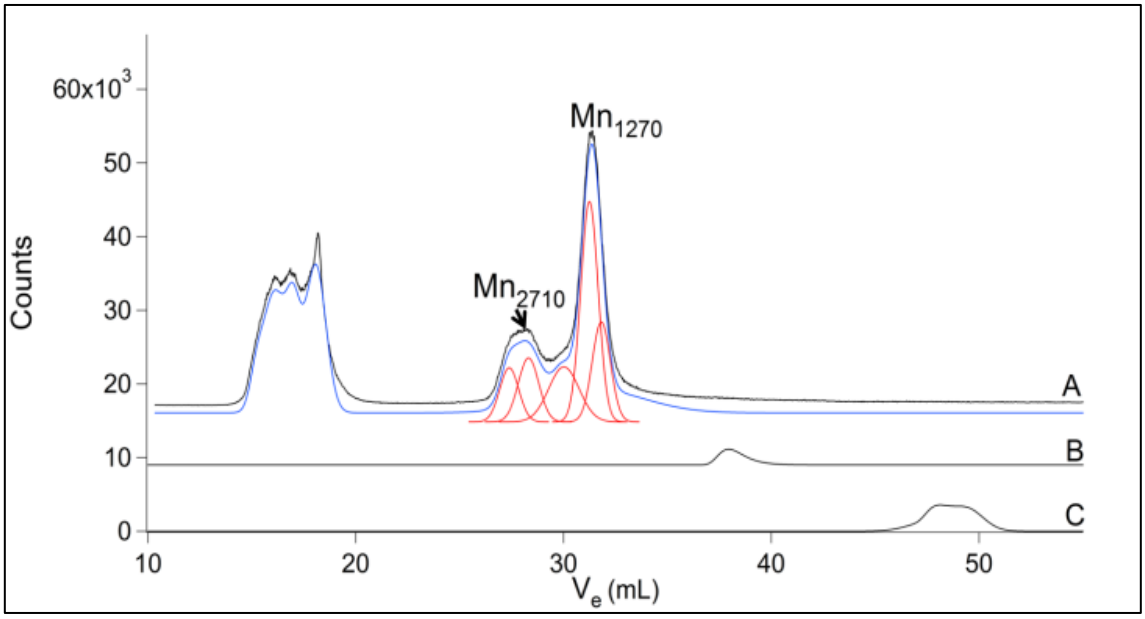

Figure C7. Manganese chromatograms of brain FTS and other Mn species. A, brain FTS; B, Mn^{II}(EDTA); and C, aqueous Mn.

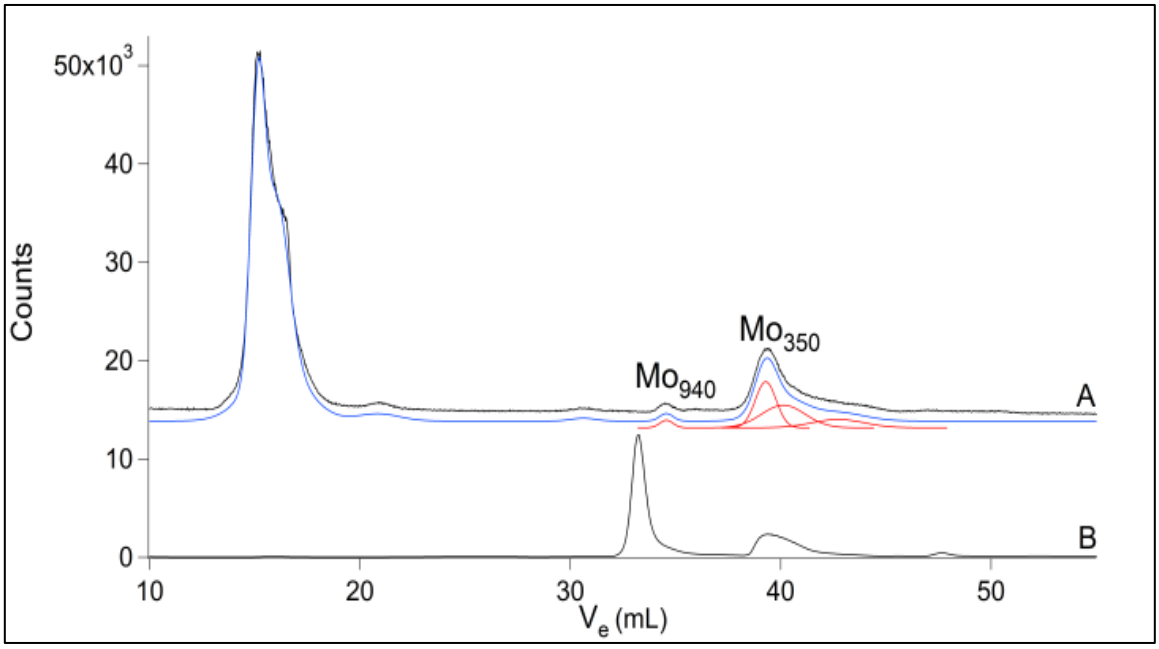

Figure C8. Molybdenum chromatograms of brain FTS and molybdopterin extract from xanthine oxidase. A, brain FTS; and B, molybdopterin. The intense peak in B with MM ~1.5 kDa was not assigned.

at low temperature. We distinguished "real" from artifactual complexes by repeating the experiment 13 times and assigning a confidence probability to each species in accordance with the proportion of runs in which the species was observed (Table 1). Our results were independent of buffer used. The vast majority of metal ions loaded on the column did not adhere to it.

By these criteria, our results indicate that there are 11 Co, 5 Cu, 5 Mn, 4 Mo, 3 Fe, and 2 Zn LMM complexes in the mouse brain. Of these 30 LMM metal complexes, only 2 – 3 have masses suggesting protein ligation (Cu_{8650}, Cu_{5680} and perhaps Cu_{4230}). The rest have lower MMs which suggest either small peptides as ligands or perhaps organic/inorganic ligands.

Except for Cu, all of the metals displayed a significant gap between one edge of the HMM region (with MMs > ~ 20 kDa) and one edge of the LMM region (with MMs < 4 kDa). The absence of metal complexes between these two regions implies that the division into such groups is not arbitrary. Zhuang *et al.* reported that the shortest (non-alternatively spliced) protein in the mouse genome is 38 residues, which corresponds to 4.2 kDa.(*111*) This suggests that the complexes in the HMM region are exclusively protein-based and it raises the possibility that the metal complexes in the LMM region are either non-proteinaceous or have peptides arising from post-translational truncations. Large natural products and siderophores (e.g. actinomycin D, glycosylated antibiotics, pyoverdine) have MMs of *ca*. 1.5 kDa.

Of the metals examined, Co exhibited the most LMM complexes and perhaps the least protein-based species. Cu and Zn displayed the opposite pattern, with numerous well-resolved metal-bound proteins and few non-proteinaceous complexes.

Our results impact the issue of whether cells contain "free" or aqueous metal ions. They indicate that there are significant concentrations of aqueous Co ions in the brain, but do not provide clear evidence of aqueous Cu, Zn, Mn, Mo or Fe ions. ICP-MS is quite sensitive, such that the concentration of aqueous metal ion would need to be < 10 nM (ca. 10^3 ions per cells; data not shown) to escape detection. In a seminal study published over a decade ago, O'Halloran and coworkers argued that there are no "free" or aqueous Cu ions in the cell, and that Cu trafficking exclusively involves transferring Cu ions from one protein chaperone to the next.(*112*) Their conclusion was based on ability of the Cu-loaded chaperone CCS to donate Cu into apo-SOD1 even in the presence of bathocurproine sulfate, a strong Cu^I chelator. Using thermodynamic binding constants, they estimated that there is < 1 aqueous Cu ion per cell. They rationalized that the intracellular milieu must have a large capacity for binding aqueous Cu ions, and that aqueous Cu would be dangerous to the cell, due to its tendency to engage in Fenton chemistry. To the limited extent that our results can detect aqueous Cu (down to ~ 300 Cu ions/cell), they support the conclusion that there are no "free"/aqueous Cu ions in the mouse brain.

Similar thermodynamic calculations involving aqueous Zn ions in the cell yield concentrations of tens to hundreds of pM. Like Cu, this translates into < 1 aqueous Zn ion per cell assuming a cell volume of 10^{-14} L. Aqueous Zn ions also inhibit human

receptor protein-tyrosine phosphatase in accordance with K_I = 21 ± 7 pM,(*113*) again suggesting very few if any intracellular aqueous Zn ions. Our results suggest the absence of aqueous Zn in the mouse brain and provide substantial evidence for protein-based Zn complexes. We propose that the Zn species released during the firing of synaptic vesicles have one or more *non-aqueous* ligands. The species released are almost certainly not "free"/aqueous Zn.

Aqueous metal ions rapidly exchange bound waters with the solvent, with rate-constants that vary in the order $Ni^{II} < Co^{II} < Fe^{II} < Mn^{II} < Zn^{II} < Cu^{II}$.(*114*) The waters on such complexes have average residence times ranging from 10^{-4} – 10^{-10} sec. At moments when a coordinated water dissociates, thousands of potential ligands in the cellular milieu could interact with the metal at the vacant coordination site. This would promote the formation of a new complex. In the likely event that the new ligand would coordinate stronger than water, the complex would become less dynamic. Even if no permanent complexes formed, the result of this dynamic exchange-reaction would be a population-distribution of closely related and rapidly interconverting species rather than a single entity. Indeed the broad structured peaks obtained from the chromatographic migration of aqueous metal ions in our study suggest such a population of species. Could such dynamical populations serve discrete physiological functions in a cell, or would they be deleterious, engaging in uncontrolled side reactions that produce toxic species? We suspect that cells could not survive the uncontrollable behavior of most aqueous transition metal ions. Moreover, the cell would be unable to regulate such ions since the coordinating ligands would not be under genetic control. Chaos would result.

Accordingly, aqueous metal ions with the fastest water exchange-dynamics would seem to be the least likely to exist in a cell, while those with slower exchange-dynamics might be sufficiently stable. Our detection of aqueous Co ions in FTSs supports this possibility, since, of the metals examined, aqueous Co^{II} exchanges water ligands slowest. To test this idea further, aqueous Ni^{II} ions, which exhibit even slower water exchange-dynamics, were added to a FTS prior to passage through the column. A single peak with the MM of aqueous Ni^{II} was detected. When other aqueous metal ions, including Fe, Cu, Zn and Mn were added to the FTS, the only aqueous ion detected in the resulting chromatograms was Co (data not shown).

The fast ligand exchange-dynamics inherent to metal ions are slowed with polydentate ligands. Polydentate metal complexes would likely exist as single autonomous entities that are not in a dynamic equilibrium with other potential ligands in the cell. Slower exchange dynamics would minimize toxic side reactions because they would not have dynamically-free sites. Moreover, such ligands would need to be synthesized and thus regulated by the cell. The shape of such large complexes would allow other cellular components (e.g. membrane-bound protein transporters) to recognize and distinguish one complex from another. All of these factors favor the occurrence in the cell of metal complexes with polydentate ligands. Undoubtedly all of the LMM metal complexes characterized in this study are of that type.

We are particularly interested in metal complexes involved in metal ion trafficking – assuming such complexes exist. For such complexes, the coordinating polydentate ligands must bind strong enough to avoid the problems mentioned above,

yet also allow the metal to be transferred to downstream acceptors. In some well-documented cases, altering the redox state of the metal(*115*) or the pH(*116*) of the solution are sufficient to labilize the ligands. Binding to a protein or macromolecular complex might also labilize the ligands coordinating a metal.

Determining the physiological role of each LMM metal complex in the brain that we have described in this study will be a challenge that will require multiple "orthogonal" approaches. The LC-ICP-MS approach used here is complementary to that of treating cells or tissues with custom-designed chelators that react with and sense labile metal complexes.(*72, 81, 82, 97*) The advantage of the chelator-based method is the ability to detect labile metal ions in *intact live* cells. The disadvantages are that such chelators may react with multiple species in the cell, and that the process of detection destroys the complexes of interest. The advantage of the LC-ICP-MS approach is that individual metal complexes can be detected undisturbed (barring potential degradation reactions occurring during workup). The disadvantage is that the cell itself must be disrupted such that critical information regarding cellular compartmentalization is lost. Merging these approaches, e.g. using LC-ICP-MS to assess which particular complexes react with designer metal sensors, will undoubtedly yield the greatest insight into metal ion metabolism in cells and super-cellular structures such as the brain.

APPENDIX D

REFERENCES

1. MacKenzie, E. L., Iwasaki, K., and Tsuji, Y. (2008) Intracellular iron transport and storage: from molecular mechanisms to health implications, *Antioxid Redox Signal 10*, 997-1030.
2. Leskinen, J., Eskelinen, A., Huhtala, H., Paavolainen, P., and Remes, V. (2012) The incidence of knee arthroplasty for primary osteoarthritis grows rapidly among baby boomers: a population-based study in Finland, *Arthritis Rheum 64*, 423-428.
3. Wei, W. Q., Leibson, C. L., Ransom, J. E., Kho, A. N., Caraballo, P. J., Chai, H. S., Yawn, B. P., Pacheco, J. A., and Chute, C. G. (2012) Impact of data fragmentation across healthcare centers on the accuracy of a high-throughput clinical phenotyping algorithm for specifying subjects with type 2 diabetes mellitus, *J Am Med Inform Assoc 19*, 219-224.
4. Hay, C., Pacey, M., Bains, N., and Ardal, S. (2010) Understanding the Unattached Population in Ontario: Evidence from the Primary Care Access Survey (PCAS), *Healthc Policy 6*, 33-47.
5. Horowitz, M. P., and Greenamyre, J. T. (2010) Mitochondrial Iron Metabolism and Its Role in Neurodegeneration, *J Alzheimers Dis 20*, S551-S568.
6. Fitzpatrick, P. F. (1999) Tetrahydropterin-dependent amino acid hydroxylases, *Annu Rev Biochem 68*, 355-381.

7. Ortiz, E., Pasquini, J. M., Thompson, K., Felt, B., Butkus, G., Beard, J., and Connor, J. R. (2004) Effect of manipulation of iron storage, transport, or availability on myelin composition and brain iron content in three different animal models, *J Neurosci Res 77*, 681-689.

8. Neufeld, L. M., Ramakrishnan, U., Rivera, J., Villalpando, S., Gonzalez-Cossio, T., and Martorell, R. (2001) Prevalence of anemia and iron deficiency during pregnancy of women supplemented with iron or iron and multiple micronutrients, *Faseb J 15*, A641-A641.

9. Beard, J., Erikson, K. M., and Jones, B. C. (2003) Neonatal iron deficiency results in irreversible changes in dopamine function in rats, *J Nutr 133*, 1174-1179.

10. Halliwell, B. (2006) Oxidative stress and neurodegeneration: where are we now?, *J Neurochem 97*, 1634-1658.

11. Green, D. R., Galluzzi, L., and Kroemer, G. (2011) Mitochondria and the autophagy-inflammation-cell death axis in organismal aging, *Science 333*, 1109-1112.

12. Gerlach, M., Benshachar, D., Riederer, P., and Youdim, M. B. H. (1994) Altered Brain Metabolism of Iron as a Cause of Neurodegenerative Diseases, *Journal of Neurochemistry 63*, 793-807.

13. Wu, L. J. C., Leenders, A. G. M., Cooperman, S., Meyron-Holtz, E., Smith, S., Land, W., Tsai, R. Y. L., Berger, U. V., Sheng, Z. H., and Rouault, T. A. (2004)

Expression of the iron transporter ferroportin in synaptic vesicles and the blood-brain barrier, *Brain Research 1001*, 108-117.

14. Fishman, J. B., Rubin, J. B., Handrahan, J. V., Connor, J. R., and Fine, R. E. (1987) Receptor-Mediated Transcytosis of Transferrin across the Blood-Brain-Barrier, *Journal of Neuroscience Research 18*, 299-304.

15. Zecca, L., Gallorini, M., Schunemann, V., Trautwein, A. X., Gerlach, M., Riederer, P., Vezzoni, P., and Tampellini, D. (2001) Iron, neuromelanin and ferritin content in the substantia nigra of normal subjects at different ages: consequences for iron storage and neurodegenerative processes, *J Neurochem 76*, 1766-1773.

16. Bell, S. H., Weir, M. P., Dickson, D. P. E., Gibson, J. F., Sharp, G. A., and Peters, T. J. (1984) Mossbauer Spectroscopic Studies of Human Hemosiderin and Ferritin, *Biochim Biophys Acta 787*, 227-236.

17. Gerlach, M., Trautwein, A. X., Zecca, L., Youdim, M. B. H., and Riederer, P. (1995) Mossbauer Spectroscopic Studies of Purified Human Neuromelanin Isolated from the Substantia-Nigra, *Journal of Neurochemistry 65*, 923-926.

18. Bou-Abdallah, F., Santambrogio, P., Levi, S., Arosio, P., and Chasteen, N. D. (2005) Unique iron binding and oxidation properties of human mitochondrial ferritin: A comparative analysis with human H-chain ferritin, *J Mol Biol 347*, 543-554.

19. Pushie, M. J., Pickering, I. J., Martin, G. R., Tsutsui, S., Jirik, F. R., and George, G. N. (2011) Prion protein expression level alters regional copper, iron and zinc content in the mouse brain, *Metallomics 3*, 206-214.

20. Rodrigue, K. M., Haacke, E. M., and Raz, N. (2011) Differential effects of age and history of hypertension on regional brain volumes and iron, *Neuroimage 54*, 750-759.

21. Meguro, R., Asano, Y., Odagiri, S., Li, C. T., and Shoumura, K. (2008) Cellular and subcellular localizations of nonheme ferric and ferrous iron in the rat brain: a light and electron microscopic study by the perfusion-Perls and -Turnbull methods, *Arch Histol Cytol 71*, 205-222.

22. Connor, J. R., Menzies, S. L., Stmartin, S. M., and Mufson, E. J. (1992) A Histochemical-Study of Iron, Transferrin, and Ferritin in Alzheimers Diseased Brains, *Journal of Neuroscience Research 31*, 75-83.

23. Glaser, T. (2011) Mossbauer spectroscopy and Transition Metal Chemistry. Fundamentals and Applications., *Angew. Chem., Int. Ed. 50*, 10019-10020.

24. Garber Morales, J., Holmes-Hampton, G. P., Miao, R., Guo, Y., Munck, E., and Lindahl, P. A. (2010) Biophysical characterization of iron in mitochondria isolated from respiring and fermenting yeast, *Biochemistry-Us 49*, 5436-5444.

25. Holmes-Hampton, G. P., Miao, R., Garber Morales, J., Guo, Y., Munck, E., and Lindahl, P. A. (2010) A nonheme high-spin ferrous pool in mitochondria isolated from fermenting *Saccharomyces cerevisiae*, *Biochemistry-Us 49*, 4227-4234.

26. Cockrell, A. L., Holmes-Hampton, G. P., McCormick, S. P., Chakrabarti, M., and Lindahl, P. A. (2011) Mossbauer and EPR Study of Iron in Vacuoles from Fermenting *Saccharomyces cerevisiae*, *Biochemistry-Us 50*, 10275-10283.

27. Boutaleb, S., Pouget, J. P., Hindorf, C., Pelegrin, A., Barbet, J., Kotzki, P. O., and Bardies, M. (2009) Impact of Mouse Model on Preclinical Dosimetry in Targeted Radionuclide Therapy, *P Ieee 97*, 2076-2085.

28. Lindahl, P. A., Morales, J. G., Miao, R., and Holmes-Hampton, G. (2009) Chapter 15 Isolation of *Saccharomyces cerevisiae* mitochondria for Mossbauer, EPR, and electronic absorption spectroscopic analyses, *Methods Enzymol 456*, 267-285.

29. Vanderford, D. A., Greer, P. K., Sharp, J. M., Chichlowski, M., Rouse, D. C., Selim, M. A., and Hale, L. P. (2010) Alopecia in IL-10-deficient mouse pups is c-kit-dependent and can be triggered by iron deficiency, *Exp Dermatol 19*, 518-526.

30. Beard, J. L., Wiesinger, J. A., Li, N., and Connor, J. R. (2005) Brain iron uptake in hypotransferrinemic mice: Influence of systemic iron status, *Journal of Neuroscience Research 79*, 254-261.

31. Oshtrakh, M. I. (1998) The features of Mossbauer spectra of hemoglobin in relation to the quadrupole splitting and heme iron stereochemistry, *Z Naturforsch A 53*, 608-614.

32. Koeppen, A. H. (2003) A brief history of brain iron research, *Journal of the Neurological Sciences 207*, 95-97.

33. Drayer, B., Burger, P., Darwin, R., Riederer, S., Herfkens, R., and Johnson, G. A. (1986) Magnetic-Resonance-Imaging of Brain Iron, *Am J Neuroradiol 7*, 373-380.

34. Wansapura, J. P., Holland, S. K., Dunn, R. S., and Ball, W. S. (1999) NMR relaxation times in the human brain at 3.0 tesla, *Jmri-J Magn Reson Im 9*, 531-538.

35. Yao, B., Li, T. Q., van Gelderen, P., Shmueli, K., de Zwart, J. A., and Duyn, J. H. (2009) Susceptibility contrast in high field MRI of human brain as a function of tissue iron content, *Neuroimage 44*, 1259-1266.

36. Hopp, K., Popescu, B. F. G., McCrea, R. P. E., Harder, S. L., Robinson, C. A., Haacke, M. E., Rajput, A. H., Rajput, A., and Nichol, H. (2010) Brain Iron Detected by SWI High Pass Filtered Phase Calibrated with Synchrotron X-Ray Fluorescence, *Journal of Magnetic Resonance Imaging 31*, 1346-1354.

37. Szczerbowska-Boruchowska, M., Lankosz, M., Czyzycki, M., and Adamek, D. (2011) An integrated experimental and analytical approach to the chemical state imaging of iron in brain gliomas using X-ray absorption near edge structure spectroscopy, *Analytica Chimica Acta 699*, 153-160.

38. Wang, H. J., Wang, M., Wang, B., Li, M., Chen, H. Q., Yu, X. H., Zhao, Y. L., Feng, W. Y., and Chai, Z. F. (2012) The distribution profile and oxidation states of biometals in APP transgenic mouse brain: dyshomeostasis with age and as a function of the development of Alzheimer's disease, *Metallomics 4*, 289-296.

39. Dubiel, S. M., Zablotna-Rypien, B., Mackey, J. B., and Williams, J. M. (1999) Magnetic properties of human liver and brain ferritin, *Eur Biophys J Biophy 28*, 263-267.

40. GalazkaFriedman, J., Bauminger, E. R., Friedman, A., Barcikowska, M., Hechel, D., and Nowik, I. (1996) Iron in parkinsonian and control substantia nigra - A Mossbauer spectroscopy study, *Movement Disord 11*, 8-16.

41. Bartzokis, G., Tishler, T. A., Shin, I. S., Lu, P. H., and Cummings, J. L. (2004) Brain ferritin iron as a risk factor for age at onset in neurodegenerative diseases, *Redox-Active Metals in Neurological Disorders 1012*, 224-236.

42. Keen, C. L., Lonnerdal, B., Sloan, M. V., and Hurley, L. S. (1980) Effect of Dietary Iron, Copper and Zinc Chelates of Nitrilotriacetic Acid (Nta) on Trace-Metal Concentrations in Rat Milk and Maternal and Pup Tissues, *J Nutr 110*, 897-906.

43. Moos, T., and Morgan, E. H. (2000) Transferrin and transferrin receptor function in brain barrier systems, *Cell Mol Neurobiol 20*, 77-95.

44. Connor, J. R., Menzies, S. L., Burdo, J. R., and Boyer, P. J. (2001) Iron and iron management proteins in neurobiology, *Pediatr Neurol 25*, 118-129.

45. Keen, C. L., and Hurley, L. S. (1980) Developmental-Changes in Concentrations of Iron, Copper, and Zinc in Mouse-Tissues, *Mech Ageing Dev 13*, 161-176.

46. Jhurry, N. D., Chakrabarti, M., McCormick, S. P., Holmes-Hampton, G. P., and Lindahl, P. A. (2012) Biophysical Investigation of the Ironome of Human Jurkat Cells and Mitochondria, *Biochemistry-Us 51*, 5276-5284.

47. Pysh, J. J. (1970) Mitochondrial Changes in Rat Inferior Colliculus during Postnatal Development - an Electron Microscopic Study, *Brain Research 18*, 325-&.

48. Dallman, P. R., Siimes, M. A., and Manies, E. C. (1975) Brain Iron - Persistent Deficiency Following Short-Term Iron Deprivation in Young Rat, *Brit J Haematol 31*, 209-215.

49. Ashkenazi, R., Benshachar, D., and Youdim, M. B. H. (1982) Nutritional Iron and Dopamine Binding-Sites in the Rat-Brain, *Pharmacol Biochem Be 17*, 43-47.

50. Mackler, B., Person, R., and Grace, R. (1985) Iron-Deficiency in the Rat - Effects on Energy-Metabolism in Brown Adipose-Tissue, *Pediatric Research 19*, 989-991.

51. Price, E. M., and Gibson, J. F. (1972) Reinterpretation of Bicarbonate-Free Ferric Transferrin Epr Spectra, *Biochem Bioph Res Co 46*, 646-&.

52. Tangeras, A., Flatmark, T., Backstrom, D., and Ehrenberg, A. (1980) Mitochondrial Iron Not Bound in Heme and Iron-Sulfur Centers - Estimation, Compartmentation and Redox State, *Biochim Biophys Acta 589*, 162-175.

53. Petrat, F., Rauen, U., and de Groot, H. (1999) Determination of the chelatable iron pool of isolated rat hepatocytes by digital fluorescence microscopy using the fluorescent probe, phen green SK, *Hepatology 29*, 1171-1179.

54. Petrat, F., de Groot, H., and Rauen, U. (2001) Subcellular distribution of chelatable iron: a laser scanning microscopic study in isolated hepatocytes and liver endothelial cells, *Biochemical Journal 356*, 61-69.

55. Wypijewska, A., Galazka-Friedman, J., Bauminger, E. R., Wszolek, Z. K., Schweitzer, K. J., Dickson, D. W., Jaklewicz, A., Elbaum, D., and Friedman, A. (2010) Iron and reactive oxygen species activity in parkinsonian substantia nigra, *Parkinsonism Relat Disord 16*, 329-333.

56. Sohal, R. S., Wennberg-Kirch, E., Jaiswal, K., Kwong, L. K., and Forster, M. J. (1999) Effect of age and caloric restriction on bleomycin-chelatable and nonheme iron in different tissues of C57BL/6 mice, *Free Radical Bio Med 27*, 287-293.

57. Magaki, S., Mueller, C., Yellon, S. M., Fox, J., Kim, J., Snissarenko, E., Chin, V., Ghosh, M. C., and Kirsch, W. M. (2007) Regional dissection and determination of loosely bound and non-heme iron in the developing mouse brain, *Brain Research 1158*, 144-150.

58. Kaur, D., Rajagopalan, S., and Andersen, J. K. (2009) Chronic expression of H-ferritin in dopaminergic midbrain neurons results in an age-related expansion of the labile iron pool and subsequent neurodegeneration: implications for Parkinson's disease, *Brain Research 1297*, 17-22.

59. Sano, H., Naruse, M., Matsumoto, K., Oi, T., and Utsumi, H. (2000) A new nitroxyl-probe with high retention in the brain and its application for brain imaging, *Free Radic Biol Med 28*, 959-969.

60. Gomi, F., Utsumi, H., Hamada, A., and Matsuo, M. (1993) Aging Retards Spin Clearance from Mouse-Brain and Food Restriction Prevents Its Age-Dependent Retardation, *Life Sci 52*, 2027-2033.

61. Cadenas, E., and Davies, K. J. A. (2000) Mitochondrial free radical generation, oxidative stress, and aging, *Free Radical Bio Med 29*, 222-230.

62. Valko, M., Rhodes, C. J., Moncol, J., Izakovic, M., and Mazur, M. (2006) Free radicals, metals and antioxidants in oxidative stress-induced cancer, *Chem-Biol Interact 160*, 1-40.

63. Galaris, D., and Pantopoulos, K. (2008) Oxidative stress and iron homeostasis: Mechanistic and health aspects, *Crit Rev Cl Lab Sci 45*, 1-23.

64. Ba, L. A., Doering, M., Burkholz, T., and Jacob, C. (2009) Metal trafficking: from maintaining the metal homeostasis to future drug design, *Metallomics 1*, 292-311.

65. Crichton, R. R., Wilmet, S., Legssyer, R., and Ward, R. J. (2002) Molecular and cellular mechanisms of iron homeostasis and toxicity in mammalian cells, *J Inorg Biochem 91*, 9-18.

66. Moos, T., and Morgan, E. H. (2004) The metabolism of neuronal iron and its pathogenic role in neurological disease - Review, *Ann Ny Acad Sci 1012*, 14-26.

67. Holmes-Hampton, G. P., Chakrabarti, M., Cockrell, A. L., McCormick, S. P., Abbott, L. C., Lindahl, L. S., and Lindahl, P. A. (2012) Changing iron content of the mouse brain during development, *Metallomics 4*, 761-770.

68. Mastroberardino, P. G., Hoffman, E. K., Horowitz, M. P., Betarbet, R., Taylor, G., Cheng, D. M., Na, H. M., Gutekunst, C. A., Gearing, M., Trojanowski, J. Q., Anderson, M., Chu, C. T., Peng, J. M., and Greenamyre, J. T. (2009) A novel

transferrin/TfR2-mediated mitochondrial iron transport system is disrupted in Parkinson's disease, *Neurobiol Dis 34*, 417-431.

69. Finney, L. A., and O'Halloran, T. V. (2003) Transition metal speciation in the cell: Insights from the chemistry of metal ion receptors, *Science 300*, 931-936.

70. Muhlenhoff, U., Stadler, J. A., Richhardt, N., Seubert, A., Eickhorst, T., Schweyen, R. J., Lill, R., and Wiesenberger, G. (2003) A specific role of the yeast mitochondrial carriers MRS3/4p in mitochondrial iron acquisition under iron-limiting conditions, *J Biol Chem 278*, 40612-40620.

71. Pamp, K., Kerkweg, U., Korth, H. G., Homann, F., Rauen, U., Sustmann, R., de Groot, H., and Petrat, F. (2008) Enzymatic reduction of labile iron by organelles of the rat liver. Superior role of an NADH-dependent activity in the outer mitochondrial membrane, *Biochimie 90*, 1591-1601.

72. Rauen, U., Springer, A., Weisheit, D., Petrat, F., Korth, H. G., de Groot, H., and Sustmann, R. (2007) Assessment of chelatable mitochondrial iron by using mitochondrion-selective fluorescent iron indicators with different iron-binding affinities, *Chembiochem 8*, 341-352.

73. Petrat, F., de Groot, H., Sustmann, R., and Rauen, U. (2002) The chelatable iron pool in living cells: A methodically defined quantity, *Biol Chem 383*, 489-502.

74. Holmes-Hampton, G. P., Miao, R., Morales, J. G., Guo, Y. S., Munck, E., and Lindahl, P. A. (2010) A Nonheme High-Spin Ferrous Pool in Mitochondria Isolated from Fermenting *Saccharomyces cerevisiae*, *Biochemistry-Us 49*, 4227-4234.

75. Pandey, A., Yoon, H., Lyver, E. R., Dancis, A., and Pain, D. (2012) Identification of a Nfs1p-bound persulfide intermediate in Fe-S cluster synthesis by intact mitochondria, *Mitochondrion 12*, 539-549.

76. Wypijewska, A., Galazka-Friedman, J., Bauminger, E. R., Wszolek, Z. K., Schweitzer, K. J., Dickson, D. W., Jaklewicz, A., Elbaum, D., and Friedman, A. (2010) Iron and reactive oxygen species activity in parkinsonian substantia nigra, *Parkinsonism Relat D 16*, 329-333.

77. Huang, K., Li, H. X., Shen, H., and Li, M. (2012) Psychological Stress Expands Low Molecular Weight Iron Pool in Cerebral Cortex, Hippocampus, and Striatum of Rats, *Biol Trace Elem Res 146*, 79-85.

78. Bitanihirwe, B. K. Y., and Cunningham, M. G. (2009) Zinc: The Brain's Dark Horse, *Synapse 63*, 1029-1049.

79. Palumaa, P., Eriste, E., Njunkova, O., Pokras, L., Jornvall, H., and Sillard, R. (2002) Brain-specific metallothionein-3 has higher metal-binding capacity than ubiquitous metallothioneins and binds metals noncooperatively, *Biochemistry-Us 41*, 6158-6163.

80. Viles, J. H. (2012) Metal ions and amyloid fiber formation in neurodegenerative diseases. Copper, zinc and iron in Alzheimer's, Parkinson's and prion diseases, *Coordin Chem Rev 256*, 2271-2284.

81. Tomat, E., and Lippard, S. J. (2010) Imaging mobile zinc in biology, *Curr Opin Chem Biol 14*, 225-230.

82. Dean, K. M., Qin, Y., and Palmer, A. E. (2012) Visualizing metal ions in cells: An overview of analytical techniques, approaches, and probes, *Bba-Mol Cell Res 1823*, 1406-1415.

83. Dittmer, P. J., Miranda, J. G., Gorski, J. A., and Palmer, A. E. (2009) Genetically Encoded Sensors to Elucidate Spatial Distribution of Cellular Zinc, *J Biol Chem 284*, 16289-16297.

84. Qin, Y., Dittmer, P. J., Park, J. G., Jansen, K. B., and Palmer, A. E. (2011) Measuring steady-state and dynamic endoplasmic reticulum and Golgi Zn2+ with genetically encoded sensors, *P Natl Acad Sci USA 108*, 7351-7356.

85. Levenson, C. W. (2005) Zinc supplementation: Neuroprotective or neurotoxic?, *Nutr Rev 63*, 122-125.

86. Chang, C. J., Nolan, E. M., Jaworski, J., Okamoto, K. I., Hayashi, Y., Sheng, M., and Lippard, S. J. (2004) ZP8, a neuronal zinc sensor with improved dynamic range; Imaging zinc in hippocampal slices with two-photon microscopy, *Inorg Chem 43*, 6774-6779.

87. Huang, Z., and Lippard, S. J. (2012) Illuminating Mobile Zinc with Fluorescence: From Cuvettes to Live Cells and Tissues, *Method Enzymol 505*, 445-468.

88. Lee, J. Y., Kim, J. S., Byun, H. R., Palmiter, R. D., and Koh, J. Y. (2011) Dependence of the histofluorescently reactive zinc pool on zinc transporter-3 in the normal brain, *Brain Res 1418*, 12-22.

89. Gaetke, L. M., and Chow, C. K. (2003) Copper toxicity, oxidative stress, and antioxidant nutrients, *Toxicology 189*, 147-163.

90. Zheng, W., and Monnot, A. D. (2012) Regulation of brain iron and copper homeostasis by brain barrier systems: Implication in neurodegenerative diseases, *Pharmacol Therapeut 133*, 177-188.

91. Zhou, B., and Gitschier, J. (1997) hCTR1: A human gene for copper uptake identified by complementation in yeast, *P Natl Acad Sci USA 94*, 7481-7486.

92. Kono, S. (2012) Aceruloplasminemia, *Curr Drug Targets 13*, 1190-1199.

93. Carr, H. S., and Winge, D. R. (2003) Assembly of cytochrome c oxidase within the mitochondrion, *Accounts Chem Res 36*, 309-316.

94. Culotta, V. C., Strain, J., Klomp, L. W. J., Casareno, R. L. B., and Gitlin, J. D. (1997) The copper chaperone for superoxide dismutase, *Mol Biol Cell 8*, 574-574.

95. Stasser, J. P., Siluvai, G. S., Barry, A. N., and Blackburn, N. J. (2007) A multinuclear copper(I) cluster forms the dimerization interface in copper-loaded human copper chaperone for superoxide dismutase, *Biochemistry-Us 46*, 11845-11856.

96. Macreadie, I. G. (2008) Copper transport and Alzheimer's disease, *Eur Biophys J Biophy 37*, 295-300.

97. Domaille, D. W., Zeng, L., and Chang, C. J. (2010) Visualizing Ascorbate-Triggered Release of Labile Copper within Living Cells using a Ratiometric Fluorescent Sensor, *J Am Chem Soc 132*, 1194-+.

98. Hirayama, T., Van de Bittner, G. C., Gray, L. W., Lutsenko, S., and Chang, C. J. (2012) Near-infrared fluorescent sensor for in vivo copper imaging in a murine Wilson disease model, *P Natl Acad Sci USA 109*, 2228-2233.

99. Culotta, V. C., Yang, M., and O'Halloran, T. V. (2006) Activation of superoxide dismutases: Putting the metal to the pedal, *Bba-Mol Cell Res 1763*, 747-758.

100. Brown, D. R. (2010) Metalloproteins and neuronal death, *Metallomics 2*, 186-194.

101. Hille, R., Nishino, T., and Bittner, F. (2011) Molybdenum enzymes in higher organisms, *Coordin Chem Rev 255*, 1179-1205.

102. Carmi-Nawi, N., Malinger, G., Mandel, H., Ichida, K., Lerman-Sagie, T., and Lev, D. (2011) Prenatal Brain Disruption in Molybdenum Cofactor Deficiency, *J Child Neurol 26*, 460-464.

103. Vijayakumar, K., Gunny, R., Grunewald, S., Carr, L., Chong, K. W., DeVile, C., Robinson, R., McSweeney, N., and Prabhakar, P. (2011) Clinical Neuroimaging Features and Outcome in Molybdenum Cofactor Deficiency, *Pediatr Neurol 45*, 246-252.

104. Stangl, G. I., Schwarz, F. J., and Kirchgessner, M. (1999) Cobalt deficiency effects on trace elements, hormones and enzymes involved in energy metabolism of cattle, *Int J Vitam Nutr Res 69*, 120-126.

105. Kalhan, S. C., and Marczewski, S. E. (2012) Methionine, homocysteine, one carbon metabolism and fetal growth, *Rev Endocr Metab Dis 13*, 109-119.

106. Dixon, M. M., Huang, S., Matthews, R. G., and Ludwig, M. (1996) The structure of the C-terminal domain of methionine synthase: Presenting S-adenosylmethionine for reductive methylation of B-12, *Structure 4*, 1263-1275.

107. Matthews, R. G., Koutmos, M., and Datta, S. (2008) Cobalamin-dependent and cobamide-dependent methyltransferases, *Curr Opin Struc Biol 18*, 658-666.

108. Deistung, J., and Bray, R. C. (1989) Isolation, in the Intact State, of the Pterin Molybdenum Cofactor from Xanthine-Oxidase, *Biochem J 263*, 477-483.

109. Veiga, N., Torres, J., Mansell, D., Freeman, S., Dominguez, S., Barker, C. J., Diaz, A., and Kremer, C. (2009) "Chelatable iron pool": inositol 1,2,3-trisphosphate fulfils the conditions required to be a safe cellular iron ligand, *J Biol Inorg Chem 14*, 51-59.

110. Bronowicka-Adamska, P., Zagajewski, J., Czubak, J., and Wrobel, M. (2011) RP-HPLC method for quantitative determination of cystathionine, cysteine and glutathione: An application for the study of the metabolism of cysteine in human brain, *J Chromatogr B 879*, 2005-2009.

111. Zhuang, Y. L., Ma, F., Li-Ling, J., Xu, X. F., and Li, Y. D. (2003) Comparative analysis of amino acid usage and protein length distribution between alternatively and non-alternatively spliced genes across six eukaryotic genomes, *Mol Biol Evol 20*, 1978-1985.

112. Rae, T. D., Schmidt, P. J., Pufahl, R. A., Culotta, V. C., and O'Halloran, T. V. (1999) Undetectable intracellular free copper: The requirement of a copper chaperone for superoxide dismutase, *Science 284*, 805-808.

113. Wilson, M., Hogstrand, C., and Maret, W. (2012) Picomolar Concentrations of Free Zinc(II) Ions Regulate Receptor Protein-tyrosine Phosphatase beta Activity, *J Biol Chem 287*, 9322-9326.

114. Lincoln, S. F. (2005) Mechanistic studies of metal aqua ions: A semi-historical perspective, *Helv Chim Acta 88*, 523-545.

115. Nunez, M. T., Gaete, V., Watkins, J. A., and Glass, J. (1990) Mobilization of Iron from Endocytic Vesicles - the Effects of Acidification and Reduction, *J Biol Chem 265*, 6688-6692.

116. Sargent, P. J., Farnaud, S., and Evans, R. W. (2005) Structure/function overview of proteins involved in iron storage and transport, *Curr Med Chem 12*, 2683-2693.